

N67-24606
(ACCESSION NUMBER)
290
(PAGES)
CR-81603
(NASA CR OR TMX OR AD NUMBER)

FACILITY FORM 602

(THRU)

(CODE)

(CATEGORY)

VOLUME 3 OF 8

Final Report

ATS - 4

PREPARED BY

FAIRCHILD HILLER
SPACE SYSTEMS DIVISION

FOR

NASA
Goddard Space Flight Center

DECEMBER 1966

SSD 102.3

ATS-4 STUDY PROGRAM

FINAL REPORT

(Contract NASW-1411)

Volume THREE of EIGHT

N67 24606

prepared by

FAIRCHILD HILLER SPACE SYSTEMS DIVISION

Sherman Fairchild Technology Center

Germantown, Maryland

for

GODDARD SPACE FLIGHT CENTER

NATIONAL AERONAUTICS AND SPACE ADMINISTRATION

December 1966

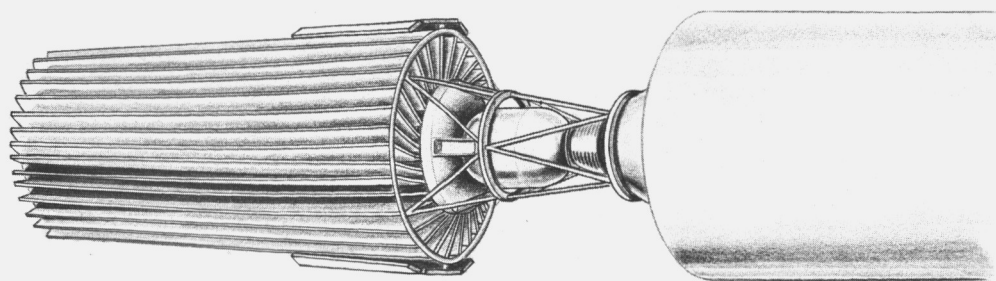
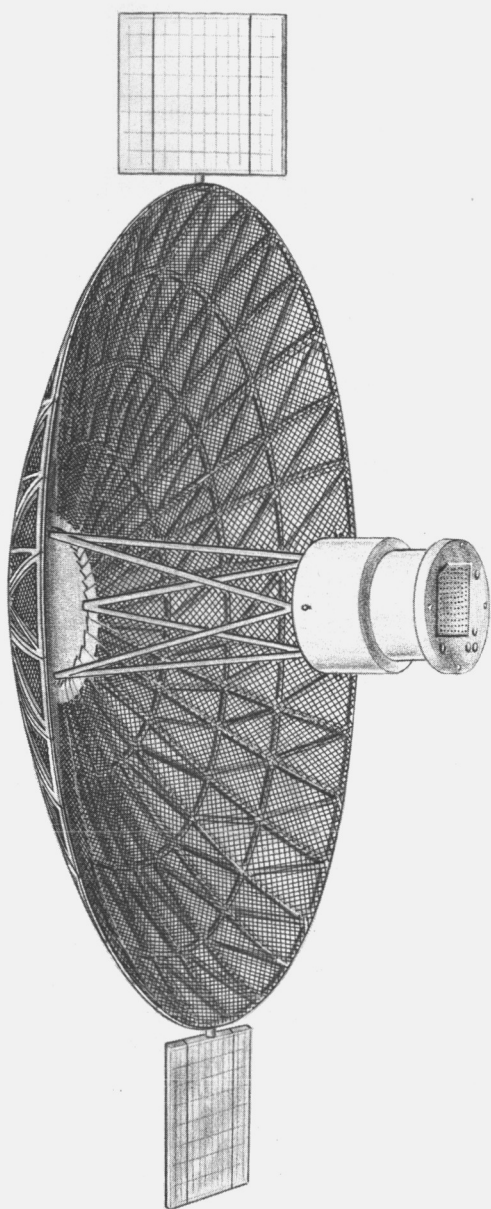


TABLE OF CONTENTS

VOLUME ONE

Section	Title	Page
1.0	Summary	1-1
1.1	Objectives and Justification	1-1
	1.1.1 Utilization	1-2
	1.1.2 Implementation	1-4
1.2	Program Feasibility	1-6
	1.2.1 Parabolic Antenna	1-6
	1.2.2 Stabilization and Control System	1-8
	1.2.3 Phased Array	1-11
	1.2.4 Interferometer	1-12
1.3	Subsystem Summaries	1-13
	1.3.1 Configuration Description	1-13
	1.3.2 Parabolic Reflector	1-19
	1.3.3 Parabolic Antenna Feed	1-22
	1.3.4 Attitude Stabilization and Control System	1-24
	1.3.5 Launch Vehicle - Ascent and Orbit Injection	1-27
	1.3.6 Interferometer System	1-32
	1.3.7 Phased Array	1-33
	1.3.8 In-Orbit Maneuvers and Auxiliary Propulsion System	1-35
	1.3.9 Additional Experiment Capability	1-37

TABLE OF CONTENTS

VOLUME TWO

Section	Title	Page
2.0	Systems Analysis	2-1
2.1	Mission Profile and Operations Plan	2-1
2.1.1	Mission Profile	2-1
2.1.2	Operations Plan	2-20
2.2	Experiment Plan	2-20
2.2.1	Parabolic Antenna Experiment	2-20
2.2.2	Monopulse System Operation	2-30
2.2.3	Phased Array Experiment	2-32
2.2.4	Orientation and Control Experiment	2-45
2.2.5	Interferometer Experiment	2-49
2.2.6	Additional Communication Experiments	2-54
2.3	Power Profiles	2-58
2.3.1	Preorbital Power	2-58
2.3.2	Experiment Evaluation	2-61
2.3.3	Experiment Demonstration	2-61
2.3.4	Power System Margin	2-61
2.3.5	Experiment Loads	2-64
2.4	Antenna Accuracy Considerations	2-68
2.4.1	Reflecting Surface Errors	2-68
2.4.2	Feed Location Errors	2-73
2.4.3	Frequency Limitations on Gain	2-74
2.4.4	Summary of Antenna Error Effects	2-76
2.5	Antenna Efficiencies	2-79
2.5.1	Parabolic Antenna	2-79
2.5.2	Phased Array Figures of Merit	2-82
2.6	Faisure Modes	2-91
2.6.1	System Considerations	2-91
2.6.2	Parabolic Antenna	2-91
2.6.3	Stabilization and Control System	2-93
2.6.4	Phased Array	2-98
2.6.5	Antenna Experiment Electronics	2-100
2.6.6	Phased Array Monopulse Operation	2-103
2.7	Weight Summaries	2-105

TABLE OF CONTENTS

VOLUME THREE

Section	Title	Page
3.0	Vehicle Engineering	3-1
3.1	Concept Evolution	3-1
	3.1.1 Trade-off Parameters	3-1
	3.1.2 F/D Trade-offs	3-6
	3.1.3 Spacecraft Concepts	3-8
3.2	Concept Evaluation and Reference Concept	3-21
	3.2.1 Launch Vehicle Choice	3-21
	3.2.2 Split Module Concept	3-21
	3.2.3 Reference Concept	3-25
	3.2.4 Concept Comparison	3-29
	3.2.5 Titan IIIC Adaptability	3-29
3.3	Reflector Design	3-33
	3.3.1 Design Evolution and Alternate Approaches	3-33
	3.3.2 Petal Hinging Concepts	3-38
	3.3.3 Petal Structural Design	3-40
	3.3.4 Deployment System	3-47
	3.3.5 Tolerance Considerations	3-47
	3.3.6 Reflecting Surface	3-50
	3.3.7 Petal Locking System	3-53
3.4	Reflector Fabrication	3-57
	3.4.1 Fabrication Considerations	3-57
	3.4.2 Aluminum Substructure	3-57
	3.4.3 Wire Mesh Forming	3-59
	3.4.4 Sub-Assemblies	3-60
	3.4.5 Tooling	3-60
	3.4.6 Assembly Procedure	3-64
	3.4.7 Measurement of Surface Deviations	3-65
3.5	Structural and Dynamic Analyses	3-71
	3.5.1 Analytical Methods and Approach	3-71
	3.5.2 Preliminary Analysis	3-77
	3.5.3 Integrated Spacecraft-Launch Configuration	3-104
	3.5.4 Integrated Spacecraft-Orbit Configuration	3-115
	3.5.5 Orbit Maneuvering	3-121

TABLE OF CONTENTS

VOLUME THREE (Continued)

Section	Title	Page
3.6	Thermo/Structural Analysis	3-129
	3.6.1 Thermal Requirements and Approach	3-129
	3.6.2 Design Orbit	3-133
	3.6.3 Petal Thermal Analysis	3-135
	3.6.4 Thermoelastic Analysis of Reflector	3-154
	3.6.5 Feed Mast Thermal Analysis	3-166
	3.6.6 Thermal Deformation of Feed Mast	3-172
	3.6.7 Spacecraft Thermal Control	3-175
3.7	Dimensional Stability	3-178
	3.7.1 Introduction	3-178
	3.7.2 Precision Elastic Limit	3-179
	3.7.3 Residual Stress	3-179
	3.7.4 Design Application	3-180
	3.7.5 References for Dimensional Stability	3-182
	Discussion	
3.8	In-Orbit Measurement of Antenna Surface	3-183
	Accuracy	
	3.8.1 Basic Techniques	3-183
	3.8.2 Operational Considerations	3-183
	3.8.3 Antenna Surface Errors	3-185
	3.8.4 Equipment Location	3-185
	3.8.5 Conceptual Design	3-186
	3.8.6 Error Resolution Requirements	3-189
	3.8.7 Sampling Surface Measurements	3-191
	3.8.8 The Axial Four Camera System	3-192
	3.8.9 Illumination of the Antenna	3-208
	3.8.10 System Operation	3-209
	3.8.11 General Comments	3-209
Appendix		
3A	Expandable Truss Antennas	3-211
3B	Inflatable Antennas	3-225
3C	Rigid Panel Antennas	3-230
3D	Petal Axis of Rotation Determination	3-248

TABLE OF CONTENTS

VOLUME FOUR

Section	Title	Page
4.0	Power Systems	4-1
4.1	Solar Panel Configuration Study	4-2
4.2	Solar Cell Radiation Degradation	4-6
4.2.1	Radiation Environment	4-6
4.2.2	Background Flux	4-7
4.2.3	Power Margin	4-10
4.3	Battery Characteristics	4-10
4.3.1	Nickel-Cadmium Battery	4-13
4.3.2	Silver-Cadmium Battery	4-13
4.3.3	Silver-Zinc Battery	4-15
4.3.4	Battery Comparison	4-15
4.4	Battery Charging and Control	4-23
4.4.1	Constant Current Charging	4-23
4.4.2	Constant Voltage Charging	4-24
4.4.3	Modified Constant Voltage Charging	4-26
4.4.4	Tapered Charging	4-26
4.4.5	Recommendation	4-26
4.5	Concept Power Subsystem	4-28
4.5.1	Design Approach	4-28
4.5.2	Battery Complement	4-32
4.5.3	Solar Array	4-35
4.5.4	Power Conditioning and Control	4-36
5.0	Orbital Analysis	5-1
5.1	General	5-1
5.2	Apogee Injection Stages	5-2
5.3	Ascent Trajectories	5-4
5.3.1	Requirements and General Considerations	5-4
5.3.2	Synchronous Injection - Single Apogee Impulse	5-7
5.3.3	Subsynchronous Injection - High Altitude Parking Orbit	5-10
5.3.4	Recommended Centaur Ascent Trajectory	5-18
5.4	Orbit Payloads	5-23
5.4.1	General	5-23
5.4.2	SLV3A/Agena and SLV3C/Centaur	5-23

TABLE OF CONTENTS
VOLUME FOUR (Continued)

Section	Title	Page
	5.4.3 Titan IIIC	5-30
	5.4.4 Payload Data Summary	5-30
5.5	Orbit Injection Errors	5-32
	5.5.1 Error Values	5-32
	5.5.2 Associated Latitude-Longitude Deviation	5-33
	5.5.3 Associated Corrective Velocity Impulse Requirements	5-36
5.6	Orbit Perturbations	5-39
	5.6.1 General	5-39
	5.6.2 Earth Oblateness and Extraterrestrial Perturbations	5-39
	5.6.3 Terrestrial Perturbations - Equatorial Ellipticity	5-41
	5.6.4 Associated Corrective Velocity Impulse Requirements	5-45
5.7	Auxiliary Propulsion System	5-48
	5.7.1 Velocity Impulse and Thrust Requirements	5-48
	5.7.2 Initial APS Comparison Study	5-48
5.8	Orbit Guidance	5-57
	5.8.1 General Requirements	5-57
	5.8.2 Orbit Injection Error Correction	5-58
	5.8.3 Station Keeping and Repositioning	5-63
5.9	References and Symbols for Orbital Analysis	5-65
	5.9.1 References	5-65
	5.9.2 List of Symbols	5-67

TABLE OF CONTENTS

VOLUME FIVE

Section	Title	Page
6.0	ATTITUDE STABILIZATION AND CONTROL SYSTEM	6-1
6.1	Attitude Stabilization and Control Requirements	6-1
6.1.1	Mission Requirements	6-1
6.1.2	Pointing Accuracy	6-1
6.1.3	Control Modes	6-1
6.2	Attitude Reference Subsystem	6-2
6.2.1	Alternate Approaches	6-2
6.2.2	Candidate Reference Sensors	6-11
6.2.3	Selected Configuration	6-22
6.2.4	Sensor Performance	6-23
6.3	Disturbance Torque Model	6-25
6.3.1	Meteoroid Import	6-25
6.3.2	Gravity Gradient	6-34
6.3.3	Magnetic Disturbance	6-35
6.3.4	Internal Rotating Equipment	6-35
6.3.5	Solar Pressure	6-35
6.4	Torquer Subsystem	6-52
6.4.1	Control Impulse Requirements	6-52
6.4.2	Candidate Reaction Jet Types	6-59
6.4.3	Inertia Wheel Subsystem	6-63
6.4.4	Selected Torquer Configuration	6-69
6.5	Computation and Data Handling	6-71
6.5.1	On-Board Computation	6-71
6.5.2	Up-Data Commands	6-71
6.5.3	Down-Data Monitor	6-71
6.6	System Operational Description	6-75
6.6.1	Control Mode Operation	6-75
6.6.2	System Block Diagram	6-85
6.6.3	Sensor Update	6-89
6.7	System Performance	6-90
6.7.1	Pointing Accuracy	6-90
6.7.2	Acquisition	6-93
6.7.3	Control System Dynamics	6-93
6.7.4	Reliability	6-117
6.8	System Physical Description	6-124
Appendix		
6A	Preliminary Control Torque and Impulse Requirements	
6B	Preliminary Reaction Jet Considerations	
6C	Preliminary Inertia Wheel Considerations For Candidate Vehicle Configurations	
6D	Preliminary Combined Wheel/Jet System Considerations	
6E	Preliminary Transfer Orbit Control Mode Analysis	

TABLE OF CONTENTS

VOLUME SIX

Section	Title	Page
7.0	Communications Experiments	7-1
7.1	Parabolic Antenna	7-1
	7.1.1 Beam Scanning	7-1
	7.1.2 Parabolic Antenna Feeds	7-14
	7.1.3 Aperture Blockage	7-32
	7.1.4 Paraboloid Performance	7-42
7.2	Phased Array	7-58
	7.2.1 Transdirective Array	7-59
	7.2.2 The Butler Matrix Array	7-63
	7.2.3 Space Fed (Lens) Array	7-65
	7.2.4 Corporate-Fed Array	7-71
	7.2.5 Corporate-Fed Phased Array Design Considerations	7-79
	7.2.6 Antenna Definition	7-92
	7.2.7 Digital Beam Steering Unit	7-102
	7.2.8 Packaging Configuration	7-108
7.3	Communications Equipment	7-111
	7.3.1 Transmission Parameters	7-111
	7.3.2 Systems Description	7-113
	7.3.3 Weight, Volume and Power Summary	7-134
	7.3.4 System Performance Summary	7-137
Appendix		
7A	Four Paraboloid Off-Set Feed Configuration	7-139
7B	Ionospheric Effects on Wave Polarization	7-147
7C	Separate 100 MHz Antennas	7-159
7D	Communication Components	7-165

TABLE OF CONTENTS

VOLUME SEVEN

Section	Title	Page
8.0	Radio Interferometer Experiment	8-1
8.1	Introduction	8-1
8.2	Study Approach	8-3
8.3	Candidate Interferometer Concepts	8-5
8.4	Candidate Interferometer Systems	8-11
	8.4.1 Selection Criteria	8-11
	8.4.2 System Block Diagrams	8-11
8.5	Selection of Preferred Concept	8-25
	8.5.1 Candidate Evaluation and Selection of Preferred System	8-25
	8.5.2 Phased Array as an Interferometer	8-44
8.6	Design of Preferred Interferometer System	8-48
	8.6.1 General Circuit Description	8-48
	8.6.2 Mechanical and Thermal Design	8-59
	8.6.3 Interferometer Attitude Sensor Interface	8-68
	8.6.4 Physical Characteristics	8-85
8.7	Error Analysis of Preferred Concept	8-86
8.8	Conclusions and Recommendations	8-116
8.9	Bibliography and Glossary	8-117
Appendix		
8A	Interference Reduction by Correlation	8-136
8B	RF Link Calculation	8-138
8C	Interferometer Angular Error Due to Mutual Coupling	8-141
8D	System Polarization	8-146
8E	Derivation of the Received Voltage Phases on an Elliptically Polarized Interferometer Antenna Pair with an Incident Elliptically Polarized Wave	8-165
8F	Alternative Antenna Switching Systems - Direct Phase Reading Interferometer	8-172
8G	Derivation of Counter Equation	8-180
8H	Gating Time Error Analysis	8-182
8I	Conversion of θ_s into Attitude	8-187
8J	Limitation of Range and Range Rate Capability	8-201
Volume 8	Program Budgetary Costs and Schedules	10-1

TABLE OF CONTENTS

VOLUME SEVEN (Continued)

Section	Title	Page
9.0	Summary	9-1
9.1	Data Flow	9-2
	9.1.1 Definition	9-2
	9.1.2 Requirements	9-2
	9.1.3 Model of the Data Flow	9-3
9.2	Telemetry System	9-8
	9.2.1 Data Handling Requirements	9-8
	9.2.2 Data Handling System Design	9-9
	9.2.3 Data Handling System Configuration	9-17
	9.2.4 Data Transmission System Design	9-23
	9.2.5 Data Transmission Link Calculation	9-28
	9.2.6 System Size, Weight and Power Estimates	9-44
	9.2.7 Equipment Implementation	9-44
9.3	Command System	9-47
	9.3.1 Definition	9-47
	9.3.2 Requirements	9-47
	9.3.3 Word Format	9-50
	9.3.4 Description and Operation of the Onboard System	9-53
	9.3.5 Estimates of Physical Characteristics	9-60
	9.3.6 Transmission Link Power Requirements	9-62
	9.3.7 Equipment Implementation	9-64
	9.3.8 Ground Equipment Requirements	9-65
9.4	Range and Range Rate Transponder	9-69
	9.4.1 Accuracy Requirements	9-69
	9.4.2 Transponder Operating Frequency Selection	9-69
	9.4.3 UHF Transponder Characteristics	9-70
	9.4.4 Equipment Implementation	9-71
9.5	Ground Station Requirements	9-72
	9.5.1 Ground Equipment Description	9-72
9.6	References	9-84
	Appendices	
	9A Commutator Channel Assignment	9-85
	9B Modulation Index Calculations (Mode I)	9-101
	9C Solving for Receiver Noise Power and Channel Bandwidth Ratios (Mode I)	9-103
	9D Solving for Receiver Noise Power and Channel Bandwidth Ratios (Mode II)	9-105
	9E Command Signal Catalog	9-106
	9F Telemetry Signal Catalog	9-116
	9G Data Questionnaire	9-131

LIST OF ILLUSTRATIONS

VOLUME ONE

Figure	Title	Page
1.3-1	Fairchild Hiller ATS-4 Concept	1-14
1.3-2	Reference Concept	1-15
1.3-3	Spacecraft Module Detail	1-18
1.3-4	Multiband Prime Focus Feed	1-23
1.3-5	SCS Block Diagram	1-29
1.3-6	ATS-4 Ascent Trajectory	1-31

LIST OF ILLUSTRATIONS

VOLUME TWO

Figure	Title	Page
2.1-1	Satellite Ground Track	2-2
2.1-2	Spacecraft/Sun Orientation in Transfer Orbit	2-4
2.1-3	Satellite Ground Track and Ground Station	2-12
2.1-4	Gross Data Flow Concept	2-17
2.2-1	Major Plane Location and Arts for Antenna Measurement	2-22
2.2-2	Ground Terminal Layout for Monopulse Calibration	2-33
2.2-3	Major Planes and Beam Positions for Station Pattern Tests	2-35
2.2-4	Multiple Pattern Arts Using Two Ground Stations	2-41
2.2-5	Crosstalk Measurement	2-41
2.2-6	Major Plane Arts - Interferometer	2-53
2.2-7	Pointing of the Z-Axis for Interferometer Measurement	2-53
2.3-1	Typical Experiment Evaluation Profile	2-62
2.3-2	Power Profile with Additional Experiments	2-62
2.3-3	Experiment Demonstration Maximum Profile	2-63
2.4-1	Classification of Parabolic Antenna Errors	2-69
2.4-2	Reflector Errors	2-71
2.4-3	Feed Location Errors	2-75
2.4-4	Feed Location Errors ($F/D = 0.3$)	2-78
2.4-5	Frequency Limitation on Gain	2-78
2.5-1	X-Band Radiation Pattern	2-81
2.6-1	Failed Reaction Wheel Backup Subsystem	2-94

LIST OF ILLUSTRATIONS

VOLUME THREE

Figure	Title	Page
3.1-1	Antenna Feed Location	3-3
3.1-2	C.G. Location Study	3-5
3.1-3	Concept SK513-10	3-13
3.1-4	Concept SK513-12	3-15
3.1-5	Concept SK513-11	3-16
3.1-6	Concept SK513-13	3-17
3.1-7	Concept SK513-14	3-18
3.1-8	Concept SK513-16	3-19
3.2-1	Concept SK513-18	3-23
3.2.2	Concept SK513-17 (Reference Concept)	3-24
3.2-3	Spacecraft Module Detail	3-27
3.2-4	Concept Comparison Chart	3-31
3.2-5	Reference Concept on Titan IIC	3-32
3.3-1	Conic Scissors Parabolic Antenna	3-34
3.3-2	Inflatable Parabolic Antenna	3-36
3.3-3	Retentive Memory Petal Concept	3-39
3.3-4	Non-Radial Petals, Sheet One	3-41
3.3-5	Non-Radial Petals, Sheet Two	3-42
3.3-6	Petal Concept Parabolic Antenna	3-43
3.3-7	Skewed Hinge Design	3-45
3.3-8	Petal Structural Assembly and Hinge Details	3-46
3.3-9	Deployment Synchronizer	3-49
3.3-10	Mesh Segment Installation	3-51
3.3-11	Mesh Reflector Characteristics	3-52
3.3-12	Inter-Petal Locks	3-55
3.3-13	Inter-Petal Lock - Preferred Concept	3-56
3.4-1	Shaping of Mesh Reflecting Surface	3-58
3.4-2	Master Tool	3-58
3.4-3	Assembly Bonding Fixture	3-62
3.4-4	Hinge and Latch Alignment Fixture	3-63
3.4-5	Measurement of Surface Deviations	3-67
3.5-1	Truss Feed Mast Weights	3-78
3.5-2	Truss Feed Mast Frequencies	3-79
3.5-3	Single Tube Feed Mast Analysis	3-81
3.5-4	Four Tube Feed Mast Weights	3-82
3.5-5	Four Tube Feed Mast Frequencies	3-83
3.5-6	Analysis of Quadruped Feed Mast Structure	3-84

LIST OF ILLUSTRATIONS

VOLUME THREE (Continued)

Figure	Title	Page
3.5-7	Quadruped Feed Mast Frequencies	3-85
3.5-8	Analysis of Tripod Feed Mast Structure	3-86
3.5-9	Tripod Feed Mast Frequencies	3-87
3.5-10	Reflector Petal Loading	3-94
3.5-11	Spacecraft, Injection, Motor and Adapter Structural Properties	3-94
3.5-12	Launch Integrated S/C - Analytical Model	3-96
3.5-13	Orbit Configuration - Mass Model	3-102
3.5-14	Preferred Configuration and Analytical Model	3-105
3.5-15	Petal Restraint and Stiffness	3-106
3.5-16	Mass Point Locations and Weights	3-107
3.5-17	YY Direction Mode Shapes	3-109
3.5-18	XX Direction Mode Shapes	3-110
3.5-19	Analytical Model - Orbit Configuration	3-116
3.5-20	Frequency and Mode Shapes - Orbit Configuration, Sheet One	3-118
3.5-21	Frequency and Mode Shapes - Orbit Configuration, Sheet Two	3-119
3.5-22	Frequency and Mode Shapes - Orbit Configuration, Sheet Three	3-120
3.5-23	Response to Single Finite Duration Pulse (Roll Correction Maneuver)	3-124
3.5-24	Response to Single Finite Duration Pulse (Yaw Correction Maneuver)	3-125
3.6-1	Yearly Change in Orbit Position Relative to Sun Vector	3-134
3.6-2	Petal Thermal Analysis	3-136
3.6-3	Relation of Thermal Analysis Nodes to Orbit Position	3-136
3.6-4	Feed Module Shadowing	3-137
3.6-5	Reflection Mesh Sunlight Blockage	3-139
3.6-6	Mesh and Antenna Hub Shadowing	3-141
3.6-7	Coordinate System for Thermal Analysis	3-142
3.6-8	Antenna Feed Shadowing	3-144
3.6-9	Beam Temperatures	3-147
3.6-10	Petal Beam Cross-Section	3-151
3.6-11	Mesh Standoff Fittings	3-151

LIST OF ILLUSTRATIONS

VOLUME THREE (Continued)

Figure	Title	Page
3.6-12	Beam Geometry	3-153
3.6-13	Petal Thermal Model	3-159
3.6-14	Radial Displacement Geometry	3-159
3.6-15	Deformation of Radial Member	3-159
3.6-16	Reflector Surface Mesh Geometry	3-165
3.6-17	Surface Mesh Chord Position	3-165
3.6-18	Feed Mast Geometry	3-167
3.6-19	Electrical Simulation, Uninsulated Mast	3-168
3.6-20	Electrical Simulation, Insulated Mast	3-168a
3.6-21	Temperature of Node 4, Uninsulated Mast	3-170
3.6-22	Temperature of Node 4, Insulated Mast	3-170a
3.6-23	Feed Mast Shadowing on Support "A"	3-171
3.6-24	Feed Mast Thermal Model	3-171a
3.6-25	Feed Mast Distortions	3-174
3.6-26	Passive Control Areas Average Temperature versus Dissipation	3-176
3.8-1	Volume Available for Measurement Equipment	3-187
3.8-2	Mirror Position above Camera	3-187
3.8-3	Converse Mirror below Camera	3-187
3.8-4	Concave Mirror below Camera	3-188
3.8-5	Sighting Angles	3-188
3.8-6	Effective Mesh Spacing	3-188
3.8-7	Composite Converse Mirror	3-192
3.8-8	Basic Four Camera Axial System	3-192
3.8-9	Full View Camera System	3-194
3.8-10	Normal Deflection Geometry	3-194
3.8-11	Ring Viewing Angles	3-194
3.8-12	Vidicon Image Dimensions	3-196
3.8-13	Central Circle in Vidicon Image	3-196
3.8-14	Radial and Circular Scan Patterns	3-198
3.8-15	Rim Marker Pattern	3-198
3.8-16	Modified Marker Coding	3-198
3.8-17	Reversed Marker Pattern	3-201
3.8-18	Marker Pattern without 1/2 Inch Plates	3-201
3.8-19	Pattern for Third Ring	3-202
3.8-20	Pattern for Second Ring	3-202

LIST OF ILLUSTRATIONS

VOLUME THREE (Continued)

Figure	Title	Page
3.8-21	Pattern for Central Ring	3-202
3.8-22	Pattern of Perfect Match of Image and Standard Negative	3-203
3.8-23	Pattern of Mismatch of Image and Standard Negative	3-203
3.8-24	Marking Pattern from Deformed Mesh Wires	3-207
3.8-25	Deformed Wires Positioned along a Parabola	3-207
3.8-26	Illumination by Columnar Light Sources	3-208
3.8-27	Illumination by Toroidal Light Sources	3-208

LIST OF ILLUSTRATIONS

VOLUME FOUR

Figure	Title	Page
4.1-1	Flat Plate Array, Two Degrees Of Freedom	4-3
4.1-2	Flat Plate Array, One Degree Of Freedom	4-3
4.1-3	Flat Plate Array, Fixed	4-3
4.1-4	Two Flat Plates Array, Fixed	4-4
4.1-5	Three Flat Plates Array, Fixed	4-4
4.1-6	Cylindrical Array, Fixed	4-4
4.1-7	Double Faced Flat Plate Array	4-5
4.1-8	Double Faced Two Flat Plates Array	4-5
4.1-9	Double Faced Three Flat Plates Array	4-5
4.2-1	Solar Cell Radiation Degradation	4-8
4.2-2	Power Loss Due To Radiation Effects	4-11
4.3-1	Nickel-Cadmium Battery Life	4-14
4.3-2	Energy Per Unit Weight For Various Batteries	4-17
4.3-3	Energy Per Unit Volume For Various Batteries	4-18
4.3-4	Capacity vs. Temperature For Various Cells	4-18
4.3-5	Silver-Zinc Battery Cycle Life	4-19
4.3-6	Silver-Cadmium Battery Cycle Life	4-19
4.3-7	Nickel-Cadmium Battery Cycle Life	4-20
4.3-8	Umbra and Penumbra Patterns For A Synchronous Equatorial Satellite	4-22
4.4-1	Recommended % Overcharge is Temperature	4-25
4.4-2	Overcharge Pressure Vs Current	4-25
4.4-3	Maximum Limiting Voltage Vs. Temperature	4-27
4.4-4	Tapered Charge Characteristic	4-27
4.5-1	Typical Experiment Evaluation Power Profile	4-29
4.5-2	Power Profile With Additional Experiments	4-29
4.5-3	Experiment Demonstration Maximum Demand Profile	4-29
4.5-4	Power System Weight Vs. Load Duration	4-29
4.5-5	Power System Block Diagram	4-37

LIST OF ILLUSTRATIONS

VOLUME FOUR (Continued)

Figure	Title	Page
5.3-1	Ascent Trajectories	5-6
5.3-2	Earth Track of Ascent Trajectory	5-11
5.3-3	Injection Station Longitude Variation	5-11
5.3-4	Effect of Launch Azimuth on Required Increase in Characteristic Velocity	5-14
5.3-5	High Altitude, Elliptic Parking Orbit Characteristics	5-16
5.3-6	Earth Track of High Altitude Parking Orbit Ascent Trajectory	5-17
5.3-7	Ground Track of Ascent Trajectories	5-19
5.3-8	Spacecraft/Sun Orientation in Transfer Orbit	5-21
5.4-1	Payload and AIS Propellant Weight vs i_c (Burner II)	5-28
5.4-2	Payload and AIS Propellant Weight vs i_c (TE364-3)	5-28
5.6-1	Satellite Semimajor Axis Perturbation	5-42
5.6-2	Satellite Inclination Perturbation	5-42
5.6-3	Long Period Oscillation	5-44
5.6-4	Required Velocity Impulse per Year	5-46

LIST OF ILLUSTRATIONS

VOLUME FIVE

Figure	Title	Page
6-1	Reference Coordinate Frame (Nominal)	6-3
6-2a	Cell Orientation	6-13
6-2b	Cell Outputs	6-13
6-2c	Sun Sensor Signals	6-13
6-3	Meteoroid Extrapolations	6-29
6-4	Percent Open Area in Each Mesh Segment as a Function of Solar Incident Angle	6-41
6-5	Antenna Projected Surface Map	6-43
6-6	Projected Antenna Shaded Area Profile	6-44
6-7	Pitch Axis Solar Pressure Disturbance Torque	6-47
6-8	Roll Axis Solar Pressure Disturbance Torque Due to Antenna and Feed System	6-48
6-9	Roll Axis Solar Pressure Disturbance Torque Due to Fixed Solar Panels Only	6-49
6-10	Roll Axis Solar Pressure Disturbance Torque	6-50
6-11	Yaw Axis Solar Pressure Disturbance Torque	6-51
6-12	Hydrazine Thruster Output Efficiency	6-62
6-13	Liquid Hydrazine System Schematic	6-64
6-14	Block Diagram - Ascent Control	6-86
6-15	SCS Block Diagram	6-87
6-16	Phase Plane Plot Sun Acquisition - Pitch Axis	6-94
6-17	Phase Plane Plot Sun Acquisition - Yaw Axis	6-95
6-18	Phase Plane Plot Earth Acquisition Roll Axis	6-96
6-19	Phase Plane Plot Star Acquisition Yaw Axis	6-97
6-20	Open Loop Bode Plot - Roll Axis	6-99
6-21	Open Loop Bode Plot - Pitch Axis	6-100
6-22	Open Loop Bode Plot - Yaw Axis	6-101
6-23	SCS and Vehicle Dynamics Block Diagram	6-102
6-24	Roll Axis - Rigid Body Amplitude Response	6-104
6-25	Roll Axis - Rigid Body Phase Response	6-105
6-26	Pitch Axis - Rigid Body Amplitude Response	6-106
6-27	Pitch Axis - Rigid Body Phase Response	6-107
6-28	Amplitude Response Roll Axis - Flexible (.01)	6-108
6-29	Phase Response Roll Axis - Flexible (.01)	6-109
6-30	Phase Response Pitch Axis - Flexible (.01)	6-110
6-31	Phase Response Pitch Axis - Flexible (.01)	6-111
6-32	Amplitude Response Roll Axis - Flexible (.005)	6-112
6-33	Phase Response Roll Axis - Flexible (.005)	6-113
6-34	Amplitude Response Pitch Axis - Flexible (.005)	6-114

LIST OF ILLUSTRATIONS

VOLUME FIVE (Continued)

Figure	Title	Page
6-35	Phase Response Pitch Axis - Flexible (.005)	6-115
6-36	Phase Plane Plot Attitude Control During Station Keeping	6-118
6-37	Reliability Diagram	6-119
6A-1	Limit Cycle Impulse Requirements	6A-7
6A-2	Disturbance Torque Impulse Requirements	6A-8
6A-3	Maneuver Impulse Requirements	6A-9
6B-1	Micro-Rocket Applicability Thrust and Total Impulse	6B-4
6B-2	Micro-Rocket Applicability Thrust and Duty Cycle	6B-5
6B-3	Estimated System Weight as a Function of On Board Total Impulse	6B-7
6B-4	Reliability Comparison of Bipropellant or Monopropellant System	6B-8
6B-5	Hydrazine Plenum System Schematic	6B-10
6B-6	Liquid Hydrazine System Schematic	6B-11

LIST OF ILLUSTRATIONS

VOLUME SIX

Figure	Title	Page
7.1-1	Prime Focus Paraboloid Scanning Performance	7-3
7.1-2	Paraboloid Gain Loss as a Function of Beamwidths Scanned	7-4
7.1-3	Beam Scanning Capability of a Multi-Element Paraboloid Switching -Feed System	7-7
7.1-4	Beam Cross-Over Level as a Function of the Beam Scanning Increment	7-8
7.1-5	Cassegrain Antenna Gain Loss with Subdish Rotation	7-11
7.1-6	Radiation Characteristics of a Tapered Circular Aperture	7-16
7.1-7	Paraboloid Subtended Angle and Feed Size as a Function of the F/D Ratio	7-18
7.1-8	S-Band Feed-Edge Taper	7-23
7.1-9	800 MHz Prime Focus Feed	7-24
7.1-10	100 MHz Prime Focus Feed	7-27
7.1-11	Spiral Antenna Monopulse Operation	7-29
7.1-12	Parabolic Antenna Gain Loss as a Function of the Blockage Ratio	7-34
7.1-13	X-Band Radiation Pattern	7-35
7.1-14	Antenna Test Range	7-38
7.1-15	Source Tower	7-39
7.1-16	Feed Support Mast	7-44
7.1-17	Paraboloid Assembly	7-45
7.1-18	Back View of Feed Support	7-46
7.1-19	Left Side View of Feed and Feed Support	7-47
7.1-20	Right Side View of Feed and Feed Support	7-48
2.1-21	Right Side View of Feed	7-49
7.1-22	Feeds, End View	7-50
7.1-23	Feeds, Side View	7-51
7.1-24	E-Plane Radiation Patterns, Frequency 4.6 GHz	7-52
7.1-25	E-Plane Radiation Patterns, Frequency 10.5 GHz	7-53
7.1-26	E-Plane Radiation Patterns, Frequency 12.0 GHz	7-54
7.1-27	E-Plane Radiation Pattern, Frequency 18.0 GHz	7-55
7.1-28	E-Plane Radiation Pattern, Frequency 29.6 GHz	7-56

LIST OF ILLUSTRATIONS

VOLUME SIX (Continued)

Figure	Title	Page
7.2-1	Transdirective Array	7-60
7.2-2	Butler Matrix Array - Block Diagram	7-64
7.2-3	Space Fed (Lens) Array - Block Diagram	7-67
7.2-4	Stripline Diplexer	7-69
7.2-5	Stripline Latching Phase Shifter	7-70
7.2-6	Corporate-Fed Array	7-72
7.2-7	Artist Conception of Corporate-Fed Array	7-75
7.2-8	Schematic of Microwave Subsystem	7-80
7.2-9	Detail of Feed Horn Assembly	7-83
7.2-10	Possible Configuration of 4 Channel Diplexer - Circulator Strip Line Module	7-86
7.2-11	Waveguide Latching Phase Shifter	7-89
7.2-12	Array Element Layout	7-94
7.2-13	Phased Array Patterns	7-95
7.2-14	Phased Array Beam Spacing	7-101
7.2-15	Block Diagram for Digital Beam Steering Unit	7-103
7.2-16	Schematic Diagram for Bit Driver	7-105
7.2-17	Plan View of Radiating Elements	7-107
7.2-18	Side View of Corporate-Fed Array	7-108
7.2-19	End View of Corporate-Fed Array	7-109
7.3-1	RF Power vs Ground Antenna Gain	7-116
7.3-2	ATS-4 Communications System	7-119
7.3-3	Frequency Generator	7-120
7.3-4	Monopulse and Phased Array X-Band Transfer Characteristics-Series 100	7-126
7.3-5	100 MHz Relay Transfer Characteristics-Series 200	7-127
7.3-6	X-Band Transponder Output-Reflector and Phased Array Transfer Characteristics-Series 300	7-128
7.3-7	800 MHz Relay Transfer Characteristics-Series 400	7-129
7.3-8	Filter Response	7-130
7.3-9	S-Band Data Link Transfer Characteristics- Series 500	7-131
7.3-10	X-Band Frequency Generator-Representative Transfer Characteristics-Series 600	7-132
7.3-11	Multipliers in Frequency Generator, Represen- tative Transfer Characteristics-Series 700	7-135

LIST OF ILLUSTRATIONS

VOLUME SIX (Continued)

Figure	Title	Page
7A-1	Four Paraboloid Offset Feed Configuration	7-140
7A-2	Radiation Pattern of a 15-Foot Paraboloid 10 db Tapered Distribution	7-141
7A-3	Radiation Pattern Four Paraboloid Array	7-142
7A-4	Monopulse Radiation Pattern of the Four Paraboloid Array	7-144
7A-5	Four Paraboloid Array Scanning Performance	7-145
7B-1	Faraday Rotation as a Function of Frequency	7-152
7B-2	Attenuation between Arbitrarily Polarized Antenna Caused by Faraday Rotation AF - Axial Ratio	7-156
7B-3	Attenuation between Arbitrarily Polarized Antennas Caused by Faraday Rotation AR - Axial Ratio	7-158
7C-1	Helical Antenna Gain as a Function of Antenna Length	7-161
7C-2	Array Element Spacing as a Function of Array Element Gain	7-163

LIST OF ILLUSTRATIONS

VOLUME SEVEN

Figure	Title	Page
8.4-1	LF Phase Reading Interferometer	8-13
8.4-2	RMS Phase Difference Reading Interferometer Technique	8-16
8.4-3	RF Cross Correlation Interferometer Technique	8-19
8.4-4	Spread Spectrum Interferometer Technique	8-22
8.5-1	Resultant Nonambiguous Pattern after Correlation	8-26
8.5-2	Partial System Schematic of Cross Correlator Interferometer	8-30
8.5-3	Monopulse Space Angle RMS Error	8-31
8.5-4	RMS Space Angle Error Direct Phase Reading Interferometer	8-33
8.5-5	Direct Phase Reading Interferometer Relationship, Space Angle Element Separation, Unambiguous Interval vs D/λ	8-36
8.5-6	Interferometer Phase Error Due to Temperature Differential in Transmission Lines	8-37
8.5-7	Layout of Phased Array	8-45
8.6-1	Direct Phase Reading Interferometer	8-48
8.6-2	Interferometer	8-53
8.6-3	Horn Design	8-63
8.6-4	Interferometer Thermal Flow Diagrams	8-66
8.6-5	Interface between the SCS and Interferometer	8-69
8.6-6	Mode Selection and Phase Measurement	8-72
8.6-7	Timing Diagram for Phase Measurement	8-74
8.6-8	Arithmetic Unit for $\epsilon'_z + \epsilon''_z$ and $\epsilon'_y + \epsilon''_y$	8-78
8.6-9	Arithmetic Unit for $\epsilon'_x + \epsilon''_x$	8-79
8.6-10	Timing Diagram for Computational Instruction	8-81
8.6-11	Time Distribution of the Arithmetic Units	8-82
8.7-1	System Model	8-87
8.7-2	Simplified Block Diagram of Direct Phase Reading Electronics	8-88
8.7-3	Basic Interferometer Relationship	8-90
8.7-4	Geometrical Relationship of Spacecraft Position and Ground Station	8-92
8.7-5	Error in Count vs θ_s	8-96
8.7-6	Refraction Effects	8-97
8.7-7	Atmospheric Effect on Elevation Angle	8-98
8.7-8	Atmospheric Effect on the Slant Range Difference	8-99

LIST OF ILLUSTRATIONS

VOLUME SEVEN (Continued)

Figure	Title	Page
8.7-9	Spacecraft Coordinate System	8-105
8.7-10	Pitch Axis 3σ Error vs Pitch Angle, θ	8-107
8.7-11	Yaw Axis 3σ Error vs Pitch Angle, θ	8-108
8.7-12	Vector Diagram of Satellite - Ground Station Geometry	8-109
8.7-13	Orientation of R_s	8-113
8B-1	ERP vs SNR	8-140
8C-1	Space Angular Error ($\Delta\theta_m$) vs Antenna Separation (D/λ) for Different Mutual Couplings (C)	8-142
8C-2	Space Angle Error Due to Mutual Coupling - Coarse Antenna Pair	8-143
8C-3	Comparison of Antenna Elements - Mutual Coupling	8-145
8D-1	Elliptically Polarized Interferometer Antenna Pair with Elliptically Polarized Incoming Wave	8-149
8D-2	Phase Angle Error vs Axial Ratio Inequality	8-152
8D-3	Phase Angle Error vs Ellipse Tilt Angle Inequality	8-155
8D-4	Phase Angle Error vs Roll Angle (δ)	8-160
8D-5	Phase Angle Error vs Pitch Angle (θ)	8-161
8E-1	Elliptically Polarized Plane Wave	8-166
8E-2	Elliptically Polarized Plane Wave Incident at Angles θ, δ	8-167
8E-3	Receive Antenna with Inclined Polarization Ellipse	8-168
8F-1	Switched Signal Lines	8-174
8F-2	Switched Oscillator Lines	8-175
8F-3	Switched IF Lines	8-176
8F-4	Switched Multipliers	8-177
8H-1	Phase Error Distribution at Start of Count	8-186
8H-2	Phase Error Distribution at End of Count	8-186
8H-3	Phase Error Density Function	8-186
8I-1	Interferometer Illumination	8-188
8I-2	Satellite Orientation	8-193
8J-1	Geometry for Range and Range Rate Analysis	8-201

LIST OF ILLUSTRATIONS

VOLUME SEVEN (Continued)

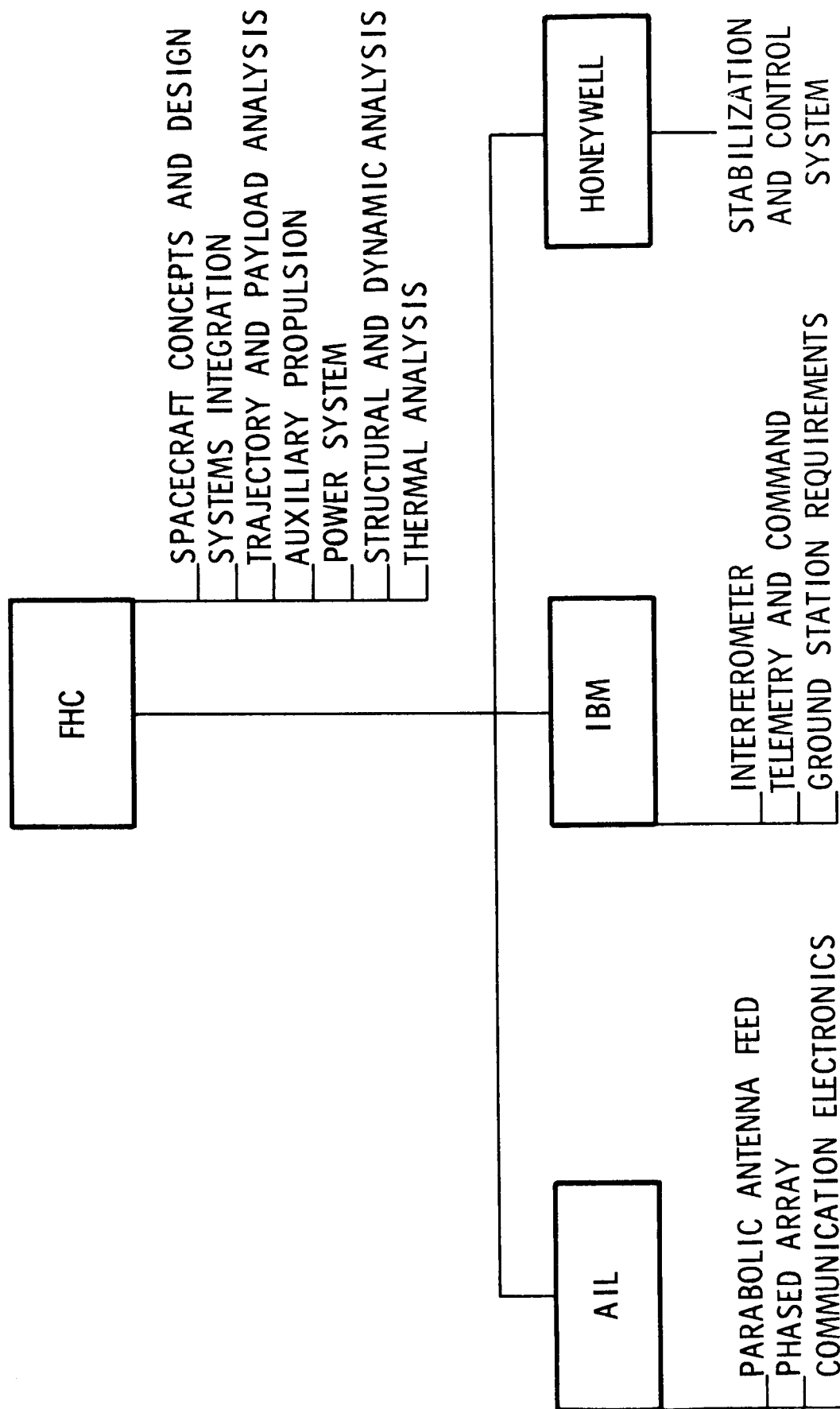
Figure	Title	Page
9.1-1	Onboard System Data Flow, Interfaces to Ground Equipment	9-4
9.1-2	Ground Station Data Flow; Interfaces to Spacecraft and Other Ground Stations	9-5
9.2-2	Basic Commutation Configuration	9-15
9.2-2	Data Handling System Configuration	9-18
9.2-3	Telemetry Data Transmission System	9-25
9.2-4	Telemetry Data Handling and Transmission Configuration	9-33
9.2-5	Block Diagram of Basic Telemetry Receiver	9-38
9.3-1	Command Word Structure	9-51
9.3-2	Command System	9-54
9.3-3	Command Decoder	9-55

PREFACE

This report covers the efforts of Fairchild Hiller Corporation and its team of subcontractors on NASA Contract (NAS-W-1411). The team organization and responsibilities during the study effort are shown on the accompanying chart. The report is divided into eight volumes, as follows:

Volume 1	Summary
Volume 2	Systems Analysis
Volume 3	Vehicle Engineering
Volume 4	Power System
	Orbital Analyses, Propulsion and Guidance
Volume 5	Stabilization and Control
Volume 6	Communication Experiments
Volume 7	Radio Interferometer Experiment
	Telemetry and Command Systems
Volume 8	Program Budgetary Costs and Schedules

ATS-4 TEAM ORGANIZATION



3.0 VEHICLE ENGINEERING

3.1 CONCEPT EVOLUTION

3.1.1 Trade-Off Parameters

The initial spacecraft concept and configuration studies concentrated on the possible alternatives in the general arrangement. The system and performance trade-offs of these configuration were assessed and are described in other sections of this report. The method of deploying the parabolic reflector was the dominant feature of all the configurations and, in a sense, served as the focal point in the generation of the various designs. The task was complicated by the booster alternatives for the study (Atlas-Agena, Atlas-Centaur and Titan 3C). In addition to the launch vehicle payload capability, the interface requirements, shroud limitations and adaptor requirements significantly impacted the spacecraft configurations. The matrix of concepts was further influenced by the apogee injection requirements. The use of Titan 3C eliminated the need of a separate apogee injection stage since the Transtage can inject a respectable payload into synchronous-equatorial orbit while at the same time providing three-axis stabilization during the transfer orbit. Use of Atlas-Agena or Atlas-Centaur necessitated the use of a separate apogee stage or motor with its attendant differences in transfer stabilization mode and the corresponding effects on configuration.

Shroud and Separation Considerations - The standard shrouds associated with the various launch vehicles limited the approaches for deploying the parabolic reflector. The concepts that lent themselves to packaging in the limited, standard shroud volumes were in general lacking in reflector surface accuracy for X-band operation. This is discussed in greater length in section 3.3 of this report. Consequently, the trade-offs regarding surface accuracy requirements necessitated the use of an OAO or extended Surveyor shroud.

The separation systems of the vehicles with separate apogee injection stages generally required two separation events after entering the parking orbit. The separation of the second stage of the launch vehicle occurred after injection into the transfer orbit. The second event took place after synchronous injection and separated the apogee stage or motor from the spacecraft. In some concepts, consideration was given to retaining the spent apogee stage to help the orbital C. G. location problem. Initial design approaches generally sought to attach the motor in a manner permitting a clean separation (not buried inside the spacecraft module), however the resultant shroud lengths exceeded the length restrictions imposed by NASA. Consequently, serious thought was given to a partially buried apogee engine.

Prime Focus vs Cassegrain - Parametric studies of cassegrain antenna configurations showed that the feed may be located anywhere between the main parabolic reflector and the hyperbolic sub-reflector (as a matter of fact, the feed may be located behind the main parabolic reflector). As the feed is located farther from the sub-reflector, the angle subtended by the sub-reflected decreases. Consequently, the feed aperture increased, in order to properly illuminate the sub-reflector. Furthermore, the shape of the sub-reflector also changed (even though the diameter was maintained constant), as the feed is moved away, in order to focus the radiation on the feed. Figure 3.1-1 is an example of the size relationships between the sub-reflector and feed as a function of a matrix of sub-reflector and feed locations for an $F/D = 0.3$. The curves show that cassegrain systems generally are larger and consequently heavier than corresponding prime focus feeds. This data when factored into the configuration studies did not point to any advantages for a cassegrain system.

Solar Panels - Considerable effort was expended studying the most effective solar panel arrangement. Previous Fairchild Hiller studies of

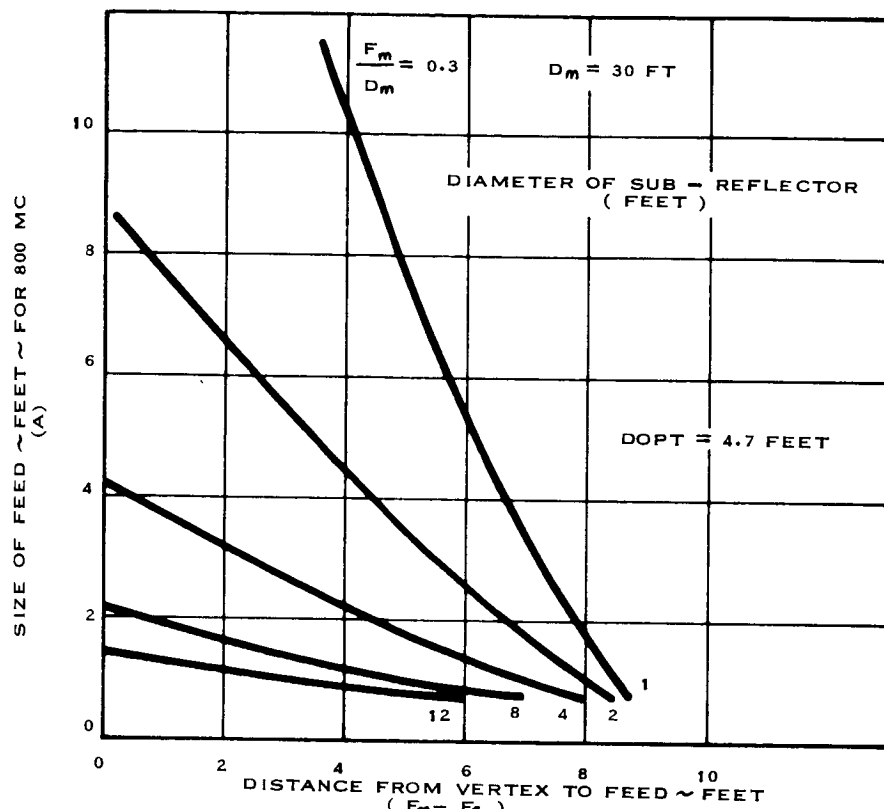


Figure 3.1-1 (a) Influence of Feed Location on Feed Size

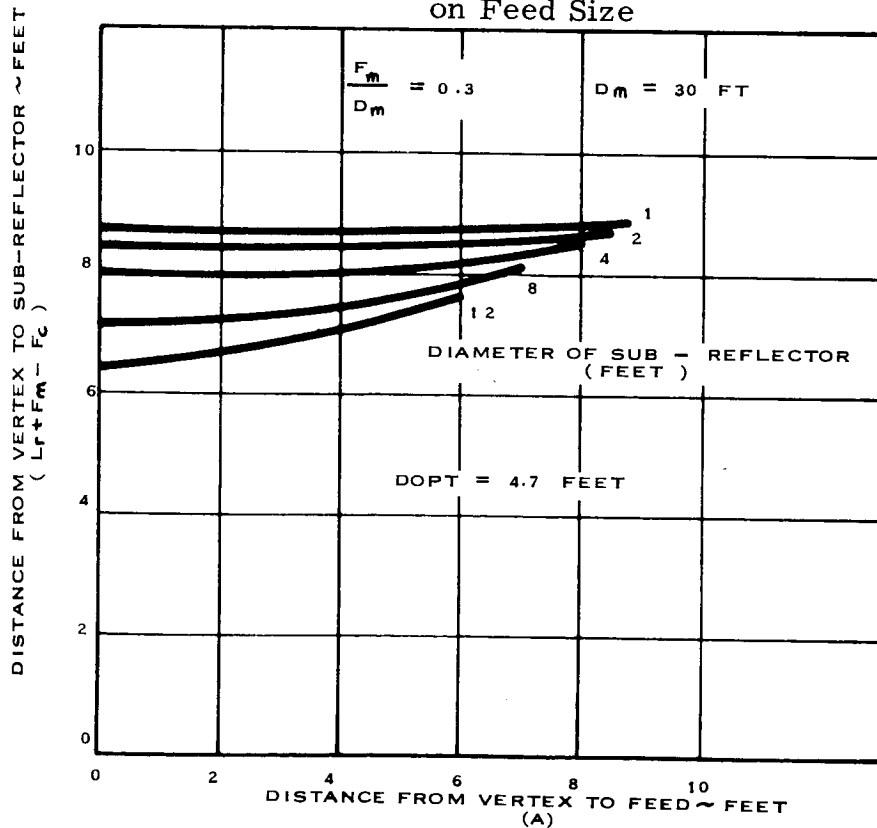


Figure 3.1-1 (b) Subreflector Position vs. Feed Location

earth oriented synchronous-equatorial satellites utilizing large parabolic reflectors concluded that the solar panels should be located at the rim of the reflector. The alternatives to this approach considered solar panel locations behind the reflector which were partially shadowed by the reflector. Utilizing a mesh reflecting surface minimized the actual shadowing (in terms of % area) for a solar vector that traverses a 2π field of view. However, the series/parallel connections required for the cells caused entire cell modules to be rendered ineffective because of shadowing of a single cell.

The solar panels attached to the rim of the reflector possessed either a single degree of freedom about the pitch axis with cells on one surface or were arranged in a fixed cruciform with cells on two surfaces. The weight trade-off was 2:1 in favor of the single degree of freedom panels with a reliability advantage for the fixed cruciform arrangement. During launch, the paddles were either "wrapped" around the body of the stowed reflector petals or stowed as disks above the experiment package. The arrangement was dependent on the configuration with a distinct advantage accruing to the "wrap around" arrangement because of its pre-orbital power capability.

Equipment Module - Several equipment module locations for the spacecraft equipment and experiment modules were studied. Locations above or below the vertex of the reflector, near the parabolic focus, and split modules were considered. One of the key configurational problems concerned itself with a C. G. location that permitted use of the auxiliary propulsion system (APS) without a major reorientation of the spacecraft. Figure 3.1-2 illustrates the mass model requirements of one of the early spacecraft concepts to achieve this goal. An APS location off the C. G. was possible if counterbalanced by a properly positioned pulsating thruster on the feed mast; however, this approach was rejected because of the complexities of the control logic and the required plumbing and nozzle installation

ASSUMPTIONS

W_1 = EXPERIMENTS FEED	1200 LB
W_2 = SPACECRAFT	
W_3 = SOLAR PANELS	60 LB
W_4 = ANTENNA	210 LB
W_5 = FEED SUPPORT	30 LB
TOTAL	1500 LB
W_6 = APOGEE ENGINE	250 LB
TOTAL	1750 LB
(WITH ENGINE)	

CONCLUSIONS

- (1.) MINIMUM F D TO PRECLUDE SOLAR PADDLES FROM BLOCKING STAR TRACKER = .325
- (2.) MAXIMUM W_1 TO PRODUCE CG AFT OF ANTENNA WHEN APOGEE ENGINE IS RETAINED = 163 LB
- (3.) MAXIMUM W_1 TO PRODUCE CG AFT OF ANTENNA WHEN APOGEE ENGINE IS JETTISONED = 59 LB

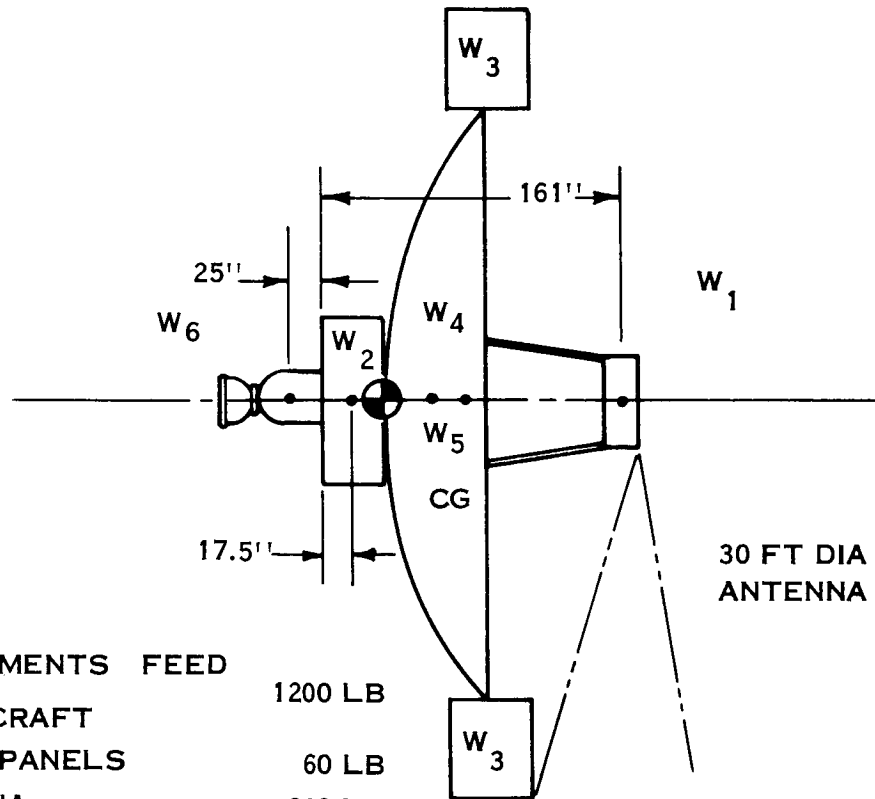


Figure 3.1-2 CG Location Study

on the feed mast. Another APS installation goal was a minimization of the distance between the nozzle and spacecraft C. G.; this was desirable to reduce the attitude fuel requirements during thrusting due to nozzle angular installation tolerances.

The installation of the attitude control jets at the tips of the reflector was considered but the reliability problems of a flexible joint coupled with the development status of micro-pound thrusters made this approach unattractive. Consequently the attitude control jets were placed on the outside of the equipment module and configured in a manner to thrust away from the reflector surface and sensors.

Many of the early spacecraft concepts assumed equipment modules near the maximum shroud diameter. However, as the study progressed it became evident that the available volume exceeded the requirements. This resulted in a reduction to a five foot diameter module in some of the later concepts, including the reference concept.

The phased array, interferometer and attitude sensors all competed for space at the earth facing end of the spacecraft. These installation requirements coupled with aperture blockage considerations resulted in sizing the phased array near the minimum specified gain value (30 db).

3.1.2 F/D Trade-Offs

A major system trade-off concerned the F/D ratio. Four important factors were considered:

- Scan Capability
- Weight
- Obscuration of Star Tracker
- Illumination of Reflector

Obscuration of the star tracker set the minimum F/D ratio at a value of 0.325; the second factor (weight) dictated that the F/D ratio be as small as possible; the first factor turns out not to be a consideration, since scan requirements cannot be met by off-axis motion of the feed. A minimum F/D of 0.25 results from illumination considerations. Thus, the final choice of F/D dictated within narrow limits by the engineering trade-offs, was 0.325.

Discussion of the four factors is given in the following paragraphs:

Scan Capability - Coverage of the visible earth from synchronous orbit requires that the parabolic antenna beam be scanned about 30 beamwidths at X-band. At S-band, this is only 9 beamwidths. An examination of scan loss curves of section 7.1.1 shows that exorbitant scan losses will result, for frequencies above S-band, for both prime focus systems and cassegrain systems. For scan capabilities of 10 beamwidths, reasonable losses in the range of 1-2 db can be expected, for either configuration, for F/D ratios near 1.0. Severe weight penalties are, however, associated with large ratios of F/D.

Since earth-disk coverage at X-band cannot be achieved by motion of the feed off-axis, scanning will be accomplished by motion of the entire parabolic antenna and spacecraft. Therefore scanning is not a consideration in determining the F/D ratio of the ATS-4 large parabolic antenna.

Weight - The weight of the feed mast is very sensitive to its length (and hence to F/D ratio). The parametric curves of section 3.5 show feed mast weights ranging from less than 60 pounds for an F/D = 0.3 to more than three hundred pounds for an F/D = 0.5. Mast weights are dictated by considerations of column stability of the tripod members.

The conclusion from weight considerations is that the F/D ratio should be as small as possible. Reduction of F/D from 0.3 to 0.25 would result in a weight saving of about 30 pounds.

Obscuration of Star Tracker - To provide an unobstructed field of view for the Polaris star tracker dictates a minimum F/D of 0.325, if rotating solar panels are used. For fixed solar panels, a slightly smaller value of minimum F/D is permitted. An alternate location of the star tracker is deemed impractical, since separation of the star tracker from other control components is undesirable.

The conclusion from considerations of star tracker field-of-view is that the F/D ratio should not be less than about 0.325.

Illumination of Reflector - Reflectors with $F/D = 0.25$ require that the feeds illuminate 180° of reflector surface. It is difficult to design a single feed which has a beamwidth of 180° and also produces uniform phase on the reflector aperture. It is impractical to design four integrated feeds, operating at four bands of frequencies between 100 MHz and 9 GHz, all of which have beamwidths of 180° (or greater), because of the interference of the larger feeds on the smaller ones. A minimum F/D of 0.25 is indicated, from feed design considerations.

The conclusion indicated from the preceding trade-offs is that the F/D ratio should be about 0.3. This results in a modest weight penalty (compared to the limiting weight of a system with $F/D = 0.25$) but obviates severe problems associated with the star tracker field of view. In addition, design of the dish feeds is eased somewhat.

The recommended value of F/D is 0.325.

3.1.3 Spacecraft Concepts

Some of the concepts which incorporated the configurational trade-offs previously discussed are included in the following pages with a short description of each configuration. The concept evaluation and choice is covered in Section 3.2.

Concepts SK513-10 and -12 (Figure 3.1-3 and 3.1-4) - These concepts are similar since they represent the same weight and inertia regime and utilize identical methods for deploying the parabolic reflector. The spacecraft depicted on Figure 3.1-3 utilizes a Titan 3C launch vehicle to inject the spacecraft into the required orbit and consequently does not require an apogee kick motor for this weight class. The concept illustrated by Figure 3.1-4 is launched by an Atlas-Centaur launch vehicle and injected into synchronous orbit by the Burner II apogee injection stage. The auxiliary propulsion engine is located at the center of the phased array structure (Figure 3.1-4 only).

Both concepts utilize the OAO shroud to house the spacecraft and are assumed to be in the 1700 pound weight class. The solar panels comprise an area of 72 square feet and the phased array is 7 feet in diameter.

The parabolic reflector is formed by the deployment of 30 skewed axis rigid panels which are locked to each other after deployment. The petals are stowed in a manner permitting a substantial support truss to react the feed and phased array launch loads.

The solar panels are stowed external to the folded petals and are deployed by the motion of two oppositely located folding parabolic petals.

Disadvantages of this concept are the large separation between C. G. and auxiliary propulsion system (true of only Figure 3.1-4), feed blockage by the feed support structure and a 5% aperture blockage due to the phased array.

Concept SK513-11 (Figure 3.1-5) - This concept represents a rigid petal design again utilizing a single skewed axis of rotation to deploy each panel. The panels are stowed radially and when deployed are locked to each other to form an inverted parabola. The spacecraft module and phased array are located near the parabolic focus. The apogee injection stage

(Burner II) is located near the booster interface with the auxiliary propulsion system located above the parabolic vertex.

As depicted, it is launched by an Atlas-Centaur launch vehicle and is stowed in the forward portion of the OAO shroud with a 62 inch cylindrical extension required to adapt to the Centaur-fairing interface. The solar panels (80 ft^2 total) are stowed in dihedral fashion around the central support structure and deployed by the motion of two oppositely located folding parabolic petals.

The concept has the disadvantage of a large separation between the C. G. and the auxiliary propulsion system making it more sensitive to torques created by thrust axis misalignment. The large phased array and spacecraft location will result in about a 5% aperture blockage.

Concept SK513-13 (Figure 3.1-6) - This concept represents a vehicle launched by an Atlas SLV-3A-Agena booster and housed in "the Nimbus" shroud. The limited volume and small shroud diameter require the use of the conic scissors method of deployment and a telescoping feed. The antenna F/D is limited to 0.4 because of the shroud constraints and consequently the performance is degraded (due to method of antenna deployment - see 3.3.1).

The apogee injection motor (TE-M-364-2) is buried in the spacecraft due to volume limitations. This vehicle is spin stabilized during the transfer orbit.

The concept depicted is in the 900 lb. weight regime. The auxiliary propulsion system is along the Y axis thus simplifying the required orientation maneuvers during north-south station keeping. The inert weight of the apogee injection motor (since it is not jettisoned) yields a C. G. location that makes this arrangement feasible.

Concept SK513-14 (Figure 3.1-7) - This concept represents a vehicle launched by an Atlas SLV-3C/Centaur booster. It is in the 1700 lb. weight class and housed in an OAO or modified Surveyor shroud. The concept depicted is spin stabilized during the transfer orbit and utilizes the TE-M-364-2 engine as an apogee injection motor. The inert motor remains with the spacecraft after injection. The shroud and payload are attached at a common interface ring to a 61 inch adaptor which mates with the 120 inch O.D. of the Centaur stage.

The parabolic reflector is formed by the deployment of 36 skewed axis rigid petals previously described. This spacecraft concept is unique since it uses a deployable truss to support a cassegrain sub-reflector and phased array. The truss when folded serves to support the array and sub-reflector during launch by locking the linkage to the feed support structure. In this manner the feed blockage is minimized when the truss is deployed by its folding braces. The feed support truss also serves as the mounting frame for two dipoles which serve as the 100 megacycle feeds.

A set of horizon sensors are mounted on the array face in conjunction with an orthogonal set of Polaris Star Trackers. This will reduce the array effective aperture to near the minimum gain value (30 db).

Two circular solar panels (52 ft² total) stowed in the forward portion of the shroud provide the primary power source. The attitude control torquers are located between the apogee injection motor and spacecraft module. Two roll and pitch jets in combination with four yaw jets provide the attitude torquing systems.

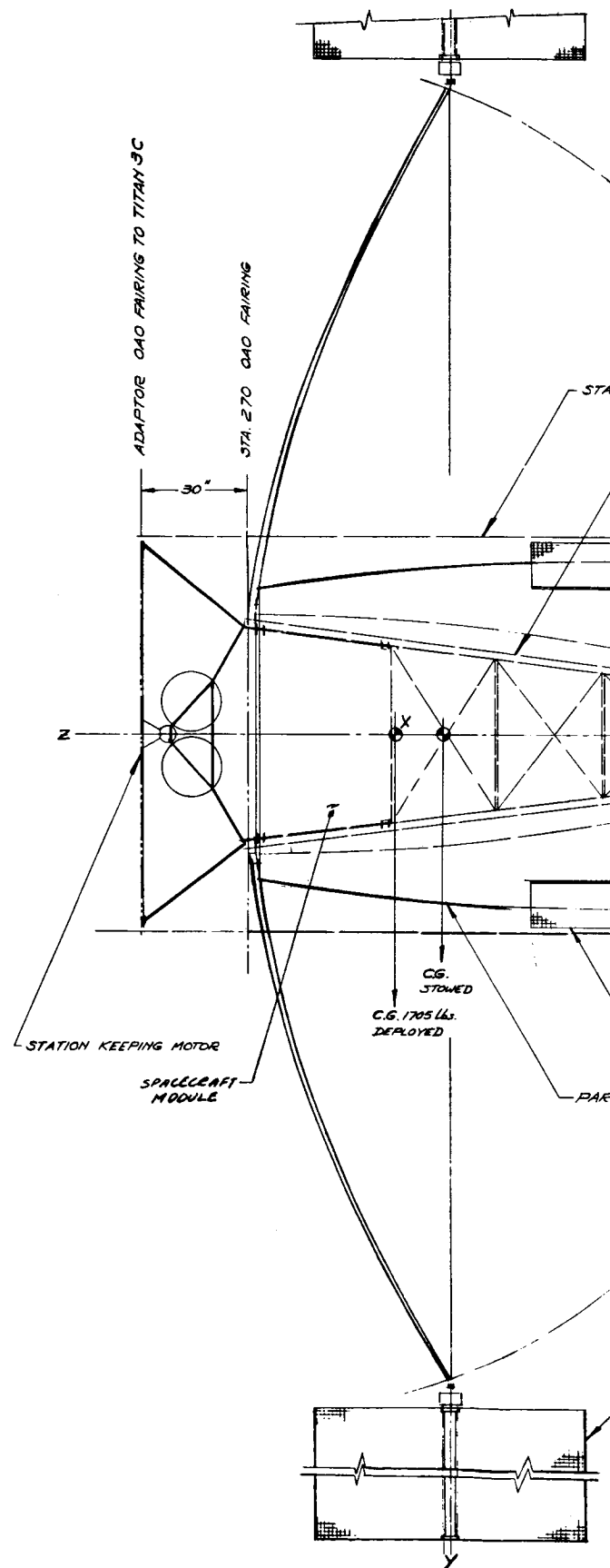
Concept SK513-16 (Figure 3.1-8) - This concept represents a vehicle launched by an Atlas SLV-3C/Centaur booster. It is in the 1500 lb. weight class and is a spin stabilized vehicle utilizing a stretched apogee motor similar to that used in the Model 946-100 series of Burner II. The spent motor remains attached to the spacecraft while in orbit and is mounted

approximately 25 inches aft of the spacecraft to achieve a vehicle C. G. aft of the vertex of the parabolic antenna.

The APS (auxiliary propulsion system) consists of three orthogonally located nozzles located at the C. G. Two of the nozzles provide east-west repositioning capability while the third nozzle is capable of north-south stationkeeping. One nozzle is sufficient for this mode since by choosing the burn compatible with the proper nodal crossing either a north or south correction is possible without vehicle reorientation.

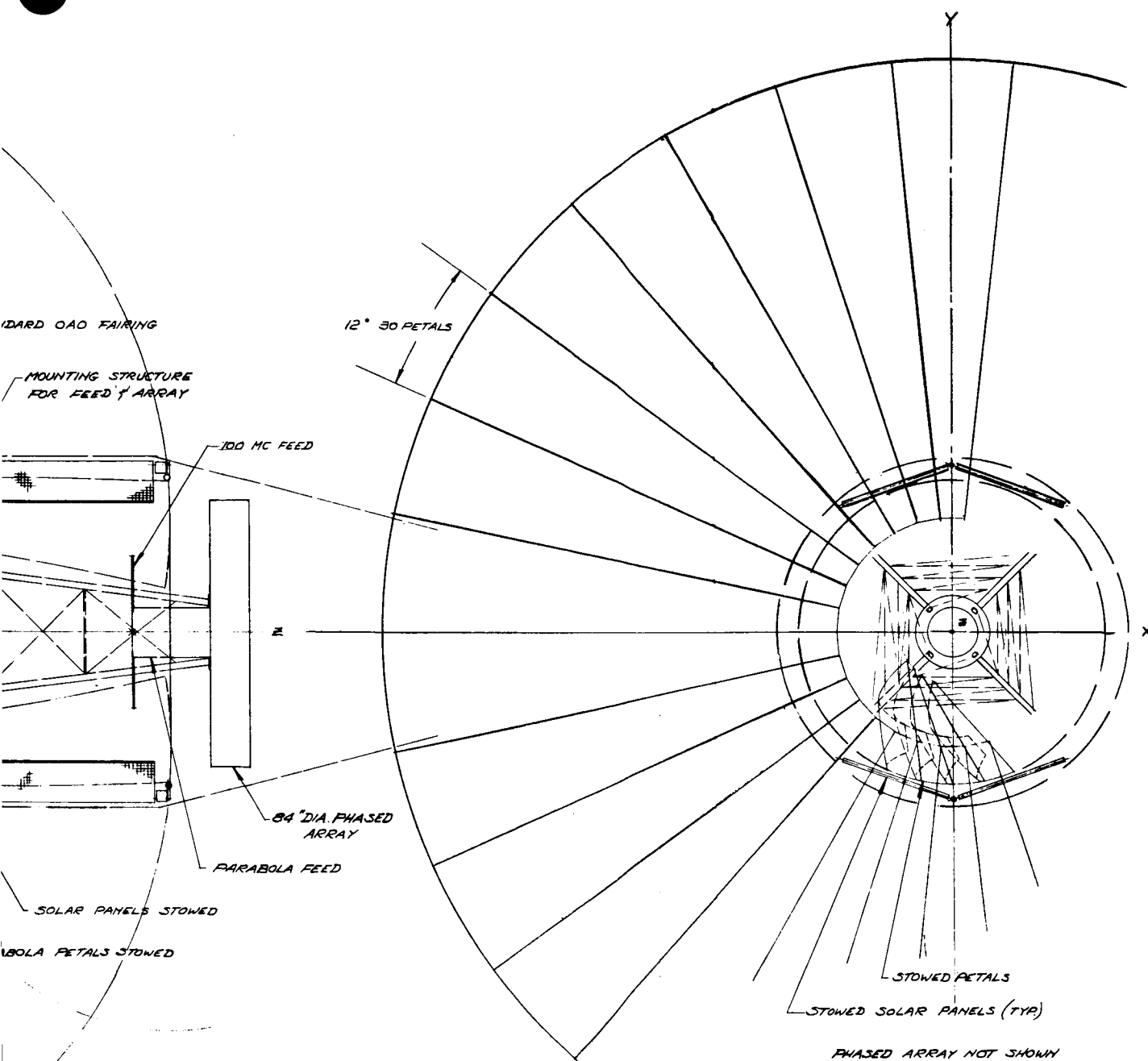
The concept as shown is housed in the Surveyor shroud with a 146 inch extension. It is mounted to a 60-inch long adaptor which attaches to the 120 inch diameter of the Centaur booster. The parabolic antenna is formed by 32 identical, non-radial petals. The non-radial petal arrangement permits a simple butt hinge. The feed support is a tripod structure which also supports the dipoles which make up the 100 MHz feed.

The F/D is .325 and represents the minimum F/D possible to preclude solar panel shadowing of the Polaris star tracker. The horizon sensor and star trackers are mounted on the array face. This concept has two circular solar panels which provide the primary power source. They have a total area of approximately 70 square feet and are stowed in the forward position of the shroud. Upon initiation of deployment, the solar panels raise up to provide clearance for the deployment of the petals. The attitude control torquers are located between the apogee injection motor and spacecraft module. Two roll and pitch jets in combination with four yaw jets provide the attitude torquing systems.



INERTIAS SLUG FT²

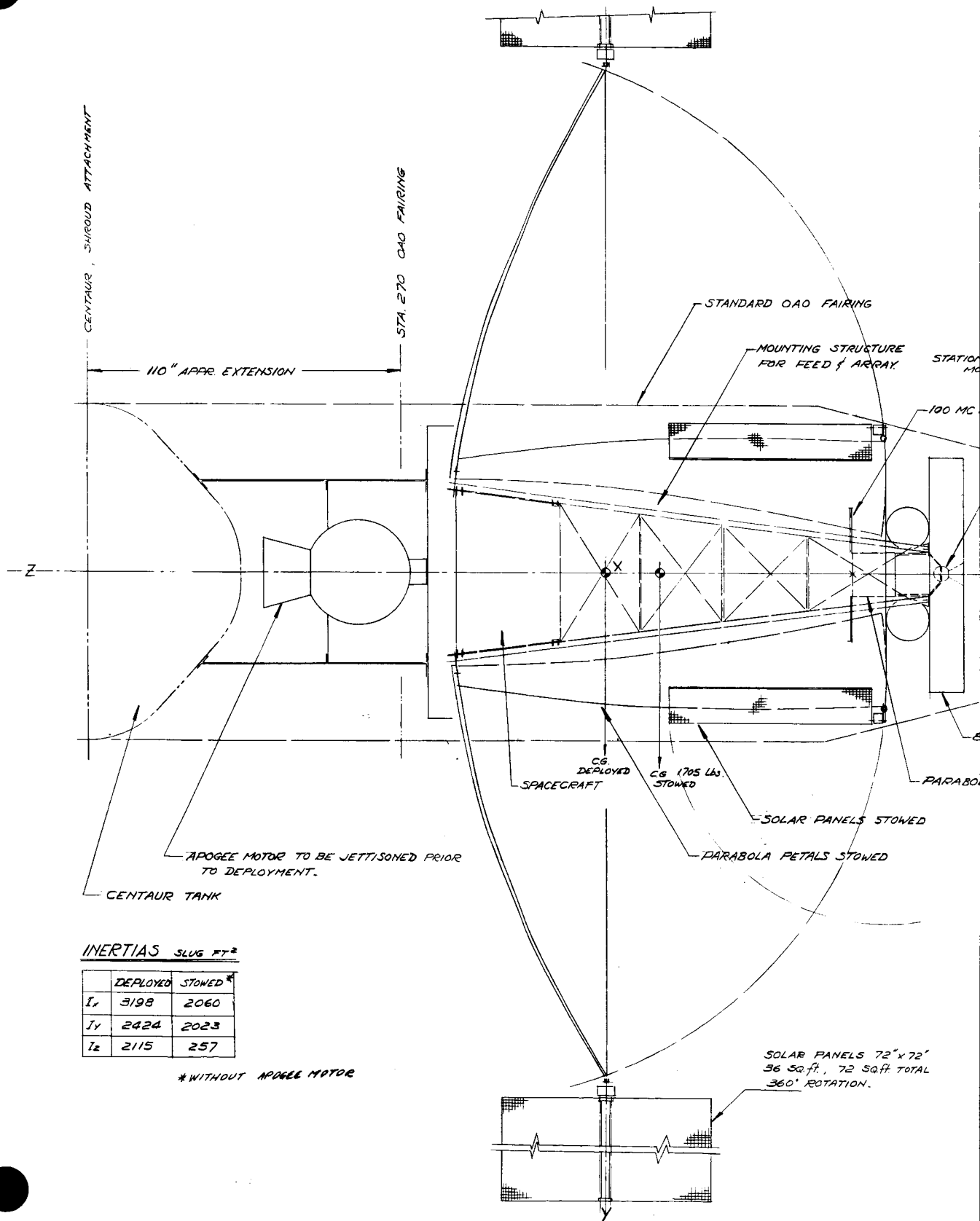
	DEPLOYED	STOWED
I_x	3198	2060
I_y	2424	2023
I_z	2115	257



SOLAR PANELS 72" x 72"
 96 sq. ft., 72 sq. ft. TOTAL
 360° ROTATION.

APPROVAL		DATE	FAIRCHILD MILLER WASHINGTON, D.C.	
DR. JUAN PEREZ		5/31/66	SPACE SYSTEMS DIVISION AREA	
CHK			PARABOLA $\frac{E}{S} = .4$ RIGID PANELS TITAN 3C (OAO STANDARD SHROUD) 1700 lbs. approx.	
APPD				
APPD				
APPD				
APPROVAL		CODE IDENT. NO.	SIZE	DRAWING NO.
APPROVAL		17232		SK-513-10
		SCALE 1:20	WT	SHEET

Figure 3.1-3 Concept SK 513-10

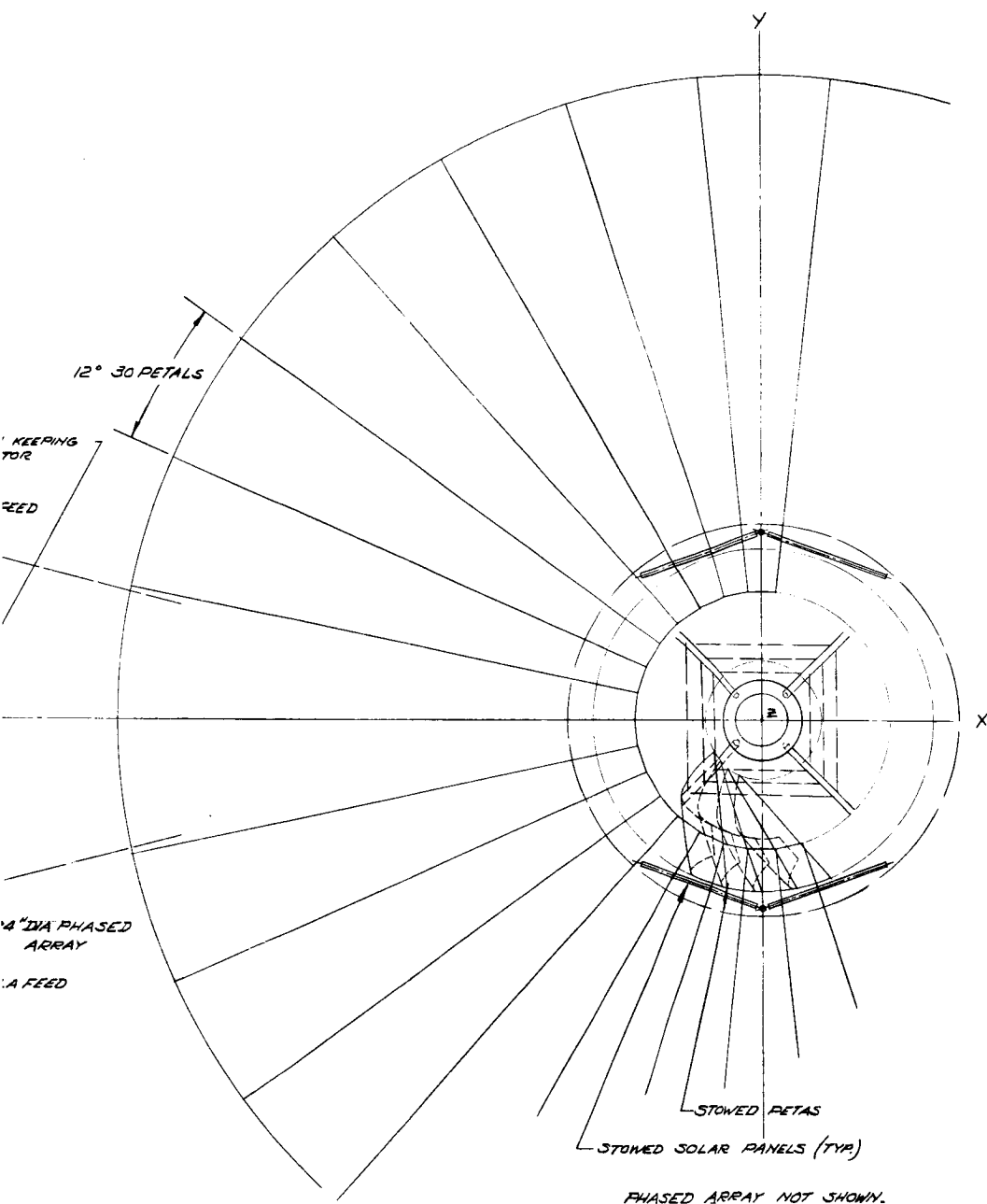


INERTIAS SLUG #F²

	DEPLOYED	STOWED*
I_x	3198	2060
I_y	2424	2023
I_z	2115	257

* WITHOUT APOGEE MOTOR

3-15-1

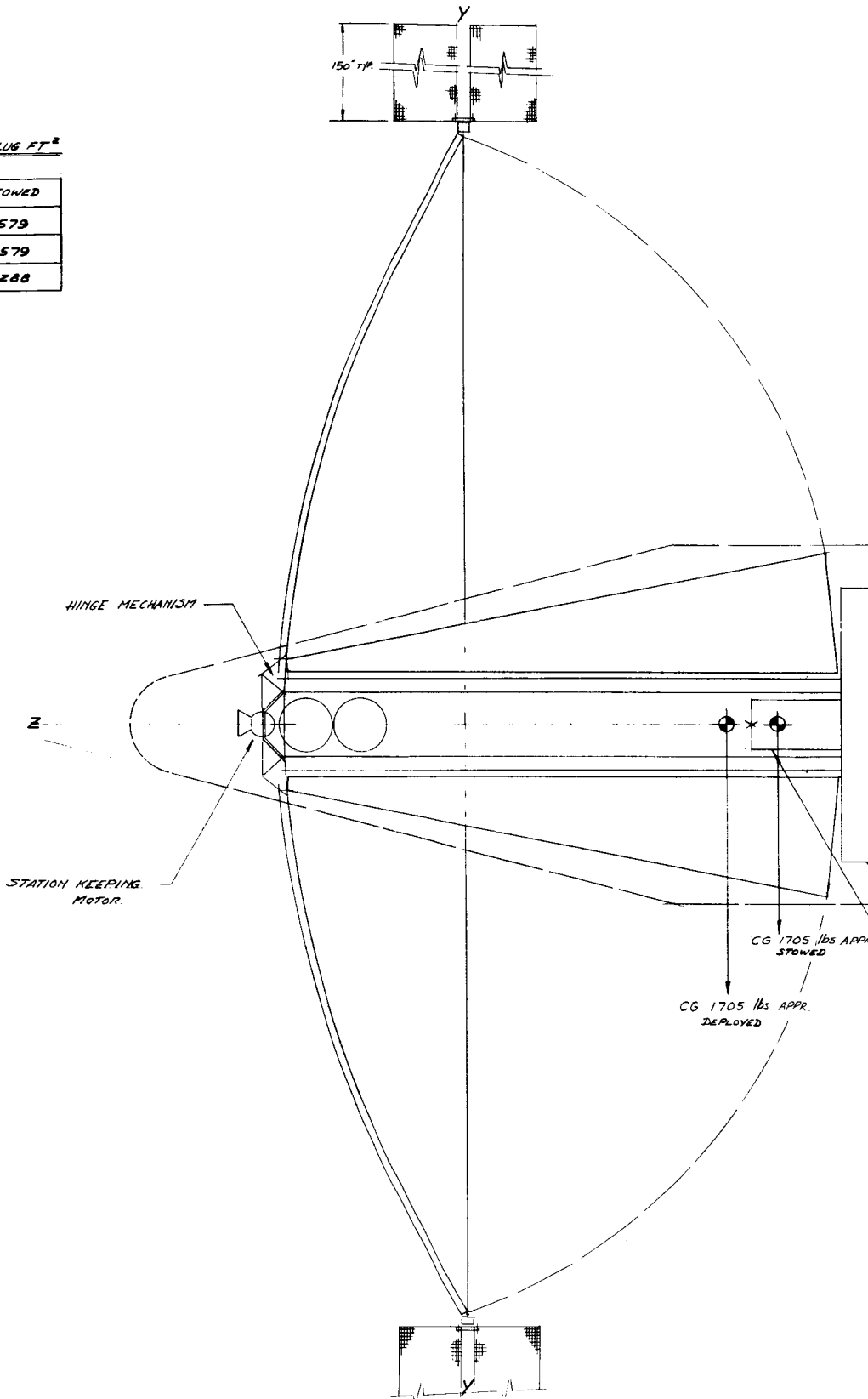


APPROVAL		DATE	FAIRCHILD HILLER WASHINGTON, D.C.		
DR <i>J. PEREZ</i>		<i>5/3/66</i>	SPACE SYSTEMS DIVISION AREA		
CHK			PARABOLA $f:1.4$ RIGID PANELS CENTAUR (OAO SHROUD WITH EXTENSION) 1700 Lbs APPR.		
APPD					
APPD					
APPD					
APPROVAL		CODE IDENT. NO.	SIZE	DRAWING NO.	
		17232		SK-513-12	
APPROVAL		SCALE 1:20	WT	SHEET	

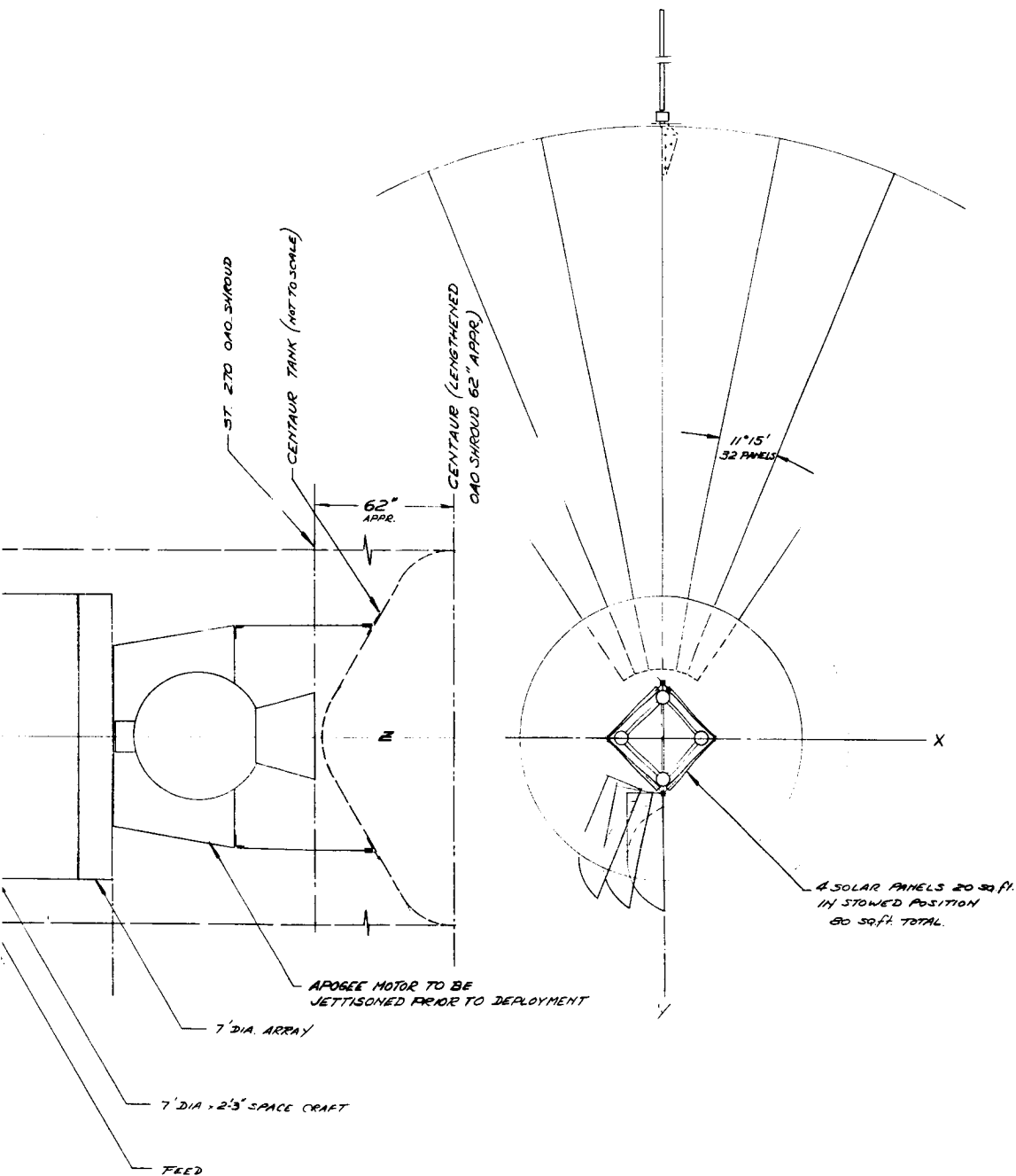
Figure 3.1-4 Concept SK 513-12

INERTIAS SLUG FT²

	DEPLOYED	STOWED
I_x	3945	1579
I_y	2780	1579
I_z	2604	288

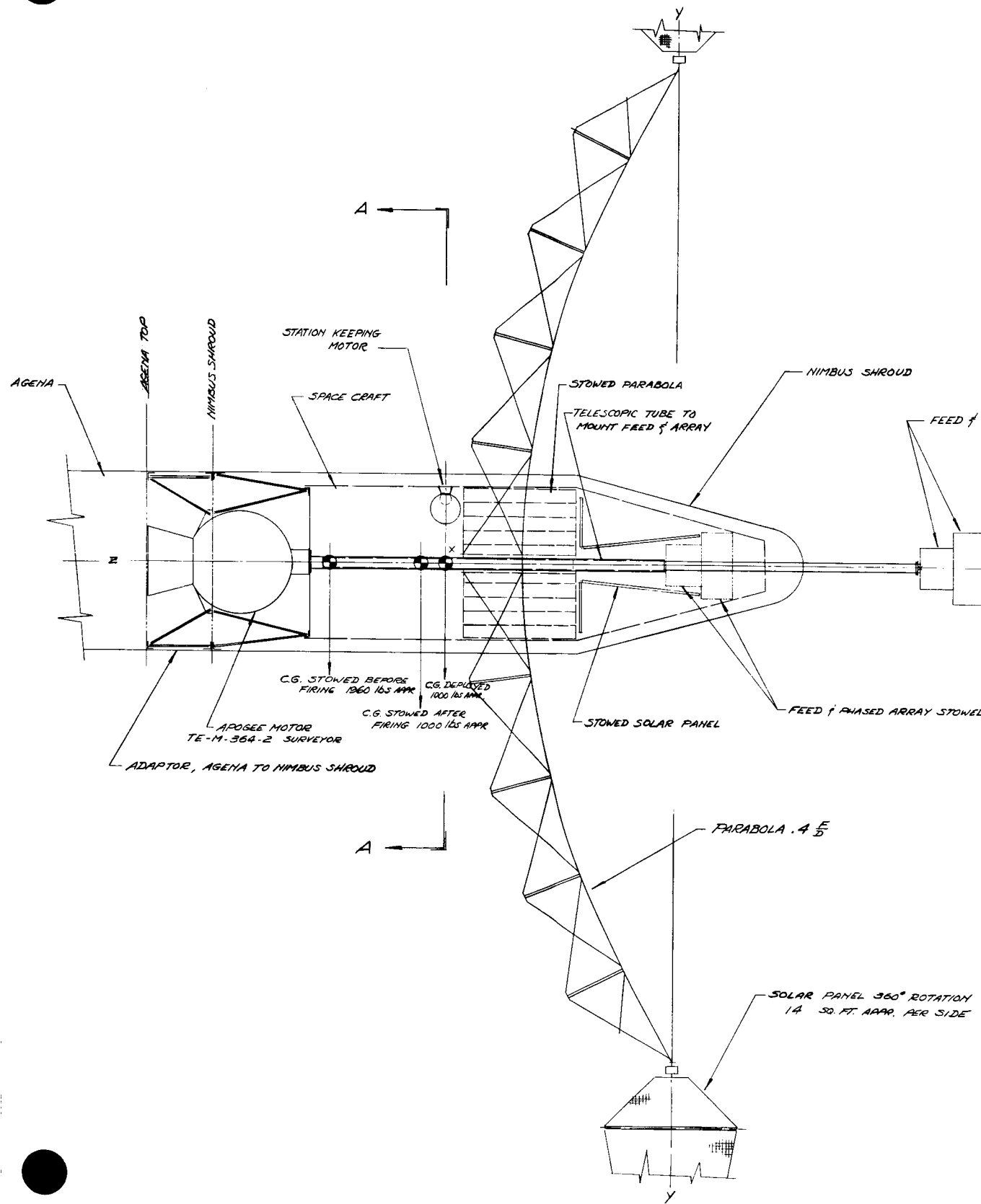


3-16-1



APPROVAL		DATE	FAIRCHILD HILLER WASHINGTON, D.C.	
DR	J. P. 17232	5/13/61	SPACE SYSTEMS DIVISION AREA	
CHK			PARABOLA $\frac{F}{S}$ - 4 SOLID PANELS ATLAS-CENTAUR (OAO MODIFY SHROUD) 1700 lbs APPR.	
APPD				
APPD				
APPD				
APPROVAL		CODE IDENT. NO.	SIZE	DRAWING NO.
APPROVAL		17232		SK- 513-11
		SCALE 1/20	WT	SHEET

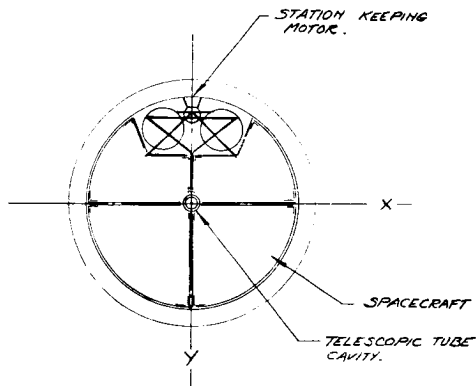
Figure 3.1-5 Concept SK 513-11



INERTIAS (SLUG FT²)

	DEPLOYED	STOWED APPROX MOTOR BEFORE FIRING	STOWED APPROX MOTOR AFTER FIRING
<i>I_x</i>	1757	1025	466
<i>I_y</i>	1059	1024	465
<i>I_z</i>	1231	164	52

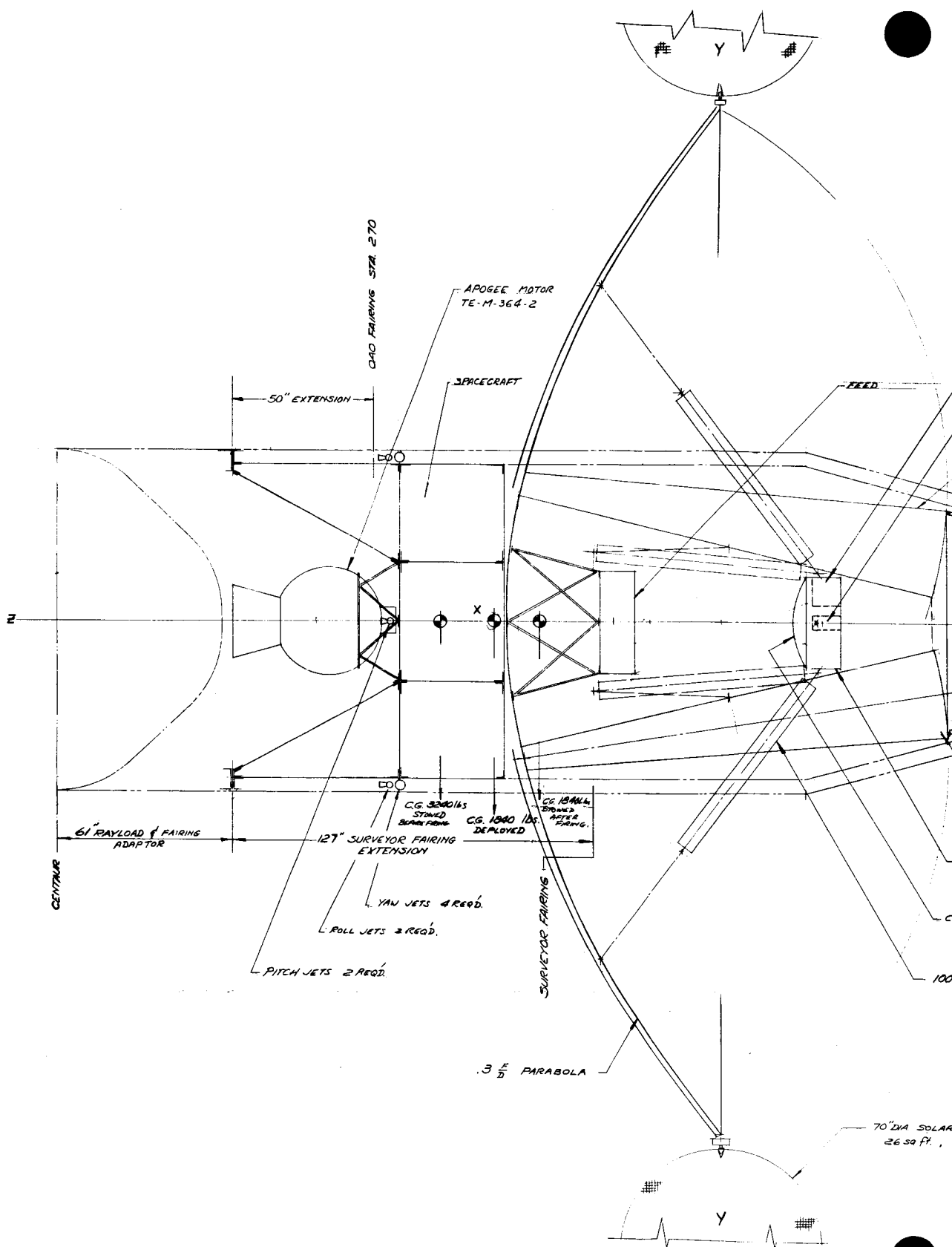
PHASED ARRAY DEPLOYED



SECTION AA

APPROVAL		DATE	FAIRCHILD HILLER SPACE SYSTEMS DIVISION		WASHINGTON, D.C. AREA
DR	J. PEREZ	6/8/66	ATS-4 CONCEPT 1000 LBS. APPR. E = .4 ATLAS / AGENA SLV-3A NIMBUS SHROUD		
CHK					
APPD					
APPD					
APPD					
APPROVAL			CODE IDENT. NO.	SIZE	DRAWING NO.
APPROVAL			17232		SK-513-13
			SCALE 1" = 20"	WT	SHEET

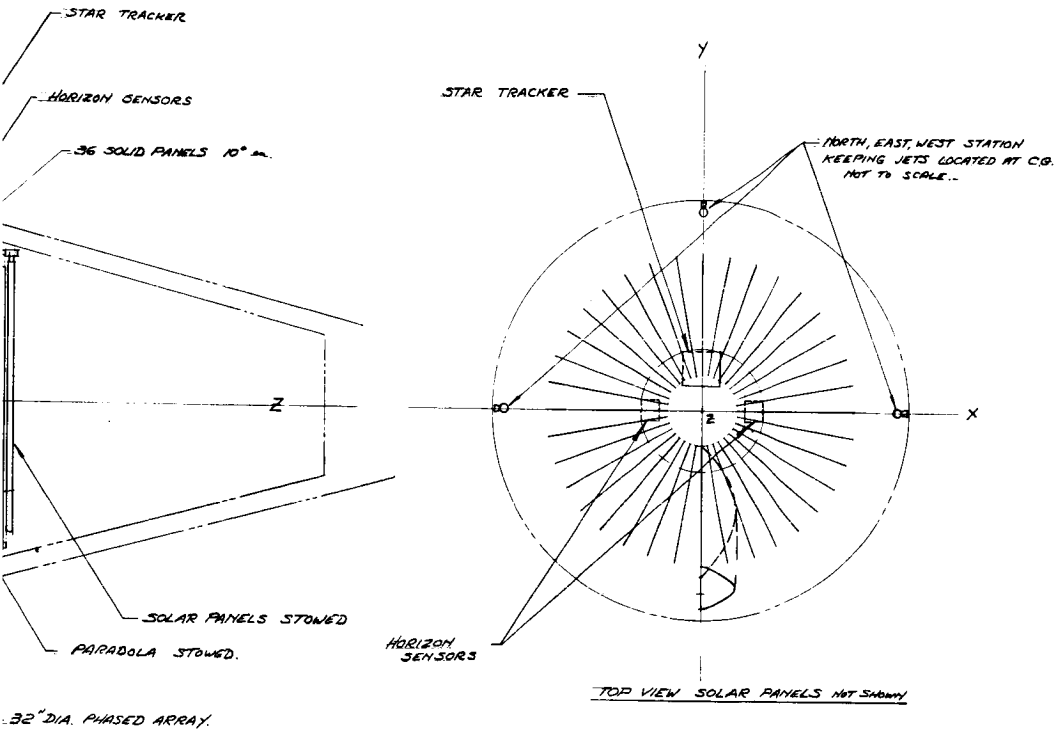
Figure 3.1-6 Concept SK 513-13



5-18-1

INERTIAS SLUG FT²

	DEPLOYED	STOWED BEFORE FIRING APOGEE MOTOR	STOWED AFTER FIRING APOGEE MOTOR
I_x	2068	2674	1733
I_y	1466	2674	1733
I_z	2186	473	442



32" DIA. PHASED ARRAY.

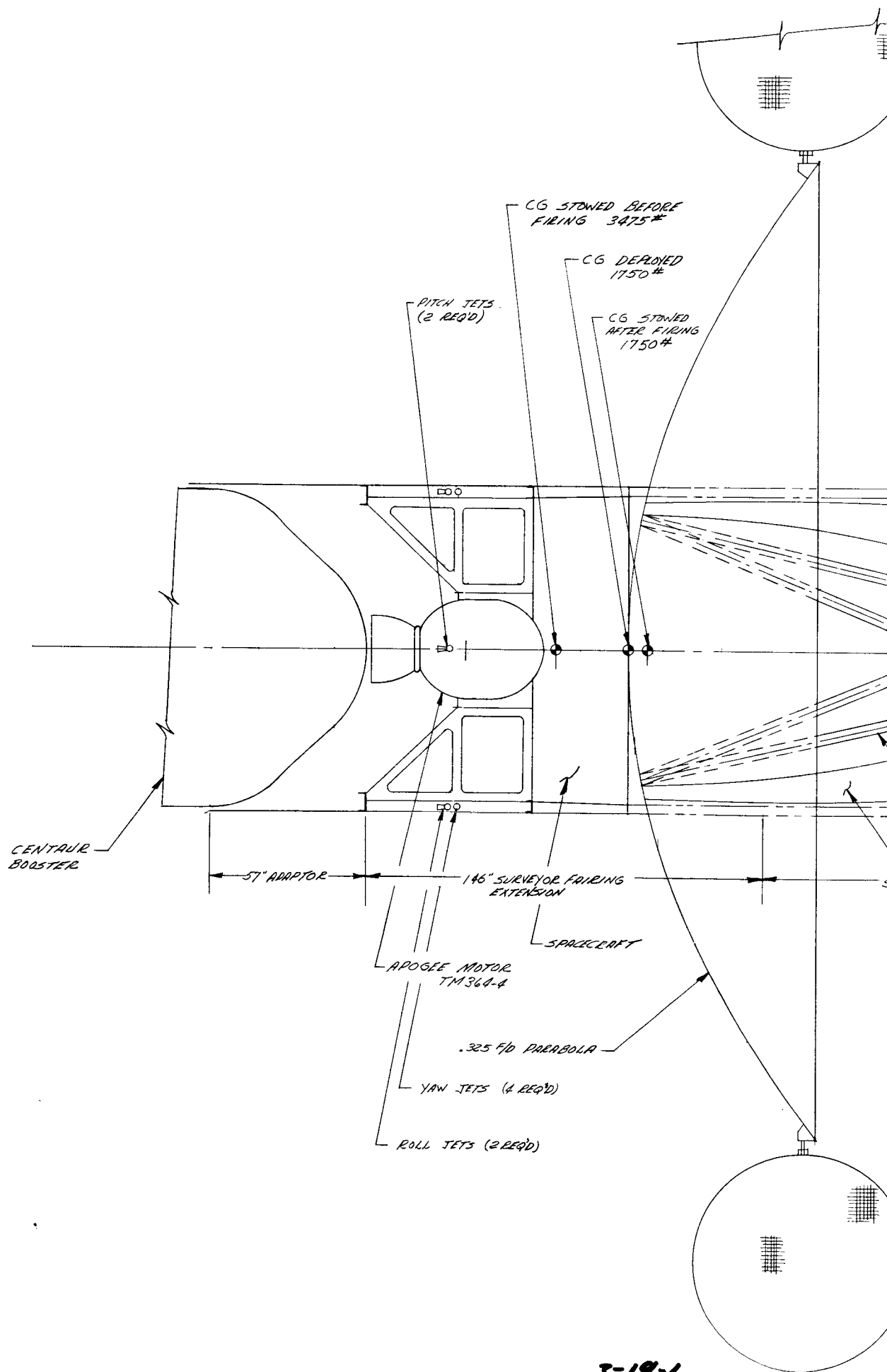
135 SEGRAIN REFLECTOR

MHE FEED (4 TUBES)

PANEL
2 SQ. FT. TOTAL

APPROVAL		DATE	FAIRCHILD HILLER		WASHINGTON, D.C.
DR	J. PEREZ	6/24/64	SPACE SYSTEMS DIVISION		AREA
CHK			ATS-4 CONCEPT 1700 LBS. APPAR.		
APPD			5-3 PARABOLA RIGID PANELS		
APPD			ATLAS SLV-3C CENTAUR		
APPD					
APPROVAL			CLC IDENT NO.	SIZE	DRAWING NO.
			17232		SK-513-14
APPROVAL			SCALE 1/20	WT	SHEET

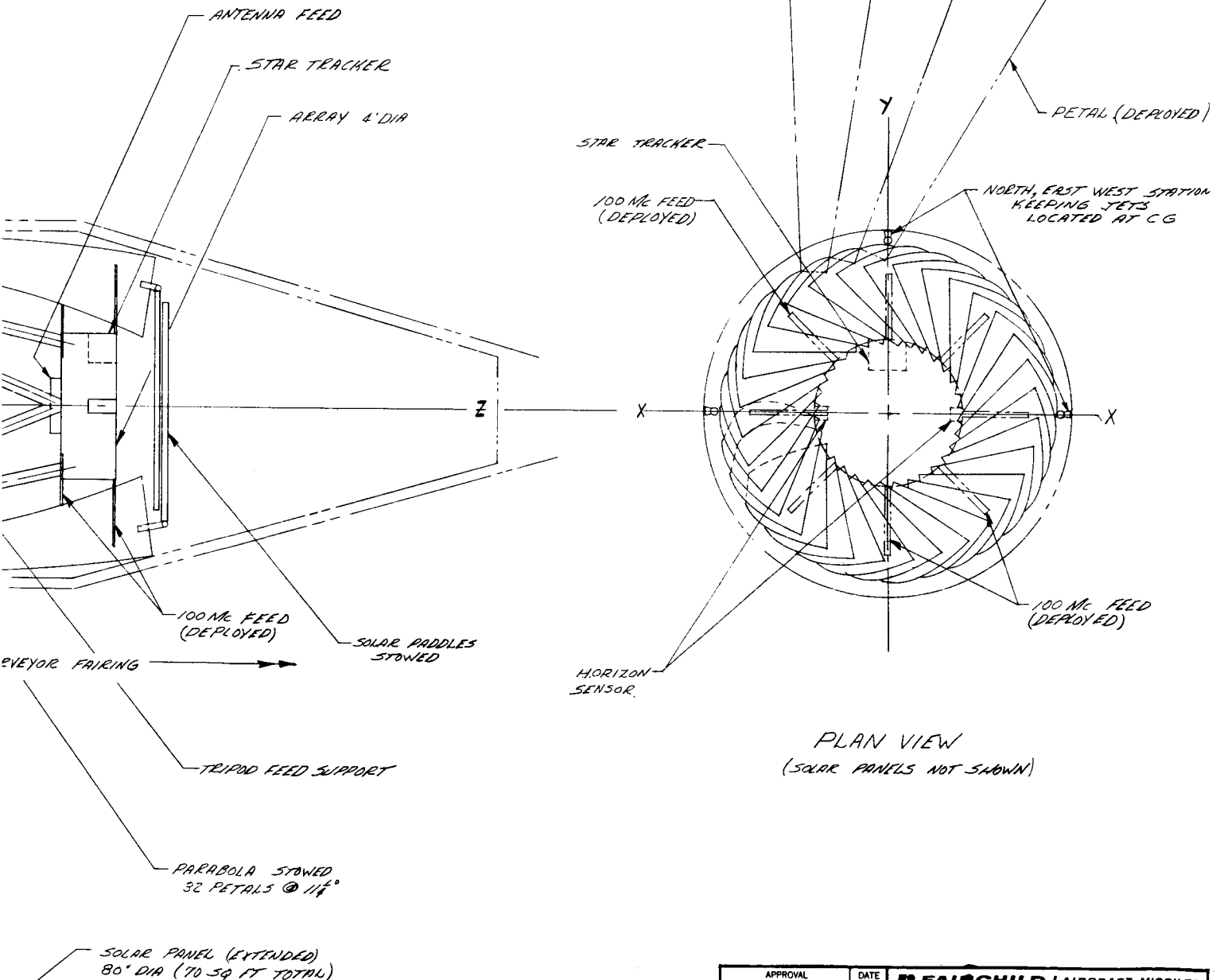
Figure 3.1-7 Concept SK 513-14



3-19-1

INERTIAS SLUG FT²

	DEPLOYED	STOWED BEFORE FIRING APOGEE	STOWED AFTER FIRING APOGEE MOTOR
I_x	2240	2962	1569
I_y	1468	2962	1569
I_z	1857	529	475



APPROVAL	DATE	FAIRCHILD STRATOS AIRCRAFT-MISSILES DIVISION HAGERSTOWN, MARYLAND	
DR <i>RTAMAS</i>	<i>9/2/66</i>	ATS-4 CONCEPT 1500* APPR	
CHK		F/D = .325 PARABOLA RIGID PETALS	
APPD		ATLAS SLV-3C CENTAUR	
APPD		CODE IDENT. NO.	DRAWING NO.
APPD		72311	SK 513-16
APPROVAL		SCALE <i>1/20</i>	SHEET

Figure 3.1-8 Concept SK 513-16

3.2 CONCEPT EVALUATION AND REFERENCE CONCEPT

3.2.1 Launch Vehicle Choice

The continuing design evolution and sub-system trade-offs discussed in other sections of this report resulted in refinements of the spacecraft weight and volume requirements. Concurrently with this effort, the payload capabilities of the various launch vehicle and apogee injection stages were computed (see Section 5.0). On the basis of the spacecraft weight and volume requirements and the booster economic and performance trade-offs, the Atlas-Centaur launch vehicle augmented by a TE-364-3 (Improved Delta Motor) solid propellant motor was chosen. Spin stabilization was selected for the transfer orbit stabilization.

One of the basic objections to the Atlas SLV-3A/Agena booster (in addition to its limited synchronous orbit payload capability) was its 5 feet diameter shroud limitation. This constraint prevented the use of a petal system for parabolic reflector deployment and consequently only systems with considerably less surface accuracy were possible.

With the choice of launch vehicle and transfer orbit stabilization the specific concepts discussed previously (Figures 3.1-3 through 3.1-8) were narrowed down to two configurations, concepts SK513-18 and SK513-17 (Figure 3.2-1 and 3.2-2).

3.2.2 Split Module Concept

Figure 3.2-1 (SK513-18) represents the family of split module concepts. The equipment module is mounted behind the reflector and the experiment module near the parabolic reflector focus.

The experiment module contains the parabolic feed, phased array, interferometer, and stabilization sensors. The equipment module contains the remainder of the spacecraft equipment including the attitude torquing

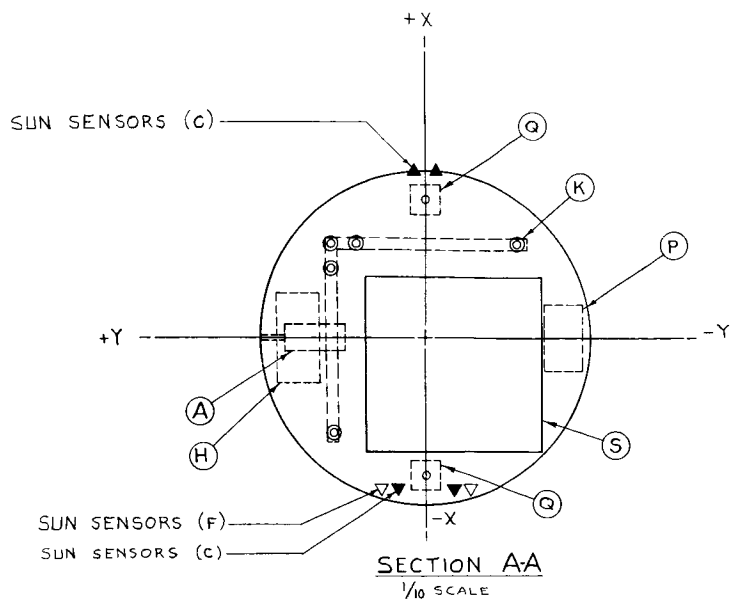
system. The parabolic antenna utilizes a multi-band feed shown in Section B-B of Figure 3.2-1. The center portion contains a waveguide horn cluster used for X - Band. The S-Band feed consists of two bowtie elements orthogonal to the plane of the paper while the 800 MHz capability is provided by a four-element square array of turnstiles. The 100 MHz feed is made up of four dipoles yielding a single turnstile antenna.

The solar panels are circular and stowed in the forward part of the shroud during launch. The pre-orbital power requirements cannot be met by this arrangement. In the deployed configuration they are fixed to the petal system in a cruciform configuration.

Telemetry coverage is provided by two antennas, one of which is attached to the outside of the equipment module while the other is attached to the experiment module. The antenna mounted to the equipment module is used for transfer orbit coverage.

Spin stabilization is employed during the transfer orbit and apogee injection is accomplished by the TE-364-3 solid propellant motor. The motor is buried in the equipment module and separated after synchronous orbit injection. Station-keeping engines are provided by two upward firing nozzles parallel to the "Z" axis. This will necessitate spacecraft re-orientation during the station-keeping maneuvers.

The reflector petals are hinged in a manner permitting storage around the experiment module. The experiment module size requirements, combined with the solar panel storage needs, dictated its location well within the folded petal extremities. Consequently, the F/D of this configuration cannot be larger than 0.25. This F/D ratio precludes a change to rotating solar panels (for more ambitious mission power profiles) since the Polaris tracker will be obscured during portions of the orbit. The petals are supported during launch by their hinges at one end and the experiment



SOLAR PANELS - STOWED

REFLECTOR PANELS - STOWED

OAO
SHROUD

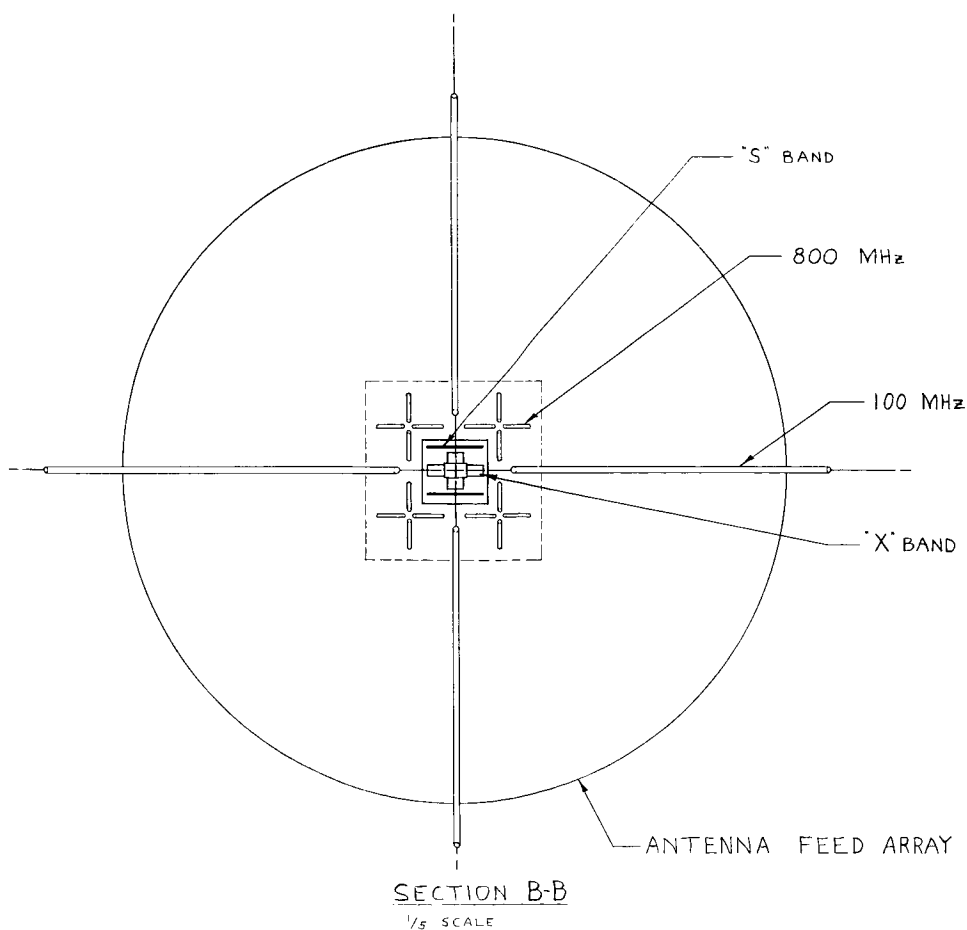
CG - DEPLOYED w/o MOTOR

CG - DEPLOYED w/ MOTOR

CG - STOWED

SOLAR PANEL

+Y



96"
EXTENSION

YAW JETS (4 REQD)

ROLL JETS (2 REQD)

PITCH JETS (2 REQD)

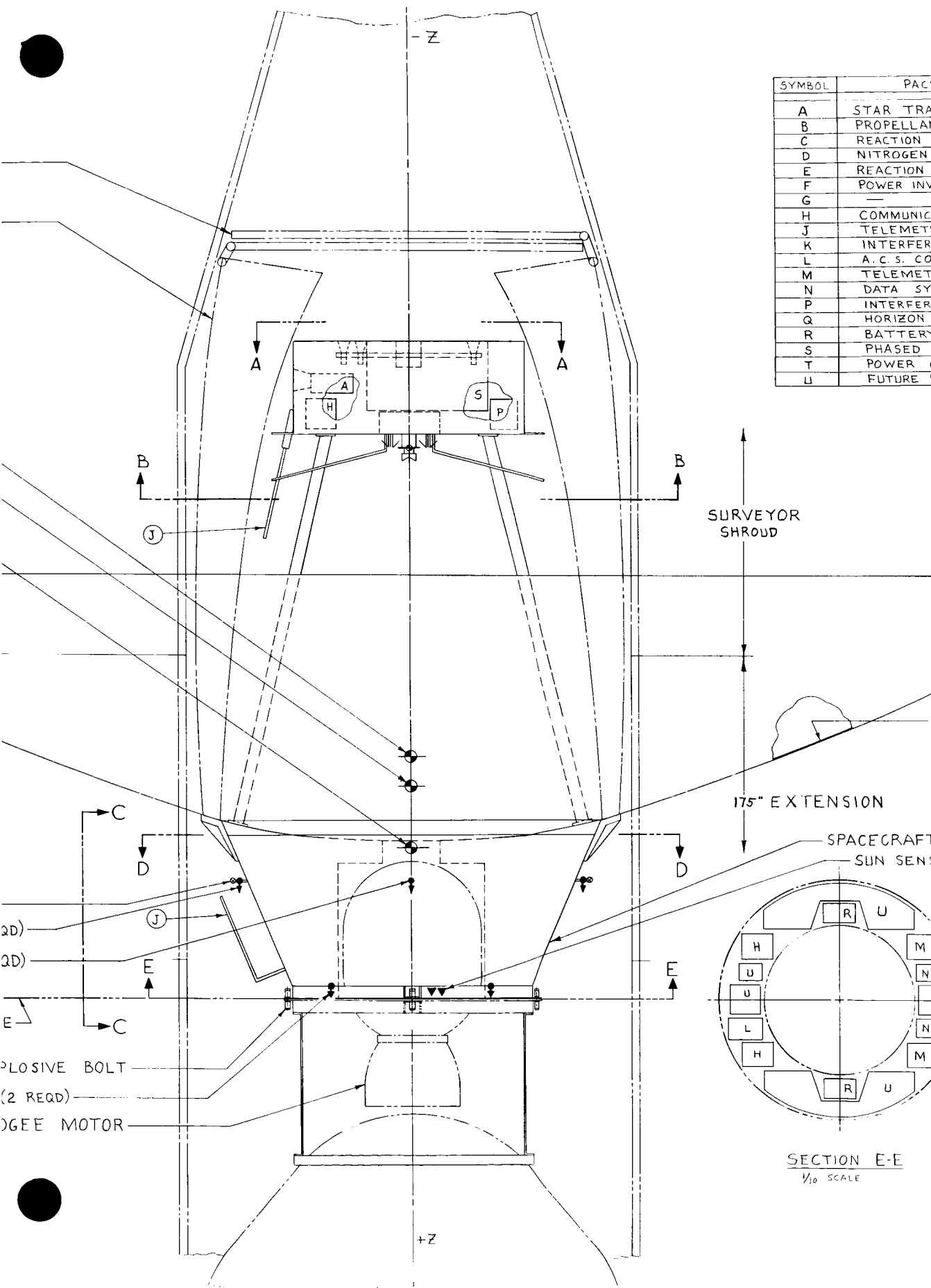
SEPARATION PLAN

EX

STATION KEEPING JETS

AP

SYMBOL	PAC
A	STAR TRA
B	PROPELLAN
C	REACTION
D	NITROGEN
E	REACTION
F	POWER INV
G	—
H	COMMUNIC
J	TELEMET
K	INTERFER
L	A. C. S. CO
M	TELEMET
N	DATA SY
P	INTERFER
Q	HORIZON
R	BATTERY
S	PHASED
T	POWER
U	FUTURE

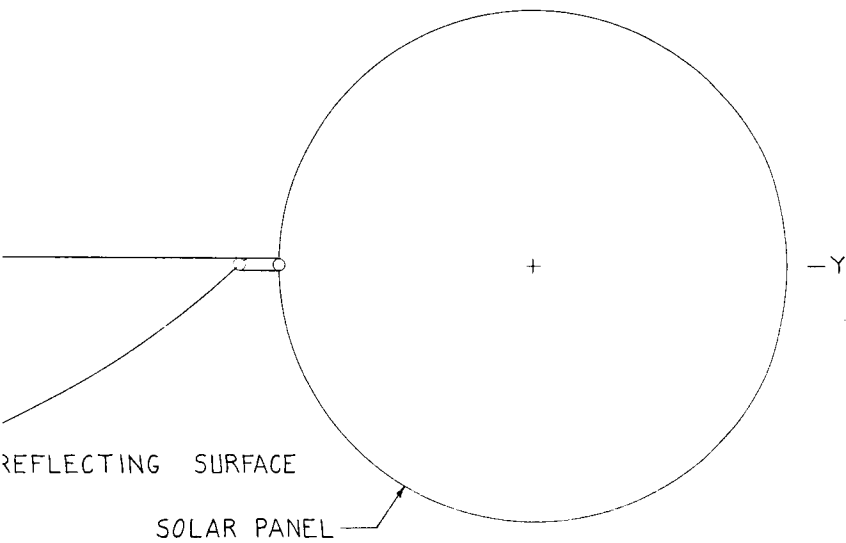


3-23-2

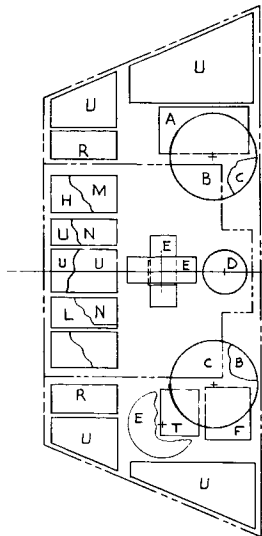
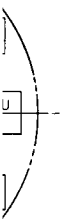
WAGE
CKER
UT TANK
FUEL TANK
TANK
WHEELS
ENTER
ATIONS SYSTEM
RY ANTENNA
OMETER
NTROLLER
RY
STEM
OMETER ELECTRONICS
SENSOR
ARRAY
CONDITIONING
EXPERIMENTS

MOMENTS (SLUG-FT ²)		
AXIS	DEPLOYED w/ MOTOR	STOWED w/ MOTOR
I _{xx}	2215	1776
I _{yy}	982	1776
I _{zz}	2066	416

$$\frac{f}{D} = 0.28$$

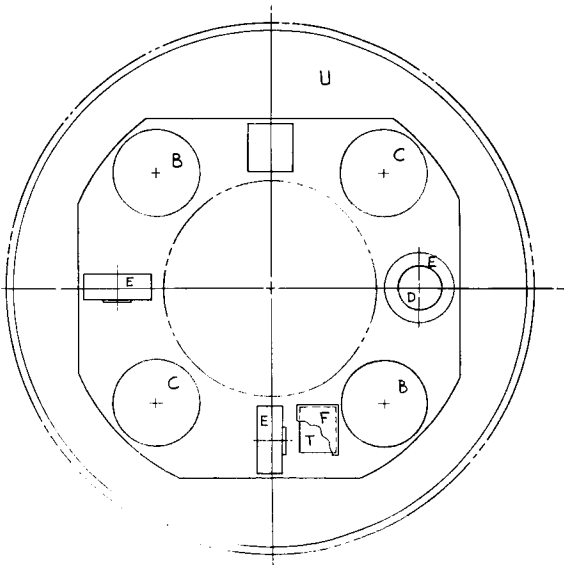


ORS (C)



SECTION C-C

1/10 SCALE
ROTATED 90° CW



SECTION D-D

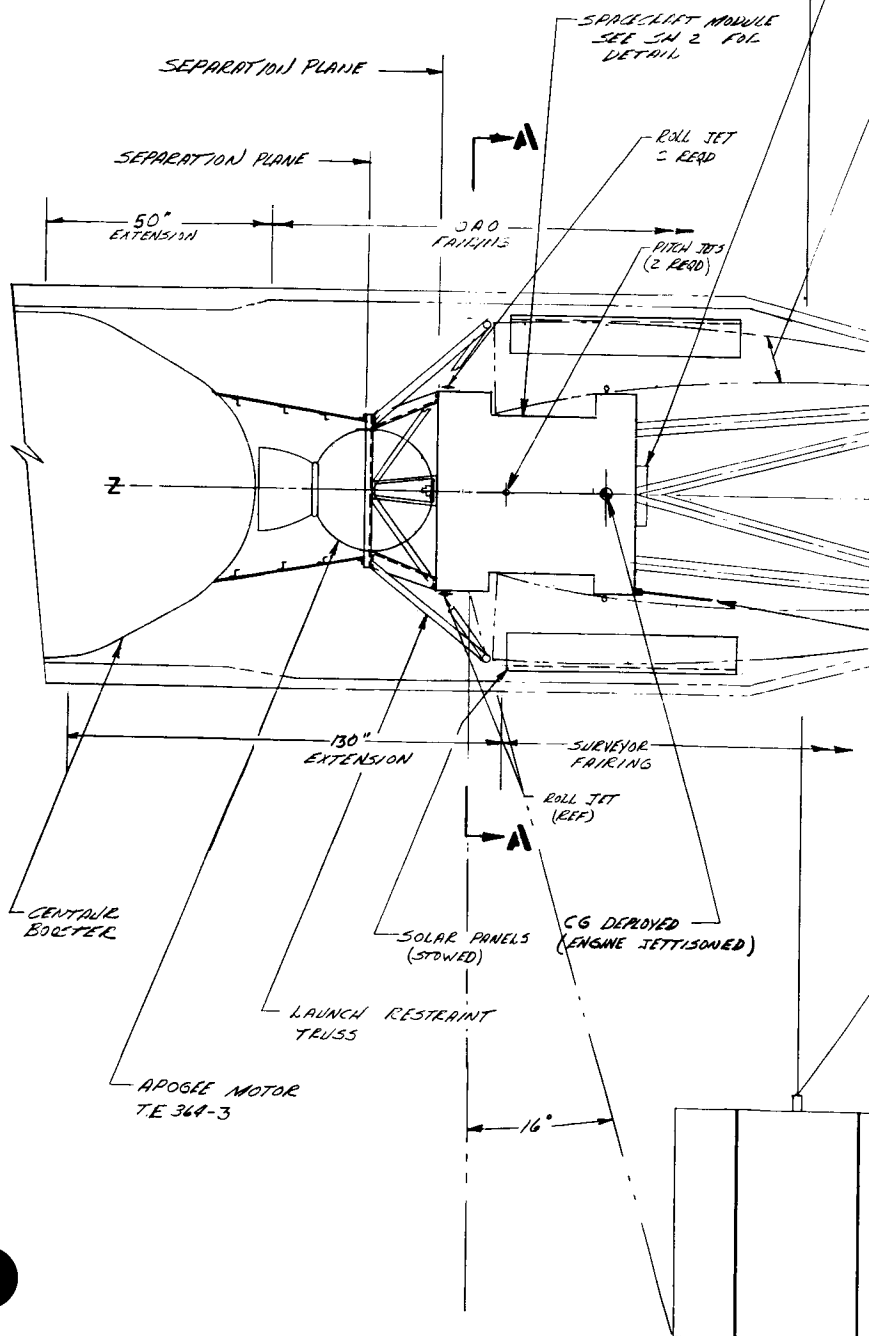
1/10 SCALE

SK-513-18		
SK-513-18	1/10 SCALE	RS

Figure 3.2-1 Concept SK 513-18

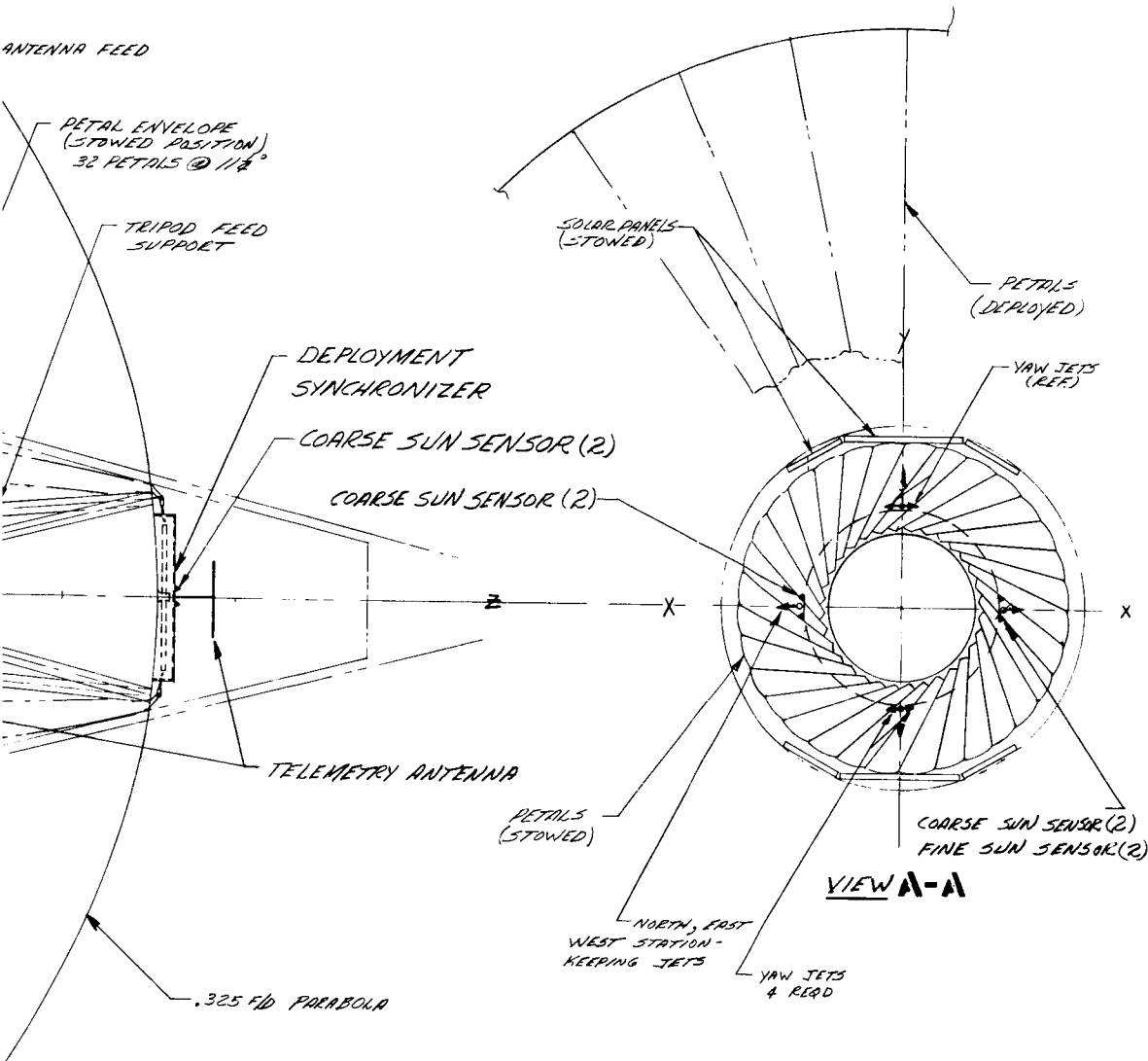
	BEFORE FIRING APOGEE MOTOR	DEPLOYED
I_x	1140	2150
I_y	1140	1226
I_z	303	1677

SLUG FT²



3-24-1

Figure 3.



SOLAR PANEL 72"x75"
(75 SQ FT TOTAL) (DOUBLE FACED)
FIXED POSITION

COMP. NO.		DATE	FAIRCHILD HILLER WASHINGTON, D.C.	
DESIGN		1976	AREA	
PROJECT			AT-5 4 CONCEPT 1400#	
REV.			f/D = .325 PARABOLA RIGID PETALS	
APP. NO.			ATLAS SLV-3C CENTAUR	
AUTHOR			DOCUMENT NO.	DRAWING NO.
CHECKED			17232	SK513-17
APPROVED			SCALE 1/20	WT
				SHEET 1

module near the tip.

3.2.3 Reference Concept

Figure 3.2-2 (SK513-17) depicts the recommended concept. It is an outgrowth of an earlier concept (Figure 3.1-5) and represents an "inverted" configuration since the petals are hinged to fold down instead of the conventional upward hinged motion. This results in a lower launch C. G. lighter feed support mast, and a solar panel configuration which is more readily adaptable to pre-orbital solar power. The C. G. in the orbit configuration is within the spacecraft module, permitting an APS (auxiliary propulsion system) installation which requires no re-orientation for the station-keeping mode. The solar panels are fixed in a cruciform arrangement and provide approximately 310 watts of primary power to the load bus. The panels are "wrapped around" the folding petals during launch. This will result in a worst case solar vector angle relative to the vehicle spin axis during the transfer orbit of 20° . Using the non-degraded value of solar cell output and an 85% power conversion efficiency results in a pre-orbital power capability of more than 60 watts.

The spacecraft module and apogee injection motor (TE-364-3 Improved Delta Motor) are attached to the standard Centaur interface by a short conical adaptor. This configuration uses a single module for all equipment, experiments and sensors. A six tube truss is provided to support the reflector hub. The rate retarding linkage for the reflector petals (described in Section 3.3) is above the reflector hub and therefore does not cause any of the structural discontinuities that might be required for the rate retarder with a conventional approach. The $F/D = .33$ and, with the resultant separation between experiment package and deployed solar paddle, no Polaris obscuration exists if the fixed solar paddles are altered to rotating paddles.

The spacecraft is housed in a modified Surveyor fairing with an

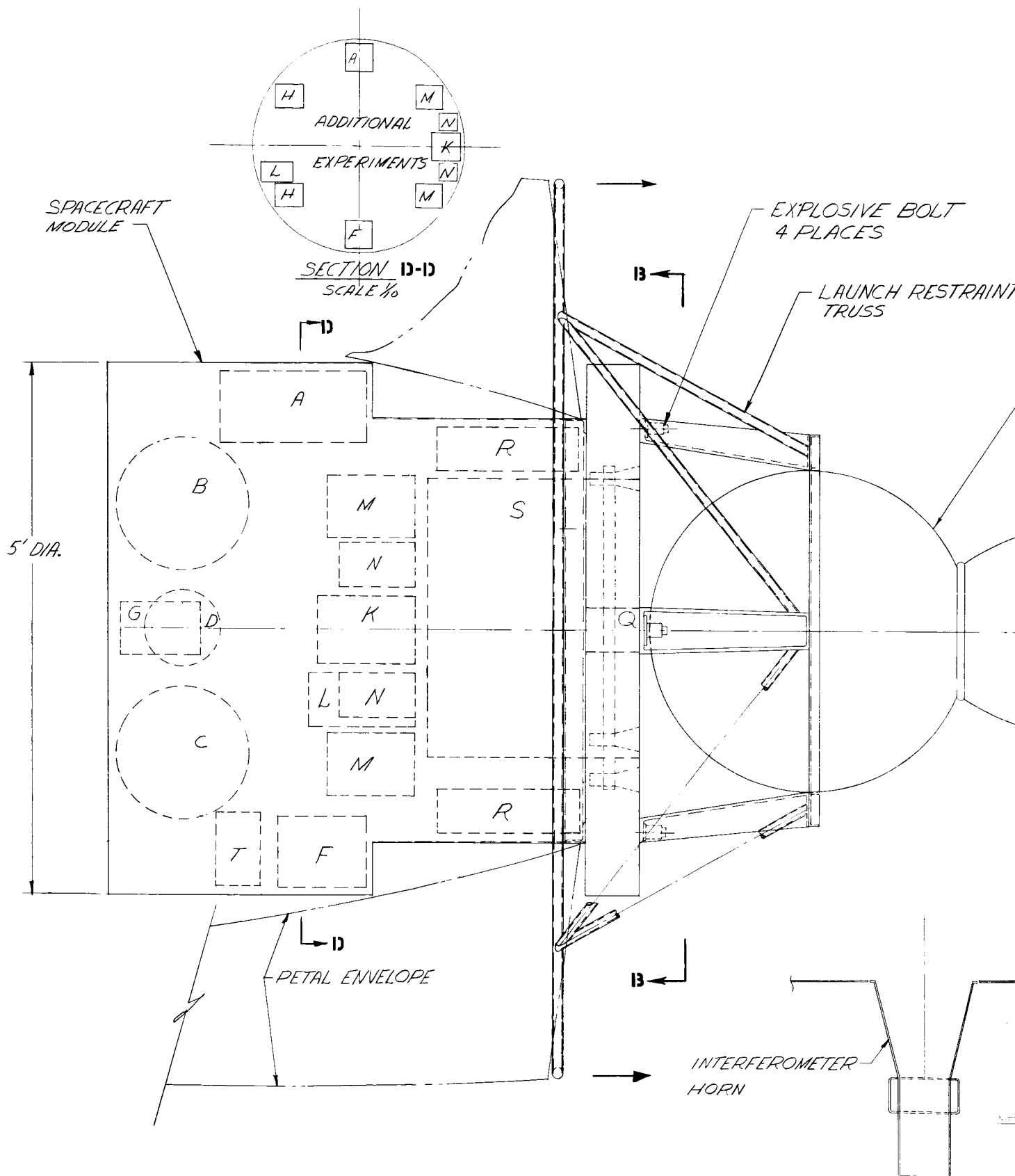
11-foot extension. A comparable split module (Figure 3.2-1) required at least three additional feet of shroud. The telemetry antenna used for transfer orbit coverage is mounted above the parabolic antenna vertex while the on-station telemetry coverage is provided by an antenna attached to the module.

The attitude control jets are positioned around the circumference of the spacecraft module. Two roll and pitch jets in combination with four yaw jets are provided for acquisition maneuvers, unloading of the inertia wheels and stabilization during the auxiliary propulsion thrusting modes. The roll jets are placed below the Polaris Star tracker to eliminate any optical problems. All the jets are arranged to thrust away from the reflector.

The APS consists of three orthogonally located nozzles at the C. G. Two of the nozzles provide east-west repositioning capability while the third nozzle is capable of north-south stationkeeping. One nozzle is sufficient for this mode since by choosing the burn compatible with the proper nodal crossing either a north or south correction is possible without vehicle reorientation.

Figure 3.2-3 depicts the spacecraft module in greater detail. The phased array, interferometer elements, and horizon sensors are on the earth-facing side and clear of any obstruction after the apogee motor is jettisoned. The phased array consists of 64 horn elements forming a 36 -inch x 31-inch planar array. The interferometer elements consist of five horn antennas mounted to a superinsulated "L" beam.

The truss structure which restrains the reflector petals during launch is jettisoned with the apogee injection motor. This is a unique fall-out of this concept and eliminates the need for an additional separation device.



PACKAGE	
A	STAR TRACKER
B	PROPELLANT TANK
C	REACTION FUEL TANK
D	NITROGEN TANK
E	REACTION WHEELS
F	POWER INVERTER
G	3 AXIS GYRO
H	COMMUNICATION SYS.
J	
K	INTERFEROMETER

PACKAGE	
L	A.C.S. CONTROL "R"
M	TELEMETRY
N	DATA SYSTEM
P	
Q	HORIZON SENSOR
R	BATTERY
S	PHASED ARRAY
T	POWER CONDITIONING

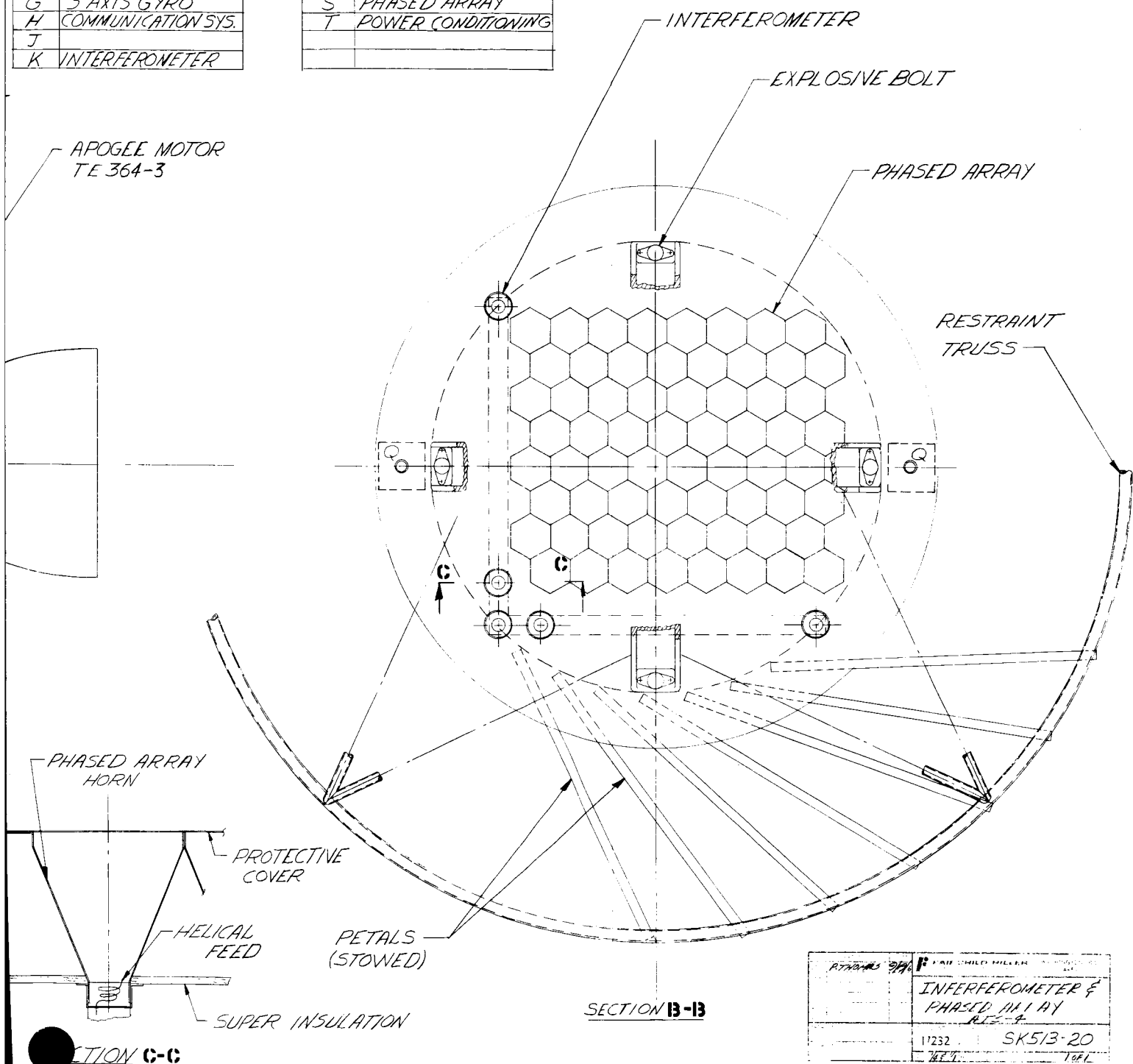


Figure 3.2-3 Spacecraft Module Detail

3-28

The transfer orbit and apogee injection attitude control thrusters are attached to the launch restraint ring. This structure also contains the transfer orbit fuel supply and mounts the de-spin yo-yo. Separation of the apogee engine and launch restraint truss is accomplished by the firing of four explosive bolts.

The spacecraft module contains all of the spacecraft electronics, fuel tanks, reaction wheels and attitude sensors. The fuel supply for attitude torquers and APS is housed in four tanks located on the "Z" axis at the C. G. The equipment volume requirements are considerably less than the space available and consequently additional experiments can be accommodated.

The parabolic antenna multi-band feed is on the reflector side of the spacecraft module and is configured like the one shown in Section B-B of Figure 3.2-1.

3.2.4 Concept Comparison

Some of the key configurational advantages of Figure 3.2-2 over Figure 3.2-1 are listed in the Concept Comparison Chart (Figure 3.2-4). It should be noted that these comparisons only involve configurational advantages. The other system type comparisons are made in other sections of this report.

3.2.5 Titan III C Adaptability

A brief study has been conducted to determine the feasibility of mounting the selected spacecraft concept on a Titan IIIC launch vehicle (Figure 3.2-5). The spacecraft is attached to the Titan interface by a truss structure instead of the monocoque adaptor used previously. Separation from the transtage will be similar to the apogee injection motor separation of Figure 3.2-4 and will free the reflector petals at separation.

The OAO shroud will house the spacecraft during launch. A 30-inch adapter section is provided to attach the OAO shroud to the Titan III C interface.

CONCEPT COMPARISON CHART


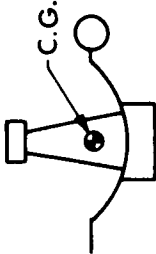
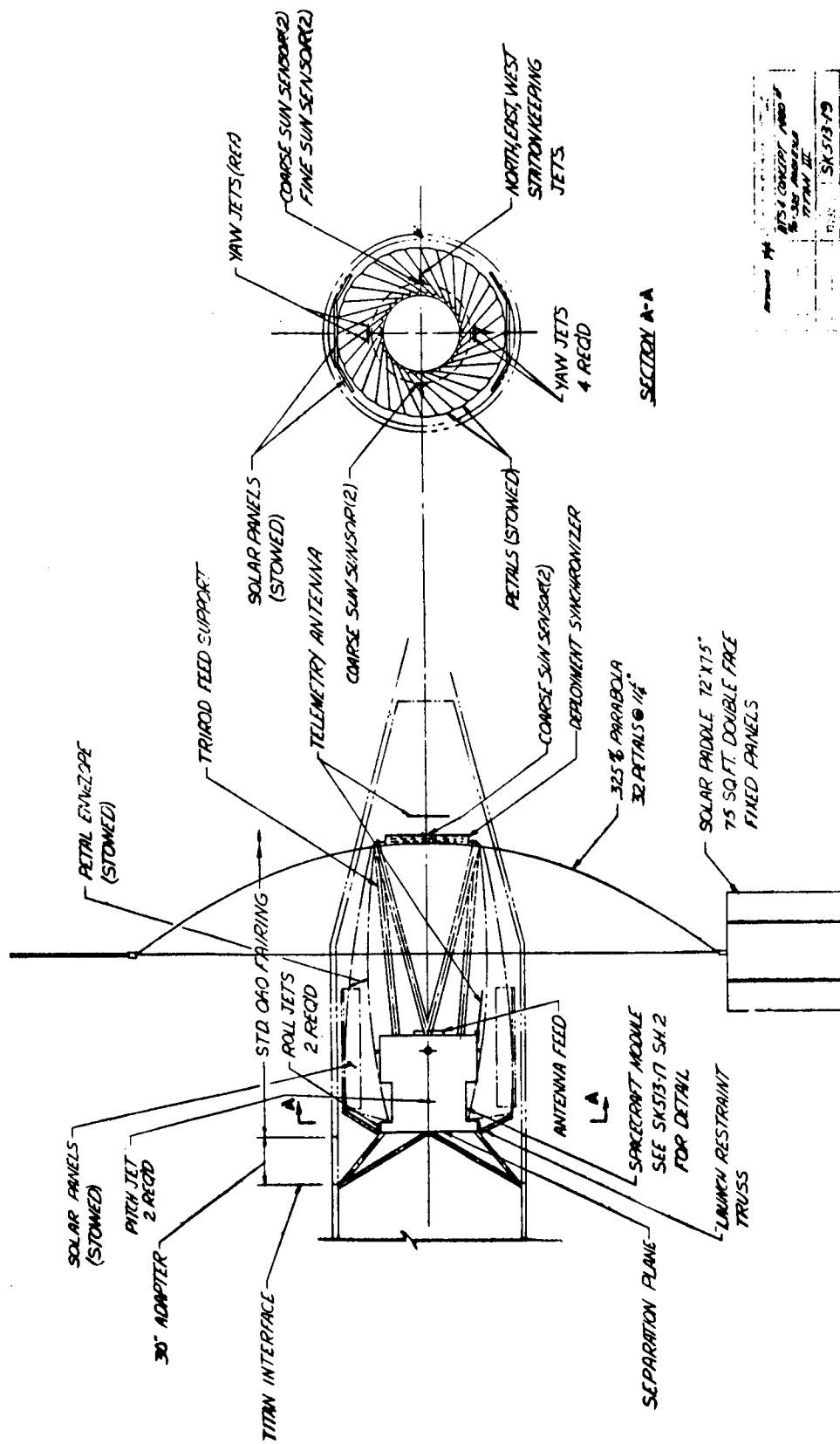
	REFERENCE CONCEPT (SK 513 - 17)	CONCEPT SK 513-18
SEPARATION SYSTEM		
ROTATING SOLAR PANEL OPTION	APOGEE MOTOR SEPARATION REMOVES PETAL LAUNCH RESTRAINT CAN BE ACCOM- PLISHED	APOGEE MOTOR JETTISONED FROM CAVITY
F/D	.33	.28
APS MODES	NO REORIENTATION REQUIRED	REQUIRES REORIENTATION
PREORBITAL POWER FROM SOLAR PANELS	GOOD	POOR
SHROUD REQUIREMENTS	11 FT EXTENSION	15 FT EXTENSION
FEED MAST WEIGHT	30 LB	120 LB
RF LINE PROBLEMS	NO MAJOR ROUTING	REQUIRE ROUTING UP FEED MAST
RATE RETARDER INSTALLATION	NO STRUCTURAL PROBLEM	INTERRUPTS LOAD PATH

Figure 3.2-4 Concept Comparison Chart

Figure 3.2-5 Reference Concept on Titan IIIC



PROJECT	SK 513-17
DATE	11/11/71
BY	SK 513-17
CHECKED	
APPROVED	
REVISION	

3.3 REFLECTOR

3.3.1 Design Evolution and Alternate Approaches

In the course of the design studies and engineering development of deployable antenna structures for the past several years at Fairchild Hiller, certain basic facts have come to light. One of these facts is that to achieve confidence in a deployable structural concept, repeated deployment tests must be performed -- not only on a test model, but on the flight models as well.

The Pegasus spacecraft provides a good example of the confidence to be gained by extensive ground deployment testing. The Pegasus prototype was deployed over 150 times, and each flight spacecraft was deployed 20 to 30 times. A television camera in the first flight Pegasus verified that the deployment system's behavior in space was a precise duplicate of its behavior on the wing deployment fixture. This result justifies the philosophy that any system designed for deployment in space must have a high confidence level established by extensive ground testing.

Previous Fairchild Hiller approaches toward the deployment of large parabolic reflectors concerned themselves with three general classes of structural concepts. A brief description of these concepts follows:

Conic Scissors Deployment - A conic scissors parabolic antenna consists of a number of equally spaced radial elements; each element is a scissor link assembly whose geometry is chosen so that, when deployed, the ends of the links define points on a parabolic curve. Figure 3.3-1 is a photo of a three dimensional model of three elements of a conic scissors. The curve is "filled in" between the points by curved members which are hinged to permit folding with the scissors when in the stowed condition. The reflecting surface is a flexible mesh or metalized mylar which is stretched between the rigid scissor link members when the antenna is stowed.

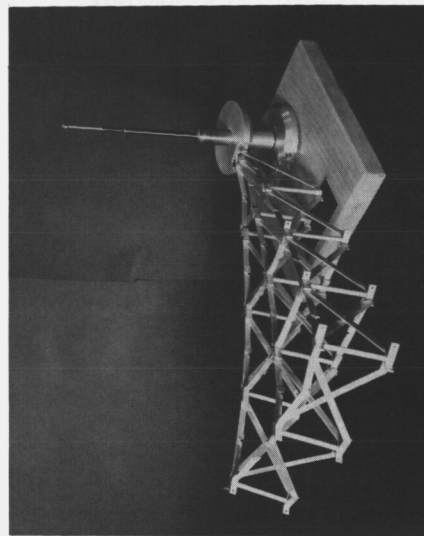
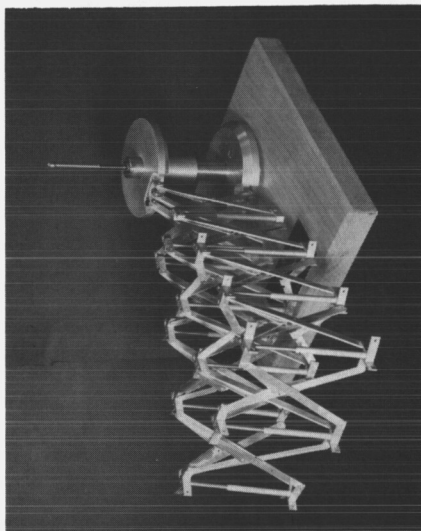
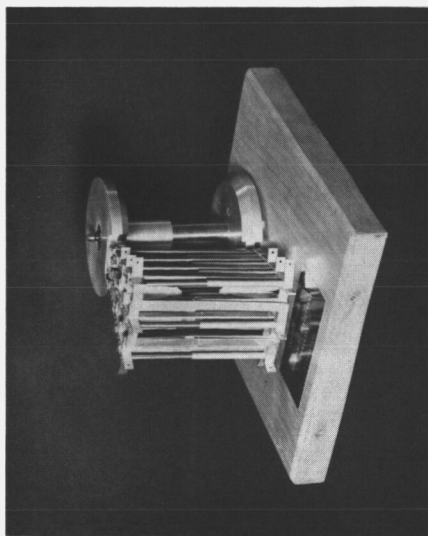


Figure 3.3-1 Conic Scissors Parabolic Antenne

The surface of this deployed parabolic reflector will deviate from that of a true parabolic reflector since the reflecting material will attempt to stretch as straight line elements between the structural members. The amount of deviation will vary as a function of F/D ratio and result in an RMS error of the order of 0.2 inches for a reflector with an F/D of 0.5. Since this error is exclusive of fabrication tolerances and thermal distortions it is far removed from the permissible deviations for an X-Band antenna.

The conic scissors deployment system presents an attractive method of antenna deployment where surface accuracy is not essential. Its packaging requirements are such that a thirty-foot reflector can be packaged in a five-foot diameter cylinder three feet in length. Additional details and analyses based on previous Fairchild Hiller studies regarding this deployment system are shown in Appendix 3A.

Inflatable System - Another method for deploying large structures uses the inflatable, rigidizing systems (Figure 3.3-2). These systems are attractive when the payload volume is limited, since they may be packaged in small canisters. They suffer from the disadvantage that repeated deployments are difficult if not impossible to simulate with the flight article; furthermore, they are extremely sensitive to pressure changes caused by thermal variations. As an example, an inflated antenna will deviate from its true parabolic shape by 0.1 inch for an inflation error as small as 0.001 psi. Another high-risk area for the pure inflatable systems is micro-meteoroid impact, since a puncture can cause the surface accuracy to deteriorate. Additional detail based on previous Fairchild Hiller studies regarding these systems is available in Appendix 3B.

Petal Systems - Fairchild Hiller studies have indicated that a rigid petal approach will result in the most precise deployed reflecting surface for the three erectable concepts considered.

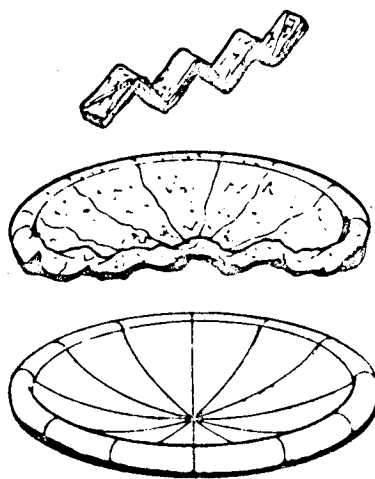


Figure 3.3-2 Inflatable Parabolic Antenna

A previous study of such a system using aluminum honeycomb is detailed in Appendix 3C. In this system the parabolic reflector is "sliced up" into a number of trapezoidal sections which are hinged to facilitate stowage in the available shroud volume. The hinging arrangement and number of petals is largely a function of the available volume.

For RMS surface accuracies of .050 inch, it becomes apparent that inflatable and scissors-type designs fall short of the accuracy requirements while the aluminum honeycomb petal design is too heavy and will result in large solar torques. Consequently Fairchild Hiller Corporation studied a rigid petal design which radically departs from the previous concepts.

It is proposed to use a rigid petal system in which each petal consists of a trussed frame which supports a formed "floating" reflector mesh. Adjacent petals are locked to each other at the rim in a manner permitting relative radial growth between petals caused by temperature differences. The petal structural beams are wrapped in super-insulation to minimize their temperature excursions and differences. The mesh is required to "float" in its contoured shape since even relatively small temperature excursions (of the order of 50° F) will cause deformations far beyond permissible tolerances if the mesh is fixed relative to the supporting substructure. (See Section 3.6.4).

The trussed frame is sized by the launch requirements and is designed to meet the structural and dynamic specifications of the entire mission profile. The design concepts presented in detail in subsequent sections shows the petals supported during launch by the fixed central hub of the reflector and, at the other extremity, by the feed mast structure or experiment module.

The petals were investigated in the launch environment for their

strength and frequency characteristics. In the orbit condition, the deployed and locked petals were investigated for the axisymmetric and antisymmetric frequency responses. The reflector mesh surface and locked petals were investigated for thermal deflections.

Candidate materials for fabricating the antenna petals included aluminum and beryllium. The high stiffness-to-weight ratio of beryllium makes the material an attractive candidate. A comparison of beryllium with aluminum indicates that beryllium structure exhibits greater stiffness for equal strength capability. This performance margin was traded-off against the high costs of the material and problems associated with its fabrication. Since thinner material gages with adequate strength and stiffness margins are feasible with an aluminum design, the high costs and technical risks inherent in a beryllium design did not appear to be warranted for an experimental program.

3.3.2 Petal Hinging Concepts

Three petal hinging concepts were studied for the parabolic reflector in addition to the one discussed in Appendix 3C. They are discussed in the following paragraphs.

Retentive Memory Concept (Figure 3.3-3) - This approach utilizes the "retentive memory" capability of elastic structures and "slices" the paraboloid into a combination of rectangular and triangular petals which are not only hinged at their roots but remain hinged to each other during deployment. During launch the petals are "flattened" and by the release of the strain energy the system can be self deploying. This concept will depend on the feasibility of achieving sufficient petal rigidity and strength to withstand the launch environment while at the same time permitting a sizeable deformation without yielding of the material. An attractive advantage of this concept, due to the "inter-petal" hinge system, is the elimination of an

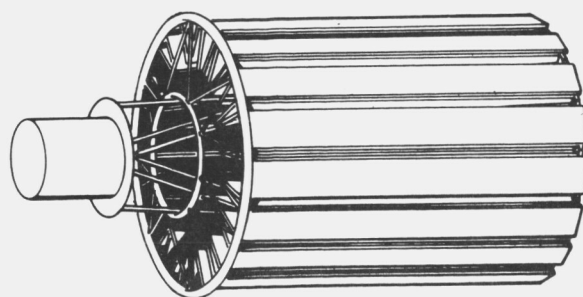
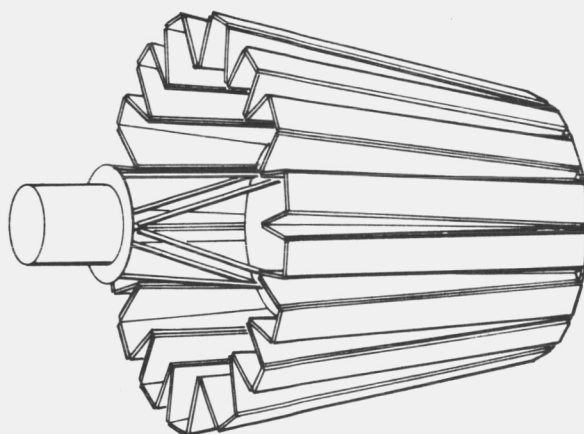
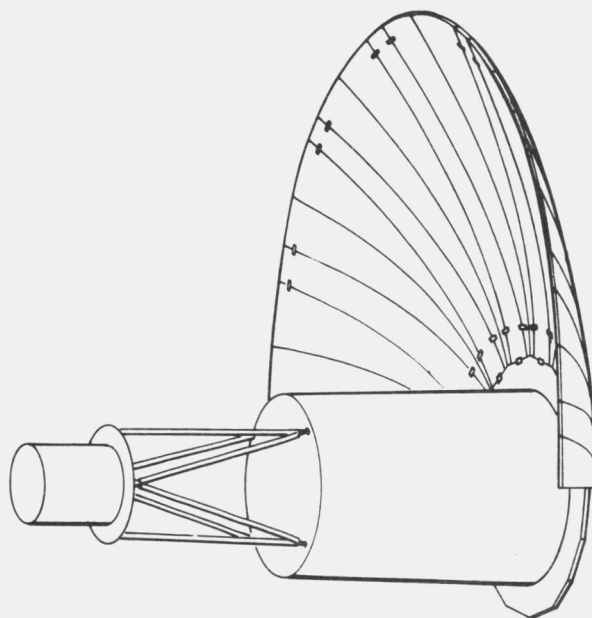


Figure 3.3-3 Retentive Memory Petal Concept

"inter-petal" lock. One problem associated with this concept is the difficulty of a practical design solution to the requirement for thermal isolation of the reflecting surface.

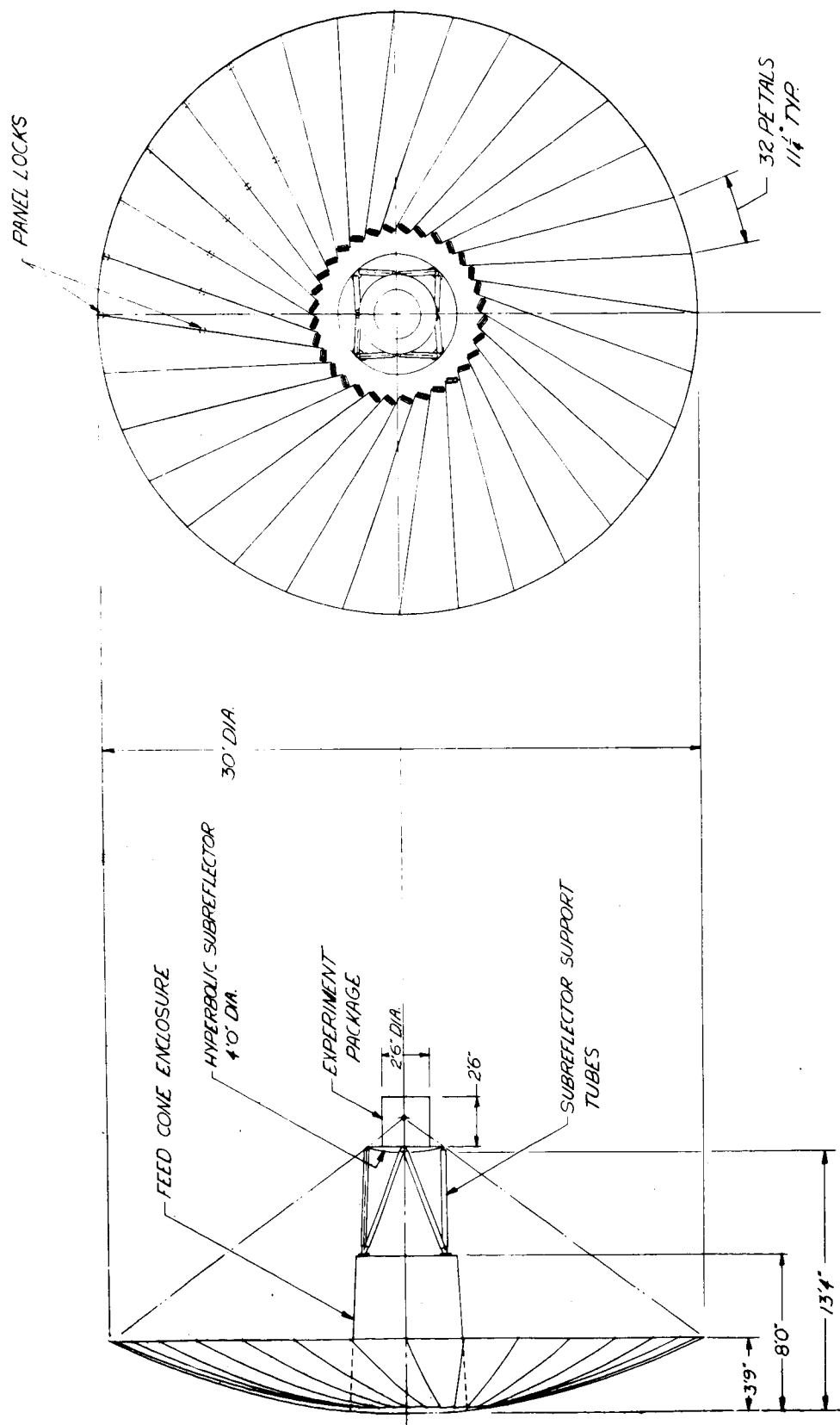
Non-Radial Petals (Figures 3.3-4 and 3.3-5) - This design approach was studied and used in many of the spacecraft concepts discussed in Section 3.1. One of its advantages lies in the simplicity of the hinge design since it permits a simple in-plane hinge. Its principal disadvantage lies in the interference action of adjacent petals in the "near extended" position which necessitates a large gap between petals.

Radial Petals - Skewed Axis - The petal hinging system used in the reference concept utilizes radial trapezoidal petals. They are rotated about a single, skewed hinge line from the stowed to the extended position. The technique for development of this axis of rotation is given in Appendix 3D with photographs of a representative model of the hinging and deployment motion shown in Figure 3.3-6. A skewed hinge design is shown in Figure 3.3-7.

3.3.3 Petal Structural Design

The petal structural design with an in-plane hinge design is shown in Figure 3.3-8 and the skewed hinge design is shown on Figure 3.3-7. The petal consists of a trussed-frame assembly made up of superinsulated aluminum rectangular beams $1 \times 3/4 \times .022$ inches. The diagonal and cross members were assumed at one-half of the cross-sectional area of the main members. The petals which support the solar panels were increased in stiffness to maintain the orbital natural frequency above 1 cps. They are represented by main beams of $2-1/2 \times 1 \times 0.032$ inch cross sections. Four sets of beams on each side of the reflector were assumed to be of this cross-section.

This petal structural configuration is chosen because of its significant weight, stiffness, strength, and thermal distortion advantages over



3-41

Figure 3.3-4 Non-Radial Petals, Sheet One

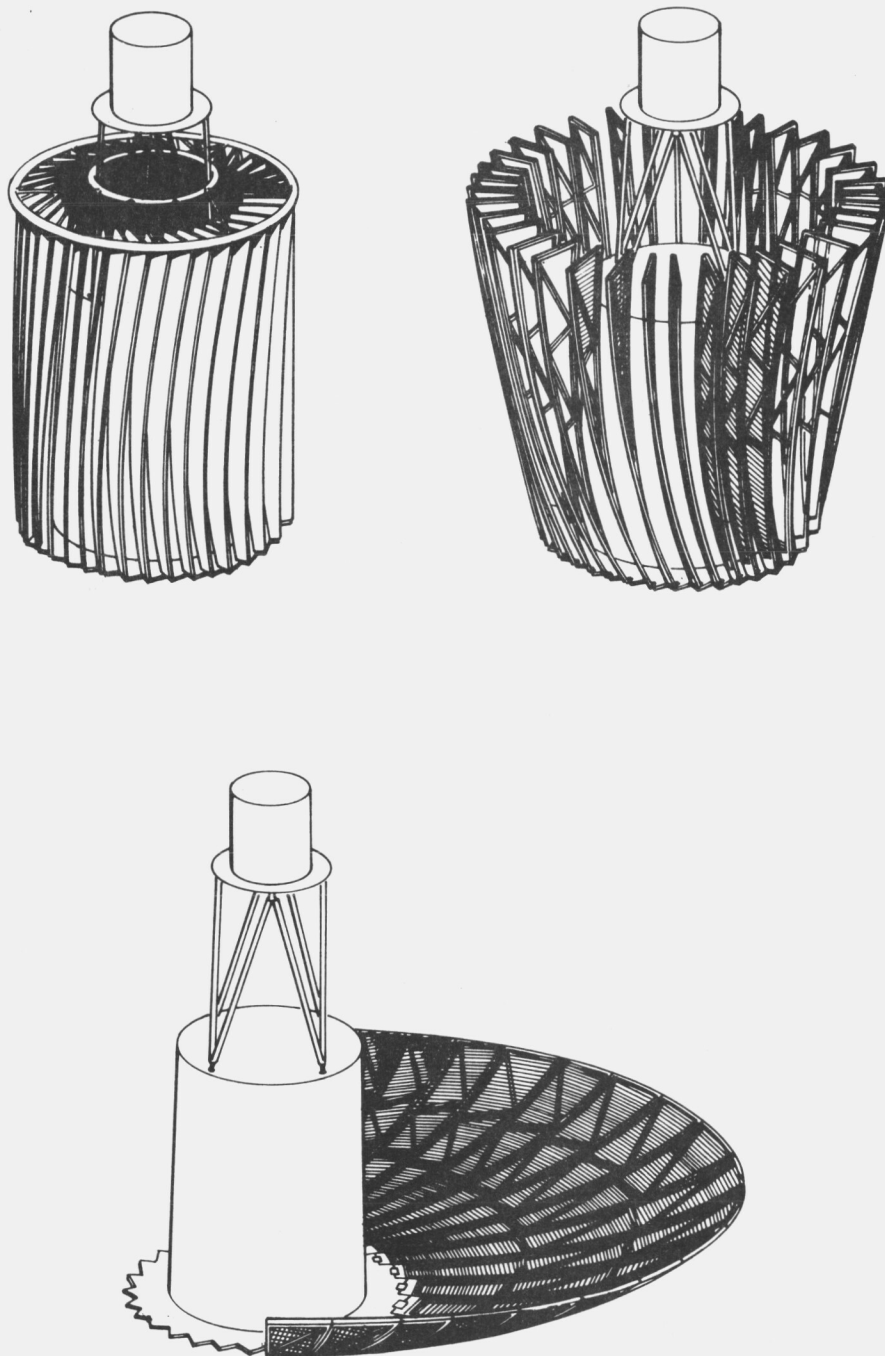


Figure 3.3-5 Non-Radial Petals, Sheet Two

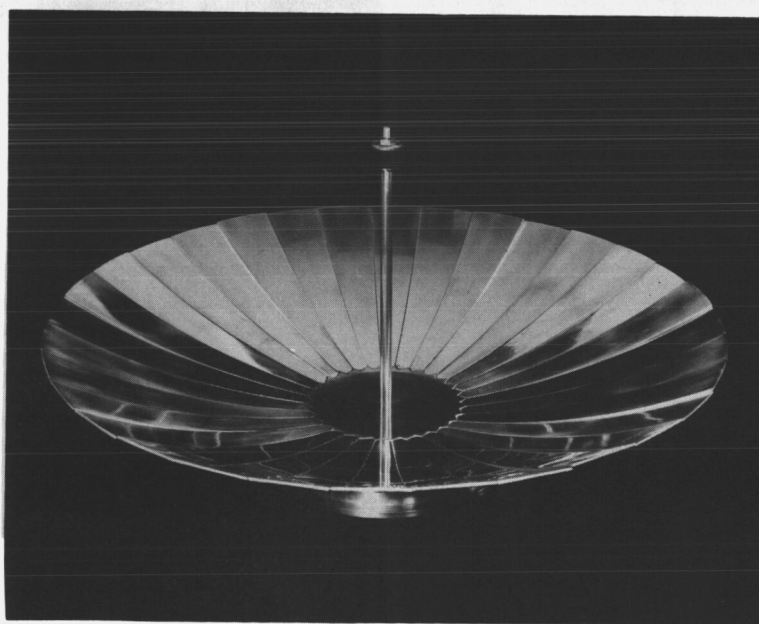
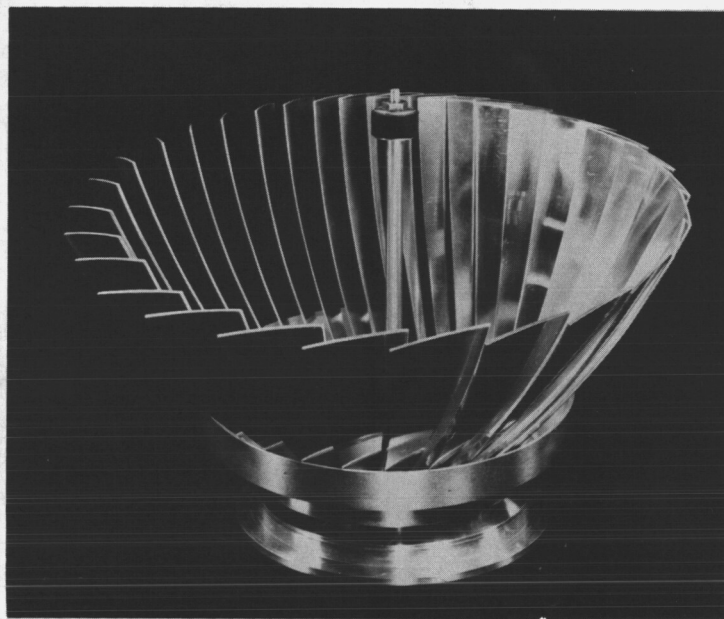
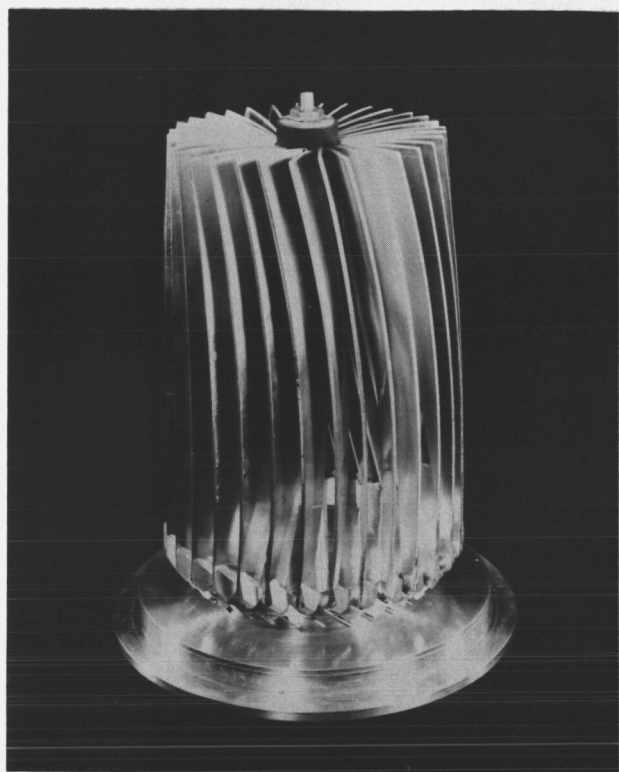
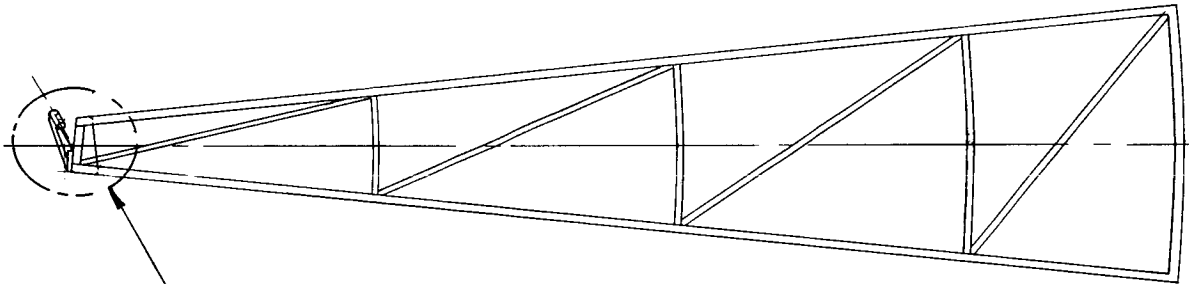


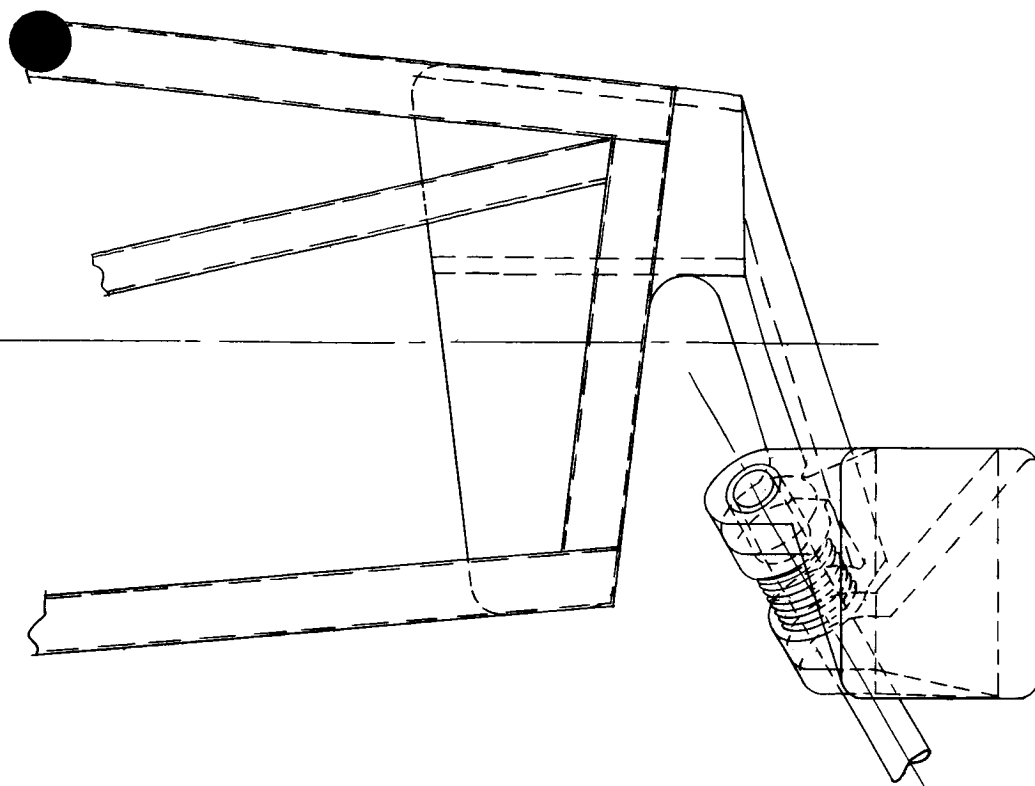
Figure 3.3-6 Petal Concept Parabolic Antenna

3-45-1

PLAN VIEW



SEE DETAIL A



DETAIL A

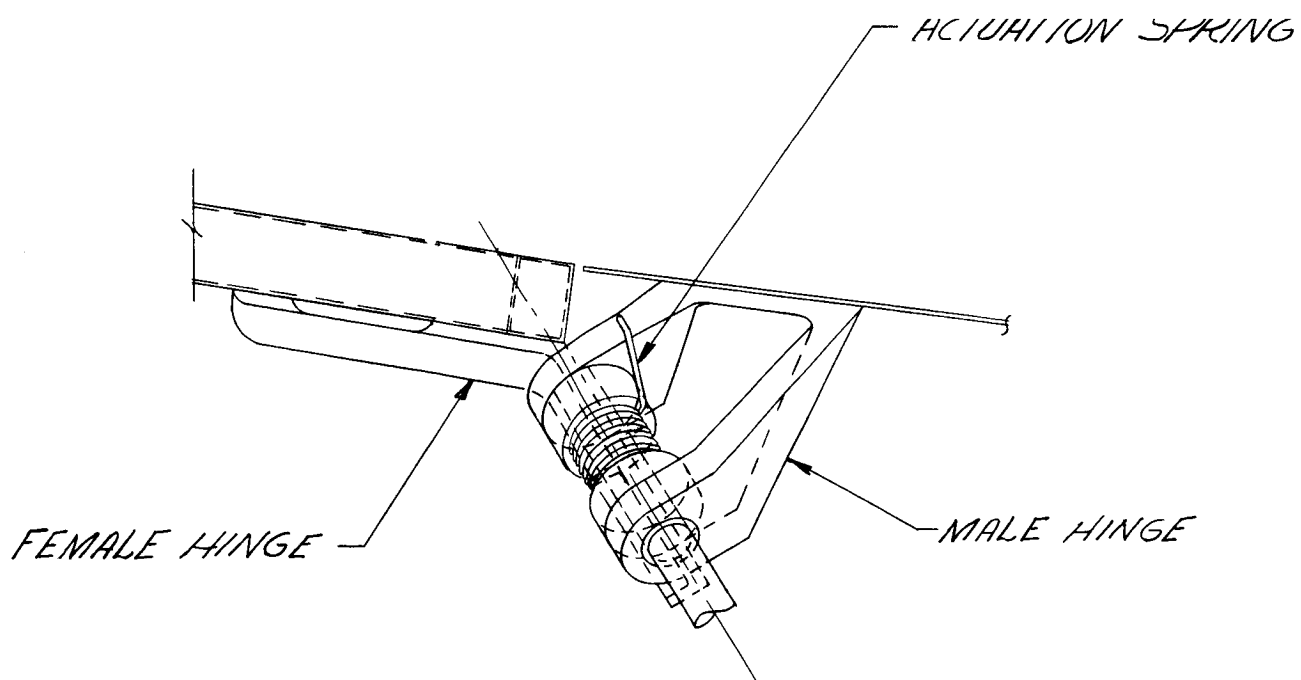


Figure 3.3-7 Skewed Hinge Design

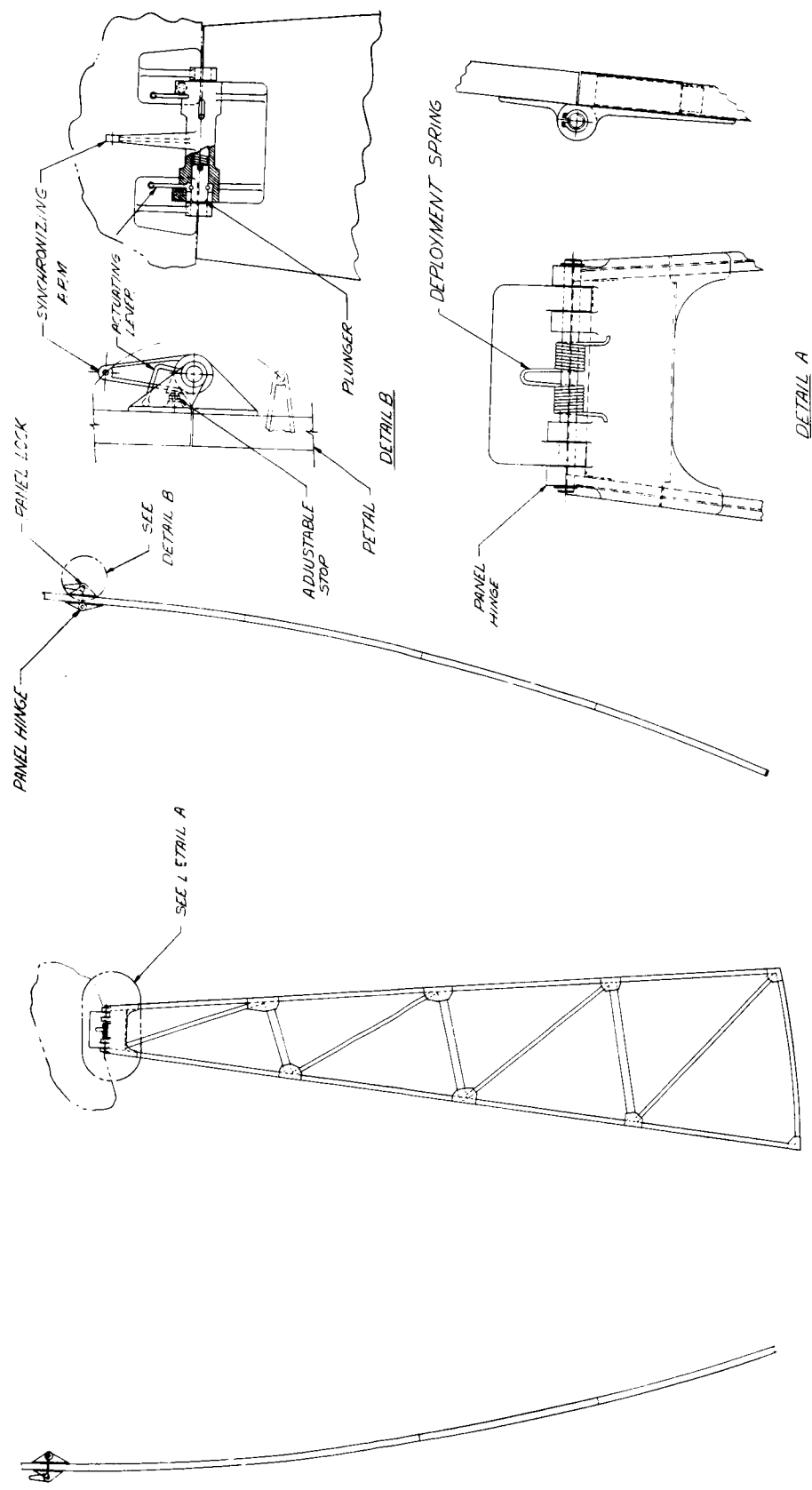


Figure 3.3-8 Petal Structure Assembly and Hinge Details

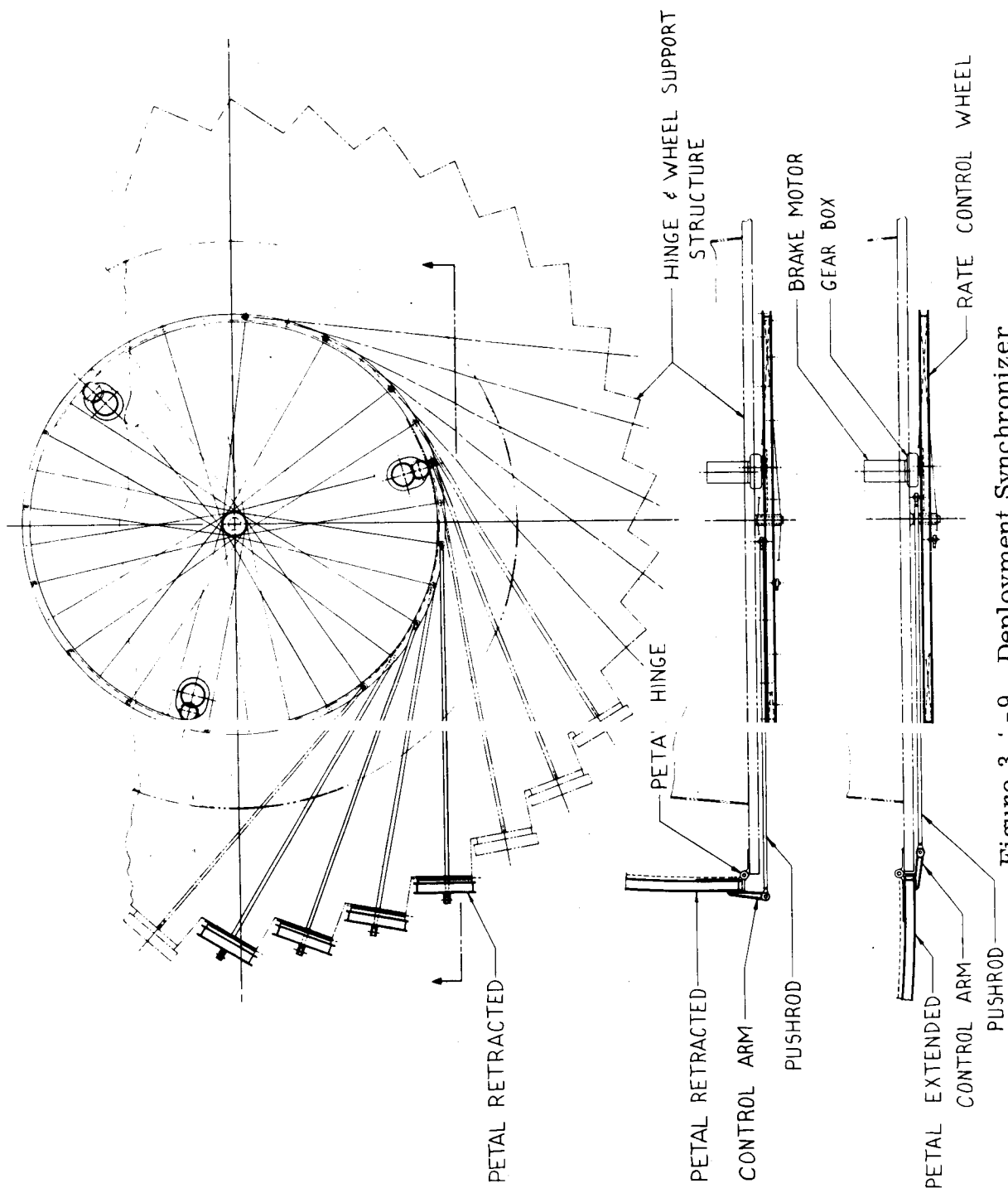


Figure 3.1-9 Deployment Synchronizer

the substructure to deviate $\pm .12$ inches with the stand-off height adjustable to achieve the final $\pm .060$ installation tolerance. Additional inter-petal adjustment can be provided at the petal locks, if required.

3.3.6 Reflecting Surface

Minimization of reflector weight and solar torques points to a mesh or perforated metal reflecting surface. The FHC design incorporates a segmented mesh where each segment covers a typical petal area bounded by adjacent circumferential beams. This arrangement is shown in Figure 3.3-10. The mesh is designed to float to preclude any thermally induced distortions or stresses. This is accomplished by means of Delrin grommets which are molded at discrete locations into the mesh periphery and serve as attachment points to the petal substructure. The grommet holes are slotted or oversize to allow the required thermal shrinkage. (The thermal analysis in Section 3.6 indicates a negative temperature excursion of the order of 300°F which is translated to a shrinkage of the order of 0.15 inches for an aluminum mesh segment 40 inches in length). The mesh is attached to stand-offs which are bonded to the substructure. The stand-offs serve a dual purpose since they also act as insulation spacers.

The design of the attachment (Figure 3.3-10) is intended merely to illustrate the concept and further design and test effort is required to insure a reliable sliding joint that is capable of providing mesh restraint during launch. Considerable thermal cycling and vibration testing of promising attachment candidates will be required to prove out the final design concept.

Another critical feature of the proposed mesh design is the stability of a contoured shape when subjected to the launch environment. Figure 3.3-11 shows the range of wire diameter and spacings that can be

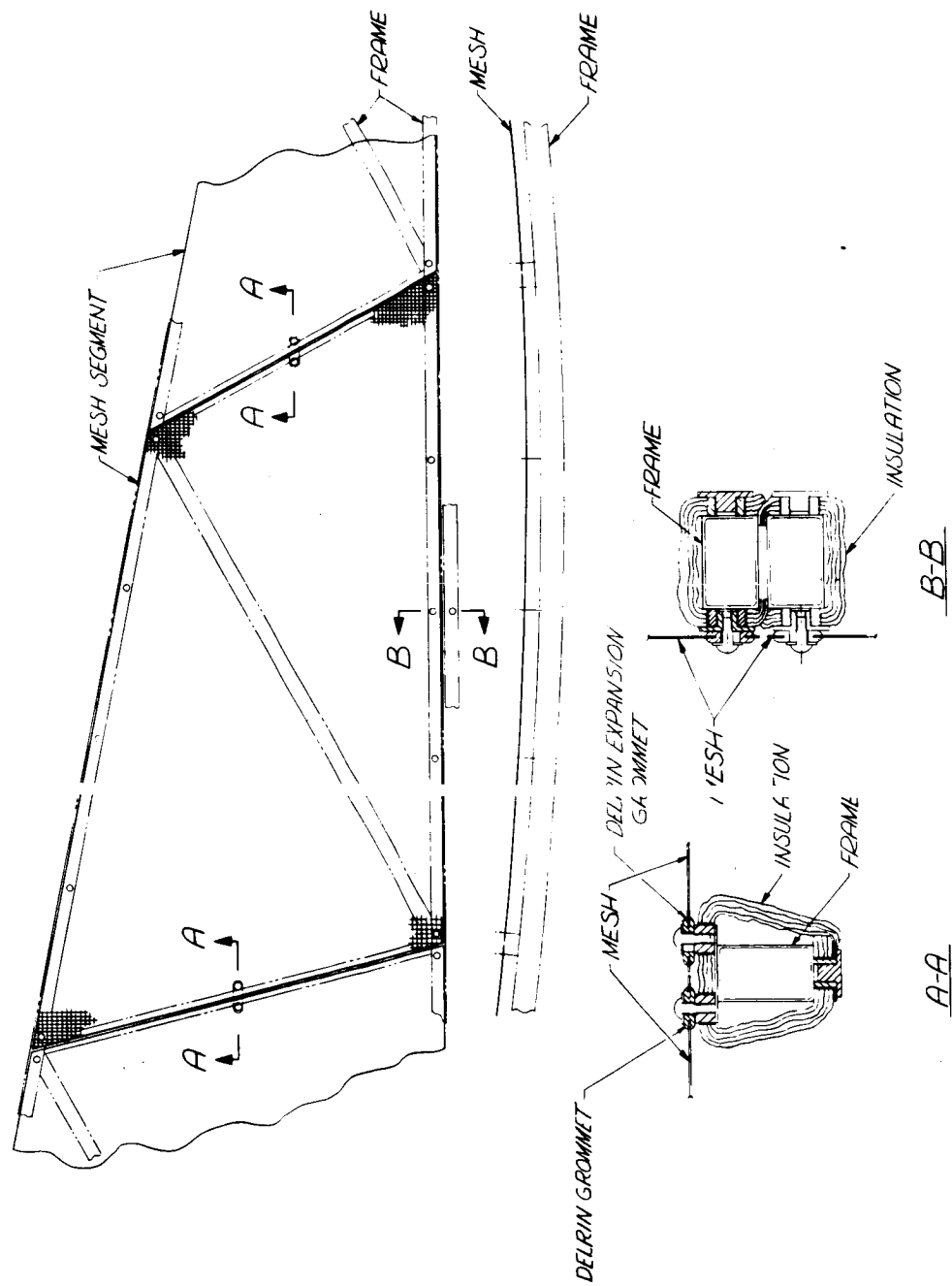


Figure 3.3-1(Mesh Segment Installation

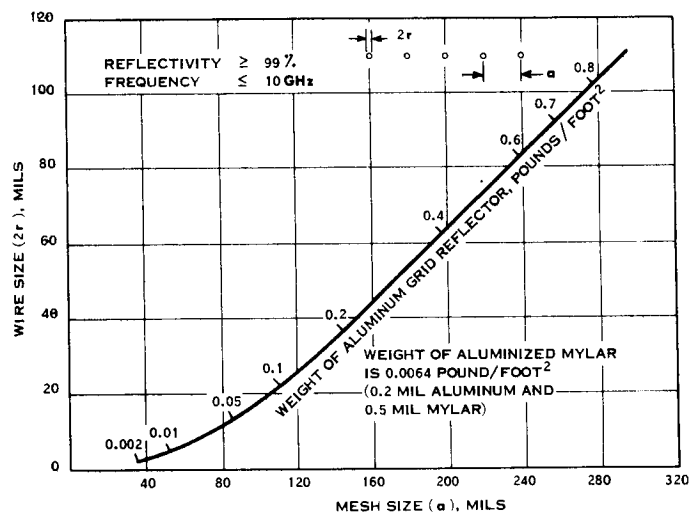


Figure 3.3-11 Mesh Reflector Characteristics

aluminum honeycomb sandwich petals which were examined in previous studies (see Appendix 3C). The detail reflector weight breakdown of this design is given in Table 3.3-1.

3.3.4 Deployment System

The hinging system shown in Figure 3.3-8 or 3.3-7 is attached to the structural skeleton and mounted to a fixed ring on the stationary part of the reflector. A torsion spring is provided to supply the deployment energy. The petals are locked at the hinge in the down position by means of a spring loaded ball-lock pin which is mechanically sequenced by panel rotation. This is accomplished by actuator arm rotation which induces pin rotation to uncage the balls. Each petal is provided with an adjustable stop which insures the "extended conformity" of the petal system. A crank is attached to the petal hinge which serves as the attachment point for a pushrod.

The rods from each petal are tied to a centrally mounted wheel which serves as the deployment synchronizer for the petal (Figure 3.3-9). By means of a gear train which is coupled to a centrifugal governor, the deployment rates can be retarded to a level which will insure a smooth-locking action and preclude prohibitive inertia loads. It is also possible to use an electric motor instead of a mechanical governor to control the deployment velocity and at the same time serve as a redundant deployment device. The latter type of system was used successfully on the Pegasus deployment system.

3.3.5 Tolerance Considerations

Fairchild proposes the use of adjustable stand-offs for reflecting surface attachment to permit some alleviation of the exacting tolerance requirement on the skeleton substructure. It is proposed to maintain the final reflecting surface accurate to within $\pm .060$ inches while permitting

TABLE 3.3-1 REFLECTOR WEIGHT

Petals (32)		Weight (Pounds)
24 at 3.69 lb.	= 88.6 lb.	164
8 at 9.43 lb.	= 75.44 lb.	
Hinges and Springs		35
Mesh		25
Inter-Petal Lock	(32)	15
Down Lock	(32)	15
Rate Control System		15
Insulation		5
TOTAL:		<hr/> 274

considered for X-Band operation. The present material choice is aluminum with a mesh spacing of 0.080 and wire diameter of 0.010. Beryllium was considered but tentatively discarded because of the development problems associated with forming this material into a mesh; it appears attractive because of its low density and low thermal coefficient of expansion when compared with aluminum. Since the total mesh weight (for 80 mil spacing and 10 mil wire diameter) is only 25 pounds the realized weight saving would not be significant.

Additional contour stability can be provided to the mesh by brazing or hard soldering at the joints. The application of a suitable polymer on the mesh of sufficient mass to promote satisfactory bonded joints is another way to obtain mesh rigidization. A polyamide such as DuPont PYRE-M-L possesses good bonding qualities over a wide temperature range and is well suited to the space environment.

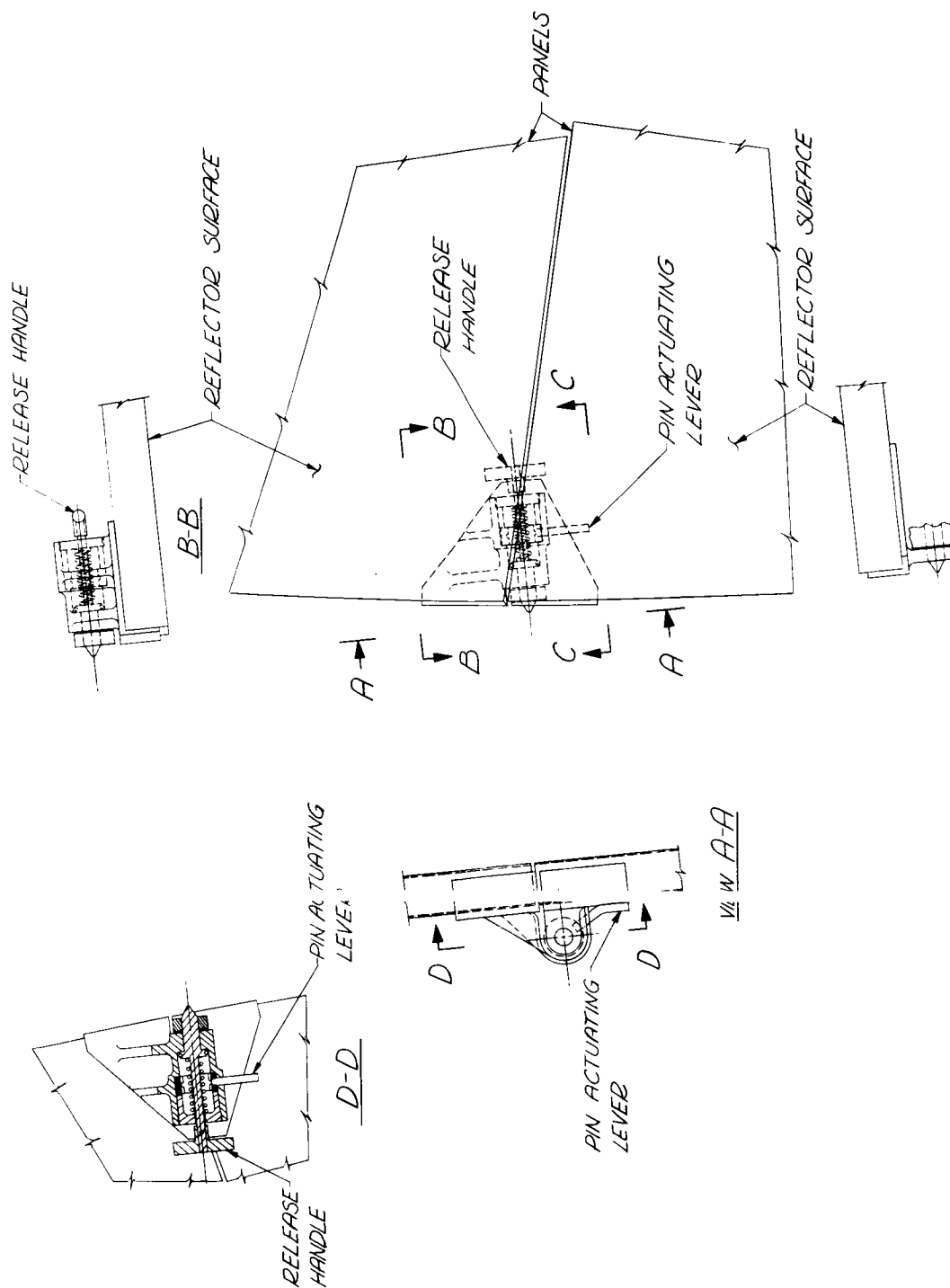
A perforated metal reflector attached in the manner previously described is another possibility. A metal sheet drawn after it is perforated and subsequently contoured, will be more rigid than a mesh; additional stiffness can be provided by the use of beaded perforations. However, since each mil of aluminum for a 30 foot diameter reflector will weigh 11 pounds it appears that the reflecting surface weight will increase if a perforated sheet reflecting surface is used.

3.3.7 Petal Locking System

In addition to the hinge lock discussed in Section 3.3.4 each petal will be locked to its adjacent petal at the rim to insure ring continuity of the deployed reflector. Two types of locks were studied for this purpose (Figure 3.3-12 and 3.3-13). Both types will incorporate a capability permitting relative radial growth between petals caused by petal temperature differences.

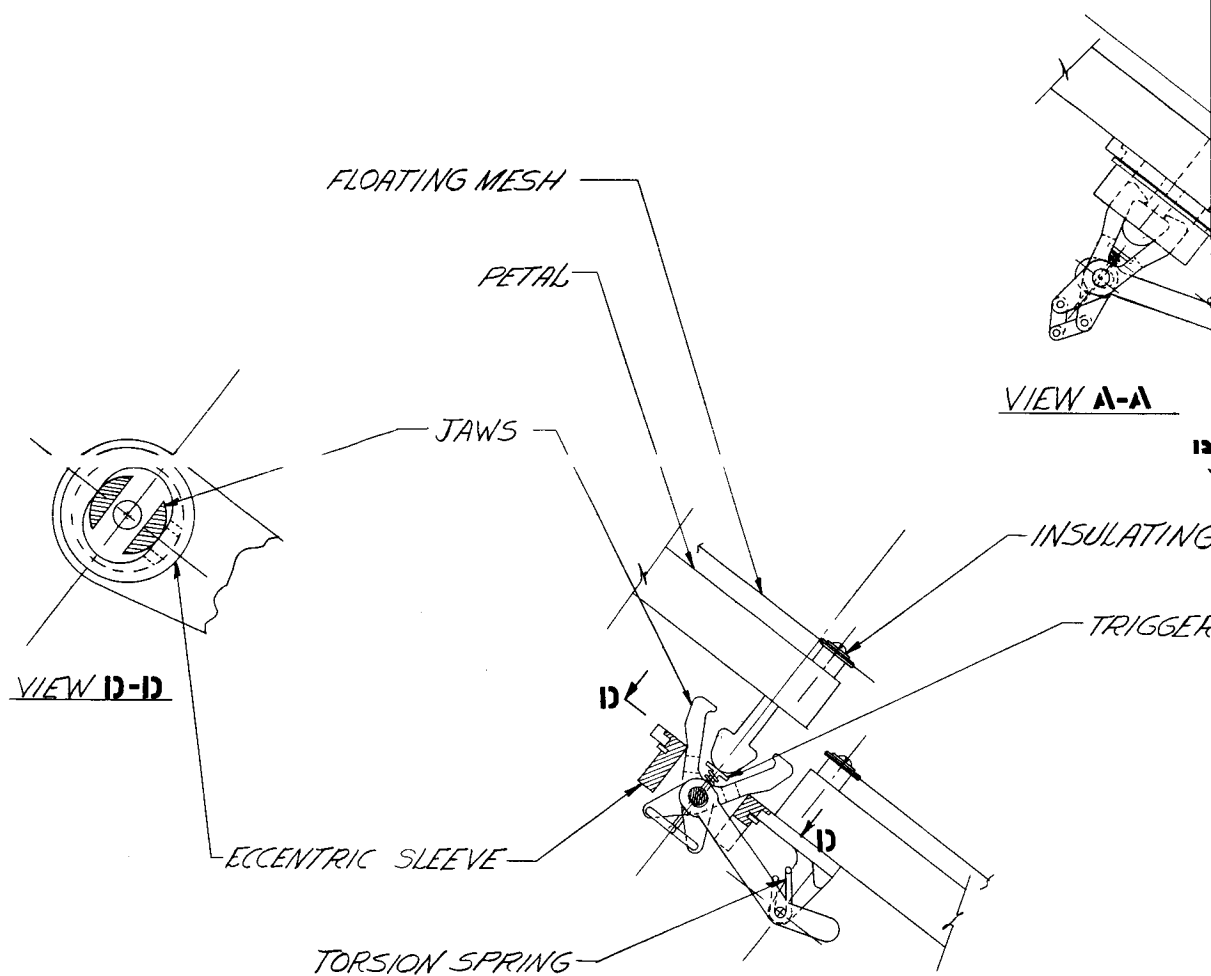
Referring to Figure 3.3-12, as each petal reaches the fully deployed position, the adjacent petal rotates an actuating lever which uncages a ball-lock pin. This action releases a spring loaded, conically pointed plunger which engages a lug on the petal that serves as the lock triggering device. A manual release handle is provided to permit simple unlock action for repeated deployments.

The lock shown on Figure 3.3-13 incorporates additional capability and is selected as the preferred approach. It permits relative vertical displacement to exist (during deployment) at the tips of adjacent petals while still assuring a reliable locking action and differential radial growth. This is accomplished by the "ice tong" device which is triggered by the movement of the over-center toggle due to plunger motion of an adjacent petal. Once the lock is triggered, the tongs provide a spring-powered locking action to pull the deflected petal into locked conformity. The petals are unlocked by a simple rotation of the camming sleeve.



C-C

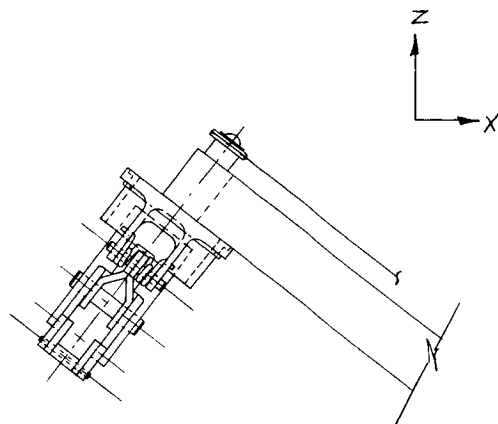
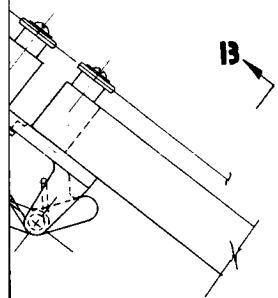
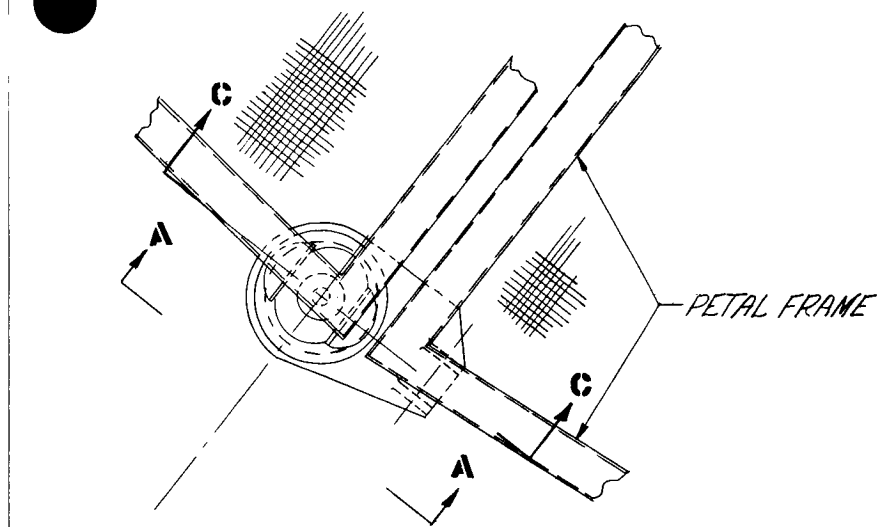
Figure 3.3-12 Inter Petal Locks



SECT. C-C

SHOWING LOCK IN
OPEN POSITION

3-56-1



VIEW B-B

APPROVAL	DATE	FAIRCHILD HILLER SPACE SYSTEMS DIVISION		WASHINGTON, D.C. AREA
DR CHK ATPC ATPC ATPC ATPC	17/66	INTERPETAL LOCK ATS-4		
APPROVAL	CODE IDENT NO	SIZE	DRAWING NO.	
APPROVAL	17232			
SCALE		WT	SHEET	

Figure 3.3-13 Interpetal Lock (Preferred Concept)

3.4 REFLECTOR FABRICATION

3.4.1 Fabrication Considerations

The two candidate materials being considered for the construction of the trussed-frame petal substructure are aluminum and beryllium. The relatively light weight, ease of fabrication, and low material cost make aluminum attractive. Beryllium offers an ideal material when thermal and weight characteristics are prime considerations and cost is secondary. This discussion treats the manufacturing approach required to produce an acceptable product in accordance with aerospace fabrication practices. Because beryllium structural members have not been produced in production quantities and required sizes, material cost is excessive and fabrication techniques are still not routine. For these reasons, Fairchild Hiller recommends the use of aluminum to manufacture the truss frame substructure. When made of aluminum, the petal frame can be assembled from extruded rectangular tubing with gusset plates and clips adhesive bonded to these members.

The reflective surfaces consist of a floating segmented aluminum alloy wire mesh stiffened by the addition of a bonding agent to preclude relative movement of longitudinal and transverse wires.

The balance of the deployable antenna assembly consists of conventional design and materials.

3.4.2 Aluminum Substructure

The fabrication of the petal truss structure in aluminum tubing can be accomplished utilizing well established tooling and forming techniques. The three basic components are structural beams, gusset plates and angle clips.

The structural truss beams of thin wall extruded rectangular tubing will be stretch-wrapped on a Hufford stretch press to the desired

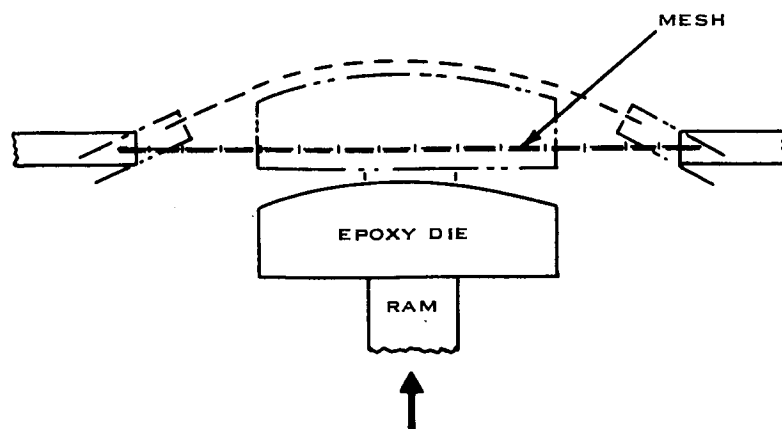


Figure 3.4-1 Shaping of Mesh Reflecting Surface

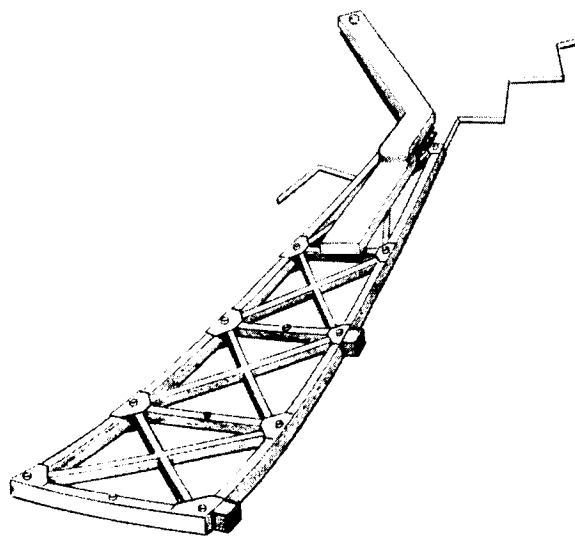


Figure 3.4-2 Master Tool

configuration. Because of the thin sections being considered, use of a filler mandrel or a secondary sizing operation may be necessary to eliminate wall deformation that may occur in the wrapping operation. Parts will be checked for final contour and cut to precise size on female check and trim blocks.

Gusset plates required at the intersection of the truss members will be formed on contoured male form blocks in a hydraulic press.

Angle clips tying the truss members together will be formed on a conventional box brake.

Final selection of the aluminum alloy material to be employed will affect the detail processing of the aluminum components. Preliminary forming trials during tool-proving of the stretch wrap dies will govern the material condition during this operation. The use of aged material (T6 condition) is preferable as the most economical approach, but if buckling or uneven elongation due to nonuniform strain hardening occurs, the part will be formed in the "W" or solution-treated condition followed by an artificial age treatment to the T6 condition. The gusset plates will be formed in the "W" condition followed by a finish form and artificial age treatment. Angle clips will be brake-formed in the T6 condition to the minimum bend radius for the material selected. All parts will be inspected to appropriate checking media to insure that all faying surfaces are flush on assembly. This is necessary to obtain a thin adhesive bond line.

3.4.3 Wire Mesh Forming

The reflective surface of wire mesh will be stretched to shape over a male die (Figure 3.4-1) coordinated to a master mockup. While the mesh is still located on the die, a bonding agent will be sprayed on the mesh to stiffen it.

3.4.4 Sub-Assemblies

It is recommended that the fabrication of the antenna assembly be accomplished by manufacturing several sub-assemblies to be joined in one final assembly. The major sub-assemblies are:

- Petal truss structure, 32 pieces
- Rate control wheel, 1 piece
- Panel hinge, 32 pieces
- Panel lock, 32 pieces
- Hinge support, 1 piece
- Panel interlocks, 32 pieces

These sub-assemblies, together with the feed sub-assembly will be assembled to complete the antenna.

3.4.5 Tooling

In order to ensure that the reflector antenna package functions properly it is necessary to have a control of critical points in the assembly. The critical points are the perimeter of the petal truss, the location of the panel hinge, the undeployed panel lock, and the deployed panel interlocks. To this end a master tool (Figure 3.4-2) can be fabricated to control the petal sub-assembly as it is built and to act as a transfer fixture to the main assembly fixture. The tool simulates the petal truss structure including the panel hinge half, panel lock half, and panel interlocks. In addition it contains the location of the wire mesh support grommets and two special pick up holes to locate the petal sub-assembly in the main assembly fixture.

An extension arm is employed to pick up a center hole in the hinge support to ensure that all petals are located at the same exact angle. For

the petal truss assembly, an assembly bonding fixture (Figure 3.4-3) is suggested, which will:

- Locate and hold all frame truss members in correct relation to each other.
- Locate and hold panel hinge half by picking up the hinge pin hole.
- Locate and hold panel lock half by picking up plunger hole.
- Contain clamping provisions for the gusset plates and angle clips.
- Contain provisions to locate and hold panel interlock halves.
- Contain provisions to locate the wire mesh support grommets.
- Contain provisions to drill two locating holes to be used to locate the sub-assembly in the main assembly.

This tool would be coordinated to an alignment fixture (Figure 3.4-4).

The balance of the sub-assembly tools are conventional in design and require no master control media.

For the major assembly a fixture, probably of rectangular welded pipe construction, would be required. Radial contour plates locate the petal assembly. The basic locating points to hold are:

- The center hole and lower surface of the hinge support plate. All other locations will be relative to these.
- The lower surface and the two pickup holes of the petal assembly.
- The periphery of the launch restraint truss.

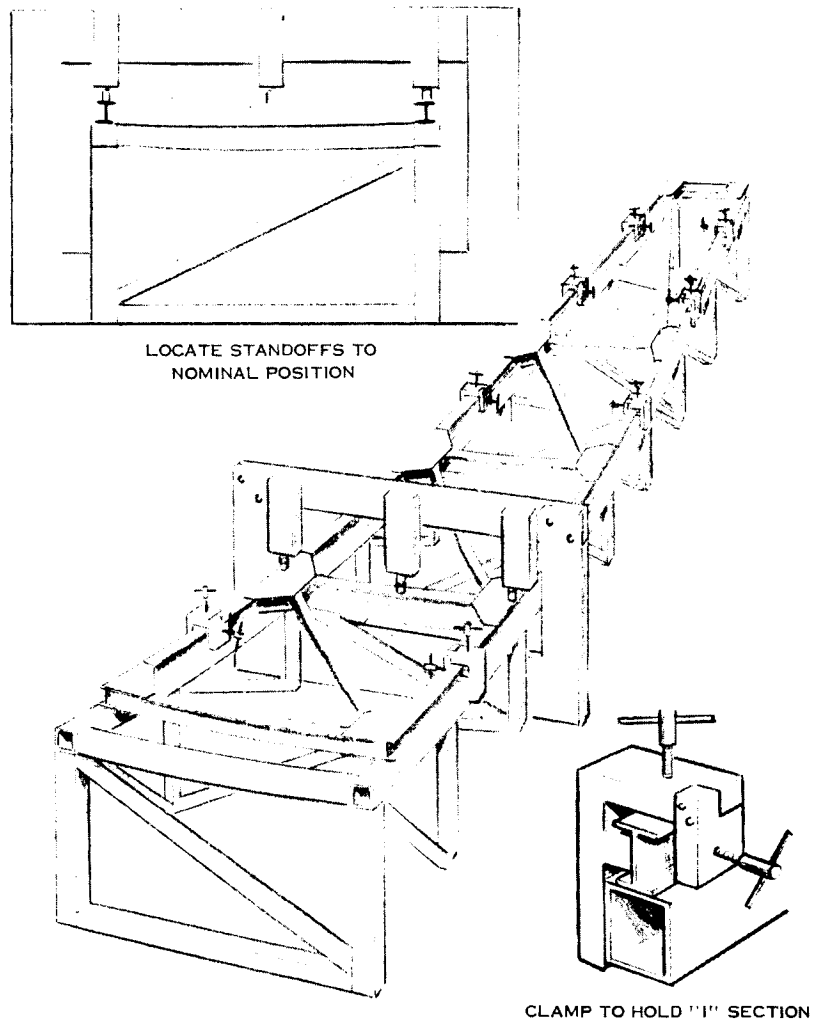


Figure 3.4-3 Assembly Bonding Fixture

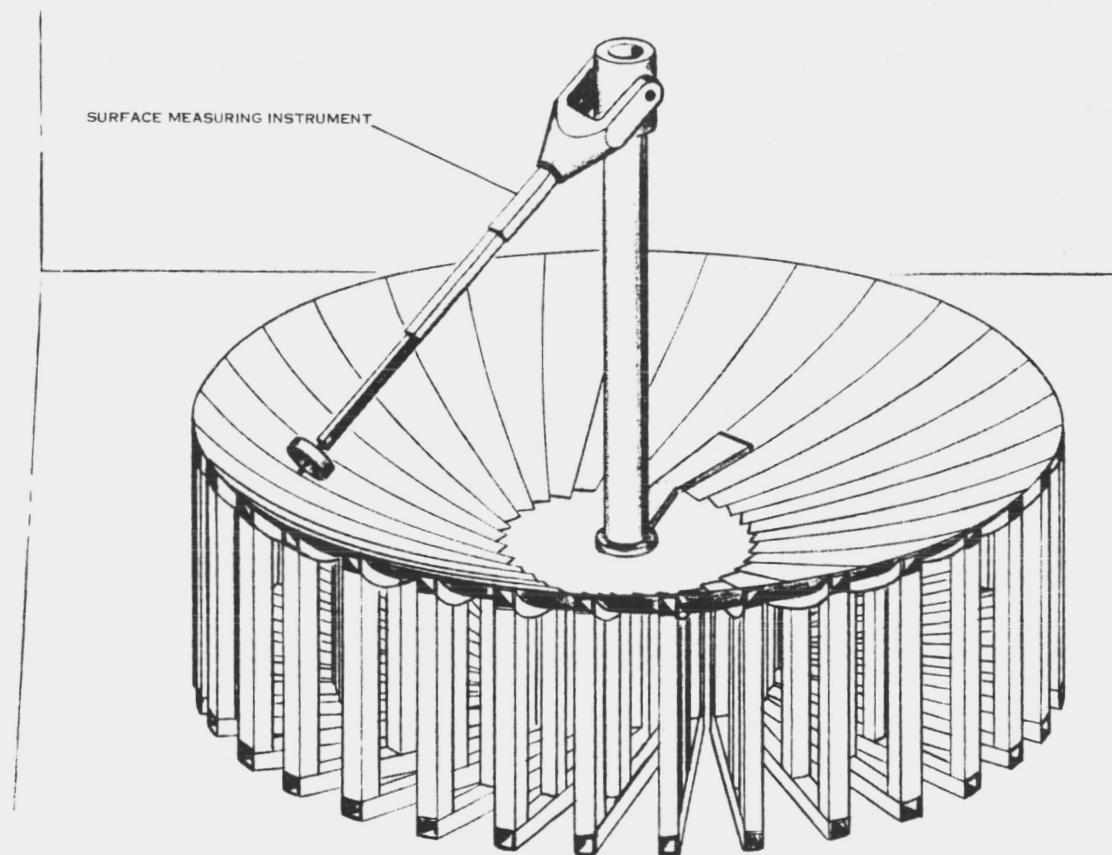


Figure 3.4-4 Hinge & Latch Alignment Fixture

A vertical beam may be employed to support portions of the fixture and also to mount a surface measuring instrument. The location of the petal supports is established by mounting the petal master tool in the assembly fixture, picking up the center hole in the hinge support plate, and employing optical tooling to establish the correct attitude. An alternate method would be to use the surface measuring instrument to locate the petal master.

3.4.6 Assembly Procedure

The petal truss frames may be assembled, in sequence, as follows:

1. Locate all components in fixture to assure good fit.
2. Remove from fixture.
3. Clean and etch.
4. Relocate in fixture.
5. Apply adhesive.
6. Clamp and bond.
7. Locate and bond mesh reflector supports.
8. Drill two master locating holes.
9. Remove from fixture.

Special attention is required to assure that all parts match perfectly to obtain a thin bond line in order to obtain near thermal uniformity in service.

The balance of the sub-assemblies are simple in nature and will be handled in accordance with standard aerospace fabrication practices.

The final assembly will require a high degree of accuracy to ensure perfect functioning of the deployment mechanism. In concept it is relatively

simple, requiring only full utilization of the tooling and strict adherence to quality standards of workmanship. The procedure is as follows:

1. Locate the hinge support plate by picking up the center hole and banking the lower surface.
2. Locate the petal assemblies by picking up the two master locating holes.
3. Drill and ream the attachment holes through the petal hinge half and the hinge support plate.
4. Locate the launch restraint truss.
5. Locate the rate control wheel under the hinge support plate.
6. Install the rate control push rods.
7. Actuate the 32 petals to functionally check out the mechanism. Attach insulation.
8. Remove petals and locate in holding fixture. Install the wire mesh reflector and insulation.
9. Relocate petals in assembly fixture.
10. Using the surface measuring instrument mounted on the overhead cross beam, scan the surface of the reflector panels. Adjust the standoff grommets to attain the desired contour. Remove the surface measuring instrument.

3.4.7 Measurement of Surface Deviations

The measurement of the surface deviation of the paraboloid presents some problems not encountered with ordinary large dishes. These problems are traced to the fragile, easily distorted reflecting surface and to the testing proposed. The unusual requirements placed on the measuring facility are:

- It must be non-contacting.
- It must possess the ability to work through the window of an environmental chamber.
- It must possess the ability to measure small vibrations of the reflecting surface, at high frequencies, without damaging or influencing the surface.

To fulfill these requirements it is suggested that a microwave interferometer be placed on the end of a boom, in place of the usual contacting member.

A sketch of the concept is shown in Figure 3.4-5. The main elements of the facility are: (1) the boom, which supports the microwave interferometer; (2) the interferometer (part of which is on the end of the boom, and the remainder on the floor); (3) the mechanism and precision scale for shortening or lengthening the boom and for measuring the differences in length; and (4) the shaft encoders on the axes of rotation of the boom, to measure the coordinates of the point being investigated.

A brief description of each of the principal components of the equipment for measuring surface deviations follows:

- The boom is sturdy and 10 feet long. One end terminates in a two-axis gimbal at the focal point of the dish and is free to rotate about two orthogonal axes through the focal point. The other end supports the microwave interferometer on an adjustable mechanism.
- The adjustable mechanism positions the microwave interferometer with respect to the point on the reflecting surface which is being measured. A precision scale is attached to the boom and a vernier pointer is attached to the interferometer. The

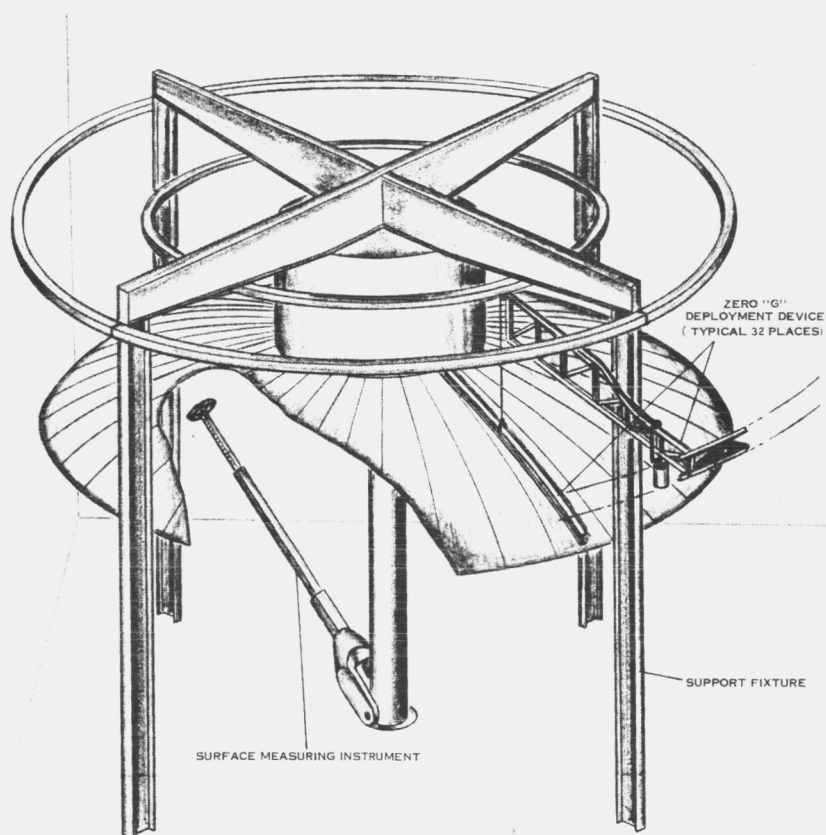


Figure 3.4-5 Measurement of Surface Deviations

movement of the interferometer with respect to the boom is read off the scale (with respect to an arbitrary reference point).

- The end of the boom at the focal point is attached to a two-axis gimbal, which allows rotation about two axes. The axes are orthogonal to one another and to the axis of the reflector. Thus, the boom can be positioned to examine any point on the surface of the reflector.
- The microwave interferometer, a commercial instrument (Weinschel Engineering Non-Contacting Displacement and Vibration Meter, Model 1802), is supported by the adjustable mechanism. Its sole purpose is to locate the far end of the boom a known precise distance from the point on the reflector which is under investigation. The instrument accomplishes this with a precision of better than 0.0001 inch - better than needed. In operation, the interferometer transmits a 35 GHz signal and detects changes in phase of the reflected signal due to relative movement of the surface with respect to the interferometer. The interferometer antenna has an elliptically-contoured surface which focuses the radiation on a spot about 0.2 inch in diameter at a distance of about 12 inches in front of it. The ellipsoid antenna is used for both transmission and reception, with the signals being separated by circulators and hybrids. Part of the transmitted signal is fed into a phase detector as a reference, while the reflected signal constitutes the other input to the phase detector. Phase differences are indicated on either a meter, a recorder, or a scope.

The use of the microwave interferometer as a sensor has the advantages of:

- Precision
- No contact
- Ability to work through the window of a temperature or vacuum chamber
- Ability to indicate the electrical position of the surface, which, in some cases, could differ from the mechanical position
- Ability to measure vibrations of the reflecting surface at frequencies up to 20 KHz without influencing the surface.

In use the procedure for measuring the error of a point on the surface would be as follows. The boom is positioned so that the vertex is being examined. The ellipsoidal antenna is positioned about a foot from the vertex point. The phase shifter inside the interferometer is adjusted to give a null. The pointer position is read off the precision scale, for reference.

The boom is then rotated to the point on the reflecting surface being examined. The ellipsoidal antenna is now moved, by means of the screw, until the interferometer again indicates the null (being careful not to change the setting of the internal phase shifter). The pointer position and the boom angles are recorded.

The difference in pointer positions is then compared to the proper (theoretical) value, to arrive at the surface error. A complete circular segment of the reflector can be measured, by rotating the boom about the axis of the reflector.

A brief discussion of the accuracy of the technique follows. The errors, beginning at the reflector surface and working toward the focus, are tabulated below.

<u>Description of Error and its Sources</u>	<u>Magnitude of Error (in. $\times 10^{-3}$)</u>	<u>Comments</u>
Distance from surface to ellipsoidal antenna	± 0.1	Gives distance from effective reflector location, at the angle of incidence of operation
Error in precision scale and pointer	± 0.1	
Error in mechanical precision of two-axis gimbal	± 3.0	Largest single source of error
Error due to imprecision in angular position of beam	± 1.0	Requires high resolution shaft encoders
Temperature changes	± 1.0	Temperature of the beam will be monitored and a correction for its thermal expansion applied

The total inaccuracy of the surface measuring facility should not exceed ± 6.0 mils. This value is considered acceptable.

3.5 STRUCTURAL AND DYNAMIC ANALYSES

3.5.1 Analytical Methods and Approach

The structural analysis of the ATS-4 integrated spacecraft, like any complex structure, is essentially an iterative process. Based on functional and strength criteria, a preliminary structural configuration is chosen. Once a configuration has been selected, it can be idealized into an analytical model by judiciously lumping the masses of its components at discrete locations, the lumped masses being connected by springs representing the component stiffnesses. The response of this so-called lumped mass-spring model can be studied by conventional analytical techniques. In this manner the adequacy of the preliminary configuration can be checked and the structure optimized by a repetition of the process.

The preliminary analysis was conducted by uncoupling the spacecraft into components consisting of a feed mast, reflector, spacecraft module and adapter. For preliminary analysis purposes the criteria employed were the natural frequency and strength in the launch condition and only the natural frequency in the orbital environment.

After the preliminary structural configuration has been determined, the components are coupled to obtain a lumped mass-spring model, whose dynamic response is evaluated. Using this approach, the final reference concept was evaluated in the launch and orbital conditions as an integrated spacecraft. The dynamic response analysis consists of the determination of natural frequencies, mode shapes and magnification factors. These parameters are then employed to investigate the strength of the structure, resulting in margins of safety for the various components.

Basic Energy Analysis - The internal load solution of a complex structure subjected to steady state or dynamic forces is programmed for a 7090 digital computer. The solution uses the minimum energy-force method in matrix format. The program is in such form that changes in the applied loads and structural stiffness can be accomplished rapidly. with

Utilizing Castigliano's theorems and principles of superposition yields the general solution:

$$\text{where: } \delta_{ij} = \int \frac{S_i S_j dx}{\alpha} \quad (2a)$$

$$\text{and } \frac{S_i S_j dx}{a} = \left\{ \frac{M_i M_j dx}{EI} + \frac{P_i P_j dx}{EA} + \frac{T_i T_j dx}{GJ} + \frac{q_i q_j A}{Gt} \right\} \quad (2b)$$

$$\delta_{ij} = \delta_{11} \text{ or } \delta_{12}, \text{ etc.}$$

Equation (1) in matrix form becomes:

$$\begin{bmatrix} \delta_i \\ \mathbf{X} \end{bmatrix} = \begin{bmatrix} \delta_o \end{bmatrix} \quad (1a)$$

which by inversion yields:

$$\begin{bmatrix} \mathbf{X} \end{bmatrix} = \begin{bmatrix} \delta_i \end{bmatrix}^{-1} \times \begin{bmatrix} \delta_o \end{bmatrix} \quad (3)$$

Also, in matrix form, equations (1) and (2) lead to:

$$\begin{bmatrix} \delta_i \end{bmatrix} = \begin{bmatrix} S_i \end{bmatrix}' \begin{bmatrix} D \end{bmatrix} \begin{bmatrix} S_i \end{bmatrix} \quad (4a)$$

and

$$\begin{bmatrix} \delta_o \end{bmatrix} = \begin{bmatrix} S_i \end{bmatrix}' \begin{bmatrix} D \end{bmatrix} \begin{bmatrix} S_o \end{bmatrix} \quad (4b)$$

where $\begin{bmatrix} D \end{bmatrix}$ is a diagonal matrix of

$$\frac{dx}{EI}, \frac{dx}{AE} \text{ etc.}$$

The final internal forces are obtained from equations (3) and (4) as follows:

$$\begin{bmatrix} S \end{bmatrix} = \begin{bmatrix} S_o \end{bmatrix} - \begin{bmatrix} S_i \end{bmatrix} \begin{bmatrix} X \end{bmatrix} \quad (5)$$

$$\begin{bmatrix} S \end{bmatrix} = \text{true internal load system}$$

$$\begin{bmatrix} S_o \end{bmatrix} = \text{assumed internal load system}$$

$$\begin{bmatrix} S_i \end{bmatrix} = \text{redundant system internal loads}$$

$$\begin{bmatrix} X \end{bmatrix} = \text{redundant correction factors}$$

With the above program the $[S]$ matrix may represent a number of unit load conditions $[S_u]$. The unit load conditions represent unit mass points properly allocated on the analytical model. This unit load may be a concentrated load or of some distribution. These unit loads may represent the loading through the structure in the axial, lateral, pitch, and yaw directions. The influence of the structure due to these unit loads in their respective directions are derived in matrix form by:

$$[\delta_{inf}] = [S_u]' [D] [S_u] \quad (6)$$

With the unit solution matrix $[S_u]$ and the influence coefficient matrix $[\delta_{inf}]$, the internal loads and deflections of the modeled structure are obtained by multiplying these matrices by design factors $[F_D]$ as obtained from steady state, dynamic transmissibilities, or other criteria. The factor $[F_D]$ is n times dead weight. If $[S_u]$ is considered the unit solution, the design internal loads are:

$$[S_D] = [F_D] [S_u] \quad (7)$$

The design deflection at each unit point and in the direction of the unit point load is:

$$[\delta_D] = [F_D] [\delta_{inf}] \quad (8)$$

The above program lends itself to a thermal load analysis with proper preparation of the analytical model. The thermal loads can be determined by replacing the assumed internal loading $[S_o]$ of equation (4b) by $[\alpha \Delta T]$. The final internal loads will be obtained by:

$$[S_t] = [S_i] [X] \quad (9)$$

Frequencies and Mode Shapes - The natural frequencies and normalized mode shapes of the analytical model are obtained from:

$$\{q\} = \omega^2 [\delta_{inf}] [m] \{q\} \quad (10)$$

where $[\delta_{inf}] = [k]^{-1}$ input from energy analysis.

Sinusoidal Vibration - From an evaluation of the natural frequencies and mode shapes, a forced sinusoidal vibration analysis is accomplished for any number of frequencies. The structural damping of the analytical model can be varied for each mass point. The peak transmissibilities for each mass point are obtained from:

$$\begin{aligned} \{T\} &= \{T_r + iT_i\} = \\ &= \left[[I] - \omega^2 [\delta_{inf}] [m] + i[g] \right]^{-1} \times \\ &\quad [I] + i[g] \{V\} \end{aligned} \quad (11)$$

$$\{|T|\} = \left\{ \sqrt{T_r^2 + T_i^2} \right\} \quad (12)$$

$$\{S_{dd}\} = 386 [S_u] [m] \{|T|\} \quad (13)$$

where: $[\delta_{inf}]$ - from energy analysis

$[g]$ - structural damping (variable)

$[m]$ - mass

$\{V\}$ - coupling

$\{S_{dd}\}$ - internal design loads due to dynamic vibration

$[S_u]$ - unit solution from energy analysis

Analytical Modeling - The analytical method previously discussed lends itself to a multi-lumped mass solution of the structure in any configuration.

In the launch configuration, the stowed petals are secured to the base hub and to the feed mast structure at the upper end. The model should represent the stiffness of the feed mast structure and its associated mass as well as the spacecraft structure, adapter section and, if possible, the influence of the booster structure.

The number of unit mass load points are determined by careful study of the petals, feed mast, spacecraft, and adapter section. The petals are stacked in groups, thereby minimizing the number of mass points required to represent their influence.

The choice of the unit mass point locations representing the structural weight as a unit solution is carefully chosen to represent the total energy of the structure and determine the proper critical load areas. These same mass point locations should apply to the lateral, axial, and torsional frequencies, transmissibilities, internal loads and static load conditions.

The structural model of the deployed antenna (orbit condition) for the determination of the natural frequencies in the symmetric, anti-symmetric, and torsional directions will be different from the model for the launch condition. The choice of the unit mass point locations will be made so as to include all the energy in the structure. Each point may represent a two-or-three dimensional coupling (eg, Z forces due to Y direction inputs, etc.).

3.5.2 Preliminary Analysis

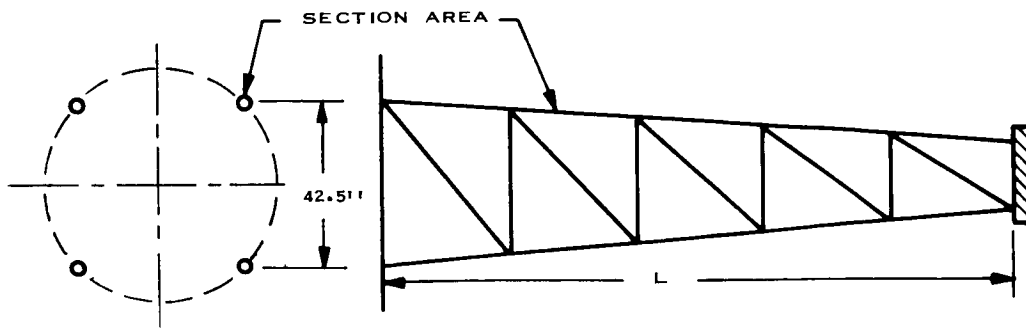
Feed Mast - The evolution of configurational concepts, described in Sections 3.1 and 3.2, shows different types of feed mast structures. In all the concepts but one (scissor concept reflector), the feed mast structure is used to support the reflector petals in the launch configuration.

Five feed mast structures were investigated; square truss, single tube, four tube, quadruped and tripod. A final comparison is made in Table 3.5-1, showing the optimum type of feed mast structure for a common 350 pound tip weight and a 12 foot length. The comparison is made on the basis of weights and frequencies.

For the feed mast configurations studied, the feed mast tip weight includes the dead weight structure acting at this point, the associated electronics and the force due to petal reactions. The parametric curves developed for each configuration consider the tip weight subjected to a magnification factor of 20.0. Structural weights under any other magnification factor may be obtained by ratioing the feed mast tip weight relative to the assumed magnification.

The strength criteria used in deriving the member sizes for all the configurations is based on 2024 aluminum with an ultimate tensile strength of 60,000 psi. Configurations primarily in bending considered a bending modulus factor of 1.25.

- Truss Configuration - Figures 3.5-1 and 3.5-2 show the results of a rectangular truss feed mast study. The mast lengths varied from 12 to 14 feet with tip weights up to 800 pounds. Figure 3.5-1 gives the required truss section area for any given tip weight and length, and in turn the total truss weight. Figure 3.5-2 shows the natural frequency of the structure for a given tip weight and length with the associated truss moment of inertia. This configuration, although adequate structurally, presented feed blockage problems.



SECTION AREA AND TOTAL WEIGHT VS FEED TIP WEIGHTS

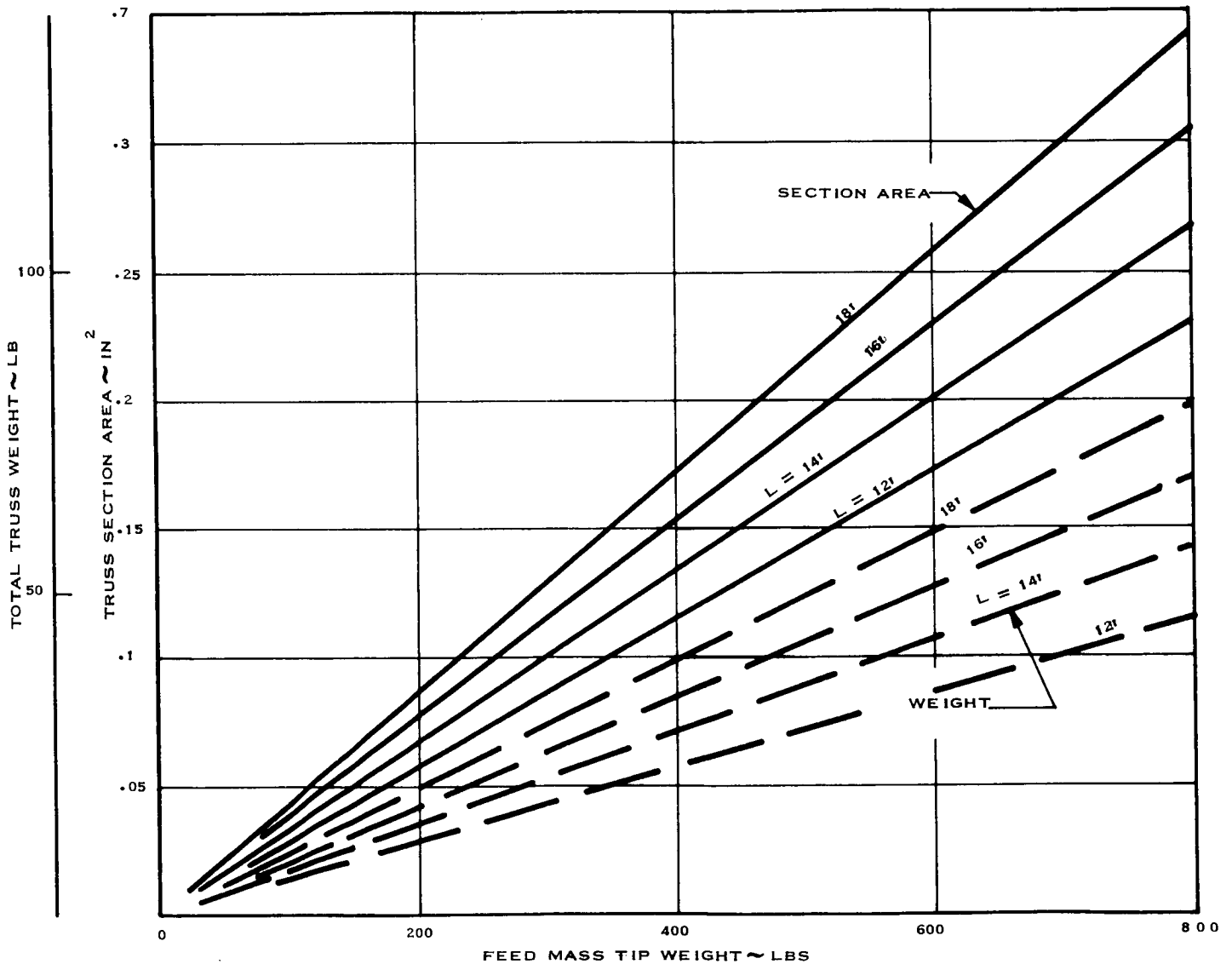


Figure 3.5-1 Truss Feed Mast Weights

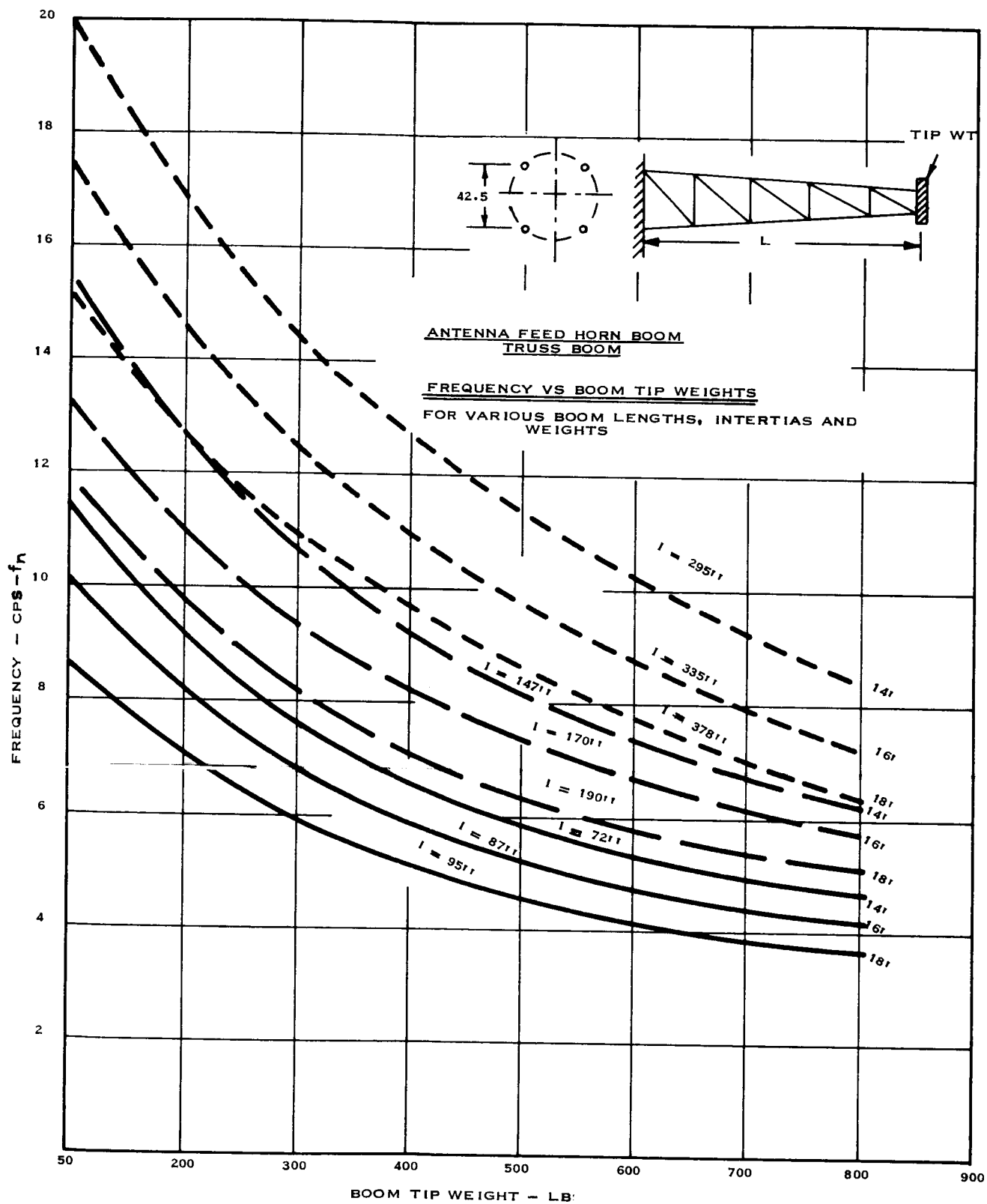


Figure 3.5-2 Truss Feed Mast Frequencies

- Single Tube Configuration - Figure 3.5-3 evaluates a single tube configuration. The figure illustrates the feed mast weight required for a tip weight while subjected to a 10, 20 or 30 g input. This configuration proved inefficient and presented feed design problems.

- Four Tube Configurations - Figures 3.5-4 and 3.5-5 show the study of a four tube feed support mast. This configuration conforms to concept SK513-14 in which it is used to support the petals in launch as a cantilevered beam but is deployed in orbit. Figure 3.5-4 shows the feed mast unit weight for any tip weight, length and various tube diameters. Figure 3.5-5 shows the frequency for a given length and tube diameter. It also evaluates the total feed mast weight for any tip weight when subjected to 10, 20 or 30 g. This configuration resulted in high feed mast weights and, since the feed mast deployment concept was dropped, this system was not further explored.

- Quadruped and Tripod Configurations - The quadruped is basically a long column truss structure composed of four sets of triangular members or a total of eight individual members. The tripod is identical except it contains only six individual members.

Figures 3.5-6 and 3.5-8 illustrate the two configurations of the feed mast structure. The two configurations are evaluated for tube diameter and wall thickness, lateral natural frequency, and structure weight, as a function of tip load and feed mast length. These parameters are plotted in Figures 3.5-6 through 3.5-9.

The structural sizes, diameter and wall thickness, are predicated on an allowable stress of 60,000 psi with 2024 aluminum material. The configuration is assumed to be a single degree of freedom system with a damping factor of .05 yielding a transmissibility factor of 20.0. The lateral natural frequency is obtained by determining the influence coefficient (δ , in/lb) of

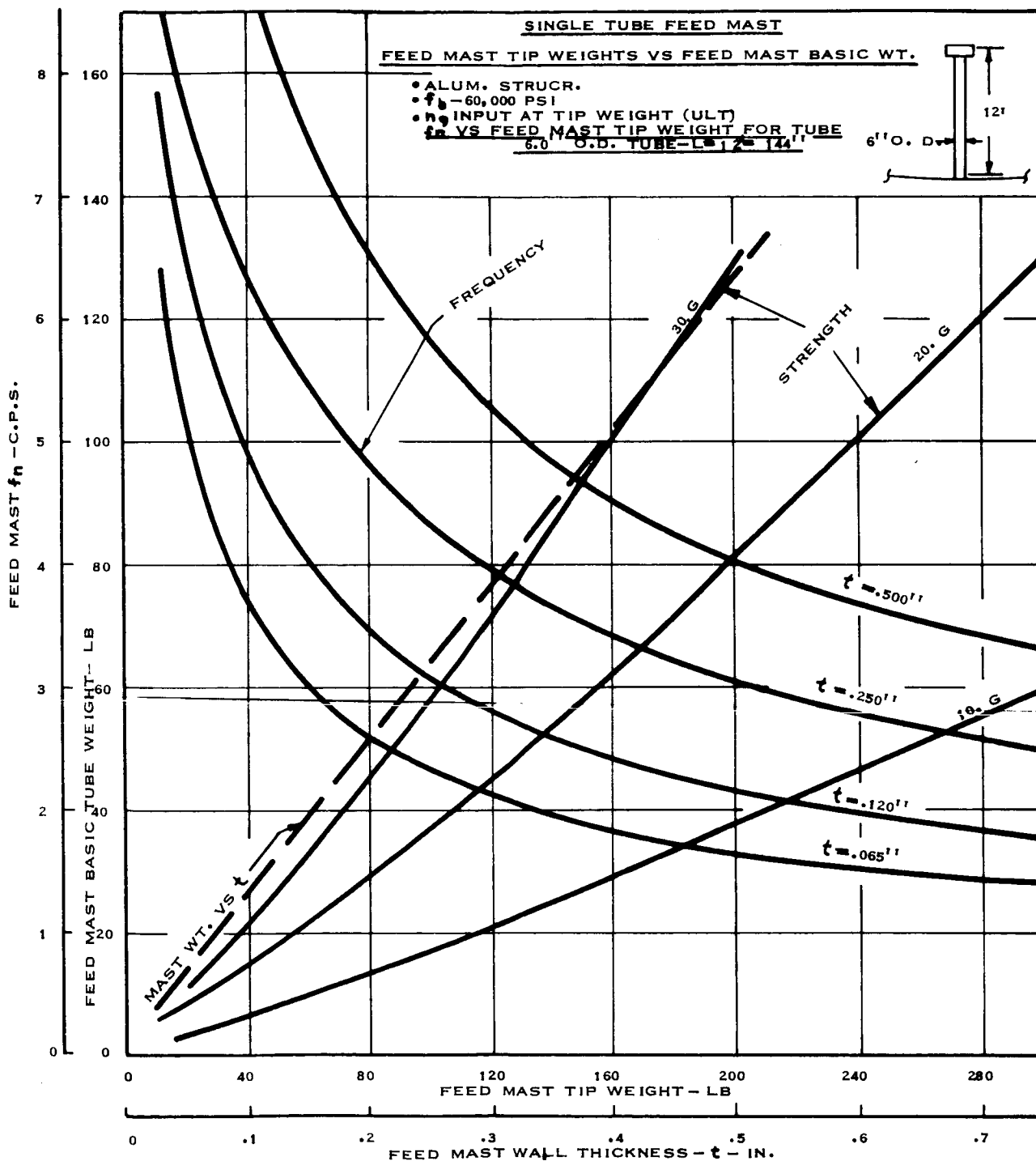


Figure 3.5-3 Single Tube Feed Mast Analysis

ALUMINUM STRUCTURE, $f_b = 75,000$ PSI, 20.G INPUT

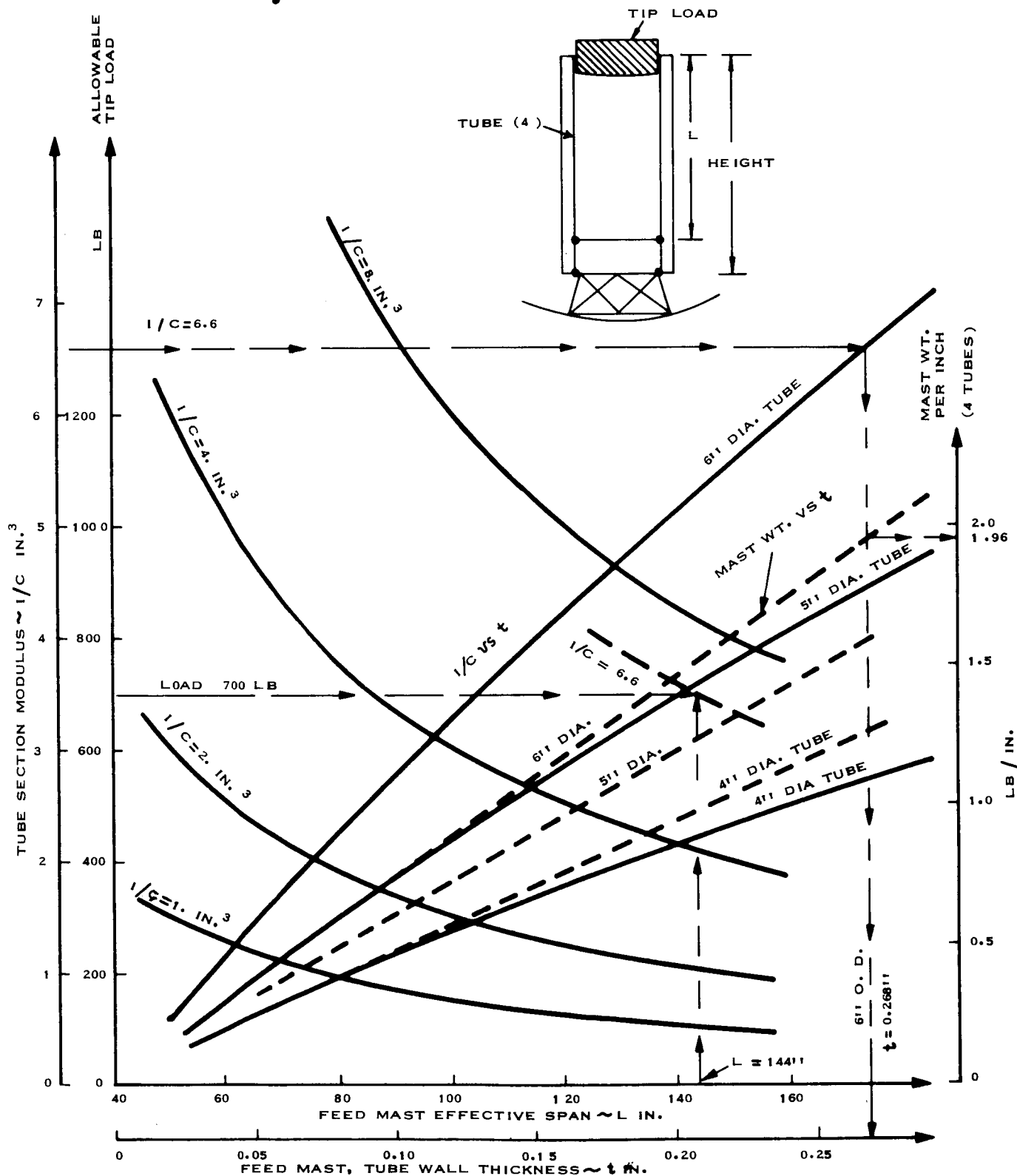


Figure 3.5-4 Four-Tube Feed Mast Weights

FEED MAST WALL THICKNESS VS MAST BASIC WT

MAST-6.0" O.D. TUBES; L=93.1"
 f_n OF FEED MAST VS FEED MAST TIP WEIGHT

- ALUM. STRUCT.
- $f_b = 60,000$
- n_g INPUT AT TIP WT.

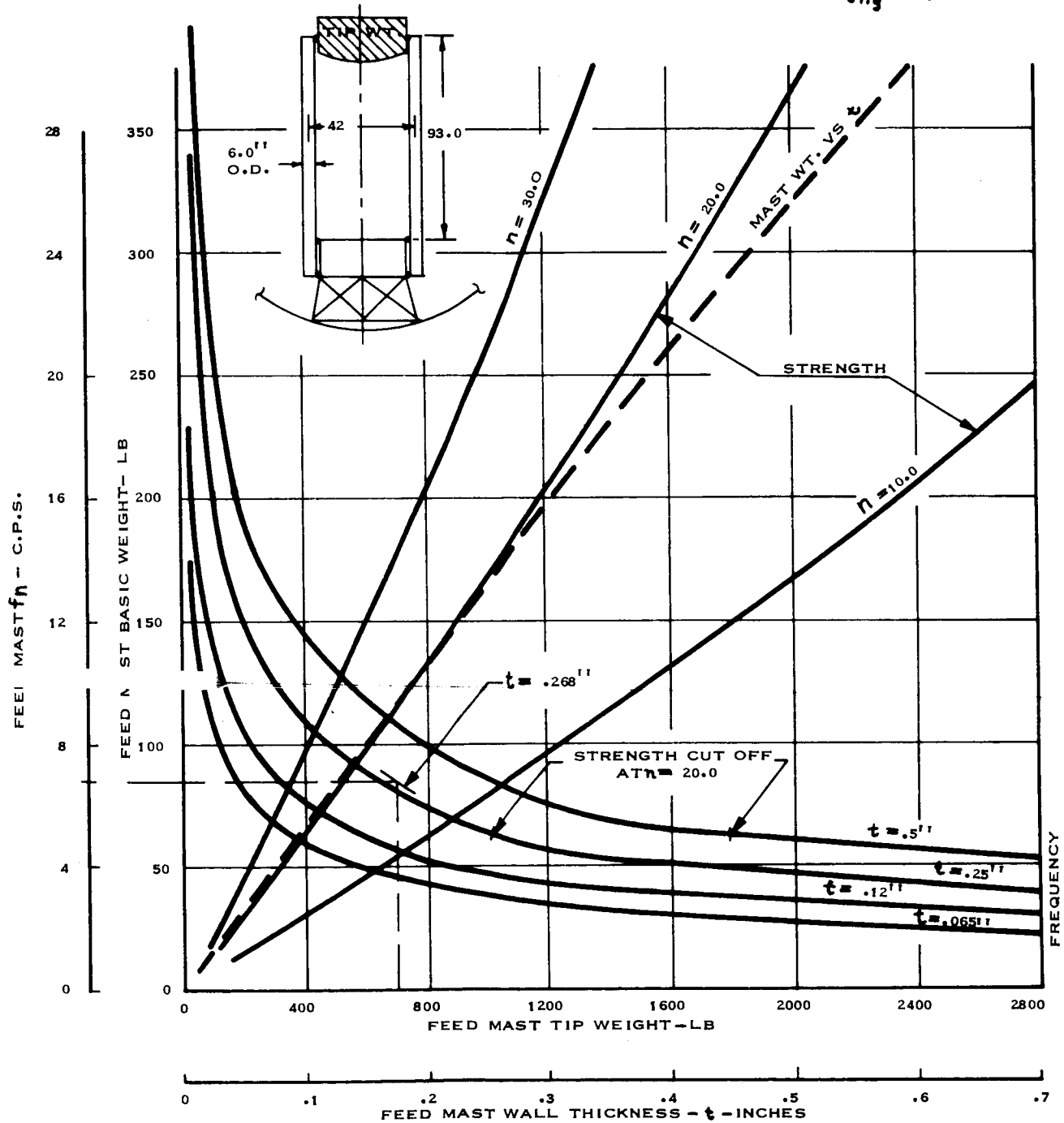


Figure 3.5-5 Four-Tube Feed Mast Frequencies

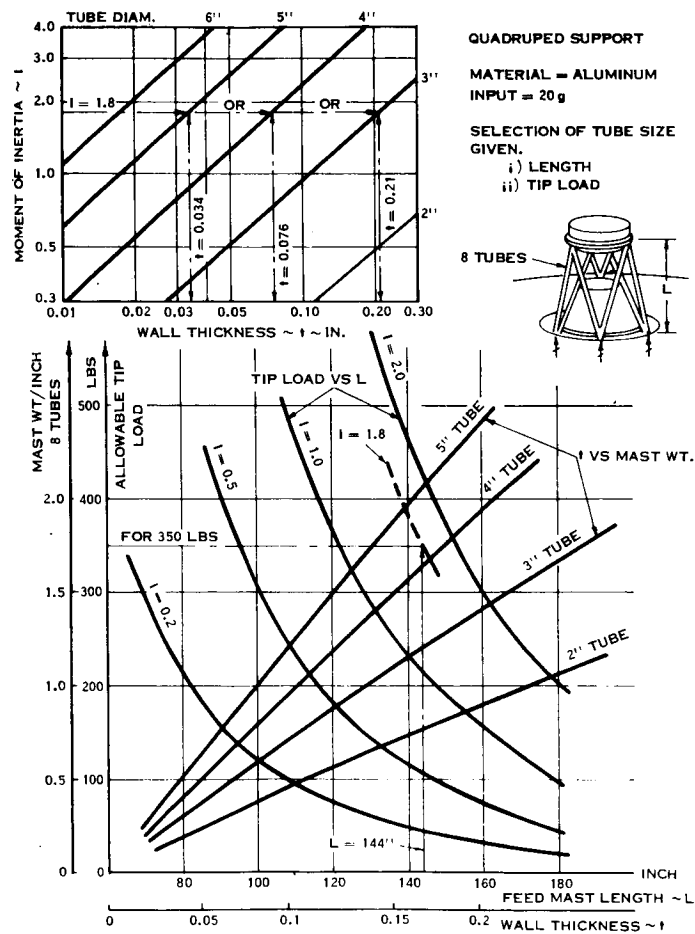
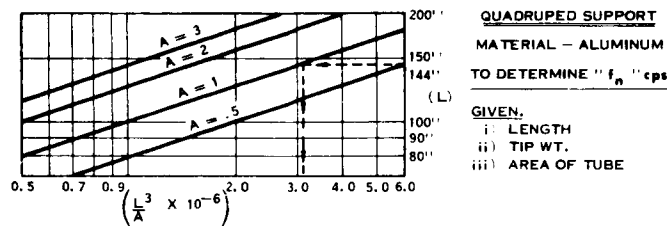


Figure 3.5-6 Analysis of Quadruped Feed Mast Support



STEPS.

- 1) GIVEN THE LENGTH AND AREA OF EACH TUBE, OBTAIN $\frac{L^3}{A} \times 10^{-6}$ FROM ABOVE
- 2) GIVEN THE TIP WT., READ " f_n " FOR CORRESPONDING $\frac{L^3}{A}$ FROM THE CURVES.

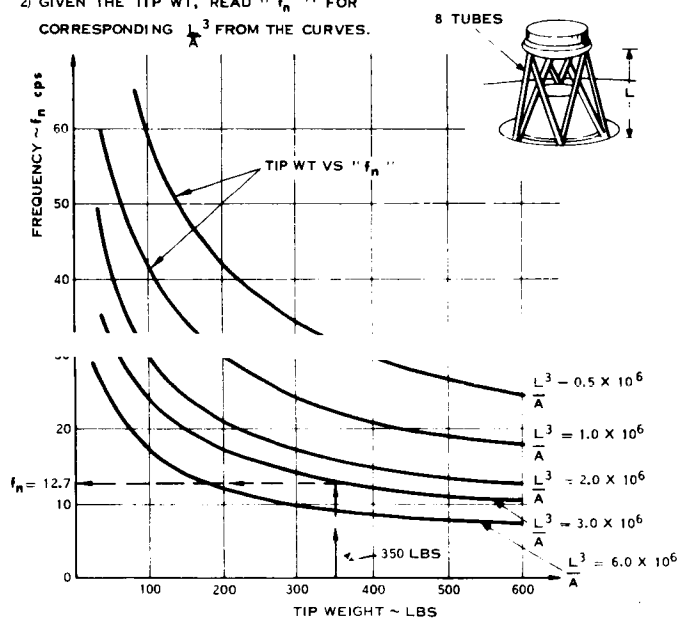


Figure 3.5-7 Quadrupel Feed Mast Frequencies

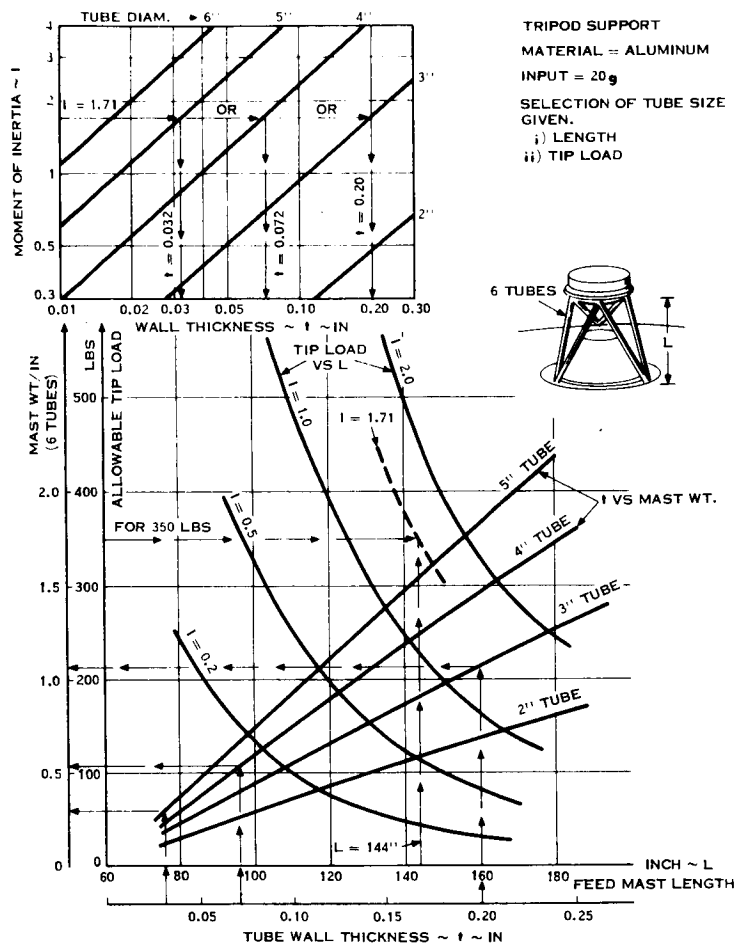
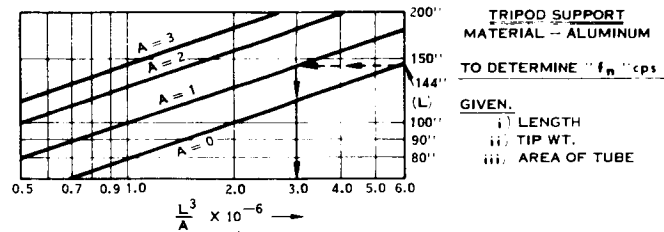


Figure 3.5-8 Analysis of Tripod Feed Mast Structure



- STEPS.
- 1) GIVEN THE LENGTH AND AREA OF EACH TUBE, OBTAIN $\frac{L^3}{A} \times 10^{-6}$ FROM ABOVE
 - 2) GIVEN THE TIP WT., READ " f_n " FOR CORRESPONDING $\frac{L^3}{A}$ FROM THE CURVES.

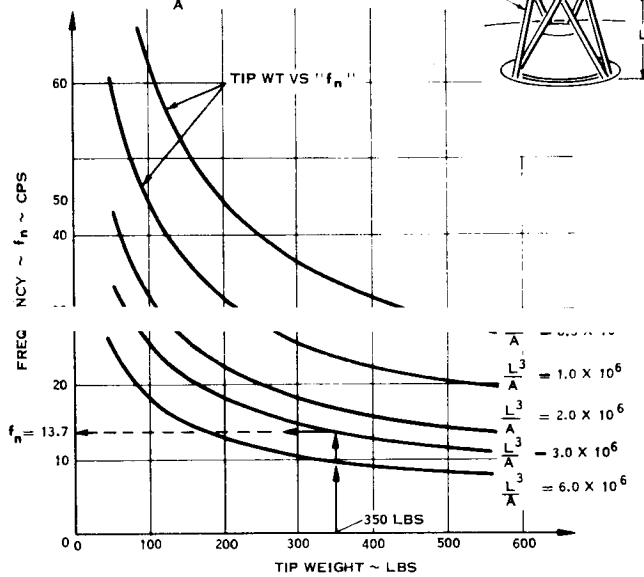


Figure 3.5-9 Tripod Feed Mast Frequencies

the tip mass. The spring constant k is $\frac{1}{\delta}$ and the lateral natural frequency is obtained from $f_n = \frac{1}{2\pi} \sqrt{\frac{k}{m}}$.

For a given tube size, the tripod is more efficient in tip load capability and lateral natural frequency (stiffness), while the quadruped possesses a 50% stiffness advantage in torsional loading.

Figure 3.5-6 can be used to select the tube size and thickness for the quadruped support for a given feed mast length and tip load. This is accomplished by entering the curves with the feed mast length and tip load and determining the required moment of inertia. Corresponding to the required moment of inertia, the inset in Figure 3.5-6 is used to obtain a tube size and wall thickness. Once a tube size and wall thickness is obtained, the mast weight per inch can be readily determined from the diagram.

The lateral natural frequency of the quadruped support structure can be obtained from Figure 3.5-7. This is accomplished by using the information obtained from Figure 3.5-6. The cross sectional area of the tube required for a given tip load and feed mast length (from Figure 3.5-6) is used along with tip weight to determine the lateral natural frequency from Figure 3.5-7. Figures 3.5-8 and 3.5-9 are similar representations of the tripod configuration.

As an example of the use of the curves, consider a quadruped support structure with a length of 144 inches and tip load of 350 lb. From Figure 3.5-6 the required moment of inertia is seen to be 1.8 in^4 (for each tube). Entering the inset of Figure 3.5-6 with the moment in inertia of 1.8 in^4 , it is seen that several combinations satisfy the inertia requirement. As an example, if a 4 inch diameter tube is selected, the wall thickness is found to be 0.076 inch. Using this wall thickness and tube size, the feed mast weight is determined to be 0.76 lb/in (from Figure 3.5-6). To determine the lateral natural frequency, enter the inset of Figure 3.5-7 with

the feed mast length (144 inches) and the cross sectional area of one tube (this can be determined from the insert in Figure 3.5-6 and for a 4-inch diameter tube of wall thickness of 0.076 inch is found to be 0.95 square inches) to obtain the parameter $\frac{L^3}{A}$. With the proper tip weight (350 lbs) and the appropriate value of the parameter $\frac{L^3}{A}$ ($= 3.1 \times 10^6$), the natural frequency obtained from Figure 3.5-7 is 12.7 cps.

- Comparison of Results - Table 3.5-1 compares the same design point of each configuration. Although the 6-inch tube diameter will cause prohibitive feed blockage it is still a valid basis for configuration comparison.

Reflector - The large aperture reflector, as dictated by the performance and weight requirements of the mission, necessitated a careful study of various deployment configurations and structural materials.

In considering weight and surface accuracy as the primary design criteria, the launch condition will basically dictate the required structure and its weight; the effect of the orbit thermal environment on the deployed structure will influence the surface deviations. A given structural configuration, then, must satisfy the launch environment for strength and the orbit

sandwich petals and trussed frame petals. For an equal section modulus, the sandwich structure is heavier, and when subjected to a dynamic environment will produce higher loads.

- Launch Condition - Stowed Antenna - The basic petal frame used for analysis is shown in Figure 3.5-10. There are 32 petals which, when deployed, form the parabolic antenna. In the stowed position, each petal is supported at the base hub hinge and at the top by the feed mast structure. With the assumption that the feed mast structure and hub structure is relatively stiff when compared to the petal, each petal may be evaluated as a simply supported beam.

Previous discussion indicated that the basic design loads are usually dictated by the lateral sinusoidal vibration. This has been true for similar structural systems in the past. Using this criterion, the petal with its mass distribution will undergo amplifications when vibrated at its natural frequency. The magnitude of these amplifications is a function of the structure's damping characteristics. Since the process of determining the amplifications requires the iteration of the system's mass and frequency, (see Analytical Methods - Section 3.5.1) some simplifying assumptions, based on experience, are made to arrive at design loads. The classical transmissibility equation for a structure of single degree of freedom, vibrating at its natural frequency with a structural damping factor of 0.05, yields a transmissibility factor of 20.

Complex structures of this type have produced transmissibility factor values of 30 in components of maximum flexibility. With these considerations, the limit loading shown in Figure 3.5-10 is assumed as the design loading on the petals.

With this assumed loading, the cross section and material chosen for this structure must be efficient in terms of stress, weight, and stiffness. The structural characteristics are investigated flatwise and edgewise since the petals are not consistently oriented to the reference axis.

Four basic sections are investigated, each being either a rectangular tube or an I beam of the same section properties.

The properties and weights of the members considered are shown in Table 3.5-2.

Knowing the section properties and dead weight loading, the stresses are determined by classical equation: $f = \frac{mc}{I}$. Since the petals are individually supported as simple beams, the natural frequencies are determined by the standard solution expressed by $f_n = \sqrt{\frac{EI}{mL^4}}$. The results of the above

TABLE 3.5-1 COMPARISON OF FEED MAST CONFIGURATIONS

(Tip Weight = 350 Lbs, Length = 144 Inches)

Configuration	Figure	Tube Diameter In.	Mast Weight Lbs.	Mast Frequency Cps.
Truss	3.5-1	---	20.0	3.6
One Tube	3.5-3	6.0	157.0	5.6
Four Tubes	3.5-4	6.0	138.0	2.9
Quadruped	3.5-6	6.0	32.0	6.5
Tripod	3.5-8	6.0	29.0	7.1

TABLE 3.5-2 REFLECTOR PETAL COMPONENTS CHARACTERISTICS

Section I or <input type="checkbox"/>	Material 2024 Aluminum	Area 2 Sides	$I(\text{in}^4)$ Flat- wise	$I(\text{in}^4)$ Flat- wise	Dead Weight Loading (lb / in)	Petal Weight (lbs)	Total Weight (lbs)
.75 x .75 x .022 All members		.1280	.0114	14.0	.0256	3.44	110.0
1.0 x 1.0 x .028 All members		.2178	.0342	24.0	.0436	5.85	187.0
1.25 x .75 x .032 Chords & Diag. 1/2 area		.2480	.0534	27.0	.0370	5.00	160.0
1.00 x .75 x .025 Chords & Diag. 1/2 area		.175	.0271	20	.0261	3.50	115.0

equations for the stresses and natural frequencies of the chosen members are shown in Table 3.5-3.

An evaluation of Tables 3.5-2 and 3.5-3 reveals the 1.0 x .75 x .025 inch section to be of adequate strength and frequency for the first approximation in the coupled system analysis.

Spacecraft, Injection Motor and Adapter - The feed mast and reflector study discussed above were treated as individual structural components. In order to evaluate the spacecraft, injection motor and adapter sections, the influence of the feed mast and reflector must be considered in determining the required structural stiffness for the launch environment.

From Section 3.2, concepts SK513-17 and -18 are used in determining the stiffness requirements of the spacecraft, injection motor and adapter. These structures are evaluated in terms of required moments of inertia for an average 46-inch diameter structure. The forces acting on this area will be the mass of the feed mast and reflector, and the assigned masses of the substructure. These forces will be subjected to a magnification factor of 20.0 for the internal bending moments.

An initial investigation, considering pure monocoque structure, resulted in thin skins and low allowable buckling stresses. A skin-stringer structure was then investigated by considering .025 skins and 16 stringers. The stringer area was sized for the bending moments and the skin for shear.

Figure 3.5-11 shows the model for the two configurations. It presents the mass, locations, and the moments of inertia used in the coupled spacecraft multimass dynamic analysis. (Also see Figure 3.5-12.)

Coupled Spacecraft - Launch and Orbit - From the above studies of the feed mast, reflector, spacecraft and adapter, the preliminary structural sizes derived are used for the integrated spacecraft's first multimass model analysis. The analytical methods used were described in Section 3.5.1.

TABLE 3.5-3 REFLECTOR COMPONENTS STRESS
AND NATURAL FREQUENCY

Section I or □	Material 2024 Aluminum	Flatwise		Edgewise	
		Stress (psi)	f_n (cps)	Stress (psi)	f_n (cps)
.75 x .75 x .022 All members		55,500	3.6	3650	127.0
1.0 x 1.0 x .028 All members		42,000	4.8	2620	126.0
1.25 x .75 x .032 Chords & Diag. 1/2 area		28,500	6.5	1950	147.0
1.0 x .75 x .025 Chords & Diag. 1/2 area		33,600	5.5	970	150

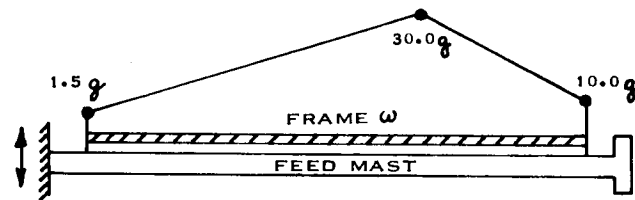
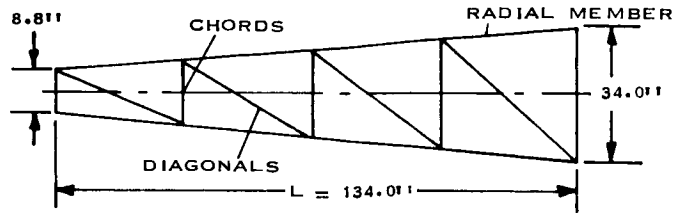
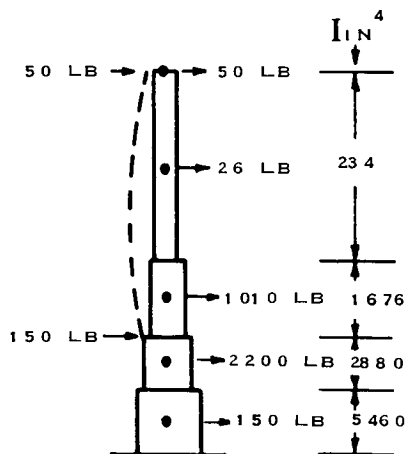


Figure 3.5-10 Reflector Petal Loading

CONFIGURATION A



CONFIGURATION B



Figure 3.5-11 Spacecraft, Injection Motor, and Adapter Structural Properties

- Launch Configuration - From Section 3.2, the concept evaluation resolved into two promising configurations shown in Figures 3.2-1 and 3.2-2. Figure 3.2-1 utilizes the split module concept where the petals are hinged from the spacecraft module. The experiment package of 200 pounds is located at the feed point. Figure 3.2-2 has panels that fold away from the spacecraft leaving the spacecraft module near the focal point. This configuration has less weight acting on the feed mast structure when subjected to the launch vibrational environment.

Figure 3.5-12 shows the two configurations and the equivalent analytical model. Figure 3.2-2 is referred to as configuration "A" and 3.2-1 as configuration "B". The model utilizes 17 mass points for which the magnification factors are calculated. The solution of both configurations is accomplished in a single computer run by varying the masses and stiffnesses.

The petal size used in this analysis is 1.0 x .75 x .025 inch, 2024 aluminum as determined in the preliminary reflector analysis. The 32 petals are stacked into four structural sets, each consisting of eight petals. The lateral sinusoidal input will affect two sets in flat wise bending and two sets in edge wise bending.

The feed mast weight and stiffness data is derived from the parametric study of the tripod. Configuration "A" considers a tip mass of 100 pounds and configuration "B" a tip mass of 350 pounds for determining the feed mast weight and stiffnesses. This resulted in feed mast tube sizes of 3.0-inch O.D., by .038-inch wall thickness and 3.0-inch O.D. by a .175-inch wall thickness with respective weights of 26.0 and 120.0 pounds.

The spacecraft module, injection motor, and adapter section stiffness data is obtained from Figure 3.5-11.

In determining the 17 unit loadings, representing the mass points, 84 element sections were used in defining the internal forces. These forces define only the bending moment energy of the integrated spacecraft structure. The unit load representing the lateral vibration of the system was applied horizontally at each mass point. The weight of the structure associated with each mass point is given in Figure 3.5-12.

The forced lateral vibration response analysis using the 7090 digital computer is presented in Table 3.5-4 for both configurations. Shown are values of natural frequencies and magnification factors for the petals and feed mast structure.

For configuration "A", data for the first seven modes of vibration are shown. The petal magnification factors for the first four modes shown are for flexure about the weak axis (flatwise bending); the values for the fifth, sixth, and seventh mode are for flexure about the strong axis (edgewise bending). Recalling that the petal is considerably stronger for edgewise bending, the larger magnification factors for the flatwise bending case are critical. A similar situation exists for configuration "B" with the difference that edgewise bending is predominant for the fifth mode rather than the seventh as was the case in configuration "A".

For the feed mast structure, the critical magnification in both configurations occurs when the petals are in edgewise bending. From the data presented for configuration "A", this critical value for the feed mast structure occurs in the seventh mode; for configuration "B", the critical magnification occurs in the fifth mode.

The strength evaluation based on the computed magnification factors are shown in Table 3.5-5. This is done by comparing the allowable moments of the structure with the computed dynamic moments. The comparison shows the preliminary petal size inadequate for the imposed dynamic

TABLE 3.5-4 INTEGRATED SPACECRAFT FREQUENCIES
AND MAGNIFICATION FACTORS
COMPUTER RESULTS

FREQUENCIES AND MAGNIFICATION FACTORS (1.0g LEVEL INPUT)											
MODE	CONFIGURATION A						CONFIGURATION B				
	MAGNIFICATION FACTORS						MAGNIFICATION FACTORS				
	f_n cps			PETALS			f_n cps			PETALS	
	TOP	MID	BOTTOM	TOP	MID	BOTTOM	TOP	MID	BOTTOM	TOP	FEED MAST
1	2.47	14.9	28.4	13.3	1.2	1.2	2.48	13.9	28.8	14.8	1.2
2	2.49	13.8	26.6	12.3	1.0	1.0	2.50	13.3	28.0	14.3	1.1
3	7.89	9.7	5.5	8.3	2.2	2.2	7.78	9.2	5.7	10.6	3.9
4	8.00	8.7	4.7	7.8	1.8	1.8	8.00	6.4	5.4	8.6	2.8
5	12.94	19.4	23.2	5.4	22.3	22.3	9.91	24.0	28.8	5.9	28.2
6	13.2	18.8	22.6	5.1	21.7	21.7					
7	13.5	24.6	29.8	6.2	28.5	28.5					

NOTE:

- 1st mode frequency critical for petals in both configurations
- 7th mode frequency critical for Feed Mast in configuration "A"
- 5th mode frequency critical for Feed Mast in configuration "B"

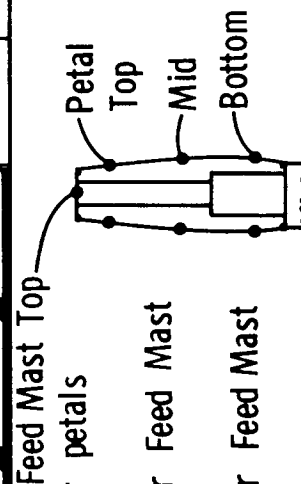


TABLE 3.5-5 STRENGTH EVALUATION
STRENGTH CHECK OF COMPUTER RESULTS - (1.g LEVEL INPUT)

PETALS

PETAL SECTION		CONFIGURATION A		CONFIGURATION B	
1.0 X .75 X .025* (ORIGINAL)	1st MODE	M_z	= 3,275 IN-LB	$M_{allow.}$	= 3,275 IN-LB
		M_c	= 4,080 IN-LB	$M_{comput.}$	= 4,130 IN-LB
1.25 X .75 X .025 (REQUIRED)		M_z	= 4,360 IN-LB	$M_{allow.}$	= 4,360 IN-LB
		M_c	= 4,080 IN-LB	$M_{comput.}$	= 4,130 IN-LB

* FROM PETAL PRELIMINARY SIZING

3-99

FEED MAST

FEED MAST TUBES		CONFIGURATION A		CONFIGURATION B	
3.0' O.D. X .038"t* (26.0 LB) (ORIGINAL)	7th MODE	M_z	= 360,000 IN-LB		
		M_c	= 447,700 IN-LB		
3.0' O.D. X .050"t (33.6 LB) (REQUIRED)		M_z	= 448,000 IN-LB		
		M_c	= 447,700 IN-LB		
3.0' O.D. X .175"t* (120.0 LB) (ORIGINAL)	5th MODE			$M_{allow.}$	= 1,500,000 IN-LB
				$M_{comput.}$	= 1,202,000 IN-LB

* FROM FEED MAST PRELIMINARY SIZING

moment. The feed mast structure for configuration "A" also is seen to be somewhat smaller than required.

The results of this analysis did not point to any clear cut structural advantage of configuration "A" over "B" (except for feed mast weight). However, it should be noted that the mass model did not include the solar panels; the inclusion of their masses would have significantly increased the feed mast amplification (and weights) for configuration "B". It should be noted that the dynamic analysis of these two configurations are intended to evaluate the effects of the feed mast-petal interaction in the launch configuration. The relationship of limit, ultimate loading and margins of safety is not considered here. The study of these results are reflected in the modified configuration "A" which is fully covered in Section 3.5.3.

- Orbit Configuration - As for the launch configuration, a lumped-mass analytical model has been constructed to represent the actual structure in the deployed condition. This analysis is limited to a frequency and dynamic response investigation with and without solar panel masses. The stiffnesses associated with the petal masses are based on the sizes chosen for the launch condition. This analysis assumes the petal system clamped to a rigid inner ring and yields a first approximation of the orbital natural frequency.

Figure 3.5-13 shows the analytical model, as deployed, with 8 idealized petals circumferentially locked at the outer edge and mid point. The analysis uses the petals as bending members and the effective ring as an axial member. The unit loads representing the 18 mass points for this model yield axisymmetric deflections.

Three separate analyses have been accomplished for this configuration. These are described below, with the corresponding results shown in Table 3.5-6.

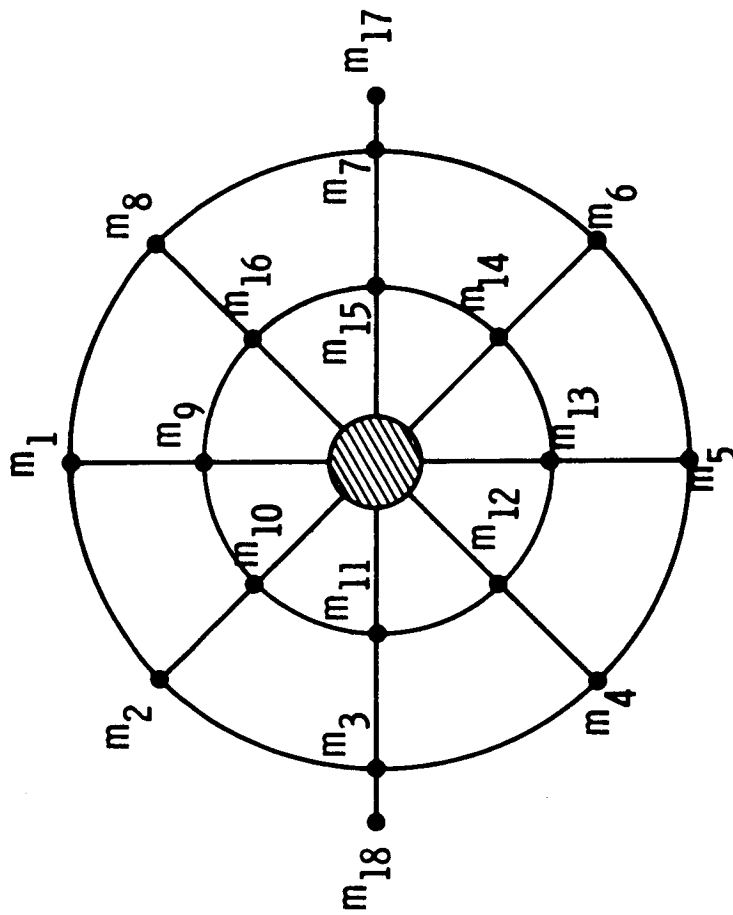
Case I: This is the basic antenna with no solar panels.

Case II: In this case two 50-pound solar panels are attached to the antenna. The stiffness of the structure is the same as for Case I.

Case III: Two 50-pound solar panels are attached to the antenna as in Case II. The stiffness of the petals supporting the solar panels was increased by a factor of 20. This was done to effectively give the supporting petals the same flexibility as the others.

The results obtained for the above cases show that the fundamental frequency of the antenna is reduced from 1.05 cps to 0.3 cps by the attachment of the solar panel masses. By increasing the stiffness of the supporting petals, the frequency becomes identical to the case without tip masses.

ANALYTICAL MODEL



MASS POINTS	WEIGHT
$M_1 - M_8$	8.2#
$M_9 - M_{16}$	11.0#
$M_{17} \text{ \& } M_{18}$	50.0#

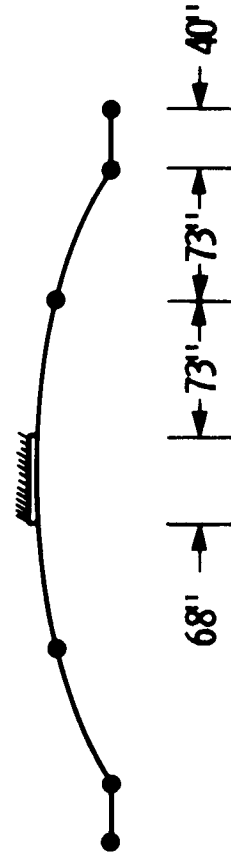


Figure 3.5-13 Orbit Configuration - Mass Model

TABLE 3.5-6 ORBIT CONFIGURATION - NATURAL FREQUENCIES

COMPUTER RESULTS

CASE I

- NO SOLAR PANELS
- FRAME SECTIONS 1.0 X .75 X .025

CASE II

- 50 LB SOLAR PANELS
- FRAME SECTION 1.0 X .75 X .025

CASE III

- 50 LB SOLAR PANELS
- SOLAR PANEL SUPPORT FRAMES INCREASED BY FACTOR OF 20.0

CASE	f_n (cps)	MAGNIFICATIONS			
I	1.05	1.0 ALL MASSES			
II	.30	m_3	m_{11}	m_{17}	
		3.03	1.60	4.12	
III	1.05	m_3	m_{11}	m_{17}	
		1.98	1.29	2.48	

3.5.3 Integrated Spacecraft - Launch Configuration

The preliminary analysis of the two configurations discussed in the previous section necessitated a modification to permit the structure to sustain a 1.5 g level input for the limit condition. A structural damping factor of 5 percent was used previously while for the modified configuration it was decided to use a more realistic 10 percent.

The preferred configuration "A" (Figure 3.2-2) is modified by an additional support at the upper portion of the spacecraft module. This support combined with the increased damping factor reduced the internal dynamic loads, and insured the adequacy of the structure used in the preliminary analysis. In addition, the structural model was updated and refined to include the solar panels.

Analytical Model - Figure 3.5-14 shows the preferred concept equivalent analytical model. The petals are stacked in four orthogonal sets of eight. The model is similar to the preliminary models but includes the solar panels and petal intermediate restraints. Figure 3.5-15 gives the stiffness data of the components and the effect of the petal restraint system.

An analysis was required in both lateral directions since the stacked petal had different stiffness characteristics in each direction due to the increased stiffness of the petals which support the solar panels. The stiffness data for the feed mast, spacecraft module, injection motor and adapter is similar to that used in configuration "A" of the preliminary analysis. Figure 3.5-16 shows the locations of the chosen 23 lumped mass points that define the dynamics of the structure. It also gives the weight assigned to each point and their sums which represent the launch configuration weights. The results are obtained by using the energy solution due to the two redundancies. The results include natural frequency, and mode shape and the dynamic response.

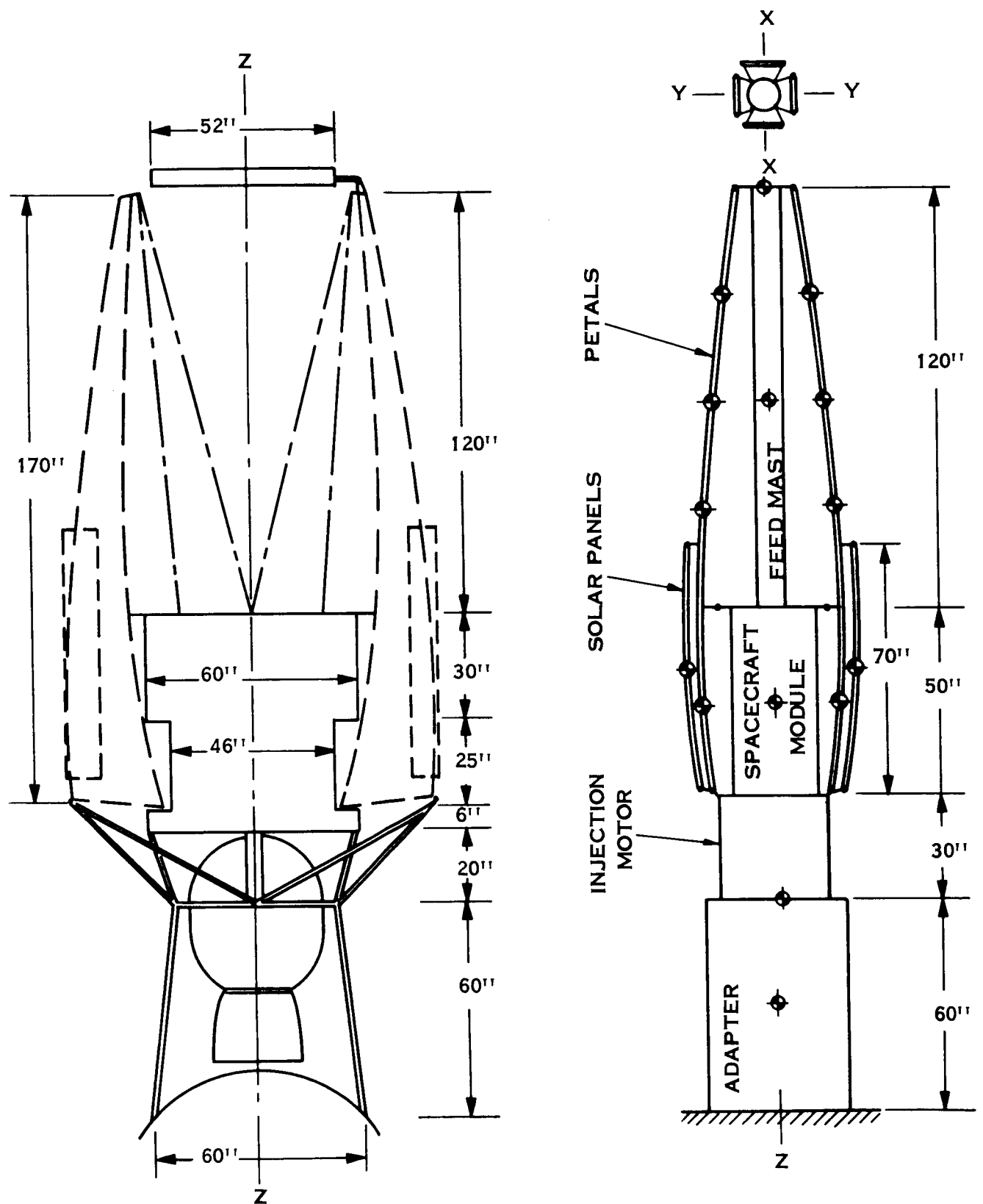


Figure 3.5-14 Preferred Configuration and Analytical Model

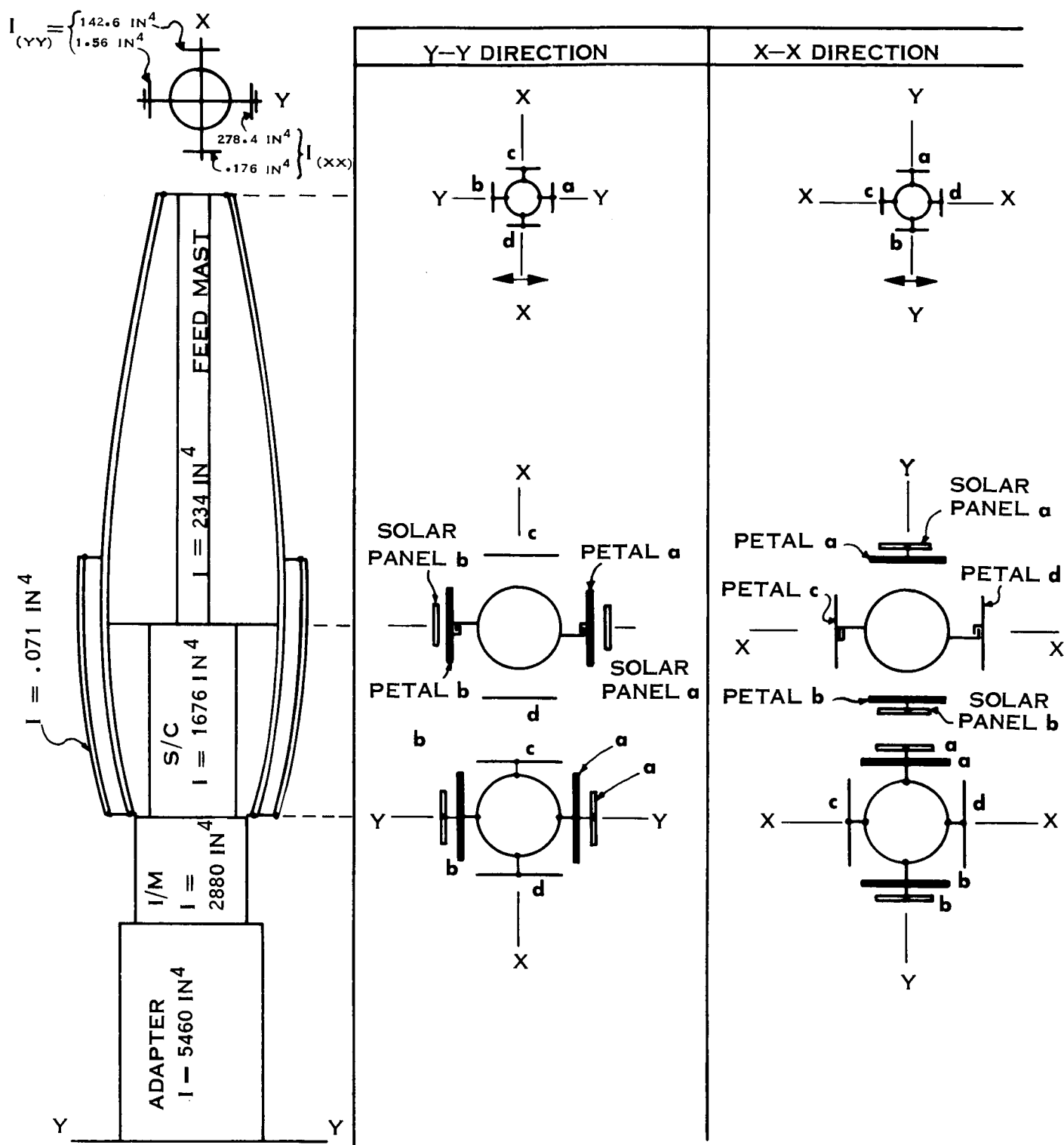
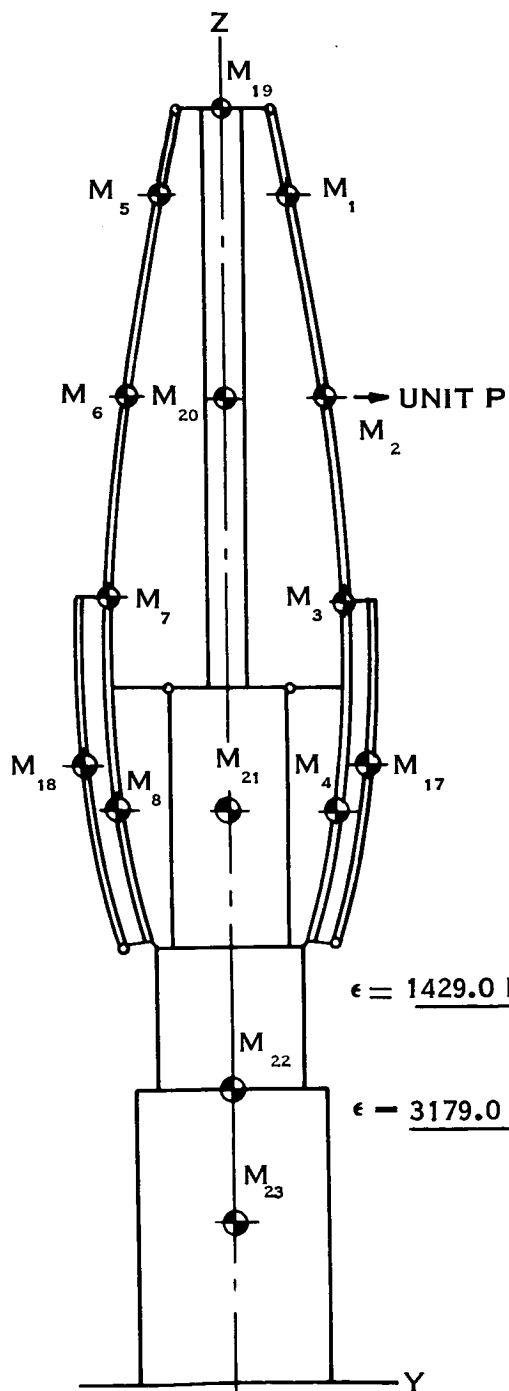
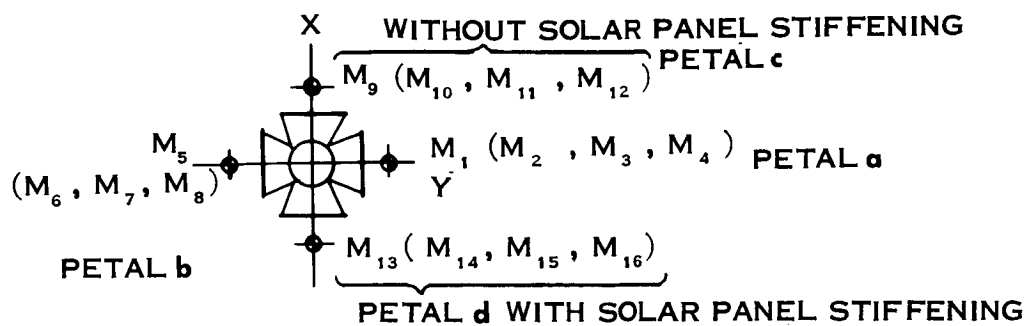


Figure 3.5-15 Petal Restraint and Stiffness



	WEIGHT - LB	MASS $\frac{\text{LB} - \text{SEC}^2}{\text{IN}}$
M_1, M_5	14.5	.03756
M_2, M_6	15.5	.04015
M_3, M_7	16.0	.04145
M_4, M_8	19.25	.04987
M_9, M_{13}	10.0	.02591
M_{10}, M_{14}	10.0	.02591
M_{11}, M_{15}	10.5	.02720
M_{12}, M_{16}	12.75	.03303
M_{17}, M_{18}	50.0	.12953
M_{19}	50.0	.12953
M_{20}	30.0	.07772
M_{21}	1032.0	2.67350
M_{22}	1600.0	4.14496
M_{23}	150.0	0.38859

Figure 3.5-16 Mass Point Locations and Weights

Computer Results - The computer was utilized in obtaining the frequencies, normalized mode shapes, magnification factors, and internal bending moments for the first fifteen (15) natural frequencies in both the yy and xx direction. Minimum margins of safety for both yeild and ultimate conditions, were calculated.

Figures 3.5-17 and 3.5-18 represent pictorially the first four significant frequencies and normalized mode shapes in the yy and xx directions. The solar panel beam modes are the same in both directions since the same stiffness was used. The results show an independent mode for this beam below the fundamental frequency of the petals. It is felt that this frequency can easily be increased by additional stiffness in the solar panels without affecting the basic system natural frequency of 7.27 cps in the xx direction. The fundamental natural frequency of the structure in the yy direction is 12.83 cps. This difference is due to the increased stiffness of the flatwise petals in the yy direction.

Tables 3.5-7 and 3.5-8 give the magnification factors and frequencies at the most significant mass points. The 12.83 cps frequency in the yy direction produced the highest magnification factors for both the petals and feed mast. This frequency produced the highest internal loads in the feed mast structure and the stiffer petals supporting the solar panels. In the xx direction, the tenth mode (36.67 cps) gave the highest magnification values on the flatwise petals. A closer study reveals that these magnifications are not in phase, thus do not produce the maximum internal loads. The fifth mode (14.80 cps) reflected in the largest magnification of the feed mast tip but did not give internal loads higher then the 12.83 cps frequency in the yy direction.

The lowest fundamental frequency of the entire structure in the launch condition is 7.27 cps in the xx direction. The magnification factors at this frequency are lower in value but are in phase and do give the highest internal loads on the less stiff flatwise petals.

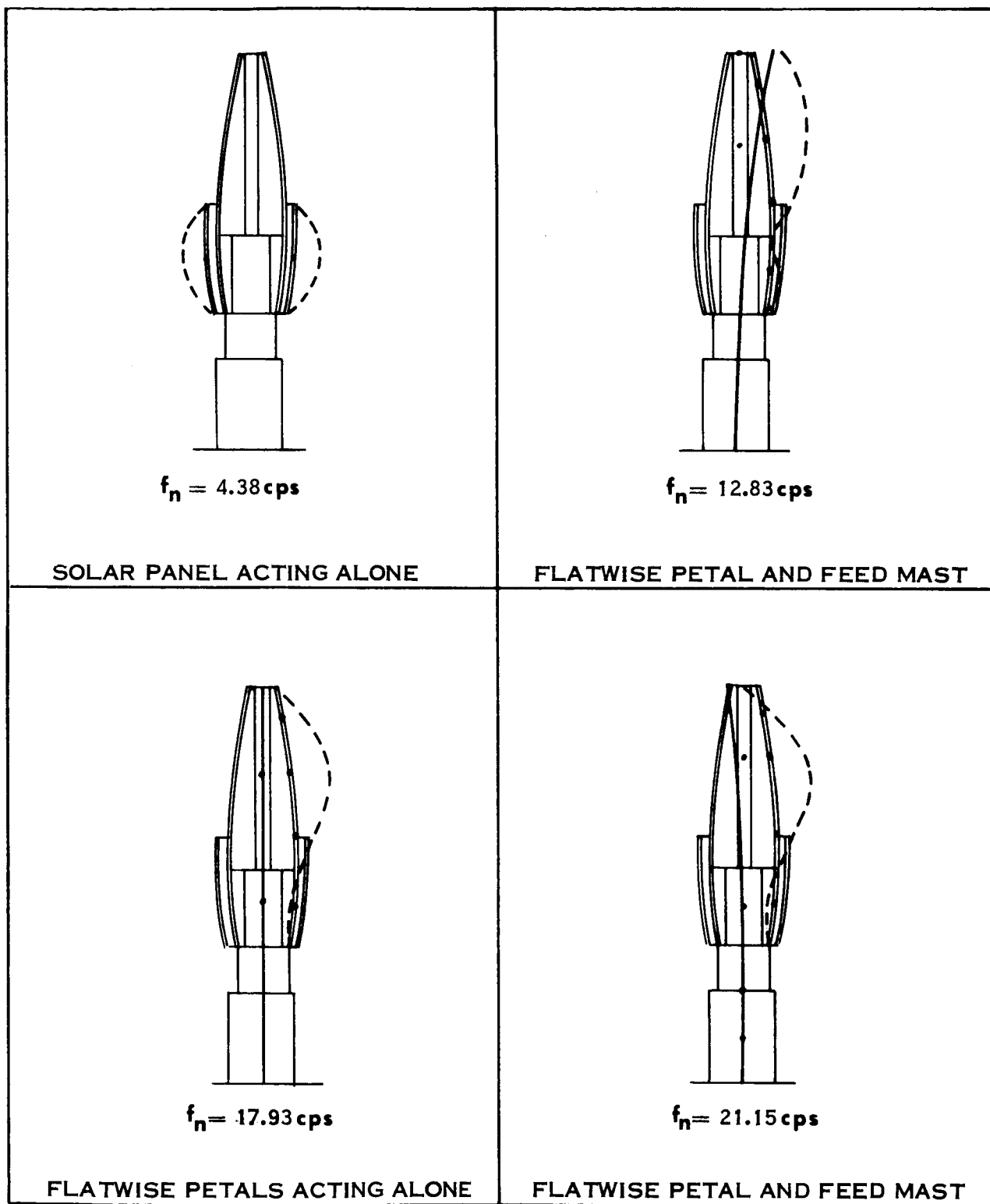


Figure 3.5-17 YY - Direction Mode Shapes

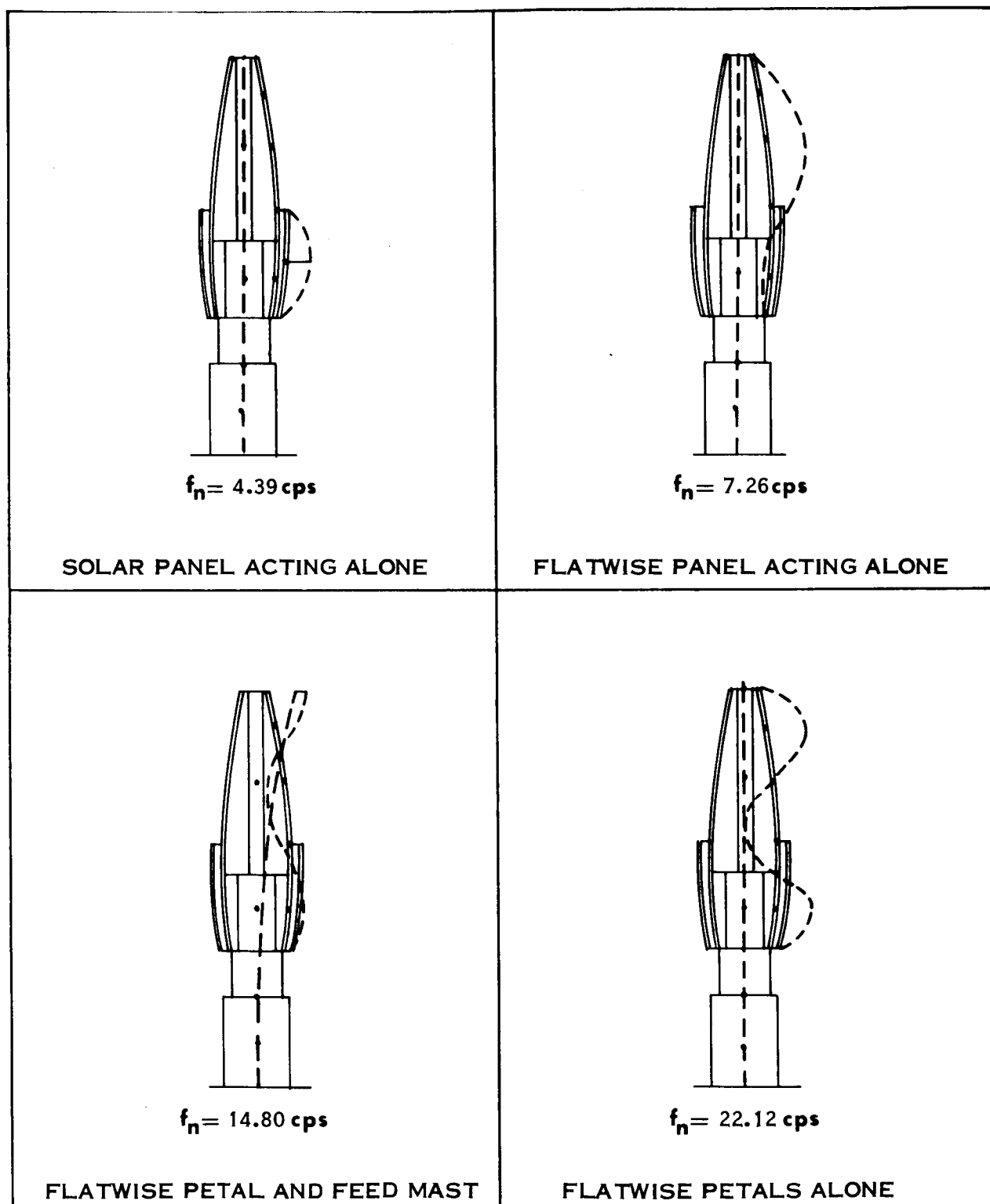


Figure 3.5-18 XX - Direction Mode Shapes

TABLE 3.5-7 LAUNCH CONDITION FREQUENCIES AND
MAGNIFICATION FACTORS, Y-Y DIRECTION

MAGNIFICATION FACTORS											
Mode	fn (cps)	PETALS			SOLAR PANELS			FEED MAST			Spacecraft
		Top	Second	Bottom	Top	a	b	Top	Mid	Mid	
1	4.38	1.28	1.28	1.14	- 1.04	10.79	10.79	1.25	1.14	1.14	1.04
2	4.39	1.27	1.27	1.13	- 1.04	10.79	- 10.79	1.24	- 1.14	- 1.14	1.04
3	12.83	22.16	21.77	9.15	1.46	- 0.705	- 0.705	17.85	8.82	8.82	2.34
4	17.93	4.88	6.9	1.62	- 2.23	- 0.014	- 0.014	1.765	- 0.58	- 0.58	- 1.19
5	21.15	- 7.57*	- 5.87*	- 4.01*	- 1.95*	- 0.11	- 0.11	- 8.375	- 3.92	- 3.92	- 1.66
6	32.9	- 14.0*	- 9.25*	- 3.84*	- 2.88*	0.18	0.18	16.19	- 5.14	- 5.14	- 9.58
7	53.92	- 2.35	- 0.248	2.62	- 2.00	- 0.0092	- 0.0092	- 0.649	1.55	1.55	- 0.84
8	54.98	2.13	0.316	- 2.35	2.52	0.0078	0.0078	- 0.702	- 1.51	- 1.51	- 0.81
9	73.13	- 5.25	2.81	2.39	5.58	0.0037	- 0.0037	- 0.749	- 1.84	- 1.84	0.52
10	75.08	6.12	- 3.56	- 2.38	- 5.70	0.0035	0.0035	- 0.935	- 1.9	- 1.9	0.65

- Notes: 1. This table gives computer results for 1.0 g level input.
2. All petals are in flatwise bending, except those marked with asterisk (*), which are in edgewise bending.
3. Critical values are underlined.

TABLE 3.5-8 LAUNCH CONDITION FREQUENCIES AND
MAGNIFICATION FACTORS, X-X DIRECTION

Mode	fn (cps)	MAGNIFICATION FACTORS									
		PETALS			SOLAR PANELS				FEED MAST		
		Top	Top Second	Bottom Second	Bottom	a	b		Top	Mid	Spacecraft
1	4.39	1.65	1.89	1.35	0.975	10.77	10.77		1.265	1.14	1.04
2	4.41	-1.64	-1.88	-1.35	-0.974	-10.76	-10.76		-1.255	-1.13	1.04
3	7.27	9.97	16.77	6.30	2.37	-0.704	-0.704		1.89	1.42	1.11
4	7.42	9.14	15.89	5.70	-2.70	-0.616	-0.616		1.58	1.26	1.08
5	14.80	19.07*	14.56*	9.87*	4.44*	-0.548	-0.548		21.27	10.14	2.41
6	22.12	-7.79	1.84	7.04	-4.10	0.020	0.020		-3.62	-0.78	-1.38
7	22.58	-7.44	-2.06	+7.04	-5.74	-0.020	-0.020		3.99	0.92	1.40
8	29.06	-22.1	13.18	7.57	24.37	-0.023	-0.023		-4.59	2.21	2.90
9	30.0	+21.53	-12.93	-6.48	-21.77	-0.015	0.015		4.48	-1.93	-2.18
10	36.67	23.33	-19.24	17.00	-8.51	-0.01	-0.01		-13.28	3.54	7.10

Notes: 1. This table gives computer results for 1.0 g level input.

2. All petals are in flatwise bending, except those marked with asterisk (*), which are in edgewise bending.

3. Critical values are underlined.

The limit and ultimate margins of safety based on the above frequency and magnification factor study is presented in Table 3.5-9. The material allowable strength is based on 2024T-3 aluminum tubing with ultimate and yield values of 64,000 psi and 42,000 psi respectively. The lowest margin of safety of a petal is 1.30 in yield which occurs at 7.27 cps in the xx direction. This reflects a stress level of 18,300 psi which is below the value of the commonly accepted precision elastic limit.

The feed mast structure requires a 0.07 inch wall thickness (3.0 inch O.D. x .038 inch wall originally assumed) to adequately sustain the loading produced by forcing loads in the yy direction at 12.83 cps. This amounts to an additional weight of 20 pounds to the feed mast structure and will not influence the dynamics of the structure to any extent..

TABLE 3.5-9 LAUNCH CONDITION INTERNAL LOADS AND ALLOWABLE LOADS

TABLE 3.5-9 LAUNCH CONDITION INTERNAL LOADS AND ALLOWABLE LOADS

Location	fn cps	INTERNAL LOAD				Allowable		Margin of Safety	
		1.0 g Input (Computer)	1.5 g (Limit)	1.5 x Limit Ultimate	Limit	Ultimate	Limit	Ultimate	
Y-Y DIRECTIONS:									
Solar Panels	4.38	9,394.0	14,080.0	21,150.0		Φ			Φ
Petal (Flat)	12.83	9,420.0	-	-	-	-	-	-	-
1.0 x .75 □	12.83	167.5	251.0	376.0	2,010.0	3,060.0	+ 7.00	+ 7.13	
2.5 x 1.0 □	12.83	2,210.0	3,310.0	4,970.0	10,250.0	15,600.0	+ 2.10	+ 2.14	
Petal (Edge)	12.83	10,335.0	-	-	-	-	-	-	-
1.0 x .75 □	12.83	1,294.0	1,940.0	2,910.0	69,500.0	106,000.0	+ 34.8	+ 35.4	
Feed Mast Base	12.83	274,057.0	411,090.0	616,635.0	412,000.0	627,000.0	+ 0.002	+ 0.017	
X-X DIRECTIONS:									
Solar Panel	4.39	9,380.0	14,060.0	21,100.0		Φ			Φ
Petal (Flat)	7.27	4,651.0	-	-	-	-	-	-	-
1.0 x .75 □	7.27	583.0	875.0	1,310.0	2,010.0	3,060.0	+ 1.30	+ 1.34	
Petal (Edge)	7.27	1,597.0	-	-	-	-	-	-	-
1.0 x .75 □	7.27	102.0	153.0	230.0	69,500.0	106,000.0	+453.0	+459.0	
2.5 x 1.0 □	7.27	298.0	447.0	670.0	202,000.0	308,000.0	+453.0	+459.0	
Feed Mast Base	7.27	52,397.0	78,596.0	117,893.0	412,000.0	627,000.0	+ 4.24	+ 4.3	
Petal (Flat)	14.8	1,982.0	-	-	-	-	-	-	-
1.0 x .75 □	14.8	248.0	372.0	558.0	2,010.0	3,060.0	+ 4.4	+ 4.47	
Petal (Edge)	14.8	16,563.0	-	-	-	-	-	-	-
1.0 x .75 □	14.8	1,060.0	1,590.0	2,380.0	69,500.0	106,000.0	+ 42.7	+ 43.5	
2.5 x 1.0 □	14.8	3,080.0	4,620.0	6,930.0	202,000.0	308,000.0	+ 42.7	+ 43.5	
Feed Mast Base	14.8	265,432.0	398,150.0	597,220.0	412,000.0	627,000.0	+ 0.035	+ 0.05	

* Allowable moment is based on 3" diameter tube .07" thick wall; which was originally .038" thick wall. Increase in weight = 20 pounds.

Φ Assumed stiffness for 50 pound solar panel produced the 4.38 frequency which is not representative of the overall spacecraft. Increasing the stiffness will result in fundamental frequencies of 7.27 and 12.83.

Critical values are underlined.

3.5.4 Integrated Spacecraft - Orbit Configuration

The preliminary orbital frequency analysis of Section 3.5.2 considered the reflector attached to a rigid feed mast-spacecraft structure which led to a vertex supported, free vibration analysis. In the analysis discussed below, the feedmast and spacecraft are coupled to the reflector and a free-free vibration and mode analysis is presented.

Analytical Model - Figure 3.5-19 portrays the analytical model and gives the locations of the 23 lumped mass points and their associated weights. Two degrees of freedom, a vertical and a lateral displacement, are considered for each point. The 32 petals are idealized into sets of 4, reducing the model to 8 petal members. The vertical and lateral bending stiffness of these members is used in determining the response by using stiffness properties identical to those used in the modified launch configuration.

The inter-petal locks that form the effective rings were not considered in this analysis. A preliminary analysis indicated that for the lowest antisymmetric mode the presence of the ring locks does not change the frequency significantly. This leaves the petals to be analyzed as individual cantilevered beams.

In determining the free-free frequency of an orbiting structure by the method of structural influence coefficients, a boundary point is required for the unit loads. The technique used provided a boundary for the structure by utilizing a spring constant which was well below that of the complete structure. The first mode of this system is the frequency of the boundary spring with the remaining structure acting as a rigid body. The second frequency is the free-free mode of the structure, well uncoupled from the boundary spring and should yield a system whose total energy is zero.

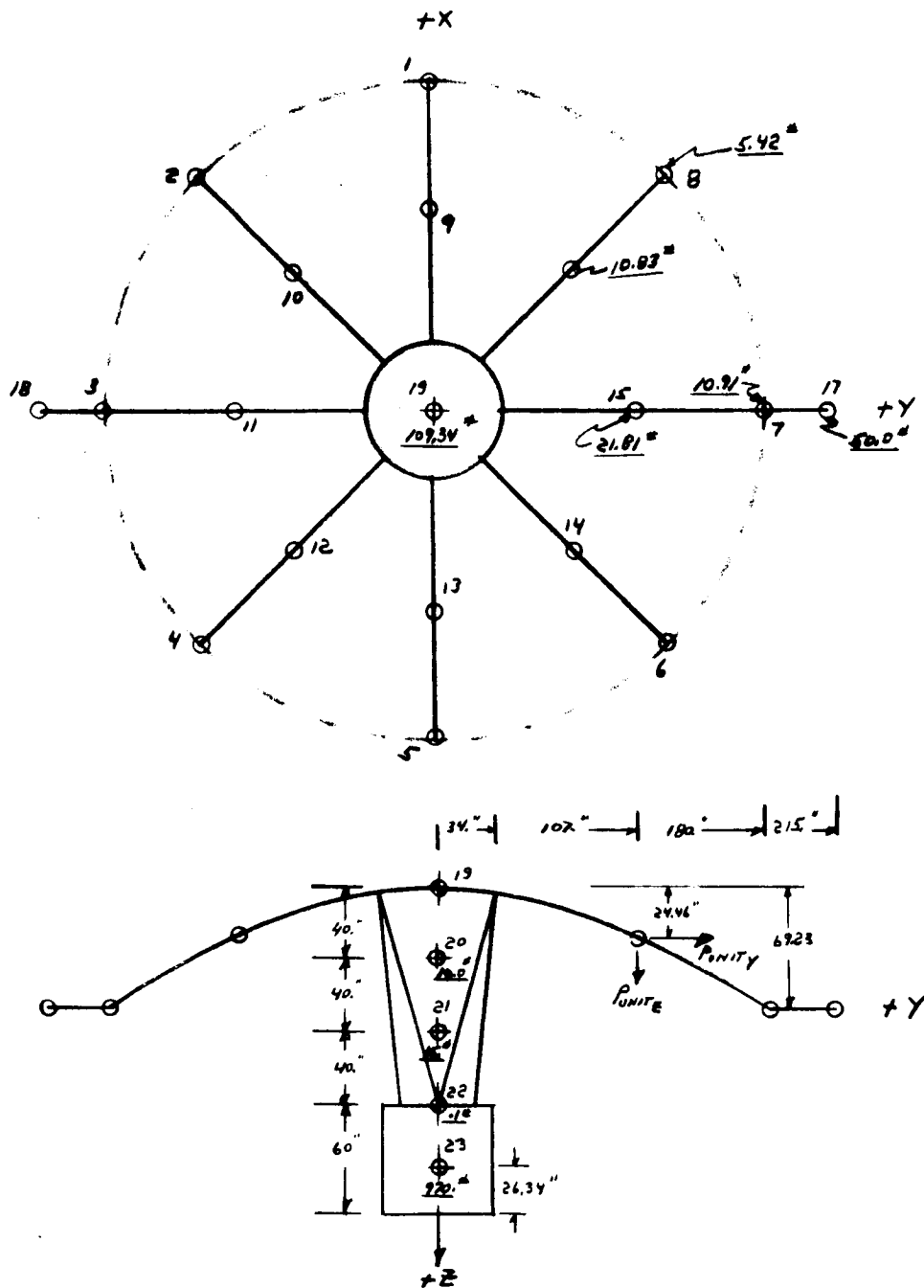
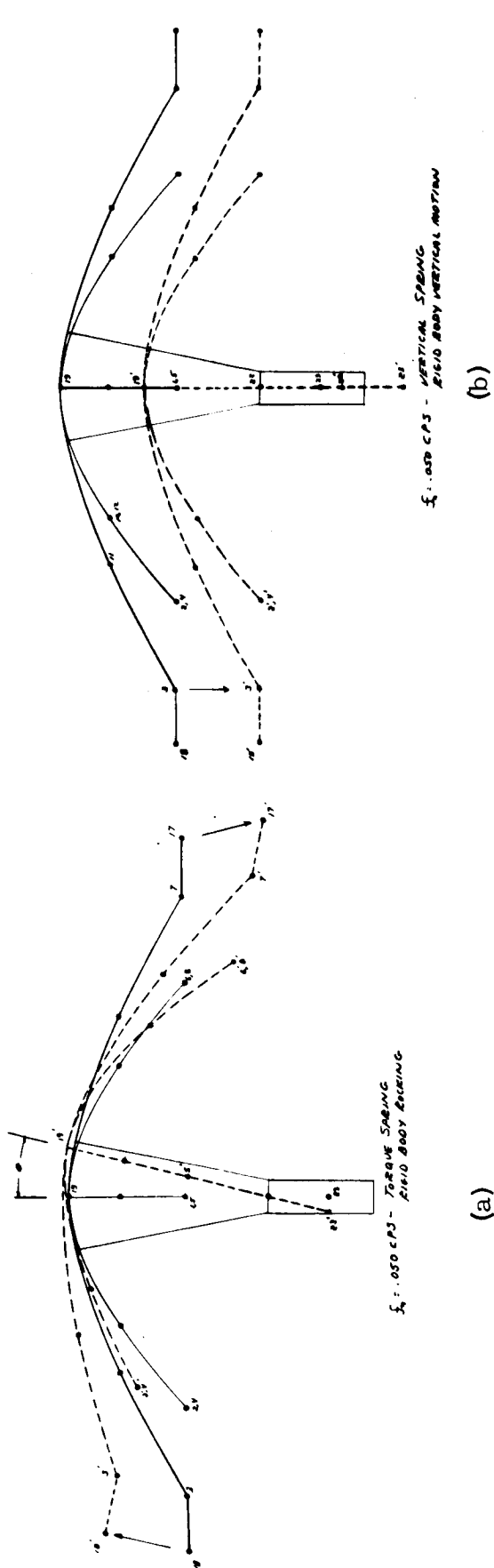


Figure 3.5-19 Analytical Model - Orbit Configuration Geometry, Mass and Mass Location

This technique is applied in this analysis by providing a vertical, horizontal, and torsional spring at the vehicles center of gravity (mass point location 22). If the resultant frequency is equal to that of the chosen spring, no coupling between structure and spring is indicated. If it is lower than the chosen spring, coupling is apparent. However when the calculated frequency is higher, the flexible structure acts as a free-free body uncoupled from the chosen spring.

The vertical, lateral and torsional springs chosen for this analysis have a frequency of .05 cps. This value is one twentieth of the natural frequency of the clamped reflector as obtained from the preliminary analysis (1.0 cps).

Computer Results - The results of 28 frequencies and their respective mode shapes were obtained by computer. The frequencies ranged from .05 cps to 80.31 cps. The first 12 are shown pictorially on Figures 3.5-20 thru 3.5-22. Of these, the first three shown are the rigid body motions of the spacecraft reacted by the .05 cps springs. The fourth, at 1.044 cps, is the first free-free frequency of the spacecraft. This is an axisymmetric mode where petals 1, 2, 4 and 5 with the feed mast are deflected upward while the solar panel support petals are deflected downward. To validate this free-free system, the algebraic sum of the products of the mass times the modal displacements was checked and found equal to zero. The most pronounced antisymmetric frequency occurred at 1.34 cps. Figure 3.5-22a shows the second order modes in the 5.6 cps range compared to the previous first order modes in the 1.0 cps range. Added to this figure are the first two frequencies where the above discussed boundary springs were made infinitely stiff. This produced a frequency of 1.0 cps indicating a wide frequency separation between the feed mast and reflector, a not unexpected result.



3-118

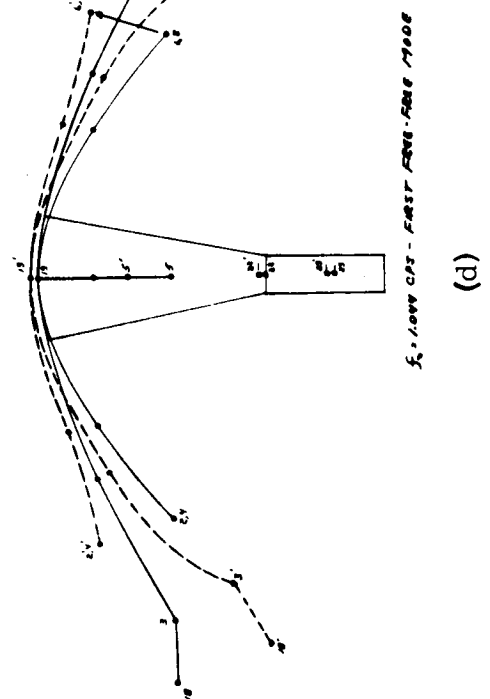
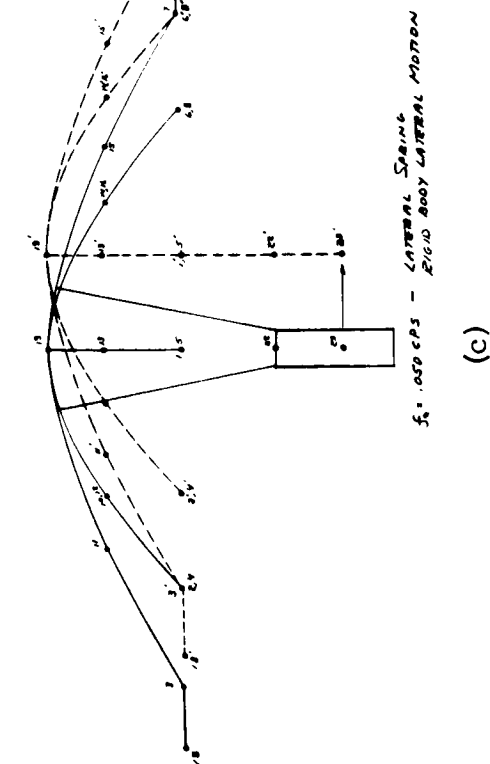
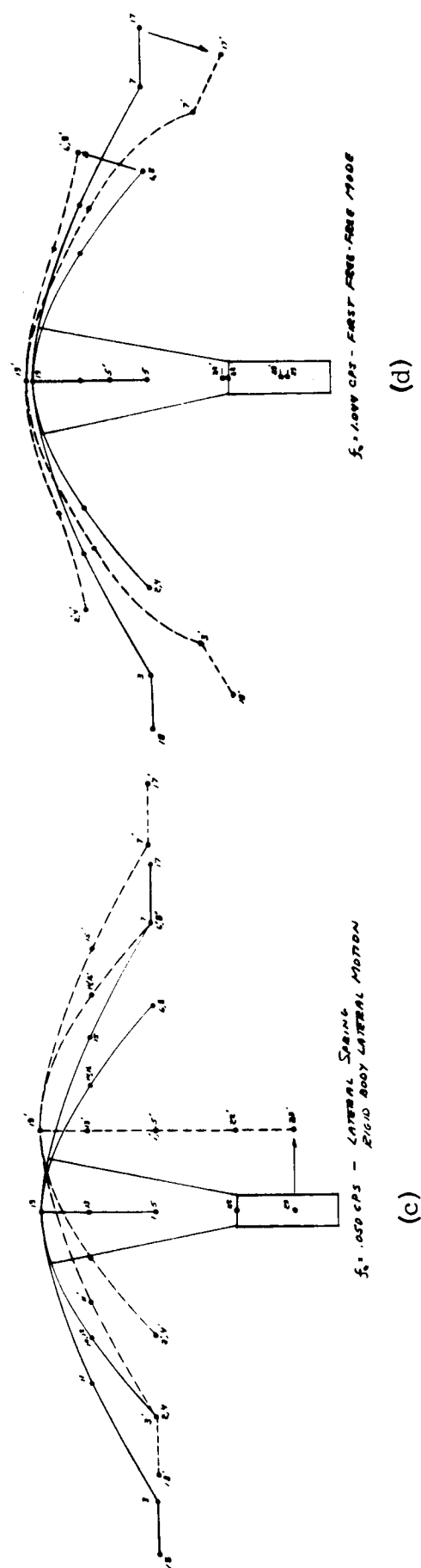
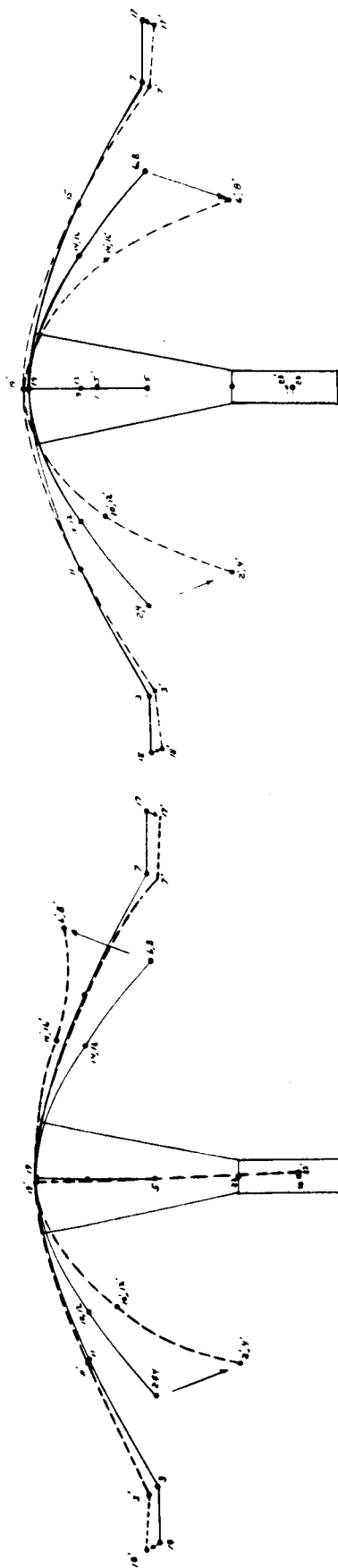
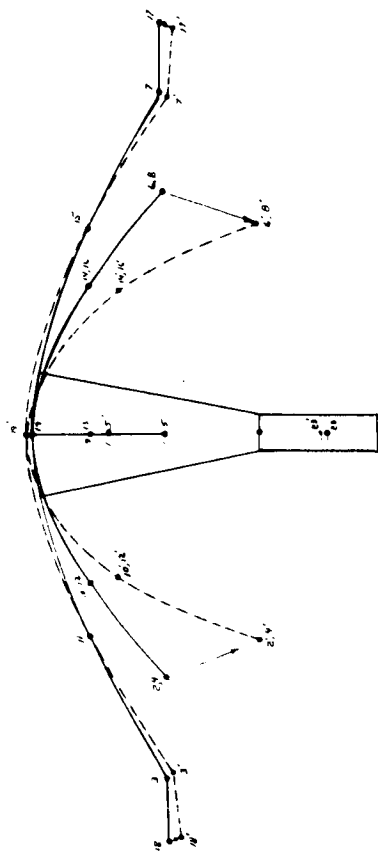


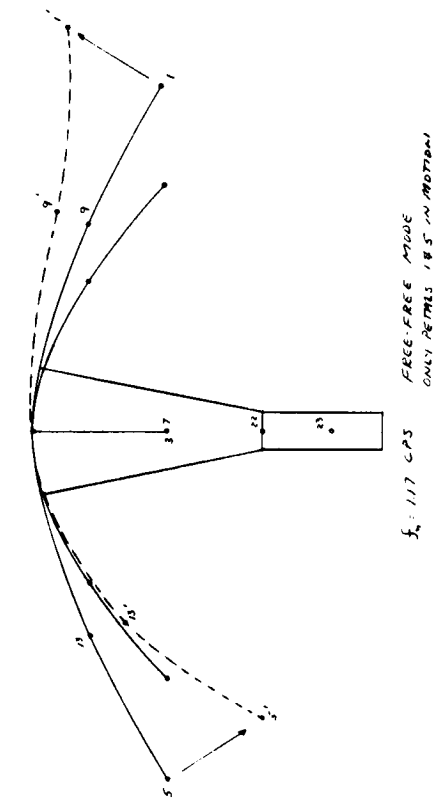
Figure 3.5-20 Frequency and Mode Shapes - Orbit Configurations



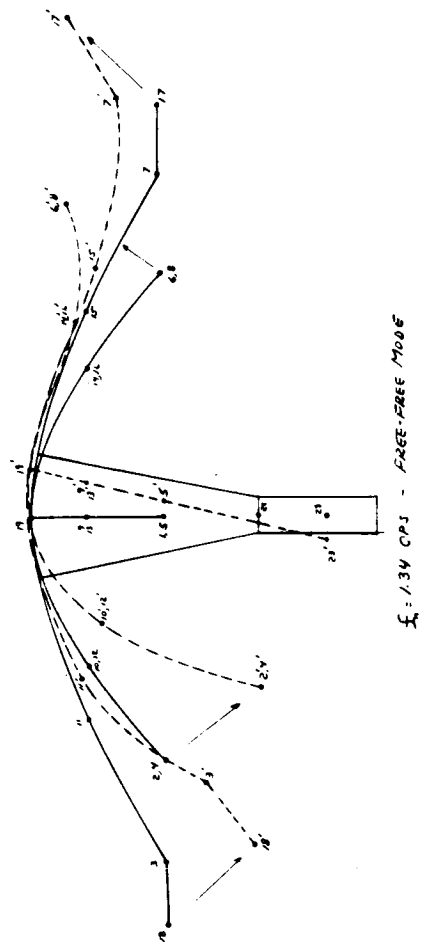
(a)



(b)

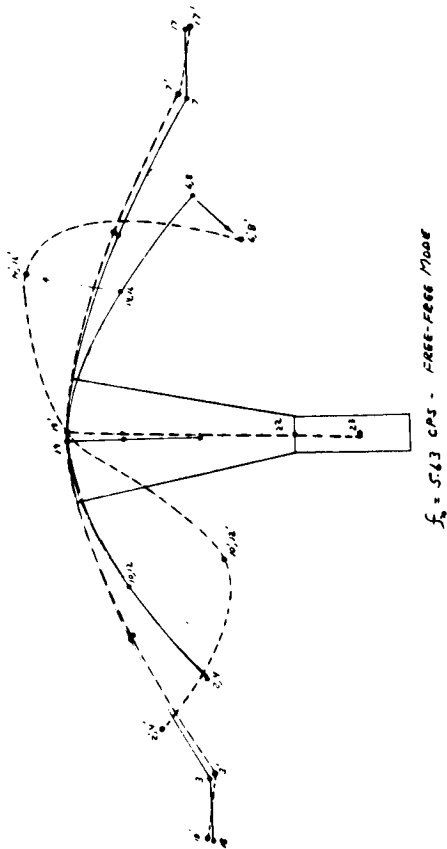


(c)

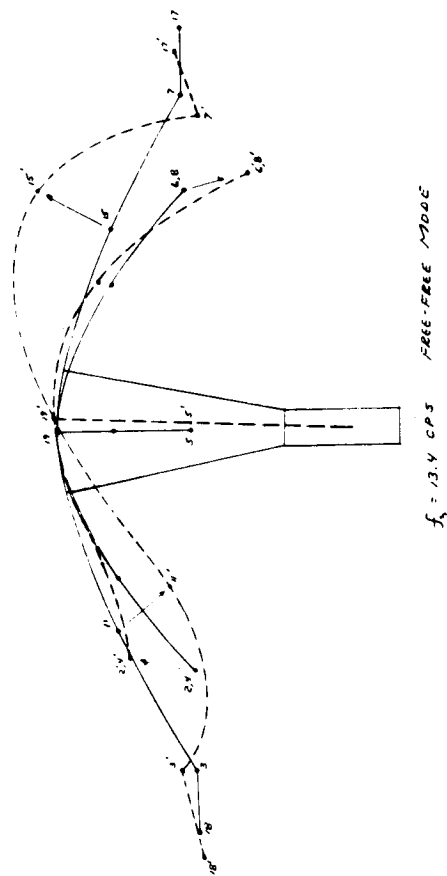


(d)

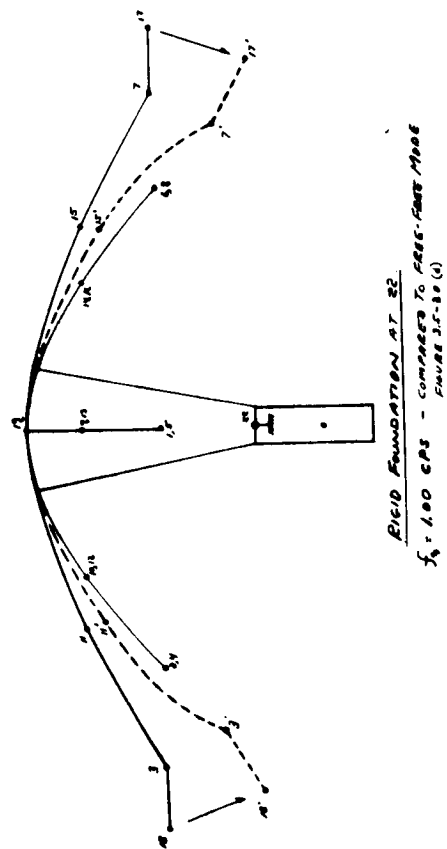
Figure 3.5-21



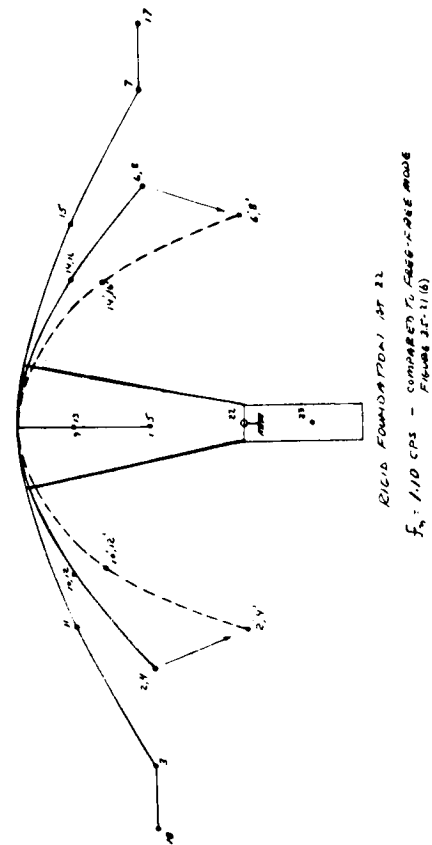
(a)



(b)



(c)



(d)

Figure 3.5-22

3.5.5 Orbit Maneuvering

The response of the orbiting spacecraft to the correcting maneuvers in orbit is considered in this section. These correcting maneuvers are brought about by the reactions of thruster jets on the spacecraft. The response of the spacecraft is a function of the time history of the thruster reactions and of course the inertial properties of the spacecraft itself.

The time history of the orbital maneuvers is relatively complex and of a random nature. It can be assumed however that the constant thruster jet reactions are suddenly applied and similarly removed, i. e. zero rise and fall time. Then there is a step function of an unknown duration. Additionally, repeated correcting maneuvers, some of which may be in opposing directions, cannot be altogether ruled out. These repeated maneuvers may be applied at arbitrary intervals and may be of arbitrary duration. Thus, the exciting forces consist of a series of rectangular pulses of constant magnitude but arbitrary duration and interval, with the further stipulation that the direction of the force pulse in any interval can be opposite to the direction in the preceding pulse.

The present analysis of the effect of the orbital maneuvers is based on the following reasoning: If a transient force is applied to the structure, the subsequent motion will be free vibrations which will decrease gradually in amplitude due to the damping present in the system. Usually the maximum displacement of the structure will occur during the time of application of the force or in the first cycle of the free vibration after removal of the force. It is known that the maximum dynamic magnification factor will be 2 for any finite transient pulse in the case of zero damping. With damping, the maximum response is dependent on the ratio of the pulse duration to the natural period and approaches static conditions for long duration pulses in highly damped systems. For long duration pulses (duration greater than approximately 2.5 times the natural period) and low

damping, the dynamic magnification is only slightly higher than unity, giving essentially static conditions.

With the above reasoning and the unknown nature of the duration and interval of the transient excitations, the first approximation is to assume a single transient rectangular pulse (with zero rise and fall time) of a duration which is large compared to the natural period of the spacecraft. In accordance with the statements in the preceding paragraph, this forcing function will evoke a response only slightly different than the static; however on sudden removal of the forcing function (zero fall time), the spacecraft will go into damped free vibrations. The decay characteristics of these free vibrations will determine the time in which the amplitude of the free vibrations has become small enough to preclude an amplitude build-up should another pulse be applied.

Since the interval between the rectangular pulses is arbitrary and the force direction reversible, a second assumption would be to ignore the interval between the rectangular pulses and to take all the rectangular pulses of the same duration. Conservatively, this may be represented by a rectangular periodic wave form. The response of the spacecraft is dependent upon the frequency of the forcing function. The most conservative assumption for the period of the forcing function is to take it equal to the natural period of the spacecraft. Obviously, the spacecraft will go into resonance under these and stresses for this situation can be readily obtained. It must be emphasized that the assumptions employed in this case - periodic forcing function and resonant conditions - are all extremely conservative and the probability of their being realized is very small.

What follows is the analysis of the spacecraft for the two cases delineated above.

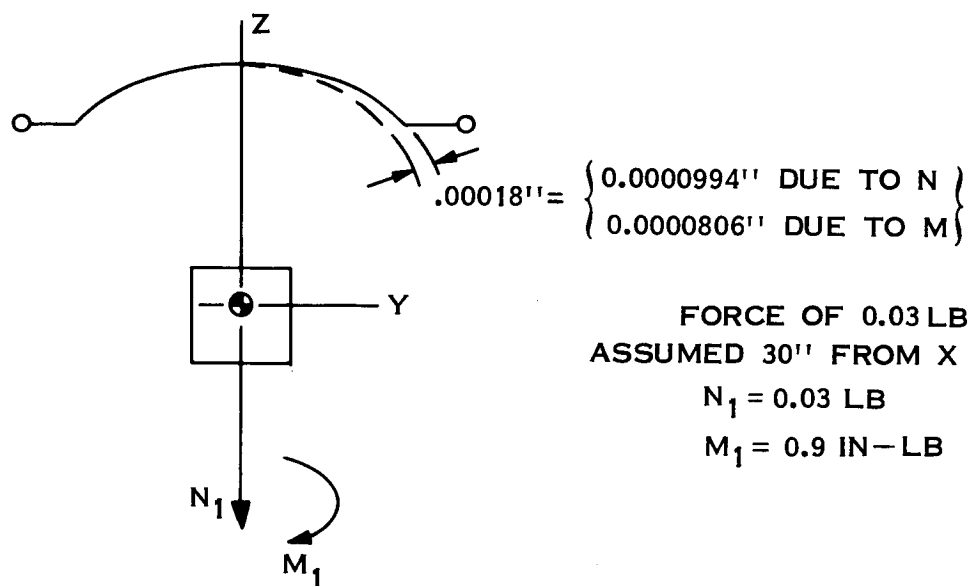
Response to a Finite Transient Pulse - For a long duration transient pulse, it has been established that the response evoked will be essentially

static. The application of a thruster reaction to the spacecraft will disturb the equilibrium; since the orbiting spacecraft is moving without constraints, it will undergo translation and/or rotation as a rigid body. Then, the mass and inertial properties of the deployed spacecraft will bring equilibrating forces into play. The nature of these equilibrating forces will be dependent on the type of disturbing force. Pure translational disturbing forces (applied at the mass center) will cause equilibrating inertial forces in any element proportional to its mass; the constant of proportionality in this case is the rigid body acceleration of the mass center. Similarly rotational disturbing forces will evoke equilibrating forces on any element proportional to its mass moment of inertia with the constant of proportionality being the rigid body rotational acceleration of the mass center.

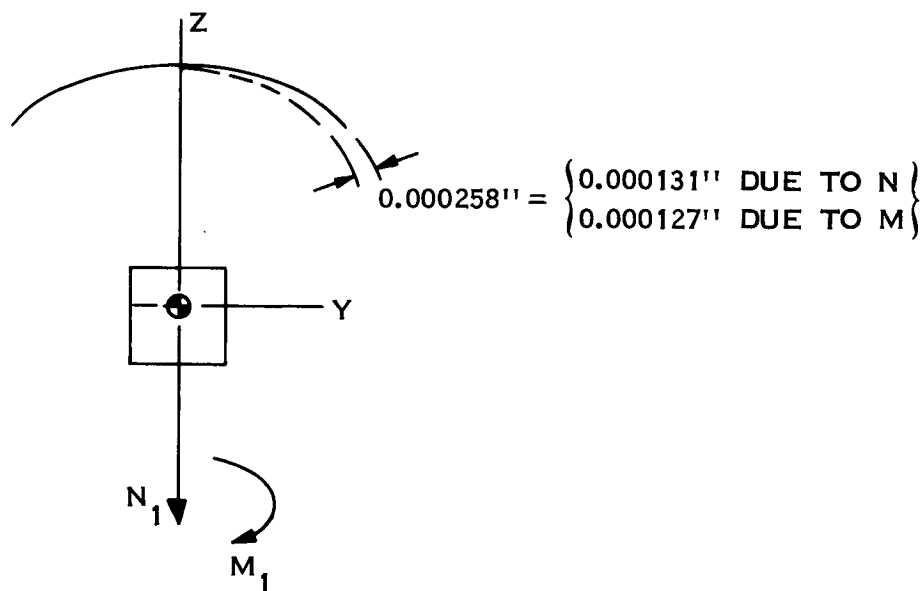
The rigid body translational and rotational equilibrating forces have been employed to determine the deformations which the petals will undergo to resist them. Two values have been computed; one is for the petals which support the solar panel mass and the other for the petals which have no such attachment. For the case where the solar panel mass is taken into account, it has been assumed that 3 petals resist the solar panel mass effect. Results of this investigation are presented in Figures 3.5-23 and 3.5-24.

Figure 3.5-23 pertains to a roll correcting maneuver, with a thrust of 0.03 lb assumed acting in the z-direction, 30 inches from the x-axis. Transferring this force to the mass center of the spacecraft results in translational and rotational equilibrating forces which in turn cause the petal deflections. The smaller deformation obtained for the petals with the solar panel mass is a direct reflection of the assumption that 3 petals contribute to resisting the solar panel mass.

The results of the analysis for a yaw correction maneuver are presented in Figure 3.5-24. The maneuvering force of 0.03 lb imposes a moment about the thrust (x) axis. In so far as the petal deformations are



(a) WITH SOLAR PANELS



(b) WITHOUT SOLAR PANELS

Figure 3.5-23 Response to Single Finite Duration Pulse
(Roll Correction Maneuver)

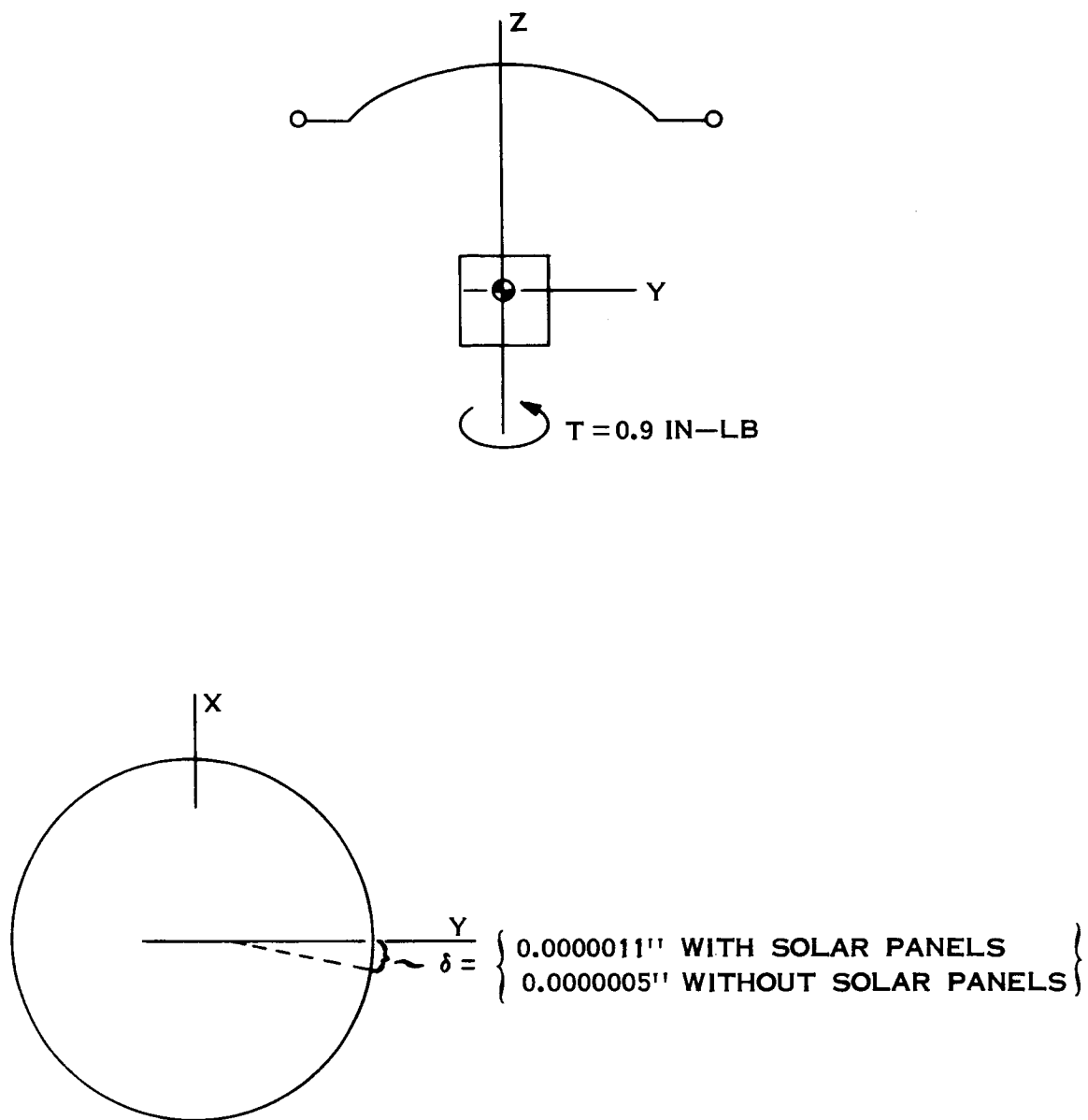


Figure 3.5-24 Response to Single Finite Duration Pulse
(Yaw Correction Maneuver)

concerned the translational effect of the maneuvering force can be ignored in this case.

As stated earlier, when the maneuvering forces are suddenly removed, the spacecraft will go into damped free vibrations. To determine the time required to reduce the amplitude of the free vibrations to a negligible value, a first assumption would be to assume the harmonic response of the spacecraft to be approximated by a viscously damped linear oscillator. Under such conditions, the ratio between two consecutive amplitudes is obtained from

$$\frac{X_{n+1}}{X} = e^{-\pi\gamma} = \text{constant}$$

or

$$\text{Log}_n \left(\frac{X_{n+1}}{X} \right) = -\pi\gamma$$

which is usually referred to as the logarithmic decrement. The parameter γ is the structural damping factor.

For finite values of γ , the ratio of consecutive amplitudes will approach but never become zero. For practical purposes, it will be assumed that the residual amplitude has become negligible when it assumes a value of 0.05 times the initial amplitude. To determine the number of cycles (N) required to get a residual amplitude of 0.05 times the initial, it is noted that since the ratio between two consecutive amplitudes is a constant, the ratio between the final and initial amplitudes is $(e^{-\pi\gamma})^N$ where N is the number of cycles. Symbolically this becomes

$$\frac{X_{\text{final}}}{X_{\text{initial}}} = (e^{-\pi\gamma})^N$$

using

$$\frac{X_{\text{final}}}{X_{\text{initial}}} = 0.05$$

we get

$$\text{Log}_n (.05) = -\pi\gamma N$$

$$N = \frac{\text{Log}_n .05}{-\pi\gamma} = \frac{.9536}{\gamma}$$

To determine the time corresponding to N cycles, it is only necessary to note that the natural period of vibration T (time for 1 cycle) is the reciprocal of the natural frequency, f . Then the time required for N cycles is

$$T = \frac{N}{f} = \frac{0.9536}{\gamma f}$$

Using this relationship, the time required to reduce the final amplitude to 0.05 times the initial amplitude has been computed for several values of the structural damping factor. These values are tabulated in Table 3.5-10.

Response to Periodic Wave Form - As discussed earlier, a conservative assumption for determination of orbital deformations and stresses is to assume a periodic wave form for the forcing function, with a forcing frequency equal to the natural frequency of the spacecraft. The spacecraft will go into resonance under such an extreme assumption. However it should be noted that this is the most critical situation that can ever occur and the possibility of its occurrence is extremely remote.

Approximating the response by a viscously damped linear oscillator subjected to a sinusoidal forcing function, the maximum magnification factor will be the reciprocal of the structural damping coefficient. Since this analysis relates to deflections and stresses under conditions which will occur infrequently, a relatively low damping coefficient of 0.001 was assumed. With these assumptions the results presented in Table 3.5-11 were obtained.

TABLE 3.5-10 RESPONSE TO FINITE TRANSIENT PULSE

Structural Damping Factor γ	Cycles to Reduce Amplitude to .05 of Initial Value	Time to reduce amplitude to .05 initial (seconds)		
		f = 1.5 cps	f = 1.0 cps	f = 0.5 cps
0.001	954	636	954	1908
0.005	191	127	191	382
0.01	95	64	95	191
0.05	19	13	19	38
0.10	9.5	6.3	9.5	19

TABLE 3.5-11 RESPONSE TO PERIODIC WAVE FORM

		Petals with Solar Panel	Petals without Solar panel
Periodic Roll Maneuver	Max. Deflection	0.180 in.	0.258 in.
	Max. Stress	510 psi.	305 psi.
Periodic Yaw Maneuver	Max. Deflection	0.0011 in.	0.0005 in.
	Max. Stress	Negligible	Negligible

3.6 THERMAL/STRUCTURAL ANALYSIS

3.6.1 Thermal Requirements and Approach

Performance criteria relative to distortion of the parabolic reflector can be met only by elimination of large temperature excursions and the corresponding thermal gradients. Design goals may be achieved by careful choice of thermal control coatings, super-insulation techniques, and the minimization of shadowing.

Thermal Coatings -- Thermal coatings may be selected so as to minimize the temperature gradients which will occur during a given orbit. Neglecting for the moment earth radiation, it may be verified that for a sun-facing surface the heating flux entering a surface is proportional to the ratio of absorptivity to emissivity (α/ϵ). Thus the temperature and temperature gradient may be minimized for low α/ϵ ratios. However, for a body transferring heat solely by radiation, the thermal time constant is inversely proportional to its surface emissivity so that minimization of ϵ is often desirable in the case of a member which is periodically shadowed. From the fact that low emissivity coatings yield large temperature variations and time constants and low α/ϵ coatings give small temperature variation and time constants, a compromise is indicated.

In the case of the parabolic structure, a large time constant is of prime importance. Emissivities in the order of 0.03 are state-of-the-art, however, the lowest α corresponding to this value is about 0.15 and it follows the ratio $\frac{.15}{.03} = 5.0$ is high. It is not possible to obtain a coating with both a low emissivity and a low α/ϵ . Silicone monoxide or S-13 white paint are two examples of thermal coatings giving α/ϵ 's of 0.3. Table 3.6-1 lists three thermal coatings with properties of interest to this study.

TABLE 3.6-1 SURFACE COATING PROPERTIES

Surface Coating	α	ϵ	α/ϵ
Silicone Monoxide	0.3	0.9	0.333
S-13 White Paint	0.3	0.9	0.333
Vapor Deposited Aluminum	0.15	0.03	5.0

TABLE 3.6-2 SURFACE COATING COMPARISON

Surface coating	Max Sink Temp	Min. Sink Temp	Petal Beam Thermal Time Constant	Insulated Petal Beam Thermal Time Constant
Silicone monoxide	-3°F	-320°F	0.33 hr.	29.52 hr.
MTL-3	-3°F	-320°F	0.33 hr.	29.52 hr.
Vapor Deposited Aluminum	440°F	-320°F	1.6 hr.	4.82 hr.

A comparison between the various thermal coatings may be made by using the properties given in Table 3.6-1 to compute the quantities given in Table 3.6-2. By way of further comparison, the effect of temperature variation during a maximum earth shadow time of 1.2 hours was considered. Results show that for a low emissivity the maximum temperature is decreased by approximately 400⁰F and the low α / ϵ coated surface decreases by about 300⁰F.

Super Insulation Blankets -- It was also shown that regardless of the coating choice temperature gradients could exist across the petal beams which would lead to large structural deflections. Therefore, it was necessary to consider other means for controlling the orbital temperature variations and gradients. Super-insulation blankets were chosen for this task. The blankets provide high resistance to heat flow and reduce temperature variations and gradients; thermal time constants are substantially increased as may be seen in Table 3.6-2. The superinsulation selected is composed of ten sheets of aluminized mylar 0.00025 inch thick sandwiched between an inner mylar support card and an outer face sheet. Similar blankets have been successfully used on the Pegasus spacecraft and are also being designed for the Nimubs D control subsystem.

The overall effective emissivity of the insulation is a function of the number of joints, penetration and discontinuities in a given enclosure design. To account for the main discontinuities, the effective emissivity was adjusted to a value of 0.03; the theoretically possible value is 0.001.

Based on the above considerations a superinsulated petal beam design using a low α / ϵ coating best minimizes the temperature variation and gradients.

Thermal Time Constant - - Thermal time constants discussed in this report are defined as:

$$\tau = \frac{C}{\mathcal{J} \Phi}$$

Where C is the thermal capacitance, and $\mathcal{J} \Phi$ is the coefficient in the linearized radiation equation. Thus

$$q = \mathcal{J} \sigma (T^4 - T_s^4)$$

$$q = \mathcal{J} \Phi (T - T_s)$$

where $\Phi = \sigma (T^2 + T_s^2)(T + T_s)$

T and T_s are defined as the body temperature and the effective sink temperature respectively. It may be noted that the "time constant" is a function of the body temperature and the effective sink temperature. Since the sink temperature and, therefore, body temperature changes with orbit position, the time constant will vary with orbit position. However, an effective time constant may be defined which does not change with orbit position. It is based on the maximum and minimum temperatures determined by using the optical properties of a body surface. This effective time constant was used to study the thermal effect of variable heat flux inputs during various orbits.

A synchronous equatorial orbit has a period of about 24 hours, and bodies with effective time constants of this order will have small temperature deviations during a given orbit. When the temperature variation is small, mean orbital fluxes may be used to calculate the mean orbital temperature of the body.

3.6.2 Design Orbit

The design orbit is defined as the orbit which results in the largest changes from the mean orbital temperatures. These deviations were assumed to occur during the orbit containing the longest shadow period which for a synchronous equatorial orbit occurs during the vernal and the autumnal equinox. During this time the antenna spends the longest period in the earth's shadow, and consequently this orbit is used for the thermal analysis. (Figure 3.6-1)

At synchronous altitudes (19,320 nautical miles) the terrestrial and reflected solar radiations are 2.16 and 1.55 percent of their respective near earth values and represent only 0.32 and 0.63 percent of the solar flux, respectively. The values used for the thermal analysis are:

Solar Radiation	442.4 B/hr. ft. ²
Reflected Solar Radiation	2.79 B/hr. ft. ²
Earth Emission	1.42 B/hr. ft. ²

● ORBIT

SYNCHRONOUS EQUATORIAL ORBIT (HEIGHT 19,320 NM)

● INCIDENT FLUXES

SOLAR	-	442.4	BTU/FT ² -HR
ALBEDO	-	2.79	"
EARTH	-	1.42	"

● DESIGN CASE

(THAT WHICH CAUSES LARGEST TEMP. VARIATION)

3-134

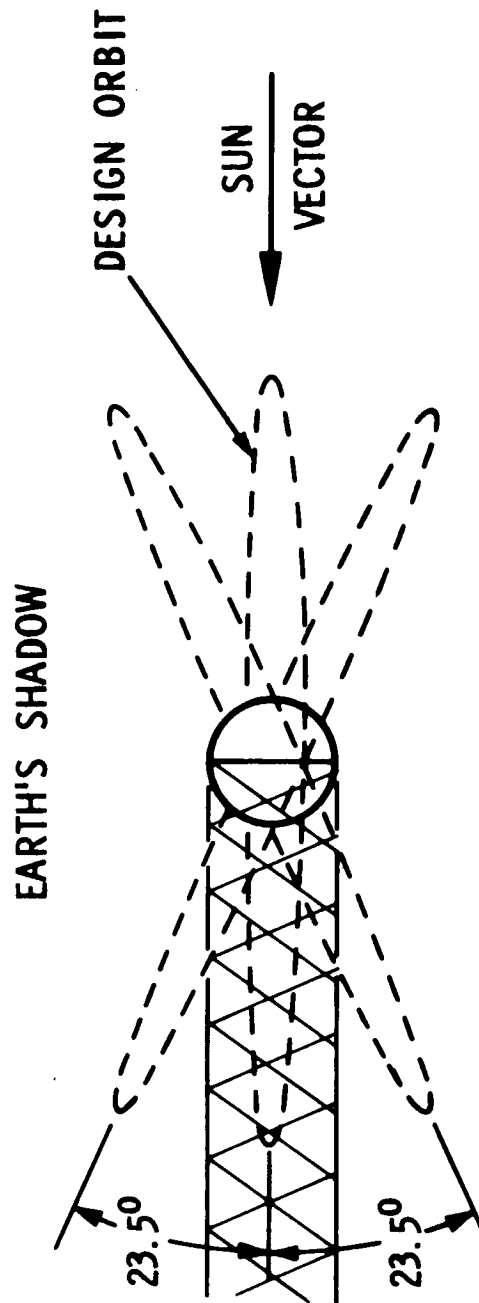


Figure 3.6-1 Yearly Change in Orbit Position Relative to Sun Vector

3.6.3 Petal Thermal Analysis

Based on the conclusions reached in Section 3.6.1 the petal beams will be superinsulated, and the insulation will be coated with a low α/ϵ coating. This construction for the petals leads to a thermal time constant of 29.52 hours, which permits the incident heating fluxes to be averaged over the orbital period and insures low temperature response during shadow periods. Furthermore, since the thermal resistance offered by the superinsulation is very large compared to that offered by the beam, the temperature differentials are carried across the blankets and not the beam.

The M.O.T. (mean orbital temperature) was determined by idealizing each petal into one radial beam with the same dimensions as an actual radial beam ($1 \times 3/4 \times 0.022$). This idealized beam was divided into three nodes each of which was assumed straight and at a constant angle to the antenna centerline. Figure 3.6-2 shows this idealization. Figure 3.6-3 shows the position of one set of nodes in relation to the design orbit and sun.

Shadow Analysis - An antenna shadow analysis was required before the mean orbital temperatures could be determined. Four shadowing conditions were considered in the analysis: (1) feed module shadowing, (2) wire mesh shadowing, (3) antenna hub shadowing, and (4) earth shadowing. These shadow conditions were analyzed using the reference design given in Figure 3.2-2 and the design orbit in Figure 3.6-1.

Descriptive geometry methods were used for the feed module shadowing analysis. For each five degrees of anomaly a layout was constructed of the antenna showing the size and position of the feed shadow on the antenna. This set of drawings was converted into curves showing the shadowing for each node. Figure 3.6-4 shows the beam shadowing as a function of anomaly for an idealized beam with a position angle, θ , equal to zero. The position angle is defined as the angle between the projection of the sun vector and

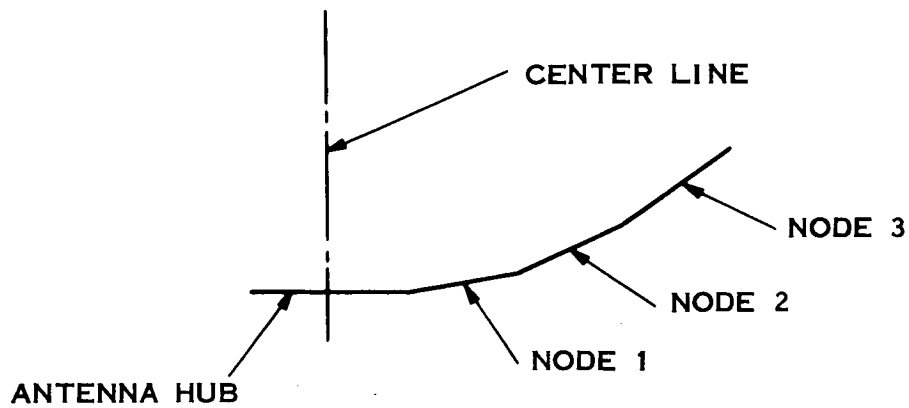


Figure 3.6-2 Petal Thermal Analysis Model

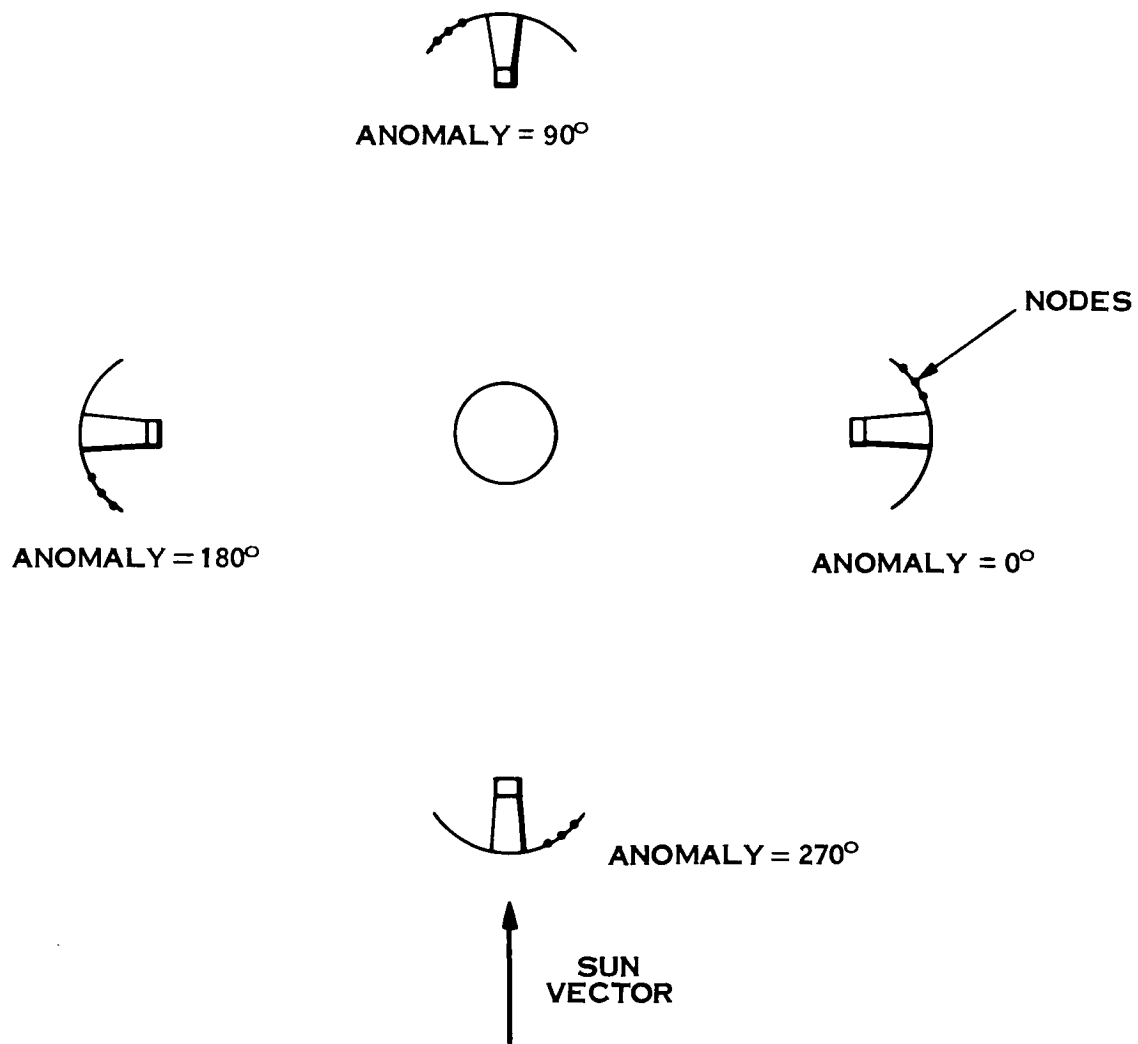


Figure 3.6-3 Relation of Thermal Analysis Nodes to Orbit Position

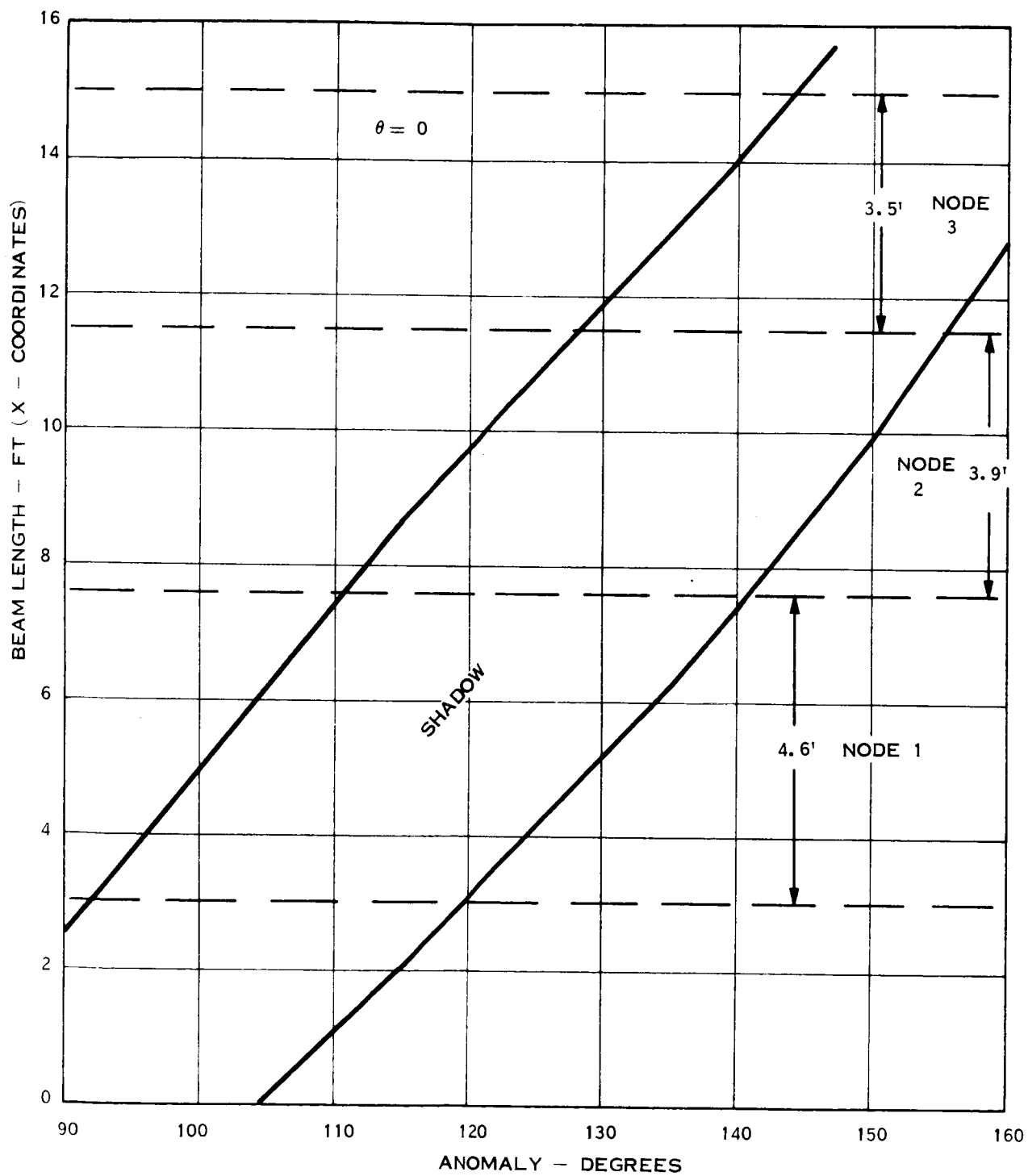


Figure 3.6-4 Feed Module Shadowing

the projection of the beam on the spacecraft x-y plane. The set of nodes shown in Figure 3.6-4 are taken with $\theta = 0^\circ$.

The wire mesh to be used for the antenna was assumed to have a diameter of 0.010 inch and spacing of 0.080 inch on center. A mesh of this type has a variable blockage depending upon the angle at which sunlight passes through it. An expression for the percent of sunlight passing through the mesh may be derived by considering Figure 3.6-5. The area inside the dotted lines need only be considered since the mesh is symmetrical about this area. The total normal area viewed by the sun at angle ξ is given by

$$A_n = S^2 \sin \xi$$

and the normal area of the wire viewed by the sun is given by:

$$A_w = Sd \sin \xi + Sd = Sd (\sin \xi + 1)$$

Therefore, the percent sun passing through the mesh with the sun at ξ angle to the mesh is given by

$$\begin{aligned} \% \text{ Sun} &= 100 \frac{(\text{Total Normal Area} - \text{Wire Area})}{\text{Total Normal Area}} \\ &= 100 \left(1 - \frac{d (\sin \xi + 1)}{S \sin \xi} \right) \end{aligned}$$

This solution is for simple angles about the Y axis, but it may easily be extended to compound angles. The normal area is thus written as

$$A_n = S^2 \sin \xi \sin \alpha$$

and

$$A_w = Sd (\sin \xi + \sin \alpha)$$

where α is the angle about the X axis. This leads to:

$$\% \text{ Sun} = 100 \left(1 - \frac{d (\sin \xi + \sin \alpha)}{S \sin \xi \sin \alpha} \right)$$

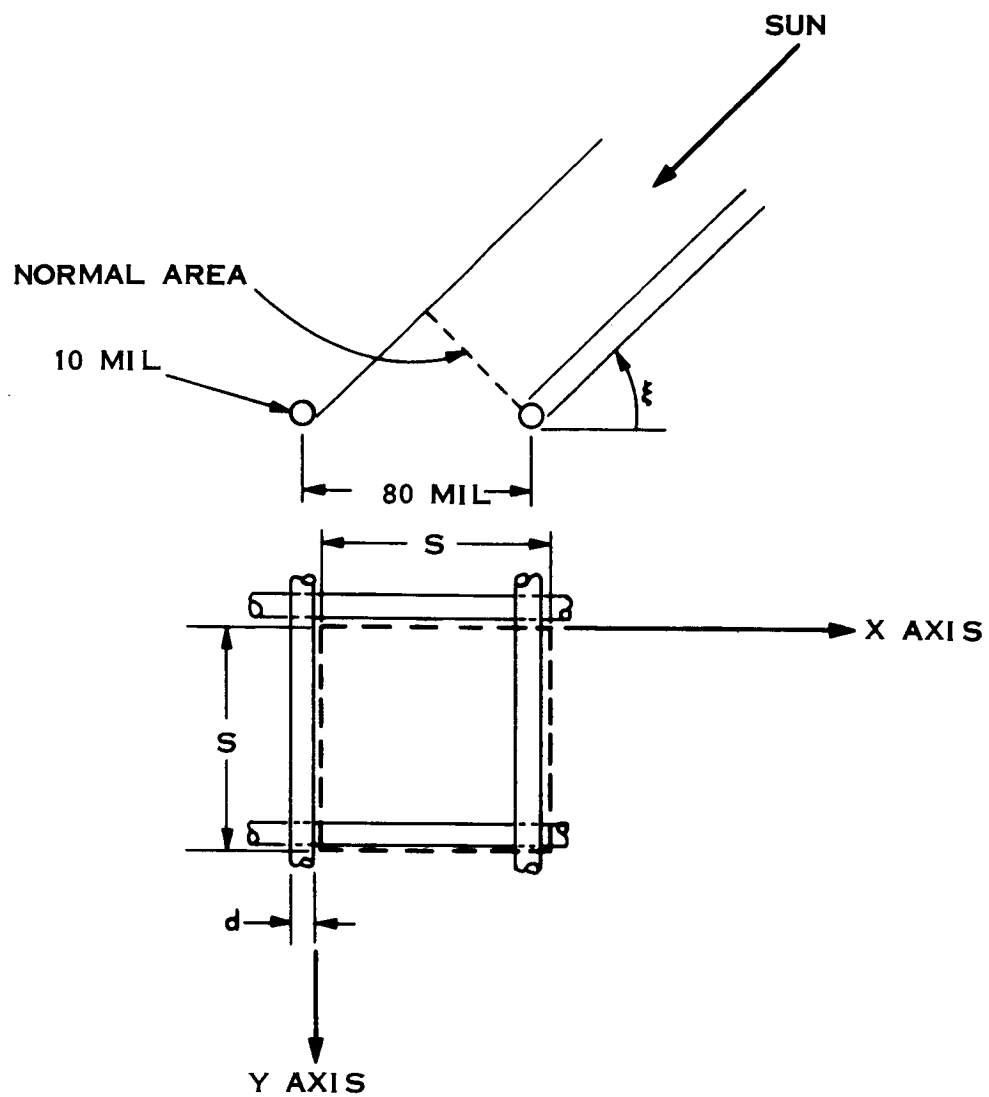


Figure 3.6-5 Reflector Mesh Sunlight Blockage

In order to find the percent sunlight passed through the mesh during periods of mesh blockage, it was necessary to determine the angles ξ and α for these conditions of anomaly. Descriptive geometry was used to find these angles for every five degrees of anomaly. Since mesh shadowing and antenna hub shadowing occur at approximately the same position this descriptive geometry analysis also pointed out the shadowing due to the antenna hub. A set of curves was then plotted for the mesh and antenna hub shadowing for each beam node. Figure 3.6-6 shows the effect of mesh and antenna hub shadowing on the beam for $\theta = 0^\circ$, node 3 and ϕ (slope of beam) = 34° .

Earth shadowing is quite simply determined from geometry. Based on an orbit of 19,320 nautical miles the antenna enters the earth's shadow at 81.5° anomaly and reappears at 98.5° anomaly for the design orbit.

Mean Orbital Flux and Temperature - With the shadowing determined the mean orbital flux was then calculated. In order to make this calculation, two general equations were developed, which described the normal fluxes to the top and bottom, and the two sides. Figure 3.6-7 depicts the coordinate system used to describe the position of any beam in relation to the sun vector. This model assumes the sun to be rotating about the y-axis, instead of the sun being stationary and the beam rotating. The sun vector, therefore, is written in the following manner

$$\vec{S} = -S_\infty[(\cos \omega t) i + (\sin \omega t) k]$$

where S_∞ = scalar flux of the sun
 ω = angular velocity, 15 degrees/hour
 t = time, hours

The unit vector to the top of the beam is

$$\vec{n}_T = (\sin \phi \cos \theta) i + (\sin \phi \sin \theta) j + (\cos \phi) k$$

and the unit vector to the side of the beam is

$$\vec{n}_S = (\sin \theta) i - (\cos \theta) j$$

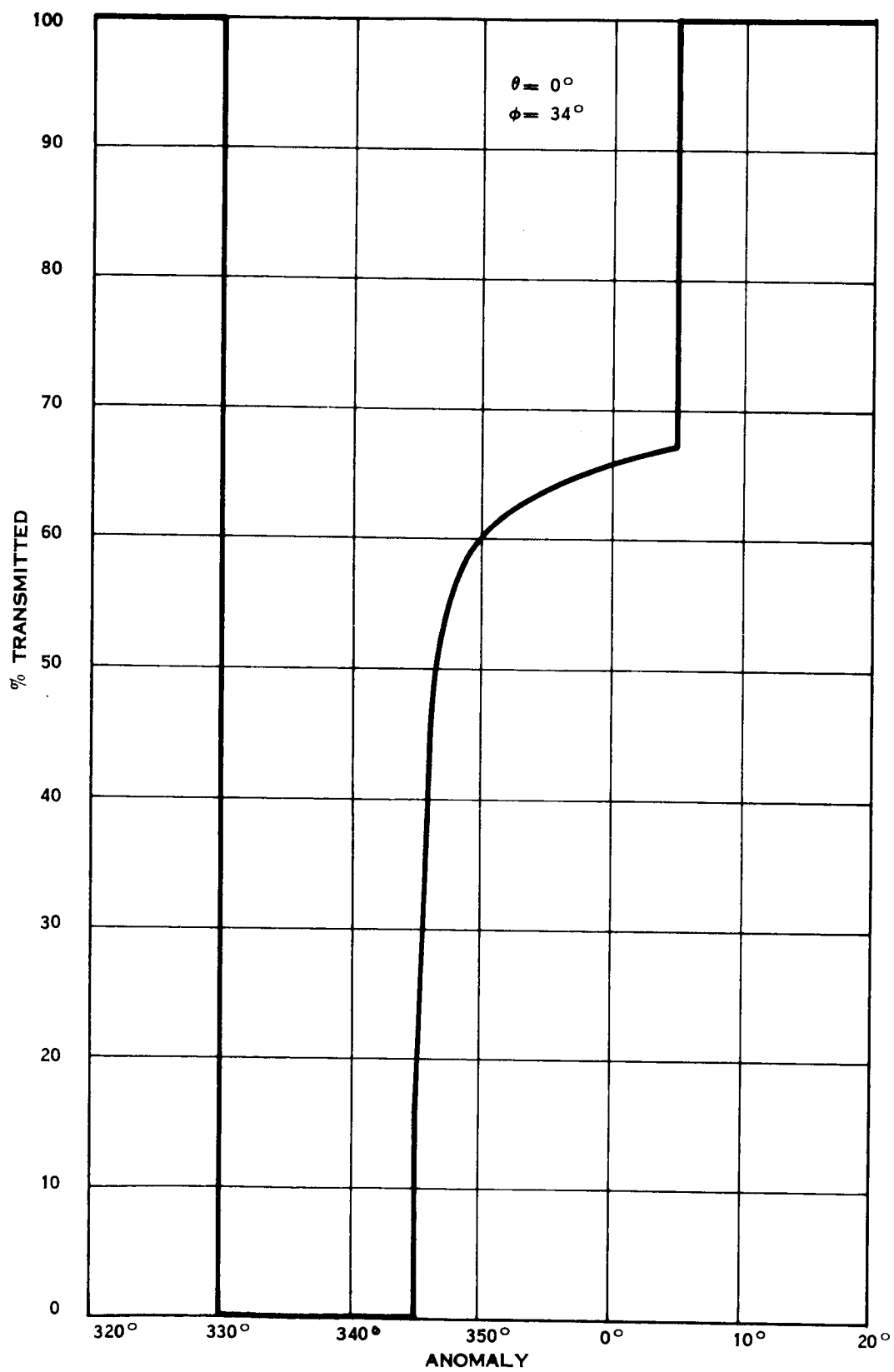


Figure 3.6-6 Mesh and Antenna Hub Shadowing

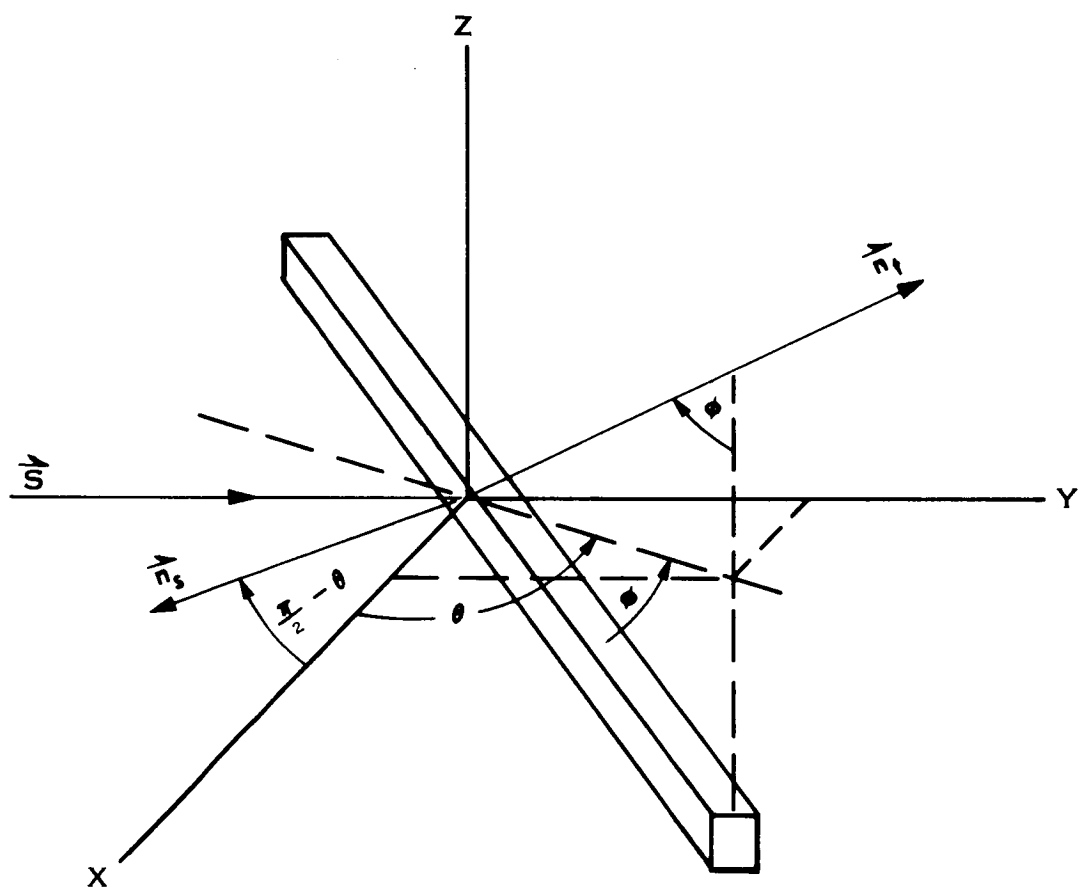


Figure 3.6-7 Coordinate System for Thermal Analysis

Taking the dot product of the sun vector and the unit vector then gives equations for the sun normal to the top and side. Normal sun to the top is

$$\vec{S}_T = \vec{S} \cdot \vec{n}_T = -S_\infty [\sin \phi \cos \theta \cos \omega t + \cos \phi \sin \omega t]$$

and normal sun to the side is

$$\vec{S}_s = \vec{S} \cdot \vec{n}_s = -S_\infty [\sin \theta \cos \omega t]$$

Note that the equation for the unit vector to the top also describes the unit vector to the bottom except for a sign difference. Recognizing this fact the equation then describes the flux to both the top and bottom and indicates the difference by a sign change. This fact is also true for the flux to the sides.

Integrating these equations for the flux to the top and bottom, and the sides over 2π gives a total flux to any node which when divided by 2π results in the mean orbital flux,

$$S_T] \text{ M.O. F. } = -\frac{S_\infty}{2\pi} \int_0^{2\pi} [\sin \phi \cos \theta \cos \omega t + \cos \phi \sin \omega t] d\omega t$$

and

$$S_s] \text{ M.O. F. } = \frac{-S_\infty}{2\pi} \int_0^{2\pi} [\sin \theta \cos \omega t] d\omega t$$

These two equations do not consider the losses due to shadowing. During a shadow period the sun does not become blocked instantaneously, but the shadow line moves across any structure at some measurable rate. This phenomenon is depicted in Figure 3.6-4, which shows the shadowing for one radial beam. The node boundaries are indicated by dotted lines enabling one to draw curves showing the percent sun on a node during shadowing. An example of this is given in Figure 3.6-8 which was obtained from Figure 3.6-4. With this the shadowing is given in terms of percent sun striking a node at any time -- it is assumed that the earth shadowing is instantaneous. The M.O.F. (mean orbital flux) for the top with shadowing accounted for may now be

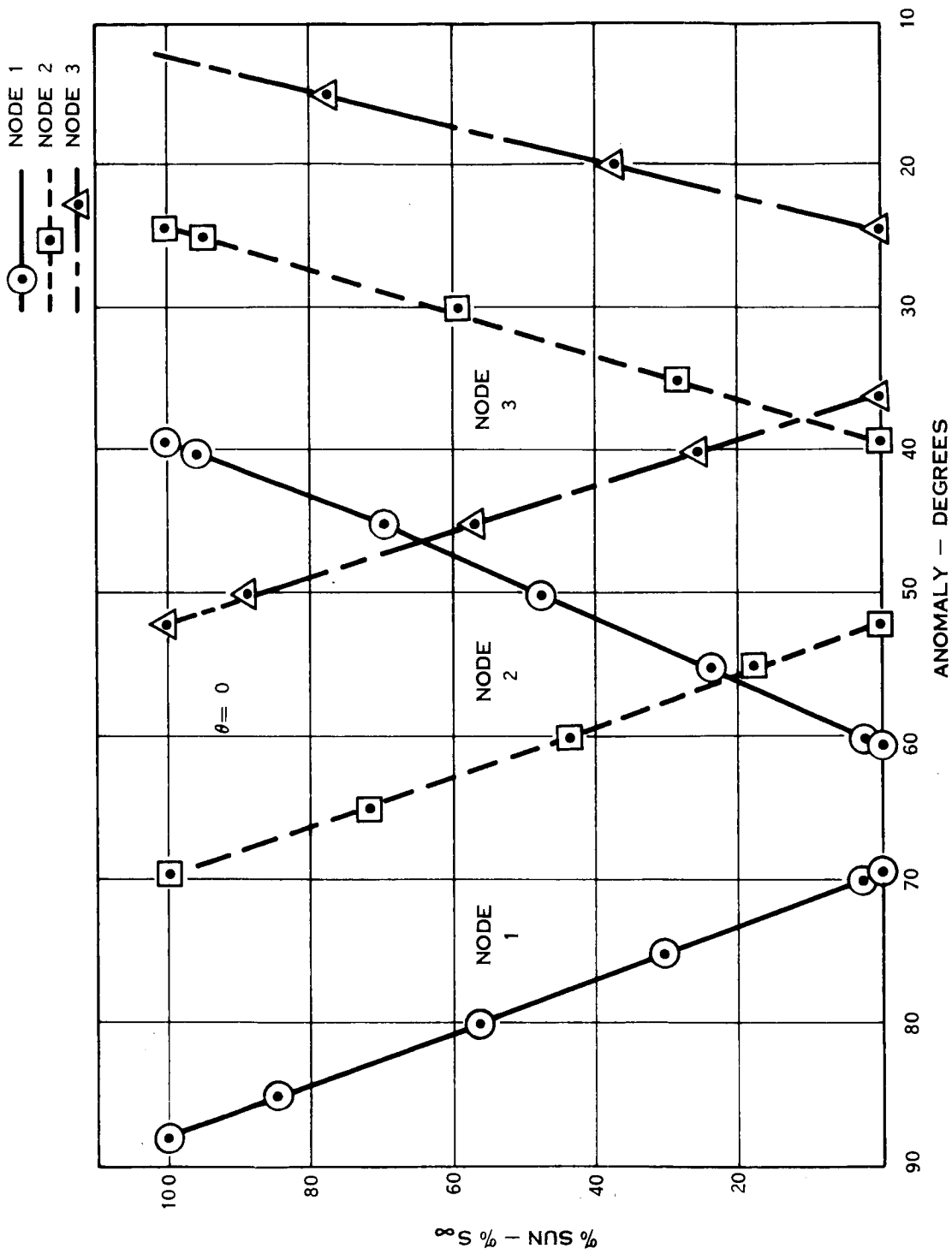


Figure 3.6-8 Antenna Feed Shadowing

written as

$$\begin{aligned} S_T] \text{ M.O.F. } &= \frac{-S_\infty}{2\pi} \int_0^{2\pi} \left(\frac{\vec{S}_T}{-S_\infty} \right) d\omega t - [S_\infty - S_{avg}] \int_a^b \left(\frac{\vec{S}_T}{-S_\infty} \right) d\omega t \\ &- [S_\infty - S_{avg}] \int_c^d \left(\frac{\vec{S}_T}{-S_\infty} \right) d\omega t - \text{etc.} \end{aligned}$$

where S_{avg} is the average sun flux seen by the node over the integral period. It is defined as

$$S_{avg} = F S_\infty$$

where F is the average percent of sun light striking the node over the integral period. The M.O.F. equation may then be written

$$S_T] \text{ M.O.F. } = \frac{-S_\infty}{2\pi} \int_0^{2\pi} \left(\frac{\vec{S}_T}{-S_\infty} \right) d\omega t - \frac{S_\infty [1-F]}{2\pi} \int_a^b \left(\frac{\vec{S}_T}{-S_\infty} \right) d\omega t - \text{etc.}$$

or

$$S_T] \text{ M.O.F. } = \frac{-S_\infty}{2\pi} \left\{ \int_0^{2\pi} \left(\frac{\vec{S}_T}{-S_\infty} \right) d\omega t - [1-F] \int_a^b \left(\frac{\vec{S}_T}{-S_\infty} \right) d\omega t - \text{etc.} \right\}$$

Similarly the M.O.F. equation for the sides may be written

$$S_S] \text{ M.O.F. } = \frac{-S_\infty}{2\pi} \left\{ \int_0^{2\pi} \left(\frac{\vec{S}_S}{-S_\infty} \right) d\omega t - [1-F] \int_a^b \left(\frac{\vec{S}_S}{-S_\infty} \right) d\omega t - \text{etc.} \right\}$$

Using the shadowing written in terms of F , the above M.O.F. equations were solved for each node. These M.O.F.'s then were used to calculate the M.O.T. for each node.

The nodes along each beam were assumed to be thermally isolated from each other, thus the simple heat radiation equation

$$2A_r \epsilon \sigma T_s^4 = \alpha (S + A) A_r + \epsilon E A_r$$

where T = Temperature
 ϵ = emissivity
 σ = Stefan - Boltzmann constant
 α = Absorptivity
 S = Solar radiation
 A = reflected solar radiation
 E = earth radiation
 A_r = Area

was used. Section 3.6.2 points out that the reflected solar and earth radiation is only 0.95% of the solar radiation, thus they were disregarded because of their negligible affect on the M.O.F. The fluxes are given for the top and bottom, and the sides i.e. S_T M.O.F. and S_S M.O.F. each of which strikes a different area, therefore, the heat radiation equation for each node is written

$$2 \epsilon \left(A_t + A_S \right) \sigma T_{M.O.T.}^4 = \alpha \left(A_S S_S + A_t S_T \right)$$

or

$$\sigma T_{M.O.T.}^4 = \frac{\alpha}{2 \epsilon} \left(\frac{A_S}{A_T + A_S} S_S + \frac{A_T}{A_T + A_S} S_T \right)$$

where A_S = area of a beam side
 A_t = area of a beam top or bottom
 $T_{M.O.T.}$ = mean orbital temperature

With the fluxes calculated, the above equation may be solved for the M.O.T.'s. The node temperature difference along any beam was no more than 6°F which justifies the assumption that each beam is at the average temperature of its three nodes. For the design orbit the mean orbital temperatures are symmetrical about the X and Y coordinates, therefore, only nine beam temperatures needed to be calculated. These temperatures are given in Figure 3.6-9.

In order to determine the excursions from these mean orbital tem-

PARABOLIC ANTENNA
F/D = 0.325
DIAMETER = 30'

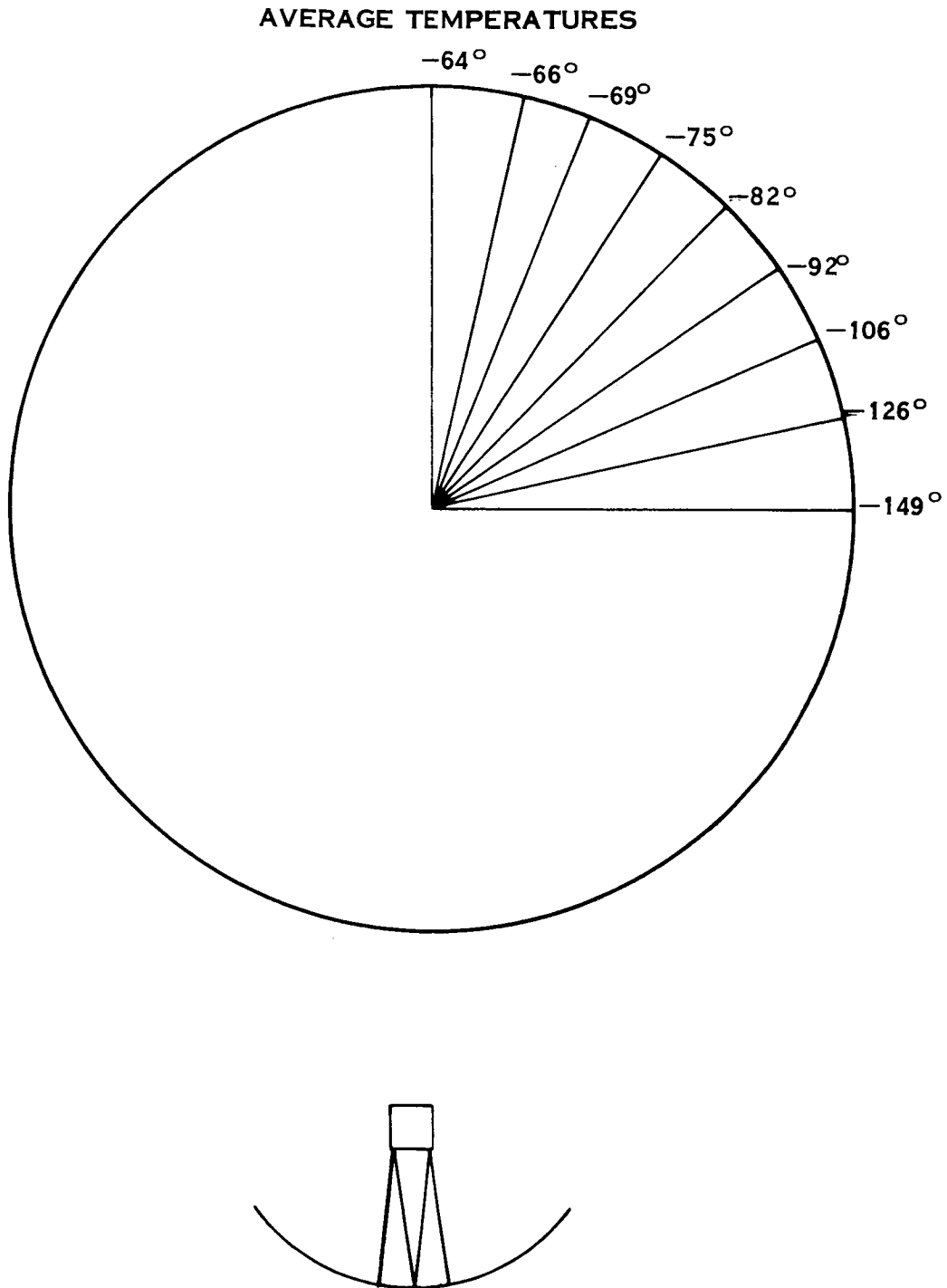


Figure 3.6-9 Beam Temperatures

peratures, a transient analysis is required for many positions around the orbit. The analysis, during this study, was simplified by calculating the temperature drop of a beam during the earth's shadow period assuming the beam enters the shadow at its maximum temperature of -3°F . This maximum temperature is the sink temperature of a beam receiving normal solar and earth flux when coated with S-13 white paint. Conversely, the minimum sink temperature, -317°F , is based on a normal earth flux only. The usual equation for this is

$$\frac{T - T_c}{T_I - T_c} = \exp - \theta/\tau$$

where θ = Time
 T = temperature at time, θ
 T_c = minimum temperature
 T_I = Temperature at $\theta = 0$

Taking $T_c = -317^{\circ}\text{F}$ (minimum possible temperature) the above equation gives a temperature drop of 12°F . This result is conservative since no beam can enter the shadow at the maximum temperature of -3°F , and, therefore, the actual drop is smaller than 12°F . In addition, the shadow study showed that the earth's shadow period is the longest shadow period of any orbit consequently, 12°F represents the largest excursion one can expect from the M.O.T.

Temperature Gradients - Earlier it was stated that temperature differentials will be carried across the insulation and not the beams. In order to determine the value of the gradient across the beam a simple calculation was made for the worst case. This worst case occurs when the sun is normal to the top or bottom surface of the $1 \times 3/4 \times 0.022$ inch insulated beams shown in Figure 3.6-10. Actually this condition occurs only twice during each orbit and for a very short time.

The maximum possible temperature gradient across the insulation was determined by a steady-state analysis. The sunlit surface of the insula-

tion was assumed to be at the highest possible temperature, -3°F , and the surface of the beam at the lowest possible temperature, -317°F (both based on the surface coating S-13). With the effective emissivity for the insulation taken as 0.03 the heat radiated through the insulation was calculated for a one foot length of the beam, using

$$q = F_{\epsilon} F_A A_r (\sigma T_2 - \sigma T_1)$$

where F_{ϵ} = effective emissivity
 F_A = view factor
 A_r = radiation area
 T_2 = insulation surface temperature
 T_1 = beam surface temperature

Solving this equation for the above case gives a value of 13.8×10^{-2} BTU/hr/ft, which must be re-radiated back to space for a steady - state condition.

With the conservative assumption that all this heat is conducted along both sides of the beam before it is re-radiated back to space, the following calculation was made. The standard heat conduction equation is rearranged for the temperature gradient necessary to conduct this heat across the beam:

$$\Delta T = \frac{q L}{K A_c}$$

where q = heat conducted along each side
 L = path length
 K = thermal conductivity
 A_c = cross-sectional area

The ΔT required to conduct the radiated heat across an aluminum beam was calculated to be 0.05°F .

Leakage Considerations - The beam temperature gradient can be significantly affected by leakage through joints, penetrations and discontinuities in the superinsulation. The affect of this leakage is normally determined

through thermal testing, but in some instances it is possible to estimate the leakage by analytical methods. The one type of leakage which can be analyzed for this design is that due to the mesh support standoffs. These standoffs are attached directly to the aluminum beam through small holes in the superinsulation, and thus, are a direct path for heat flow either in or out. (See Figure 3.6-11 (a)).

Consider the case when the sun strikes directly on top of the standoffs, which is the case for the maximum heat input to the beam through the standoffs. The thermal model assumed the standoffs to be a cylinder, 1/4 inch in diameter and 1/2 inch high, and the sides are assumed insulated so that all the heat, passing through the standoffs, reaches the beam. (See Figure 3.6-11 (b)). In order to determine the heat flow through the standoff a heat balance equation was written

$$\alpha SA_r = A_r \epsilon \sigma T^4 + \frac{KA}{L} (T - T_B)$$

where T = the top surface temperature of the standoff.
 T_B = the assumed constant temperature of the beam.

If T_B is taken to be at the coldest M.O.T. of any beam ($T_B = -149^{\circ}\text{F}$) T becomes -145.3°F and this gives a leakage of 0.0161 BTU/hr per 1 foot length of beam. This leakage has only a small affect on the temperature gradient across the insulated beam. In fact, adding this to the heat input used in the gradient calculation only raises the gradient from 0.05°F to 0.0558°F .

Temperature Differences - A temperature difference between the radial and circumferencial beams exists during different positions in the orbit. These differences can cause distortions in the petals which must be evaluated. Attachment of the radial and circumferencial beams will be accomplished in a manner to minimize resistance to heat transfer by conduction.

The maximum temperature difference between the radial and circumferencial beams occurs when the sun strikes the circumferencial beam at a normal

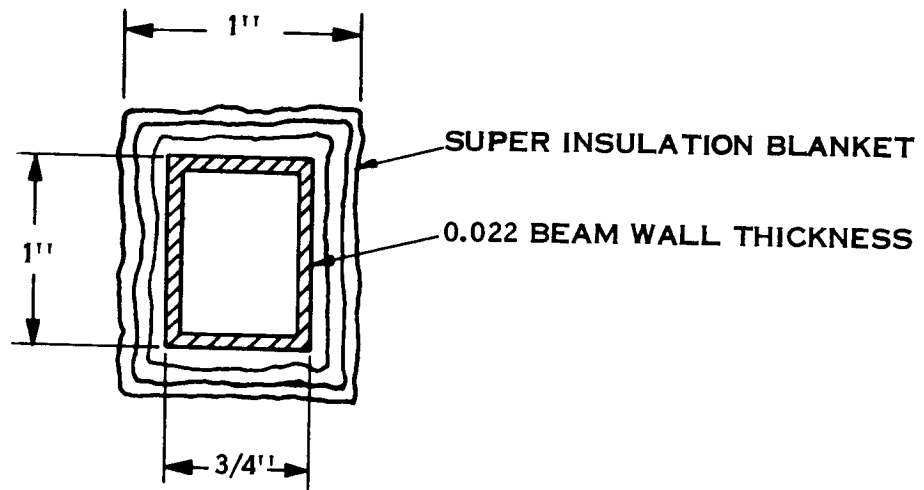


Figure 3.6-10 Petal Beam Cross-section

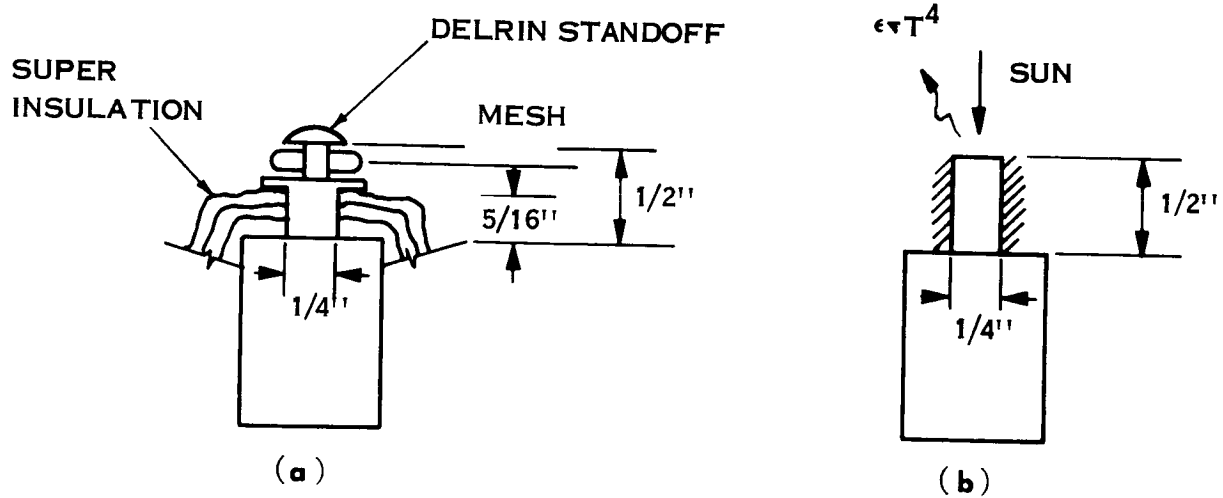


Figure 3.6-11 Mesh Standoff Fittings

angle. The sun's position relative to the beams is assumed as shown in Figure 3.6-12. Note that the radial and circumferential beams are assumed to be at 90° to each other; this is not quite the case but is a conservative assumption. Assuming that half of the total heat input to the insulated circumferential beam is conducted to each radial beam, the temperature difference necessary to do this may be computed. Using the standard equation for heat transfer by radiation the maximum heat input to the circumferential beam was calculated to be 0.612 BTU/hr. Half of this is conducted to each radial beam and the temperature difference necessary to do this is 10.7°F . This temperature difference is conservative except for the assumed perfect conduction of the attachment between the radial and circumferential beams.

Mesh Temperatures - The wire mesh used as the antenna reflector has a very small time constant enabling it to reach the maximum and minimum temperatures based on its optical properties. It is anticipated that the mesh will be coated with a silicone monoxide film giving the optical properties listed in Table 1 Section 3.6.1. These optical properties have been shown to offer the minimum temperature excursions for this application, and result in a maximum and minimum temperature of -3°F and -317°F respectively. These temperatures may change slightly depending upon the relative position of each section of the wire mesh to the earth and sun, but it is not expected to be of any significance in terms of mesh expansion and contraction.

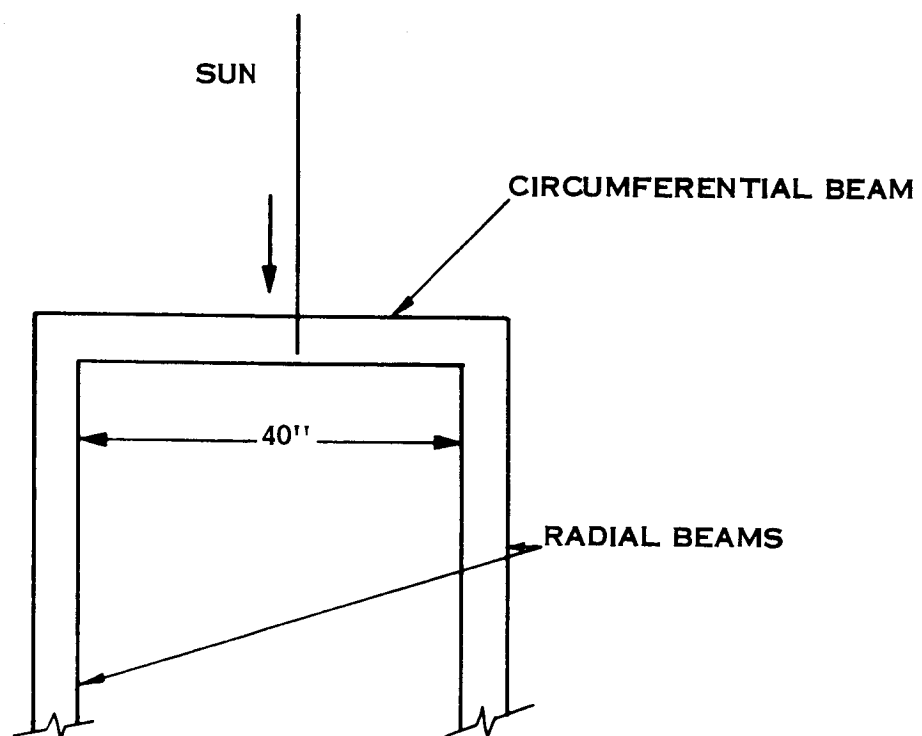


Figure 3.6-12 Beam Geometry

3.6.4 Thermoelastic Analysis of Reflector

In this section a thermoelastic analysis of the parabolic reflector is presented. Included is an analysis of the deformations and stresses induced by the thermal environment encountered by the reflector during its flight in space.

Analytical Model - The reflector is made up of petals in the form of sectors. The petals themselves are composed of radial and circumferential members. Subsequent to deployment, the petals are locked to each other at their free ends to form the parabolic reflector. The thermal deformations of this three dimensional structure under a non-uniform thermal environment are of a complex nature. For purposes of this analysis, each individual petal has been assumed to consist of a radial member clamped at its inner end to the hub and attached to a circular segment at the outer end. The extremities of the circular segments at the outer end are connected to each other, forming an effective ring. Corresponding to the reference design with 32 petals, we thus have 32 sectors, each sector having a radial member and a segment of the ring.

Under a uniform temperature, the reflector will expand or contract in such a manner that its original shape is retained. However, with a non-uniform temperature distribution the original shape will not be retained and self-equilibrating thermal forces will come into play. In the general case each sector of the reflector will have a different temperature distribution, the temperature in the radial member in any sector itself being different from that in the circumferential segment, as shown in Figure 3.6-13. Here T_R and T_D represent the temperatures of the ring segment and radial members respectively (assumed constant over their respective lengths) with the indices denoting the sector under consideration.

The internal forces introduced in the above described structure

by a non-uniform thermal environment will consist of two types, the interaction forces and the continuity forces. The forces between the radial and circumferential members of any one sector are the interaction forces. Continuity forces are the forces introduced by virtue of the connections between the sectors at the extremities of the ring segments. It should be noted that the interaction and continuity forces are inter-related because of the redundancy of the structure.

The nature of the internal continuity forces depends to a large extent on the type of locking mechanism between the sectors. The most severe case, from the point of view of analytic complexity as well as deformation integrity, would be when the connections are rigid and can transmit moment, shear and axial forces. Quite obviously, the elimination of some, if not all, internal forces would reduce the magnitude of the thermal deformations. This can be accomplished by the proper selection of the locking mechanism.

Based on the above considerations, it was decided to provide a locking device which will permit freedom of radial movement between adjacent petals. The locking device has been designed with a pin which will permit one segment of the ring to slide radially, unhindered by adjacent petals. With the radial freedom of movement provided at the locks, it follows that no radial continuity forces can develop. Additionally, the lock acts like a hinge precluding the possibility of moment transfer. The pin connection can transmit transverse shear. Thus, the only continuity forces that can come into play are the circumferential forces and transverse shear. In the present analysis, the effect of the transverse shear continuity has been ignored since the relative deflections between petals are small.

With only circumferential forces being transmitted by ring continuity, equilibrium requirements dictate that there be only a radial interaction force between the radial member and the ring segment in any sector.

In the general case where each sector or petal is at a different temperature, this interaction force will be different in each sector. There will be 32 such interaction forces.

Deformation Analysis - The analytical model of the reflector for the general case of non-uniform thermal environment leads to 32 unknown interaction forces. This is predicated on the provision of radial freedom of movement at the connections between petals and by ignoring the transverse shear redundants.

To simplify the analysis, it has been assumed that the interaction forces are equal in each sector. This is equivalent to using an average interaction force or what is the same thing, determining the interaction force from an average or mean temperature distribution. The value of the interaction force is determined from the average temperature by determining the radial displacement of the radial member and ring segment acting independently, and then finding the force required to make the relative radial displacement vanish.

A thin circular ring of radius R when subjected to a uniform temperature will experience a radial displacement Δ_R given by

$$\Delta_R = \alpha T_R R$$

where α = coefficient of thermal expansion

R = radius of ring

T_R = uniform temperature of ring.

For the ring with non-uniform temperature distribution, let T_{R_i} be the constant temperature in an elemental length Δs . Then the mean temperature is

$$T_R = \frac{\sum T_{R_i} \Delta s}{\sum \Delta s}$$

noting that

$$\sum \Delta s = 2\pi R$$

the average radial displacement becomes

$$\Delta_R = \alpha R \frac{\sum T_{Ri} \Delta S}{2 \pi R}$$

$$\Delta_R = \frac{\alpha \Delta S}{2 \pi} \sum T_{Ri} \quad (1)$$

A similar expression can be derived for the average radial displacement of the radial members. This is

$$\Delta_D' = \frac{\alpha \Delta S}{2 \pi} \sum T_{Di} \quad (2a)$$

where T_{Di} is the constant temperature in the i-th member.

In addition to different temperatures on the radial members, consider a temperature gradient T'_{Di} over the depth of the i-th radial member. This is given by

$$T'_{Di} = \frac{\Delta T_i}{d}$$

where ΔT_i = difference in temperature between the top and bottom of the i-th radial member.

d = depth of radial member.

Due to the temperature gradient T'_{Di} , a curved bar as shown in Figure 3.6-14 will experience a radial movement given approximately by

$$\Delta = \alpha T'_{Di} R \frac{h}{2}$$

Proceeding as before, the average radial displacement due to the gradient is

$$\Delta_D'' = \frac{\alpha \Delta S}{2 \pi} \sum \left(T'_{Di} \frac{h}{2} \right) \quad (2b)$$

The total radial displacement of the radial members is obtained by adding 2a, 2b and is

$$\Delta_D = \frac{\alpha \Delta S}{2\pi} \sum \left(T_{Di} + T'_{Di} \frac{h}{2} \right) \quad (2)$$

The unknown interaction force is obtained from the displacement compatibility condition which is:

$$\Delta_D + X \delta_{11} = \Delta_R - \frac{X R^2}{AE \Delta S} \quad (3)$$

where X = average interaction force

δ_{11} = radial deformation of end of radial member due to a unit radial load (see Figure 3.6-15)

A = cross sectional area of ring

E = modulus of elasticity of ring material

$\frac{X R^2}{AE \Delta S}$ = radial deformation of ring due to the interaction force

$$X = \frac{\frac{\alpha \Delta S}{2\pi} \sum \left(T_{Ri} - T_{Di} - T'_{Di} \frac{h}{2} \right)}{\delta_{11} + \frac{R^2}{AE \Delta S}} \quad (4)$$

Using the average interaction force X , the expressions for vertical and horizontal displacements of the tip of any radial member are:

$$\Delta_{Vi} = X \delta_{12} + \alpha T_{Ri} h + \alpha T'_{Di} \frac{R^2}{2} \quad (5)$$

$$\Delta_{Hi} = X \delta_{11} + \alpha T_{Ri} R + \alpha T'_{Di} R \frac{h}{2} \quad (6)$$

Noting that the middle term in each of these expressions is due to the steady state temperatures causing no out of plane deformations, we can eliminate them to obtain the final expressions:

$$\Delta_{Vi} = X \delta_{12} + \alpha T'_{Di} \frac{R^2}{2} \quad (7)$$

$$\Delta_{Hi} = X \delta_{11} + \alpha T'_{Di} R \frac{h}{2} \quad (8)$$

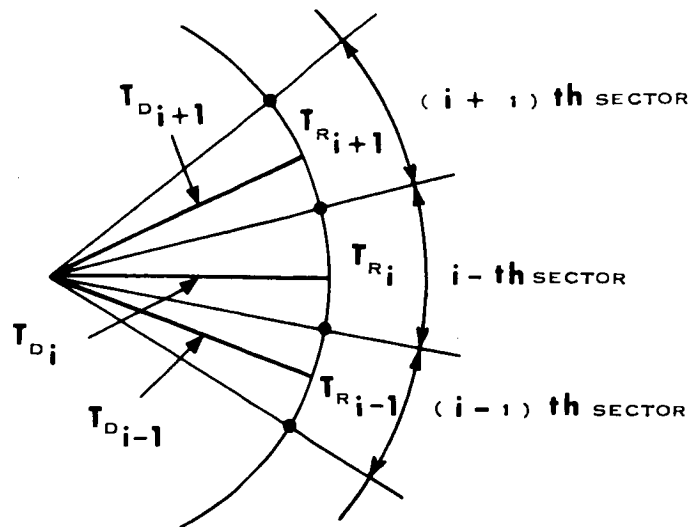


Figure 3.6-13 Petal Thermal Model

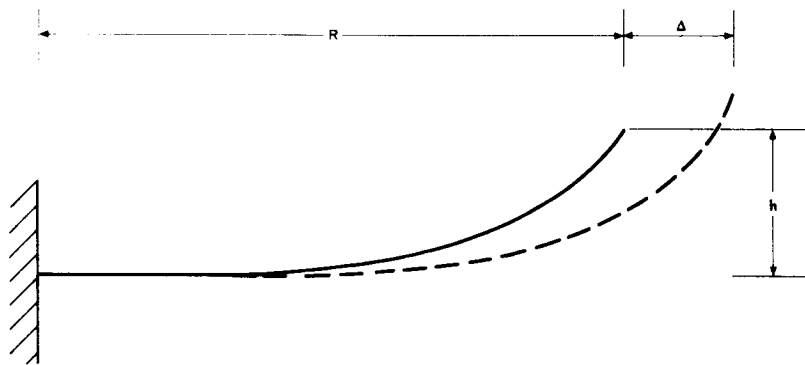


Figure 3.6-14 Radial Displacement Geometry

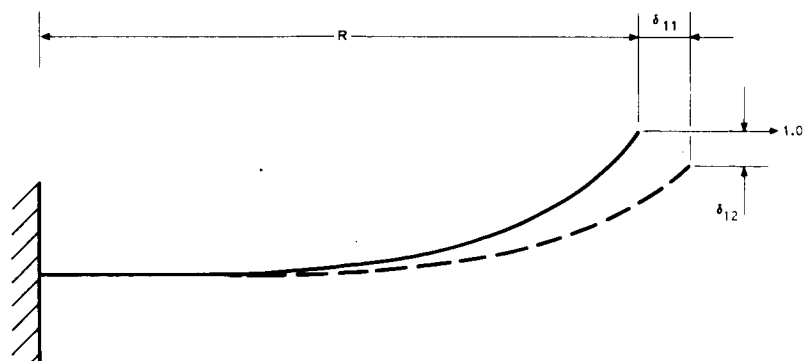


Figure 3.6-15 Deformation of Radial Member

Once the vertical and horizontal components of the displacement of a point are known, the out of plane deviation can be obtained by locating the displaced point (vectorial sum of Eqs. 7, 8) and taking the component of deformation normal to the original surface.

Results of Deformation Analysis - A mean orbital temperature map for the reflector has been included in the thermal study (Figure 3.6-9). While the mean orbital thermal map indicates no temperature difference between the radial and ring members of any sector, the thermal study includes estimates of possible temperature differences for instantaneous conditions. Similarly estimates of gradients along the depth of the members are included in the thermal study (Section 3.6.3).

Based on the results of the thermal study, the analytic approach developed in the previous sections has been used to compute deformations of the reflector. The various cases analyzed are described below and the results summarized in Table 3.6-3.

- CASE A - This is the so-called "design case" with the difference between radial and ring members (ΔT) being of the order of 10°F . The gradient along the depth of the radial members ($\Delta T'$) has been taken as 0.05°F . The magnitudes of ΔT and $\Delta T'$ given are mean orbital values occurring only in one petal (or sector); the corresponding temperature differentials and gradients in the other petals will be less. It has been assumed that ΔT and $\Delta T'$ are constant for all petals, the magnitude being the given values.
- CASE B - For this case the temperature differential between the radial member and ring segment has been taken to be 10.0°F , as in Case A. The value of the gradient, $\Delta T'$ has been taken as 0.25°F . Both values have been assumed to exist in all petals. This case represents a situation where leakage

TABLE 3.6-3 REFLECTOR THERMAL DEFORMATIONS

Case	ΔT	$\Delta T'$	δ_n
A	10° F	0.05° F	0.0736 in.
B	10° F	0.25° F	0.1584 in.
C	20° F	0.05° F	0.1261 in.

ΔT = temperature difference between radial members and ring segments.

$\Delta T'$ = temperature difference along depth of radial members

δ_n = maximum normal (out of plane) deformation at tip of radial member.

Data Used for Numerical Computation

Material - Aluminum Alloy, $\alpha = 13(10)^{-6}$, $E = 10(10)^6$

$R = 180 \text{ in.}$ $h = 69.23 \text{ in.}$

$A = 0.154 \text{ in.}^2$ $d = 1.0 \text{ in.}$

$\delta_{11} = 1.20 \text{ in.}$ $\delta_{12} = 2.23 \text{ in.}$

between connections occurs.

- o CASE C - The values used are $\Delta T = 20^{\circ}\text{F}$ and $\Delta T' = 0.05^{\circ}\text{F}$, both being assumed constant for all petals. The temperature difference of 20°F between the radial member and the ring represents the "worst case" instantaneous value in one petal. The assumption of the same temperature difference in all petals is of course highly conservative.

From the results of the thermal deformation analysis, it is seen that the maximum deformations in all three cases considered are less than the maximum permissible. To compensate for the simplifying assumptions employed in the analysis, conservatism has been introduced into the thermal conditions used. Thus, it is felt that the results are realistically accurate. It should also be noted that the deflections listed exist only at the tip and will be considerably less at other points.

Failure Mode Deformation Analysis - One of the basic assumptions employed in the analysis of the reflector deformations is the one concerning the locking mechanism between ring segments being able to provide freedom of radial growth. If radial freedom is not realized the thermal deformation analysis conducted is no longer valid. The deformation integrity requirements of the reflector cannot be achieved in the proposed system unless the locking mechanism is designed to provide freedom of radial growth.

From the mean orbital temperature map (Figure 3.6-9) it is seen that the maximum temperature difference between two petals is 23°F . The distortion caused by a sticky lock is analogous to the deflection of a curved member clamped at both ends and subjected to a temperature increase of 11.5°F . Since the ends are restrained, the curvature of this member will tend to increase causing out of plane deformations. For this condition, the maximum deformation has been computed to be 0.141 inches and occurs

at the center of the radial member.

Reflector Surface Deformations - A reflector surface formed by a grid work or mesh of inter-connected uninsulated aluminum alloy wires is considered a candidate reflector design. The grid work follows the contour of the parabolic antenna. Preliminary analysis of the grid was mainly directed towards consideration of the thermal deformations experienced by the grid in an orbital environment.

The deformations of the mesh are a function of the boundary conditions e. g., the manner in which the grid is attached to the reflector sub-structure. The gridwork is itself composed of smaller panels, a typical wire of which may be considered as wire AB, as illustrated in Figure 3.6-16.

Let us consider the situation where the ends of the gridwork panel (of which wire AB is just one element) are rigidly attached to the supporting framework. Then wire AB, which has a parabolic contour, is completely restrained at the ends. Under such conditions and assuming no change in the basic structure, when the wire experiences a steady state temperature change, its parabolic shape will not be retained. If the temperature drops, the radius of curvature will increase whereas with a temperature increase, the radius of curvature will decrease.

For the case of steady state temperature drop, the decrease in length and increase in radius of curvature corresponds to the parabolic contour flattening out. This flattening out will obviously be stress free - up to the point where the wire assumes the chord position between points A and B. For the particular dimensions under consideration, a decrease in length of 0.045 inch will cause the wire to assume the chord position, as shown in Figure 3.6-17. A decrease in length of 0.045 inch corresponds to a steady state temperature drop of 80°F . When the elemental wire under consideration assumes a chord position, the maximum normal deviation from the original contour is of the order of 0.71 inch.

The above analysis also leads to a solution to the problem. If it is assumed that the ends of wire AB are not restrained, the wire will be free to change length, maintaining its original contour and thus cause no normal deviations. The proposed method of alleviating the thermal deformations of the reflector surface gridwork consists of allowing the segments of the mesh to move freely at its attachment points. This freedom of movement will permit the mesh to retain its parabolic shape under temperature changes.

Thermal Stresses - Thermal stresses are significant in structures where thermal expansion or contraction is restrained or where large gradients are present. The reflector as well as the reflecting surface (wire grid work) in the present case does not fall into the above category. Nevertheless, approximate stress levels computed for the reflector are presented below. There are no thermal stresses in the wire grid reflecting surface since the grid is provided with attachments (to reflector sub structure) which allow complete freedom of expansion and contraction.

The thermal stresses in the reflector can be computed by noting that coupling the ring segment from the radial member causes an interaction force in the radial direction. This radial interaction force causes maximum moment at the clamped end of the radial member, from which the flexural stress can be readily computed. Table 3.6-4 summarizes the thermal stresses in the radial members for the three cases for which thermal deformations were computed (Table 3.6-3)

TABLE 3.6-4 REFLECTOR THERMAL STRESSES

Case	ΔT	$\Delta T'$	Interaction Force X (lbs)	Maximum Thermal Stress
A	5° F	0.05° F	0.01313	35 psi
B	5° F	0.25° F	0.02663	55 psi
C	20° F	0.05° F	0.04238	60 psi

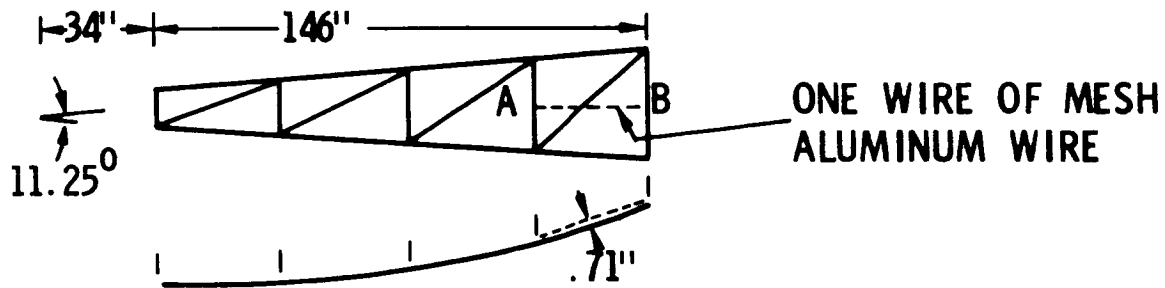


Figure 3.6-16 Reflector Surface Mesh Geometry

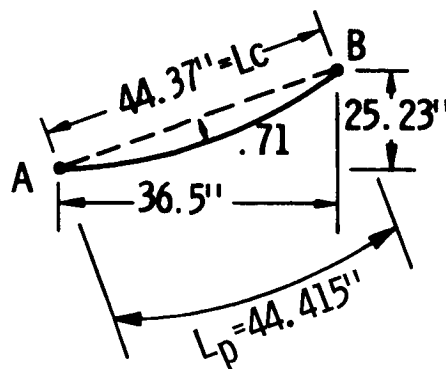


Figure 3.6-17 Surface Mesh Chord Position

3.6.5 Feed Mast Thermal Analysis

During any orbit the fluxes to the feed mast vary over a wide range, causing variations in the feed mast temperature. These temperature variations lead to errors in the feed position relative to the antenna, resulting in a loss of antenna efficiency. Furthermore, the temperature gradients occurring across the members cause distortions in the feed position. These temperatures and gradients must be analyzed in order to determine the magnitude of error in the feed position.

The antenna and spacecraft are yaw controlled, thereby, enabling the feed mast to be so placed in relation to the orbital plane that little self-shadowing occurs. Figure 3.6-18 shows the feed mast position in relation to the orbital plane. The sun vector moves through an angle of $\pm 23.5^\circ$ to the orbital plane during each year, however, with the present design it would have to move 60° out of plane to totally shadow one of the feed mast supports.

A relatively simple thermal analysis was initially conducted for the feed mast considering only one member. It was assumed in this analysis that the shadowing from the feed and antenna would not drastically affect the temperature history of the members, and further, that the shadowing would not cause large temperature differences between the members. The temperature gradients along the members were ignored since they do not affect member deflections. Insulated and uninsulated members were analyzed using a twelve-sided thermal model to simulate the cylindrical members. The electrical network analogies for these two cases are shown in Figure 3.6-19 and 3.6-20. The solar, reflected solar and earth radiation inputs were determined by computer program for every 10° of orbit with the solar vector parallel to the orbit plane.

In the uninsulated case the heat inputs are directed into each node around the member while the insulated case is simulated by assuming the

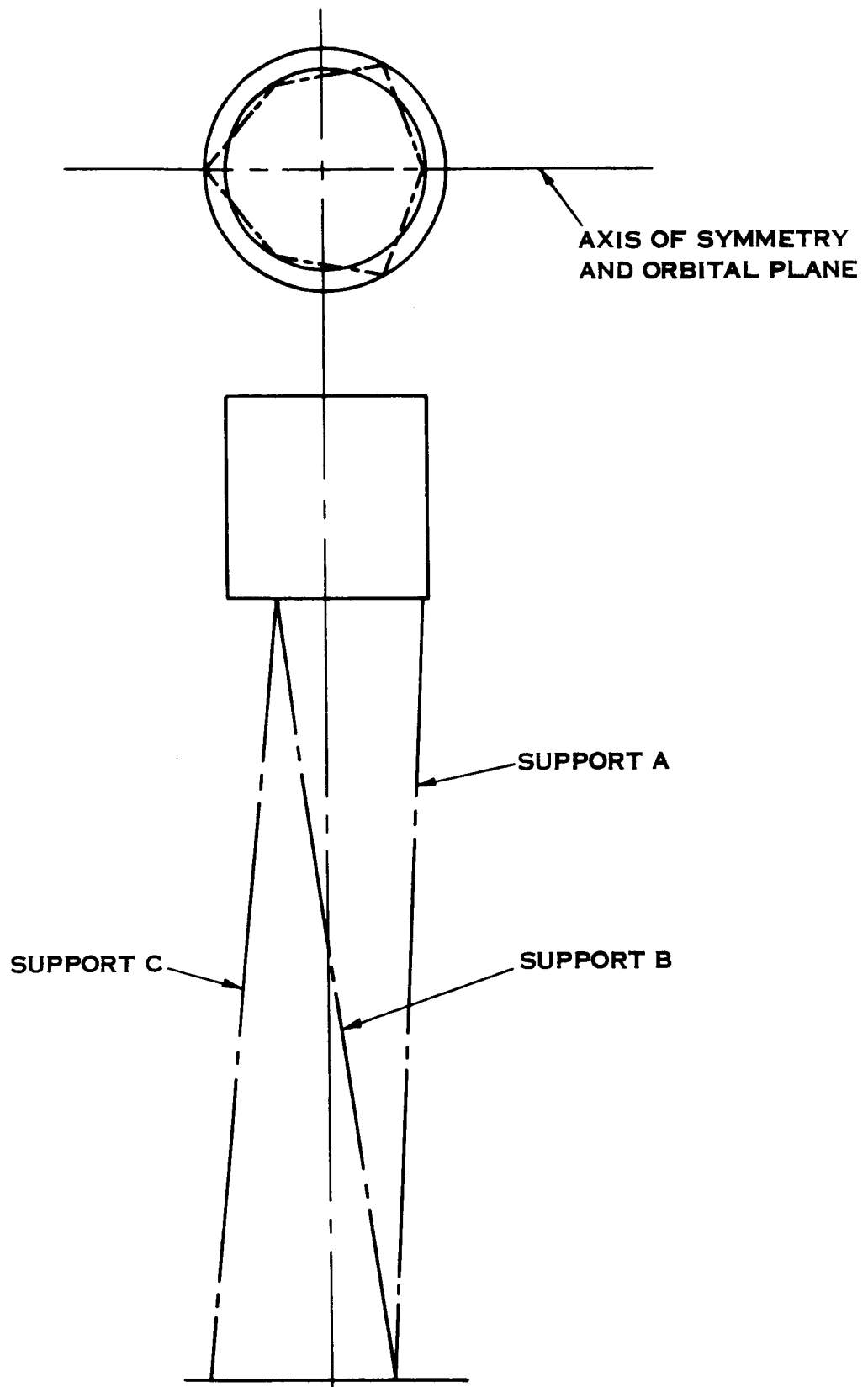
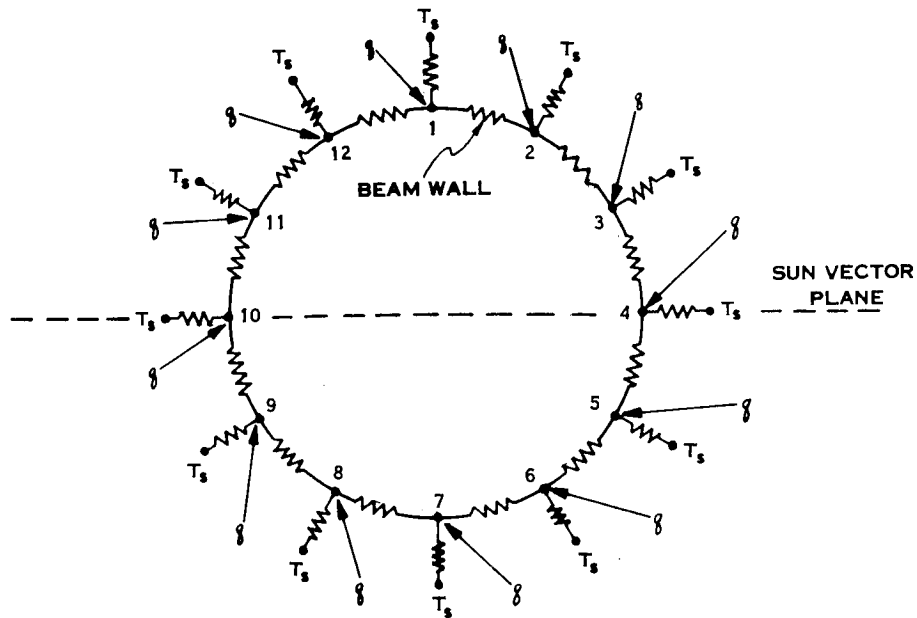
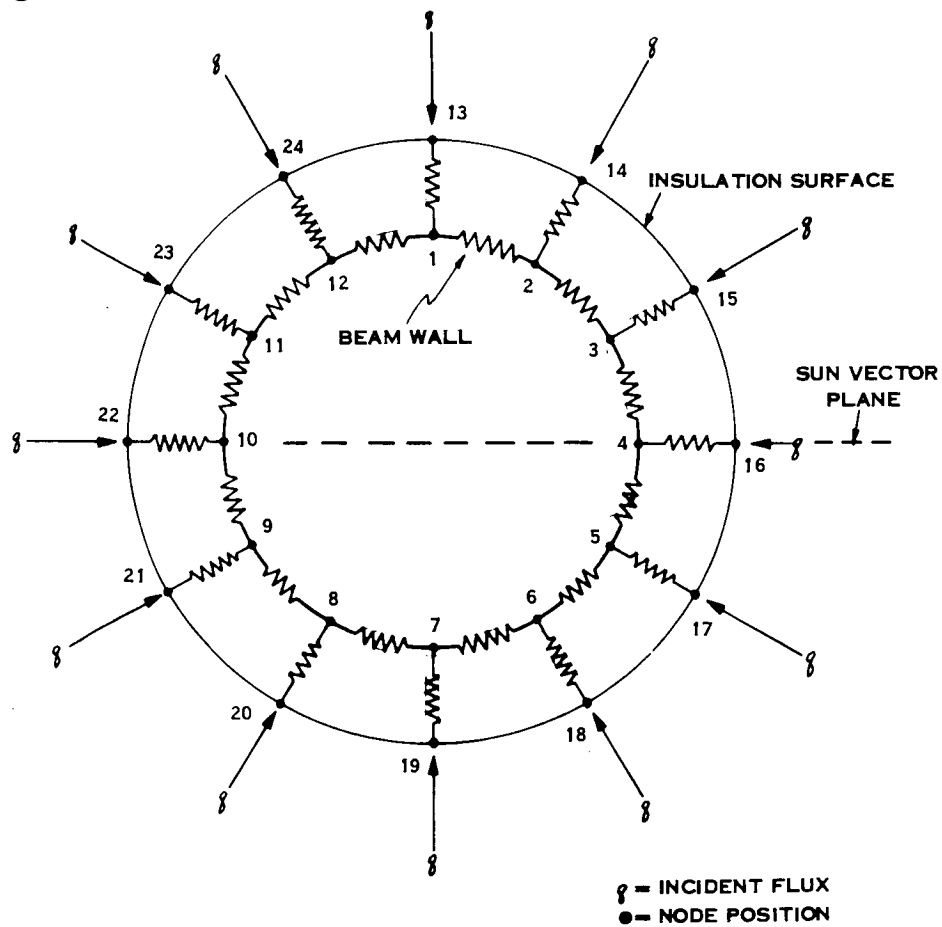


Figure 3.6-18 Feed Mast Geometry



T_s = SPACE SINK TEMPERATURE
 wavy arrow = INCIDENT FLUX
 \bullet = NODE POSITION

Figure 3.6-19 Electrical Simulation, Uninsulated Mast



wavy arrow = INCIDENT FLUX
 \bullet = NODE POSITION

Figure 3.6-20 Electrical Simulation, Insulated Mast

insulated surface to be at the sink temperature determined by the heat inputs.

$$\epsilon \sigma T_s^4 = \alpha (S + A) = \epsilon E$$

With this sink temperature the radiation interchange between the insulation and support is determined by

$$q = F_{\epsilon} F_A A \sigma (T_s^4 - T_1^4)$$

where

T_s = insulation surface temperature

T_1 = feed mast support temperature

The radiation outputs from the computer program for every 10^0 anomaly was used in the transient thermal analysis of the insulated and uninsulated case. This output was used to determine the temperature for both cases for every 10^0 anomaly. Figures 3.6-21 and 3.6-22 show a plot of the temperature variation for node 4, which together with node 10 has the largest excursions from the mean.

These results are questionable because of the simplifying assumption made on shadowing. In order to check these initial calculations a transient thermal analysis of an uninsulated feed mast was initiated with antenna and spacecraft shadowing considered. Descriptive geometry methods similar to those in the petal analysis were used to determine this shadowing. Figure 3.6-23 shows an example of the shadowing on support A due to the spacecraft. Similar curves were plotted for the antenna shadowing. The shadowing analysis was used in a computer program to find beam temperatures and temperature gradients. In the thermal model used for the computer analysis, the members were assumed to be thermally attached to each other, but isolated from the antenna and spacecraft. Figure 3.6-24 shows part of the thermal model used in the computer analysis given in terms of its electrical analogy.

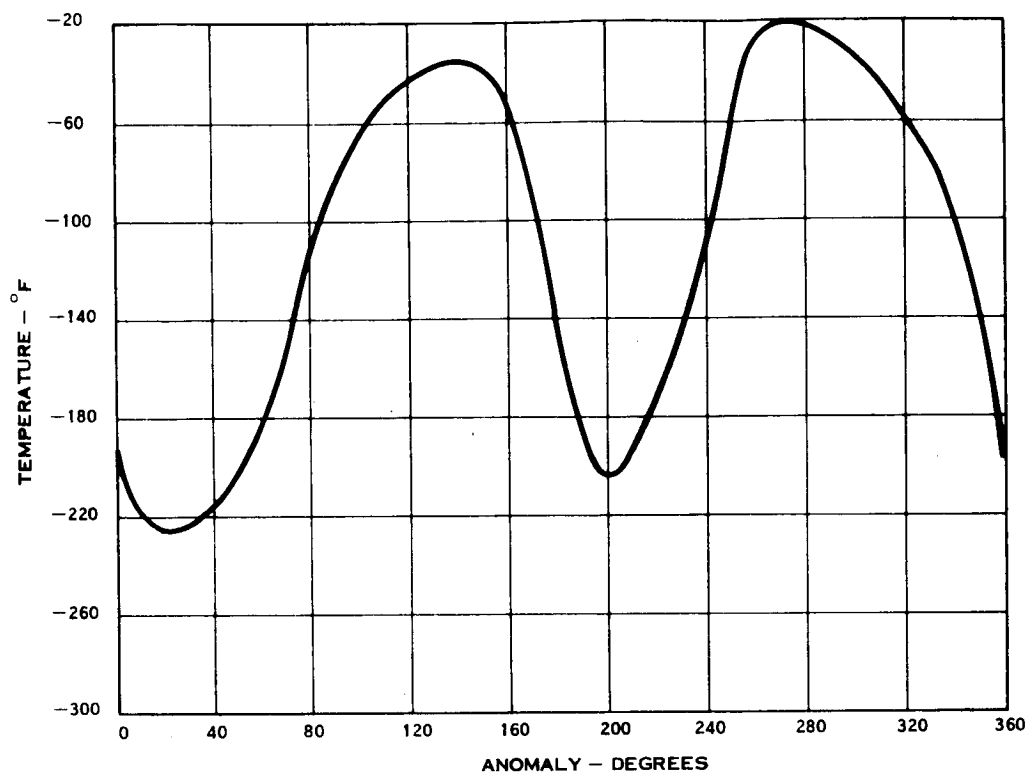


Figure 3.6-21 Temperature of Node 4 Uninsulated Support Member

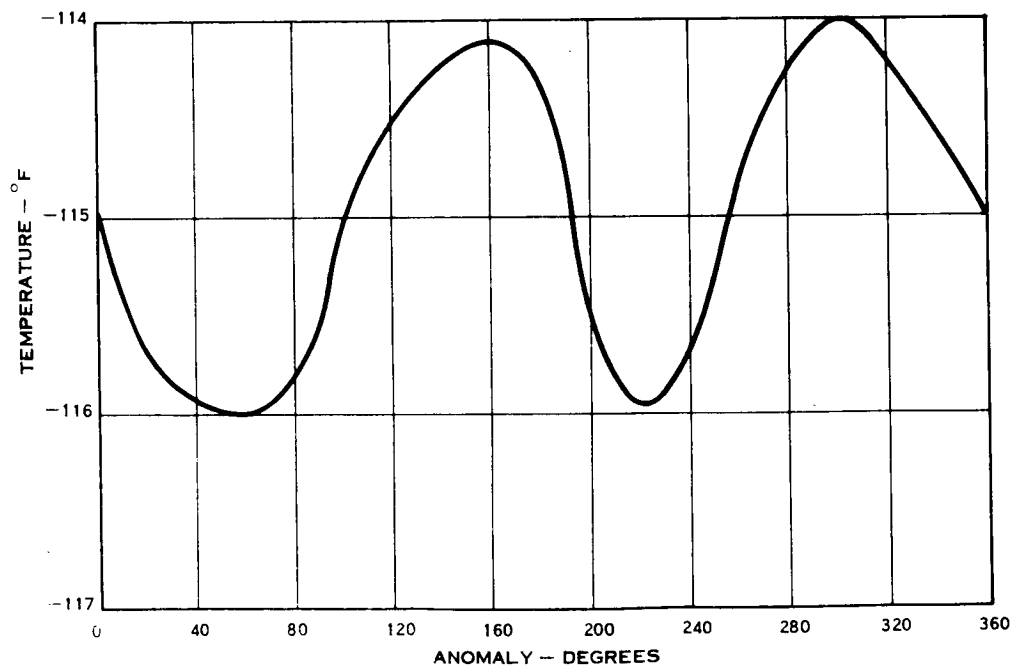


Figure 3.6-22 Temperature of Node 4 Insulated Support Member

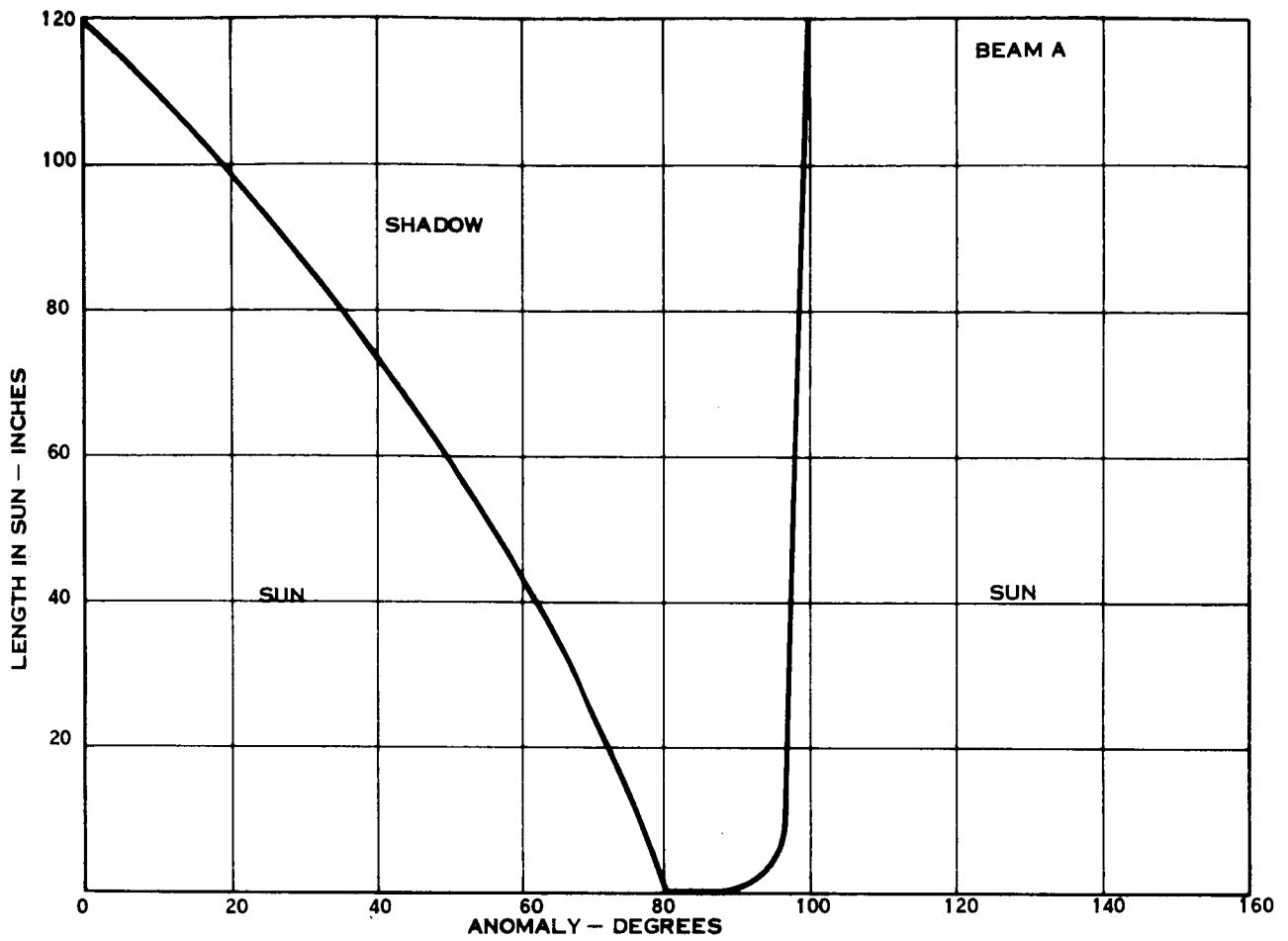
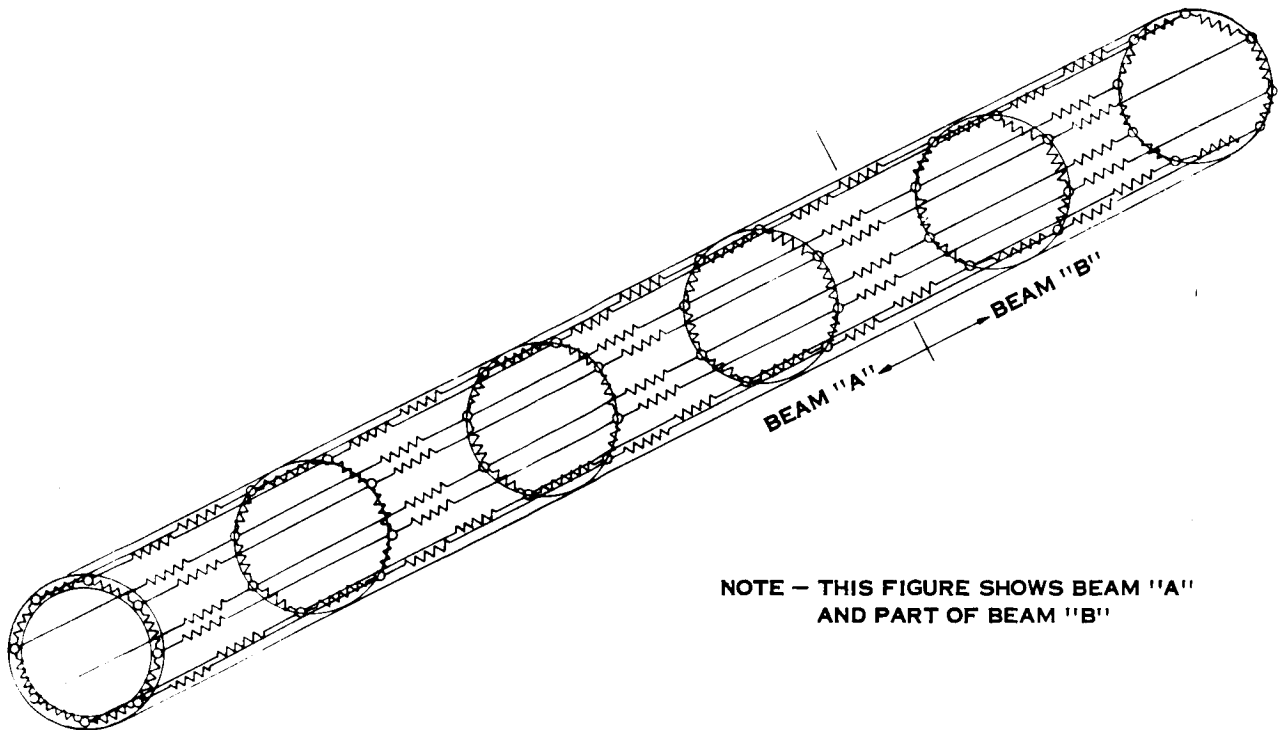


Figure 3.6-23 Feed Mast Shadowing on Support "A"



NOTE - THIS FIGURE SHOWS BEAM "A"
AND PART OF BEAM "B"

Figure 3.6-24 Feed Mast Thermal Model

In running this program on the 7090 it was found that the time steps necessary were extremely small and would require many hours of computer time to obtain temperatures for one orbit. Consequently, it was concluded, that this refined analysis was beyond the scope of this study. This decision can be justified, since the preliminary analysis proved that the use of superinsulation damps out temperature variations, due to spacecraft shadowing, to tolerable limits.

3.6.6 Thermal Deformation of Feed Mast

An approximate thermal deformation analysis of the feed mast structure is presented herein. The object of this investigation was to define the deviations of the reflector focal point due to the orbital thermal environment.

Method of Analysis - The tripod feed mast structure is composed of three triangular frames, each having two members and forming a truncated conical structure. The members of the feed mast structure are provided with pin connections. Consequently, each triangular frame of the structure will act independently.

Under a situation where all members have a similar uniform temperature distribution along their lengths, the framed feed mast structure will undergo only vertical deformations. The same situation will occur due to any gradients that may be present across the members. Such a situation will exist when the spacecraft feed mast shadowing is neglected.

For the case described above, the vertical deformation δ_v is given by (Figure 3.6-25)

$$\delta_v = \alpha \bar{T} L + \frac{\alpha \Delta T h}{2d} \left(1 - \frac{h^2}{L^2} \right)$$

where

α = coefficient of thermal expansion

\bar{T} = steady state temperature

ΔT = temperature gradient along depth of member

The first term in the above expression represents the vertical deformation due to a steady state temperature change while the second term represents the vertical deformation due to the gradient.

Results of Analysis - Using the above-described approach, vertical deflections of the feed mast, both for the insulated and uninsulated case are presented in Table 3.6-5. The components of deflection due to different situations have been determined on an individual basis.

The first component of deflection computed, that due to the mean orbital temperature (MOT) is seen to be quite large. However, if the feed is made adjustable and defocused to the MOT position prior to launch, the focal point deviations will be significantly reduced.

The sun vector orientation causing the maximum excursions from the MOT produces a gradient the effect of which is not in phase with the effect of the excursions from the MOT. Thus, when the maximum positive deflection due to MOT excursion occurs, the deflection due to the gradient has its maximum negative value. On the other hand, when the maximum negative deflection due to MOT excursion occurs, the deflection due to the gradient approaches zero. Consequently, the maximum deflection of the feed mast (or the maximum on-axis deflection of the focal point from its MOT position) will be the same as the deflection due to the maximum excursion from the MOT.

The last row in the Table 3.6-5 gives the maximum on-axis deviation from the MOT (or defocused) position.

The analysis used in this study is predicated on the assumption that all members of the structure have a similar temperature distribution. As stated earlier, this situation ignores the spacecraft shadowing effect in the determination of the thermal response. A consequence of this assumption is that the individual frames deflect only vertically since the members are pin connected.

TABLE 3.6-5 FEED MAST DEFLECTIONS

CASE	Deflection, δ_v (inches)	
	Insulated	Uninsulated
Mean orbital temperature (no ΔT)	-0.1719	-0.1839
Maximum excursions from MOT (no ΔT)	± 0.0015	± 0.1540
Maximum gradient effect (no T)	0	-0.0988
Maximum deviation from MOT position	± 0.0015	$\begin{bmatrix} -0.1540 \\ +0.0552 \end{bmatrix}$

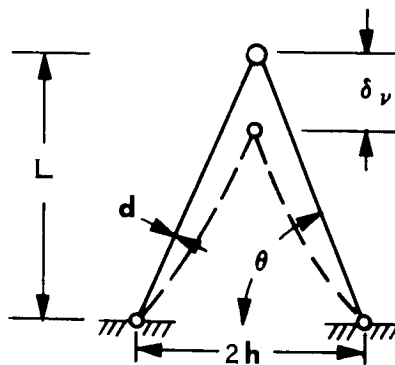


Figure 3.6-25 Feed Mast Distortions

The reasons for neglecting the shadowing effect are discussed in Section 3.6.5. In the absence of a detailed thermal analysis incorporating the shadowing effects, an off-axis deviation of the feed mast of 0.10 in. and an on-axis deviation of 0.15 in. have been assigned for the antenna performance calculations.

It is felt that these distortions represent conservative values and can in all probability be met by an uninsulated feed mast. In the event the detailed thermal analysis significantly exceeds these values, the use of superinsulation will bring the feed mast excursions within the specified limits.

3.6.7 Spacecraft Thermal Control

Temperature control of the spacecraft is necessary to insure the proper operation of the electronic components within the spacecraft enclosure. There are two basic systems which may be used for the thermal control, passive or active. The passive system uses an area exposed to space which radiates the choice of a passive control area leading to acceptable maximum and minimum temperatures. If, as will occur in many instances, the difference in maximum and minimum dissipation is large, the resulting temperature variation also is large. This temperature variation, places a limit on the application of passive control systems. An active thermal control system may use heaters, variable area radiating surfaces, etc. and may control the temperature to within tolerances much smaller than passive controls.

The minimum temperature requirement for the spacecraft is generally determined by the batteries which cannot operate at temperatures below about 32°F. The maximum temperature is dependent upon components, circuits, and detailed packaging studies. A special requirement exists for the ferrite phase shifters used in the phased array; they must be controlled to $\pm 20^\circ\text{F}$ or better.

Figure 3.6-26 was derived for a passive control system approach, based on a steady-state condition of dissipation. The curves are derived

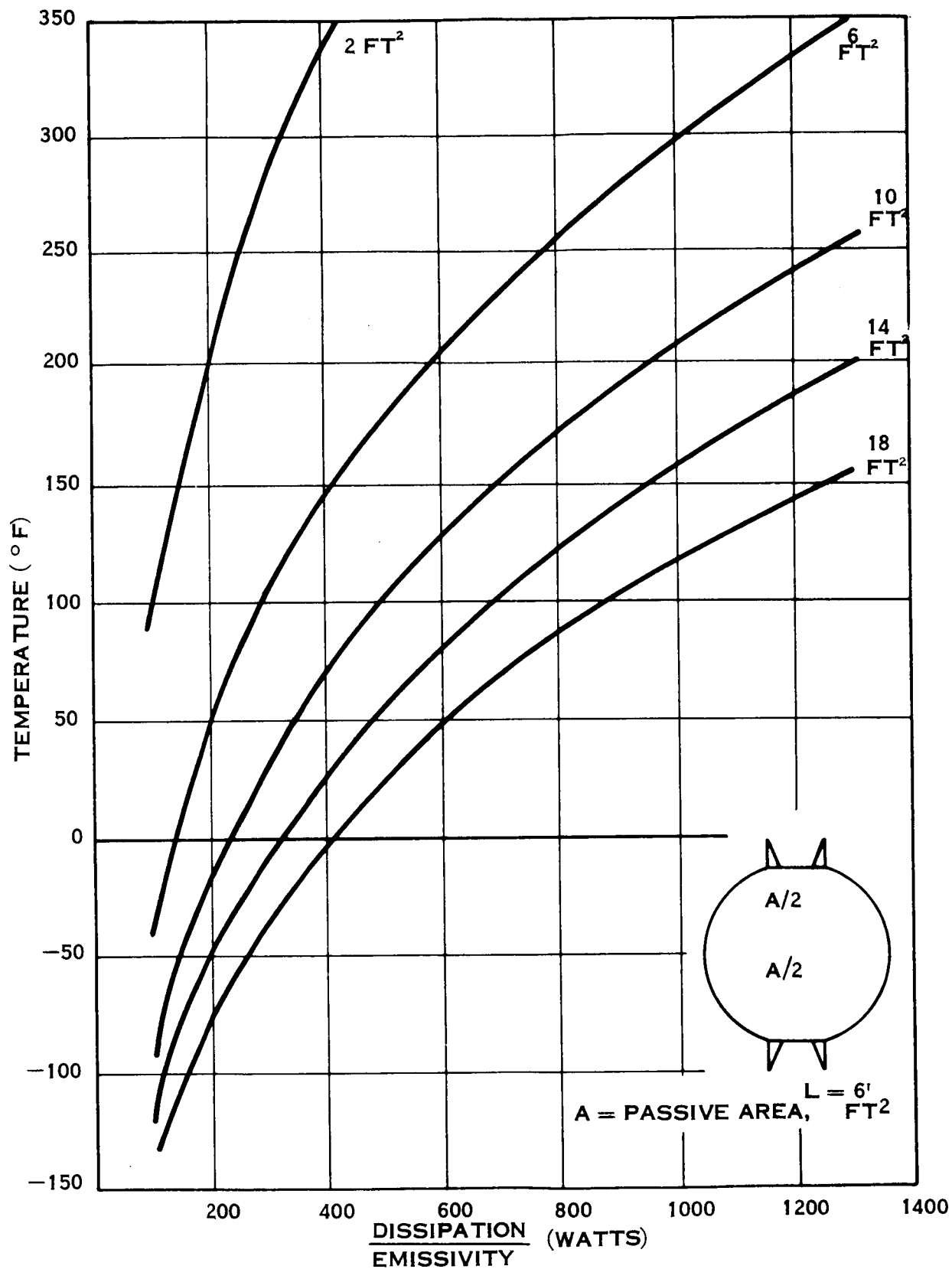


Figure 3.6-26 Passive Control Areas
 Average Temperature vs Dissipation

from the steady-state radiation equation written in the form

$$A_r T^4 = q/\epsilon$$

where

q	= the electrical dissipation
T	= the passive control surface temperature
A_r	= passive control area, assumed the spacecraft to be superinsulated with no losses through the insulation.

If the minimum dissipation for the spacecraft is 175 watts, the emissivity 0.9 and the minimum temperature 35°F, Figure 3.6-25 gives a passive control area of 6.45 square feet. The same area may then be used to calculate the temperature for a maximum dissipation of, for instance, 310 watts, and results in a temperature of 111°F. This spacecraft temperature variation exceeds the ferrite phase shifter requirement by 36°F. The maximum dissipation which will permit the ferrite phase shifters to vary less than 40°F can be determined. Using the above area of 6.45 square feet this maximum allowable dissipation is calculated to be 238.7 watts.

The above calculations are based on steady state conditions, i. e., dissipations of longer periods than the thermal time constants. The thermal time constant for the spacecraft is quite large - on the order of 200 hours. Unless the duty cycle is of this same order or larger the problem cannot be considered steady state and the above dissipation limitations are not valid. It is anticipated that the duty cycles will be much less than 200 hours, thus, resulting in smaller temperature excursions.

During the next phase of the program, concurrent with refinements of spacecraft packaging and dissipation, a more detailed analysis of the spacecraft thermal control system will be possible. It is safe to predict that the spacecraft thermal control system (unlike the reflector) offers no serious challenges that cannot be met by existing techniques.

3.7 DIMENSIONAL STABILITY

3.7.1 Introduction

This report covers a literature review of current information pertaining to the effect of residual stresses, thermal stresses and mechanical loading stresses on dimensional stability of metal structures in space. Words such as creep, micro-creep, dimensional instability, plastic movement, plastic flow, thermal flow, taking a set, relaxing, and similar verbage all relate to the plastic flow of the crystalline structure in its attempt to obtain the most relaxed alignment internally. It should be noted that dimensional changes can be on the order of microns and ranging up to fractions of a mil. This discussion does not cover the thermal expansion type of dimensional change since that kind of a change is compensated for in the original design and discussed elsewhere.

The term dimensional instability which shall be used throughout this report will be defined as "the change which occurs in metal over a period of time without assist from external loading." The general cause of these changes are metallurgical instability and residual stresses. Since advances in measuring techniques have been made and also since technological needs require more exacting dimensions the industry has not only tightened manufacturing tolerances but also "service tolerance".

Generally a material is selected for characteristics other than dimensional stability; such factors are tensile strength, density, ease of fabrication, or corrosion resistance. After satisfying these other characteristics the aspect of dimensional stability is usually evaluated. It must be realized that predictable changes such as elastic strain, thermal expansion, and thermal contractions will usually return the structure to the original state or position. Changes caused by loading which plastically deform a part are usually not recoverable. Engineering calculation will

normally predict the above kinds of change.

3.7.2 Precision Elastic Limit

Since the tensile or yield strength value is far too coarse a number for a designer to use in a space application where dimensional stability will be required for months or years the term PEL was developed. Precision Elastic Limit (PEL) is the stress at which the residual strain is one micro-inch per inch. Precision strain guages allow the designer or engineer to measure the micro strain that results at the PEL stress levels.

3.7.3 Residual Stress

Residual stress operating within metal can also be troublesome in structures such as the one proposed if they are ignored. Residual stresses that are encountered can come from two origins, mechanical and thermal. Residual stresses are relieved by plastic flow at sufficiently high temperatures. Therefore if the aluminum truss structure is welded it will be stress relieved at the proper temperature to allow residual stresses to redistribute forces thus causing a much lower residual stress entrapment within the weldment. It is felt that some residual stresses will always be present, however, it is also believed that the level will be tolerable. It should be pointed out that even though stress relieving temperatures are sufficiently high to be of benefit, the cool down must be carefully controlled to prevent cool-down stresses from being locked in the weldment. Non-heat treatable aluminum alloys can contain residual stresses, resulting from the mill fabrication practice of the aluminum producer.

For heat treatable aluminum alloys, in general, during quenching from the solution treatment temperature, the portions of a part which cool more rapidly retain compressive stresses, whereas the portions which are the last to attain room temperature contain balancing residual tensile stresses. Thus in a rapidly cooled part, the surface layers generally

contain compressive stresses and the core tensile stresses. This distribution of stresses is advantageous for the accommodation of external service loads (although they are not necessarily desirable from the dimensional stability aspect). This pattern of stresses may be further altered or rearranged by subsequent machining or cold working, resulting in warpage or loss of dimensions.

3.7.4 Design Application

In a space structure such as the proposed parabolic expandable structure the identification and evaluation of possible dimensional instability problems is not easily accomplished. Assuming that an aluminum alloy is selected for the frame and lattice construction it will be necessary to control such areas as the heat treatment, the mechanical working performed on the metal and possibly the temperature of the metal while it is being fabricated.

The combined effort of the metallurgists and fabrication specialists are required to obtain accurate, stress free structures. Proper stress relieving treatment should be used and stabilization techniques employed wherever possible. Regarding the micro-creep or dimensional stability problem from causes other than normal thermal expansion and the residual stress which will be present, it is felt that they will not present a problem. The data available regarding micro-creep is limited. However, tests conducted to date indicate that 7075 aluminum can change as much as 300μ inches/inch/year while 2024 aluminum will creep only 60μ inches/inch/year. It should be noted that as far as the reflector is concerned the length changes are of no significance if all the members grow the same amount. Since this is not necessarily the case, the unequal changes (which will cause out of plane distortion) should be considered further. Examination of some typical stability changes for 2024 aluminum for the reflector petals indicates that the member will change less than 0.009 inches per year (for a 150 inch petal). Assuming that adjacent members do not change, the amount of

distortion that will exist will be significantly less than that due to the thermal effects (see Section 3. 6. 4).

The temperature cycling effects on the petal dimensional stability can be ignored since the excursion from the mean orbital temperature (due to the superinsulation) will be less than 30°F for any one petal. Data available at this time indicates that thermal cycling over this range does not produce any dimensional changes.

Examination of the feed mast changes indicates no apparent problem due to ageing. Using 2024 Aluminum for a 100 inch feed mast will only result in a change in length of 0.006 inches. The temperature excursions of the feed mast may be more than 100°F during an orbit. This could cause significant ageing effects, but as there are no data available at this time regarding temperature cycling effects on material stability, it is impossible to predict the resultant changes.

It is probable that with a minimum weight design the precision elastic limit of the petal beam will be exceeded during the launch vibratory loads. The stresses due to these loads will be cyclic, of very short duration and flexural in nature. The data that exists presently regarding this type of stress and its effect, when the PEL is exceeded, is limited. Consequently, no clear cut evaluation is possible at this time regarding the amount of permanent distortion that can be expected. It is suggested that this area be further evaluated during subsequent phases of the program.

3.7.5

References for Dimensional Stability Discussion

1. F. C. Holden, "A Review of Dimensional Instability in Metals", DMIC Memorandum 189, March, 1964
2. R. E. Maringer, "Review of Dimensional Instability in Metals", DMIC Memorandum 213, June, 1966
3. W. M. Baldwin Jr., "Residual Stresses in Metals", Transactions, ASTM, 1949, pp 539-583
4. W. Soete and R. Vancrombrugge, "An Industrial Method for Determination of Residual Stresses" Proceedings, Society for Experimental Stress Analysis (1950) No. 1, pp 17-28
5. W. L. Fink and L. A. Willey, "Quenching of Aluminum Alloy", Transactions, AIME, 1948
6. L. McD Schetky, "Dimensional Stability in Precise Parts" Product Engineering, Sept 12, 1960
7. R. T. Myers, S. A. Kilpatrick and W. E. Backus, "Stress Relief of Aluminum Alloys for Aircraft", Metal Progress, March 1959

3.8 IN-ORBIT MEASUREMENT OF ANTENNA SURFACE ACCURACY

3.8.1 Basic Techniques

The basic technique for determination of antenna reflector deployment accuracy involves in-orbit matching of a laboratory standard negative against the image of the deployed antenna. The standard negative is prepared by photographing the accurately deployed antenna in the laboratory deployment test fixture. The antenna is photographed with the same camera which will be used for image matching in-orbit, mounted as it will be mounted in orbit. This standard negative is then accurately positioned in the image plane of the camera. In-orbit, when the shutter is opened, the antenna image is projected through the standard negative and onto a photographic film or other photosensitive surface. The resulting mismatch image is transmitted to the ground station for examination.

3.8.2 Operational Considerations

The above basic approach must be greatly modified to produce a practical operational system. Some of the factors which must be considered are:

- surface accuracy required
- manufacturing tolerances
- deployment tolerances
- resolution required for surface measurement
- mesh wire size
- marking of the reflector surface
- complete coverage versus partial coverage
- fixed coverage versus scanning coverage
- resolution of lens
- resolution of film

- resolution of vidicon
- space available
- clearances required
- location of equipment
- mounting of equipment
- use of film or direct imaging
- single versus multiple cameras
- single versus multiple vidicons
- electronic scanning versus mechanical scanning
- near and far focusing
- reflectors
- mirror shapes and positions
- sunlighting of antenna
- shadowing of antenna
- artificial lighting of antenna
- single versus multiple lights
- fixed versus scanning lights
- lighting power required
- memory circuitry required
- control circuitry required
- total power required
- thermal expansion
- bandwidth of communication channel
- bit rate of communications channel

The interrelations of these factors must be considered and experiments must be conducted to verify the theoretical conclusions.

3.8.3 Antenna Surface Errors

The surface error of the antenna will be in the form of surface displacements perpendicular to the surface. The technique described is intended primarily for detection and measurement of those displacements. The system will have a secondary capability of detecting and measuring lateral and skew displacements, but it is not optimized for them. Should a petal fail to fully deploy, that will be readily detectable. The analysis presented here, is therefore concerned primarily with resolution in the antenna's radial direction.

It is assumed that the antenna fabrication techniques will hold the reflector surface to a true paraboloid within at least 0.070 inch. The antenna, when deployed in-orbit, is desired to be true within 0.100 inch. Since the standard negative cannot be prepared from a true paraboloid but will be prepared from the actual antenna with its fabrication errors, the system must at least detect deployment errors of:

$$0.100 - 0.070 = 0.030 \text{ inch.}$$

3.8.4 Equipment Location

First, the possible locations in the antenna structure where this equipment could be positioned will be considered. There is sufficient space in the spacecraft module for a significant amount of electronic hardware. Any added equipment must not interfere with the main antenna's radiation, the interferometer, the phased array, the antenna feed, nor the stowed petals. Thus, the only large space available is within the feed mast structure, far enough from the feed so as to avoid interference with radiated energy. This is shown in Figure 3.8-1. In addition, small devices can be added elsewhere on the structure.

3.8.5 Conceptual Design

In addition to the proposed configuration, the axial four camera system, several other configurations are briefly discussed in this section. These indicate the growth and development of the concept as well as modification of the concept to suit the parameters of this spacecraft and antenna.

A rotating camera could be mounted in the available volume to scan the entire antenna surface, except for obscuration by the structural members. Since it is desirable to avoid rotating members, the entire antenna may be projected into a single image by the use of a conic-like mirror. The mirror configuration and position influences the image geometry. A mirror positioned as shown in Figure 3.8-2, with the mirror above the camera, produces the flattest (most perpendicular) view of the antenna surface. The mirror shape is not critical, as a specific geometry is not required.

However, a more tangential view is better for recording petal deformities which tend to be normal to the surface and thus perpendicular to tangential sighting lines. A configuration such as in Figure 3.8-3 provides a good tangential viewing. The configuration of Figure 3.8-3 has the disadvantage of imaging the antenna rim as a small central ring and the antenna's center ring as a large peripheral ring. Thus the mirror should be a concaved cone-like surface as shown in Figure 3.8-4. Antenna sections near the fixed center plate are then viewed more perpendicularly and the rim more tangentially. Since the greatest distortions are probably going to be perpendicular deflections at the rim, this viewing attitude is desirable.

An examination of the antenna shows that the viewing angles at various distances from the center range from 37° to 15° as shown in Figure 3.8-5. Thus, as in Figure 3.8-6, the near wires (0.010", 0.100" between centers) do not obscure more distant wires. At the antenna rim, where the view angle is 15° , the normal component of the wire separation = 0.026" and

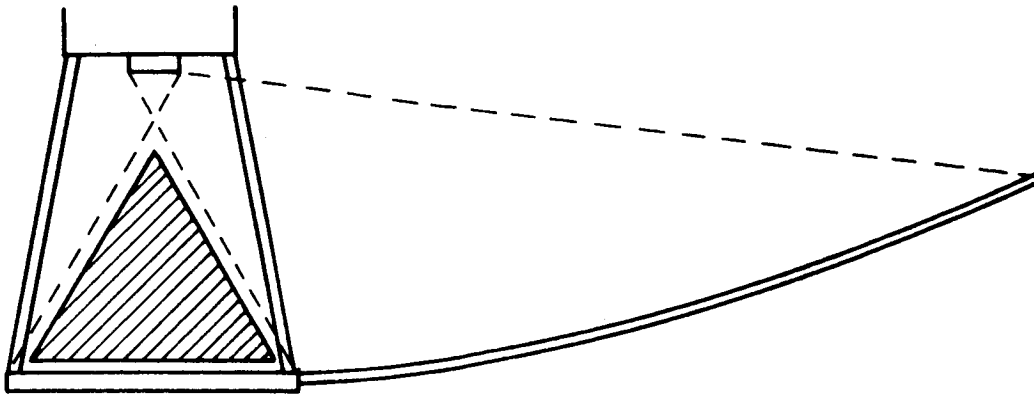


Figure 3.8-1 Volume Available for Measurement Equipment

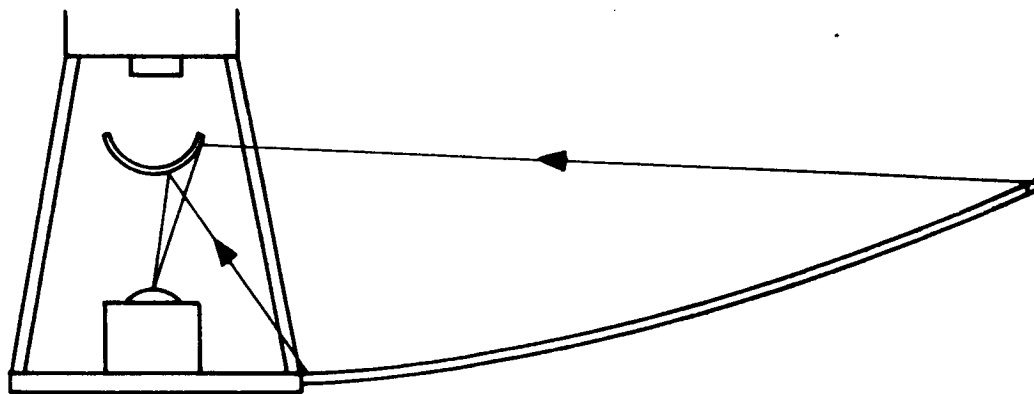


Figure 3.8-2 Mirror Position Above Camera

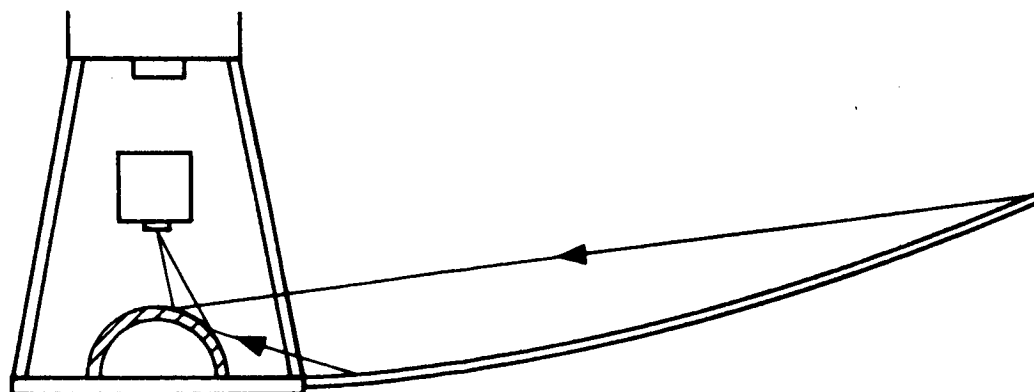


Figure 3.8-3 Convex Mirror Below Camera

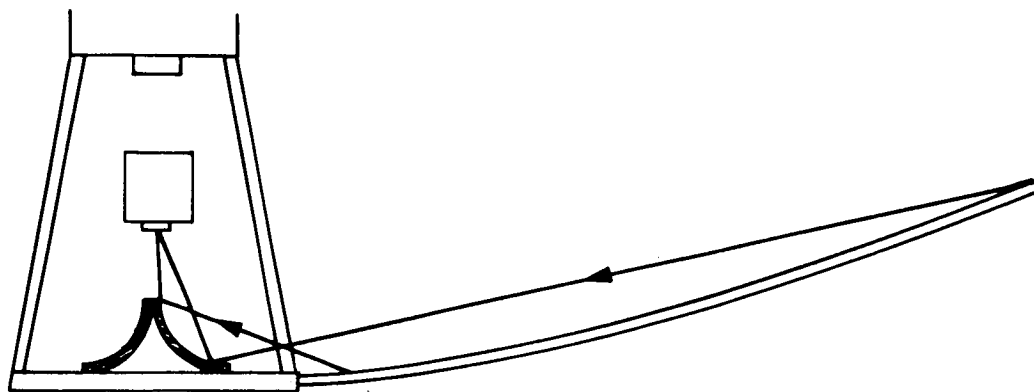


Figure 3.8-4 Concave Mirror Below Camera

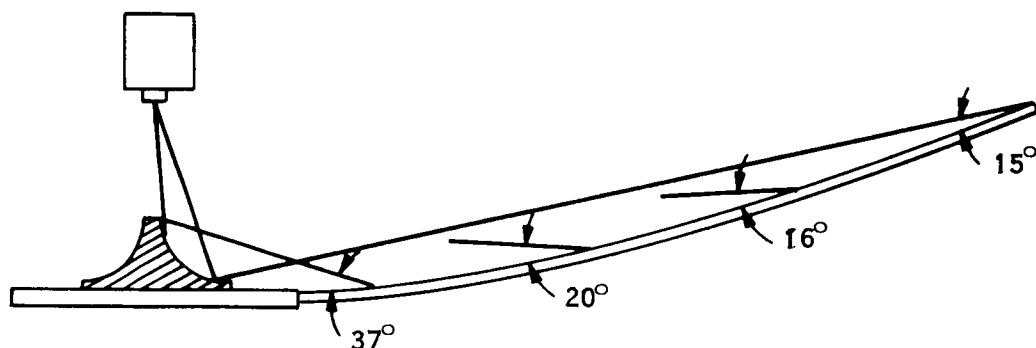


Figure 3.8-5 Sighting Angles

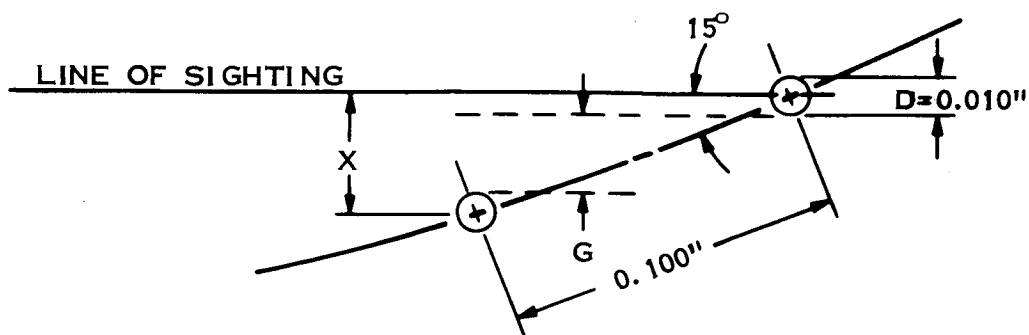


Figure 3.8-6 Effective Mesh Spacing

the normal component of the gap between wires is 0.016". In Figure 3.8-6, X is the normal component of the radial wire spacing (0.100 inch), G is the normal component of the gap between wires, and D is the wire diameter (0.010 inch).

$$\begin{aligned} X &= 0.100 \sin 15^\circ \\ &= 0.100 \cdot 0.26 \\ &= 0.026 \text{ inch} \\ G &= X - D \\ &= 0.026 - 0.010 \\ &= 0.016 \text{ inch} \end{aligned}$$

At the edge of the center section

$$\begin{aligned} X &= 0.100 \sin 37^\circ \\ &= 0.100 \cdot 0.60 \\ &= 0.060 \text{ inch} \\ G &= 0.060 - 0.010 = 0.050 \text{ inch} \end{aligned}$$

Halfway out

$$\begin{aligned} X &= 0.100 \sin 17^\circ \\ &= 0.100 \cdot 0.29 \\ &= 0.029 \text{ inch} \\ G &= 0.029 - 0.010 = 0.019 \end{aligned}$$

3.8.6 Error Resolution Requirements

As will be discussed later, the required error resolution is on the order of 0.024 inch. At this resolution, the individual wires of the mesh will not be resolved in the image. Thus, in order to determine deployment accuracy it will be necessary to increase the system resolution or to place larger markers on the antenna surface. To acceptably resolve the mesh wires of 0.010 inch would require a resolution element of less than 0.005 inch. For a perpendicular view of a 30-foot dish this dictates an image with more than a 72,000 line resolution.

$$\frac{12.30}{0.005} = 72,000$$

Since the antenna surface is viewed obliquely the effective spacing (component perpendicular to sight line) of the mesh wires (perpendicular to radii) is less than 0.100 inch. The calculation given previously shows that the "average" center-to-center effective spacing is 0.029 inch. Using this figure we can calculate the approximate image resolution required. Note that this average effective spacing is nearly the actual effective spacing over most of the antenna's area.

With petals 15 feet long, covered with a 0.100 inch mesh there are a total of 1800 cross wires.

$$\frac{15.12}{0.100} = 1800$$

With an effective spacing of 0.029 inch, the petal has an effective length of

$$0.029 \times 1800 = 52.2 \text{ inches}$$

The fixed center plate plus the length of two petals gives an effective diameter of

$$60 + 2 (52.2'') \approx 60 + 104 \\ \approx 164 \text{ inches}$$

Thus, an image with a resolution of 32,800 lines is needed

$$\frac{164}{0.005} = 32,800$$

For a 10-inch image this would be

$$\frac{32,800}{10 \times 25.4} = 129 \text{ lines/mm, which is not excessive for a lens}$$

system but does exceed the capability of high resolution vidicons (1000 lines). Hence, it is indicated that markers must be attached to the antenna surface. Only a relatively small number of markers can be added because of payload weight considerations. This also suggests a system which examines selected parts of the antenna rather than the entire antenna. The possibility

of telescopic high resolution examination of small selected areas of the antenna must be considered. It is not deemed advisable to incur the expense of having a higher resolution vidicon developed.

3.8.7 Sampling Surface Measurements

The cone-like mirror may be shaped as shown in Figure 3.8-7 to provide views of four ring sections of the antenna. Four ring sections are considered to give an adequate sampling of the surface deflection. This is, in effect, like having four different telephoto images in the same focal plane. Thus, we might use four separate telephoto cameras with their individual vidicons and standard negative masks. If they are positioned one above the other with separate conical mirrors the configuration will be as shown in Figure 3.8-8. Each camera includes a telephoto lens and receives light from the object reflected off of a straight edged cone; the cone provides no optic power to the camera. Each cone is a 45° cone. Each camera is focused for its own object distance. Each camera has high radial (antenna radius) resolution but low circumferential (antenna circumference) resolution. In order to provide an image of an entire incremental ring of the antenna surface it is necessary to accept low circumferential resolution. This is not much of a limitation as the surface deflections to be measured produce radial deviations. The cameras are looking up at the conical mirrors rather than down to provide an image which is not inside out.

The lower conical mirror may be more obtuse to provide an object ring nearer the center of the antenna. A fifth camera and mirror may be added to give a lower resolution view of the entire antenna. Such a camera would utilize a lens with a wide view angle and the mirror would be curved. See Figure 3.8-9. This is the selected configuration; the axial four camera system, and will be further discussed in Section 3.8.8.

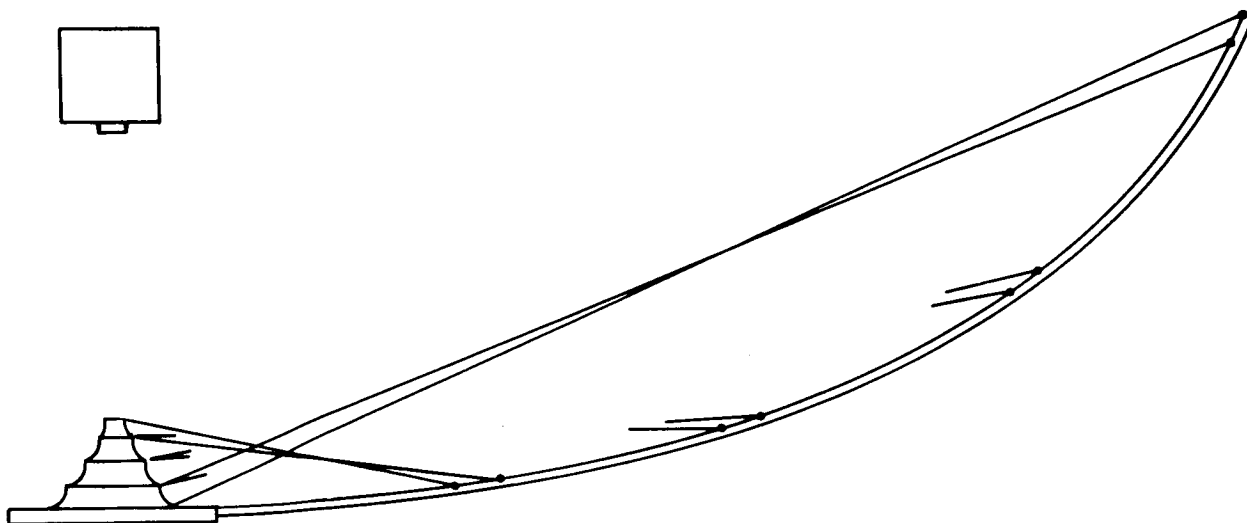


Figure 3.8-7 Composite Convex Mirror

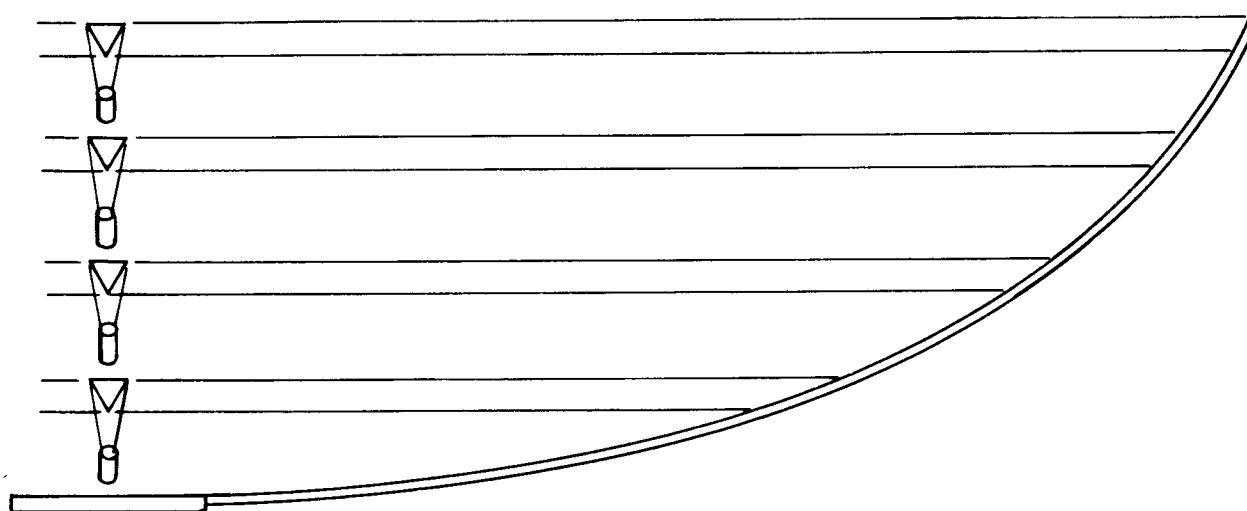


Figure 3.8-8 Basic Four-Camera Aerial System

3.8.8 The Axial Four Camera System

This basic concept is applicable to a system using any number of cameras, but since four give a good coverage of the antenna, that number will most likely be used. The available mounting space may further limit

the number of cameras. An additional whole antenna camera of lower resolution could be incorporated in a configuration as shown in Figure 3.8-9.

Radial Resolution Requirements - The radial resolution necessary to resolve the mesh wires has been discussed earlier in this report. The factors involved indicated the desirability of attaching marker plates to the antenna surface so that the system requirement becomes detection of the allowable surface deflection even though the wires cannot be resolved. The marker plates will be several times as wide as the mesh spacing.

As has been indicated in Paragraph 3.8.3, the system must be adequate to detect a deflection of 0.030 inch in the antenna surface. This 0.030 inch deflection is seen as a smaller displacement because of the viewing angle. See Figure 3.8-10 where d is the wire deflection, y is the normal displacement, and α is the viewing angle, and

$$y = d \cos \alpha$$

For the maximum allowable deflection

$$y = 0.030 \cos \alpha$$

The viewing angles at the four selected incremental rings of the antenna are 40° , 31° , 21° , and 23° as shown in Figure 3.8-11.

$$\begin{aligned} \text{At the rim of the antenna } \alpha = 40^\circ \text{ and } y &= 0.030 \cos 40^\circ \\ &= 0.030 \cdot 0.77 \\ &= 0.023 \text{ inch} \end{aligned}$$

At the next band $\alpha = 31^\circ$ and

$$\begin{aligned} y &= 0.030 \cos 31^\circ \\ &= 0.030 \cdot 0.86 \\ &= 0.026 \text{ inch} \end{aligned}$$

At the next band $\alpha = 21^\circ$ and

$$\begin{aligned} y &= 0.030 \cos 21^\circ \\ &= 0.030 \cdot 0.93 \\ &= 0.028 \text{ inch} \end{aligned}$$

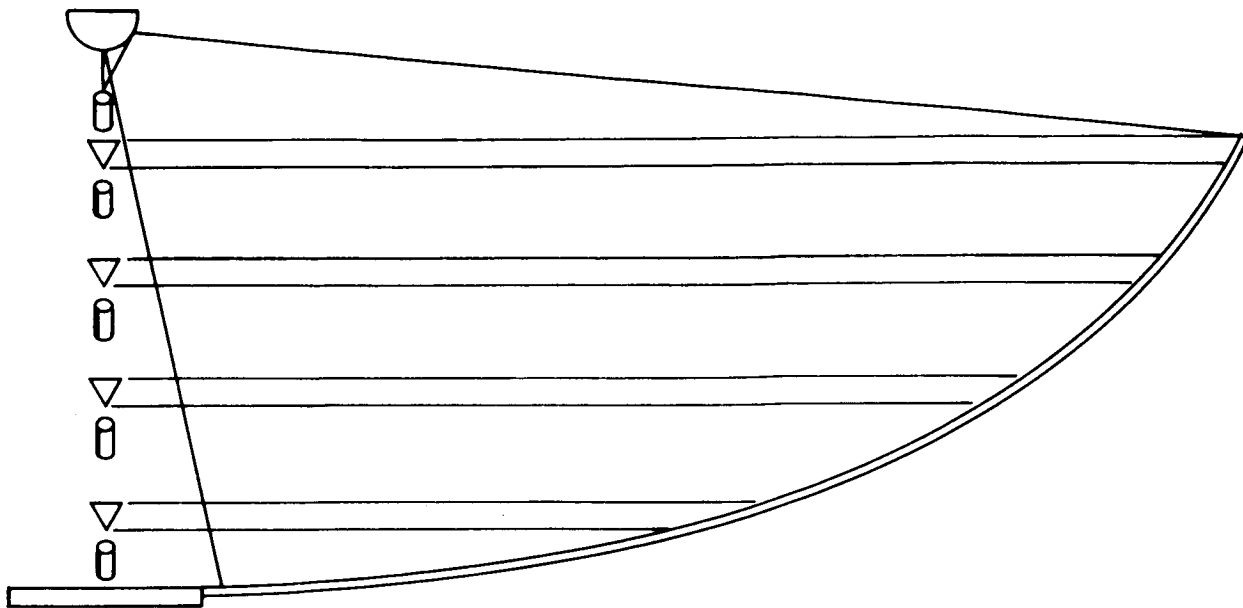


Figure 3.8-9 Full View Camera System

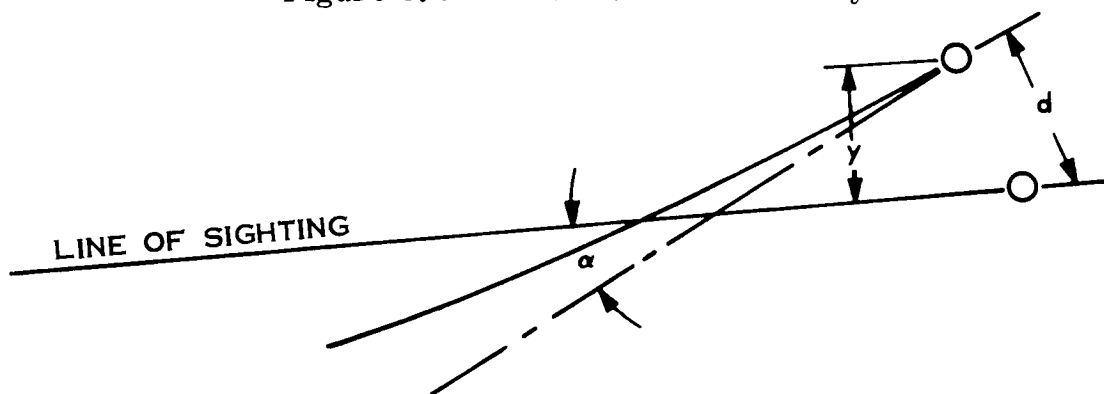


Figure 3.8-10 Normal Deflection Geometry

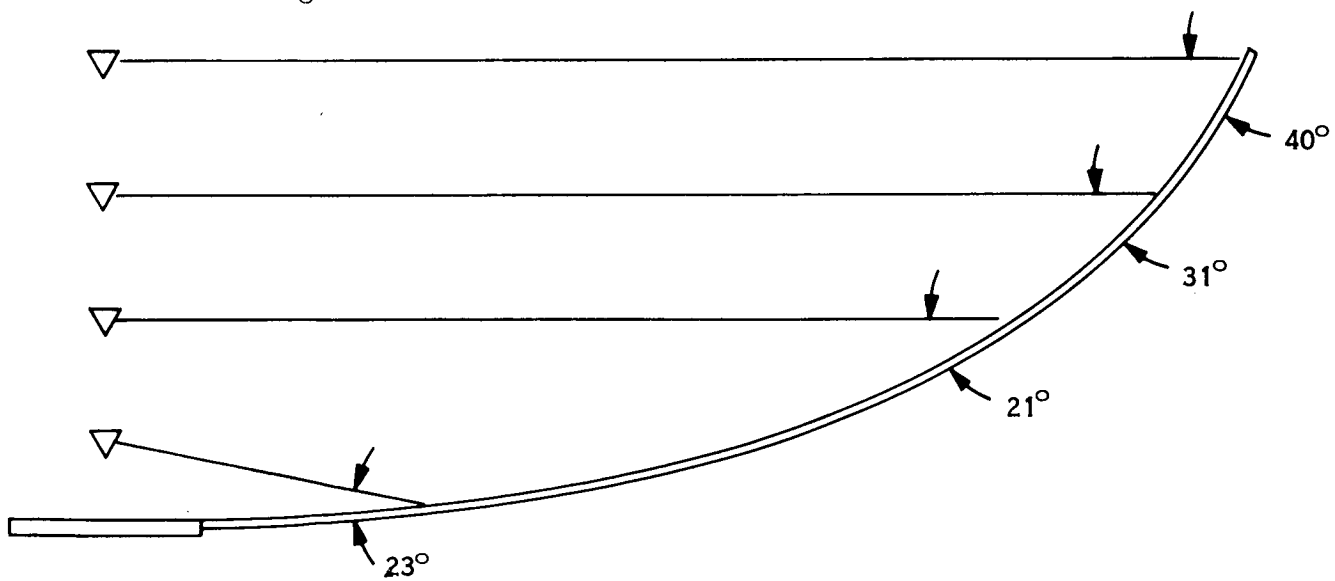


Figure 3.8-11 Ring Viewing Angles

At the next, the central, band $\alpha = 23^\circ$ and

$$\begin{aligned} y &= 0.030 \cdot \cos 23^\circ \\ &= 0.030 \cdot 0.92 \\ &= 0.028 \text{ inch} \end{aligned}$$

The resolution requirement at the four bands are not significantly different so we will use the worst case for all. The system will be designed to detect at least a 0.023 inch displacement. The lowest resolution system which can be used will resolve an element of half this size, 0.012 inch. The image formed on the vidicon face will be an annular area with width of approximately $1/4$ the width of the active area of the vidicon face. This annular area is the image of an entire ring of the antenna (see Figure 3.8-12). If a high resolution vidicon of 1000 lines is used, the radial width of the antenna ring will be scanned by $1/4 \times 1000 = 250$ lines. Thus the coverage (for each vidicon) will be a 3 inch ring on the antenna;

$$250 \times 0.012 = 3.00 \text{ inches wide.}$$

This width determines the camera view angles and thus the focal length of the lenses.

Circumferential Resolution - The circumferential resolution is not critical, as the antenna surface deviations to be measured produce radial deflections. The circumferential resolution will vary over the vidicon face. Here it will be calculated on an average basis to indicate order of magnitude.

A central circle, as shown in Figure 3.8-13, in the ring image on the vidicon face will have a circumference of

$$\pi \times 1/2 W$$

Thus, this central circle, and the ring image is effectively crossed circumferentially by

$$\pi \times 1/2 \times W \times \frac{1000}{W} \approx 1600 \text{ scan lines}$$

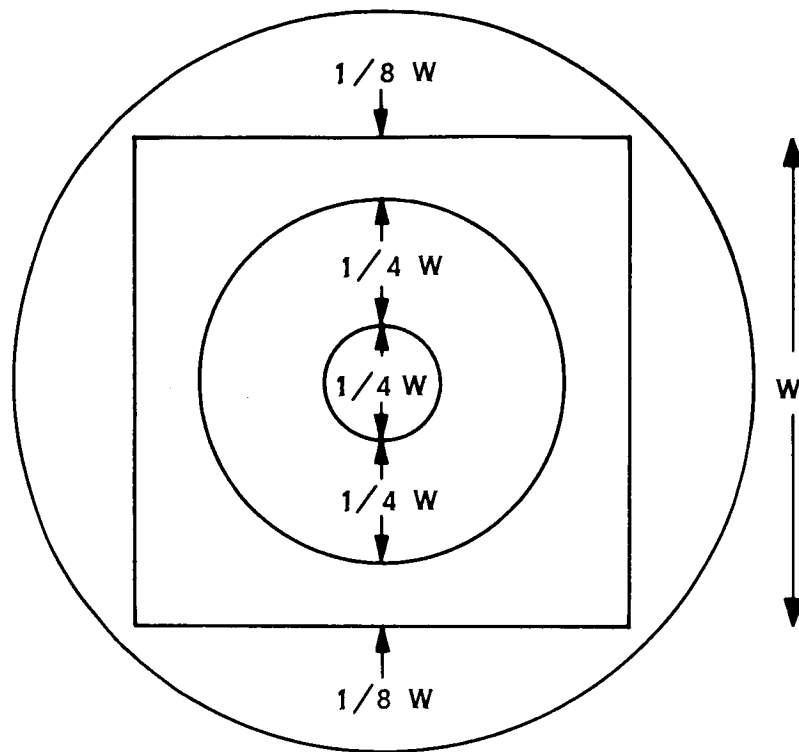


Figure 3.8-12 Vidicon Image Dimensions

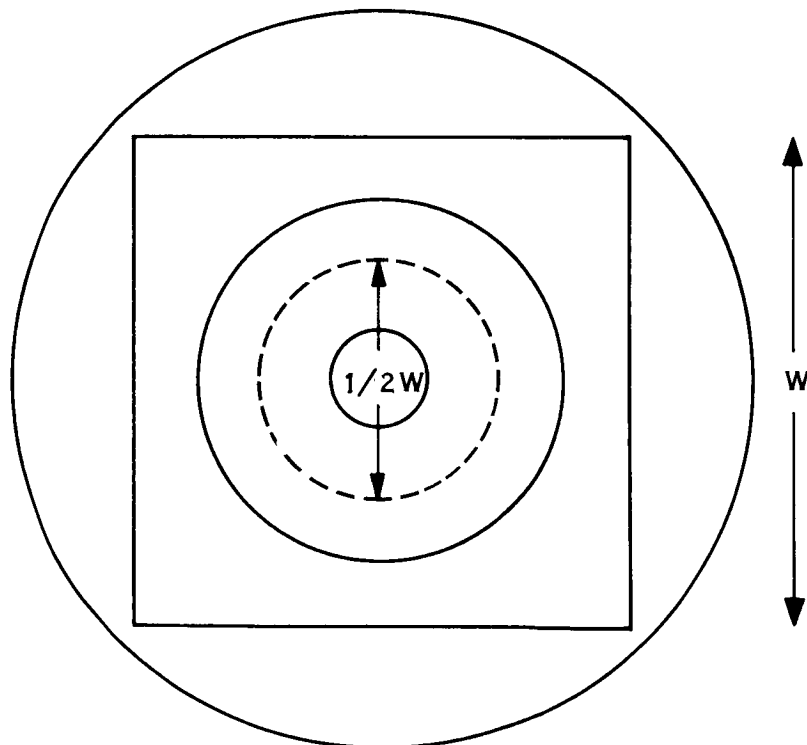


Figure 3.8-13 Central Circle in Vidicon Image

These scan lines distributed over the 100 foot circumference of the antenna rim corresponds to an average resolution element of

$$\frac{100 \times 12}{1600} = 3/4 \text{ inch}$$

These scan lines distributed over the 17 foot circumference of the inner ring corresponds to an average resolution element of

$$\frac{17 \times 12}{1600} \approx 1/8 \text{ inch}$$

Vidicon Scan Raster - Because of the circular nature of the vidicon images it may be desirable to use a spiral or radial scan as shown in Figure 3.8-14.

Marking Patterns - It is proposed to place a marking pattern at selected positions on the antenna's surface. As many as four marker patterns (one in each antenna ring) per petal may be utilized.

The antenna surface may be covered by a plastic film such as mylar which can be painted to yield the required pattern.

Various sizes for the pattern will be used. The smallest should be at least 10 resolution elements wide in the radial direction, or 0.120 inch. Here we will consider marking patterns in which the smallest plates are 1/4 inch or 1/2 inch in radial width.

Because of the poorer circumferential resolution the marker patterns will be wider in that direction. The circumferential width will be at least 6 inches at the rim and at least 1 inch at the central ring.

A number of parallel markers will be mounted along the radius in each band on each petal. If a deflection should be greater than the ring width (3 inches), a single marker would be out of view. Large deflections are more possible at the rim so the markers will be distributed over

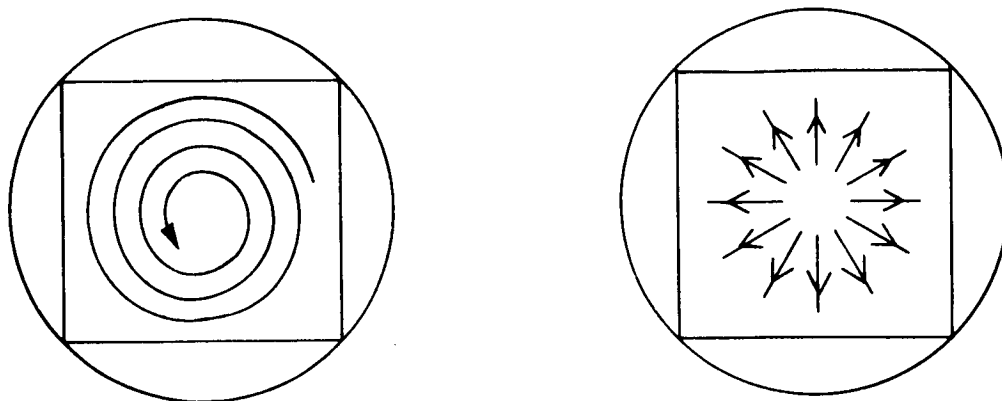


Figure 3.8-14 Radial and Circular Scan Patterns

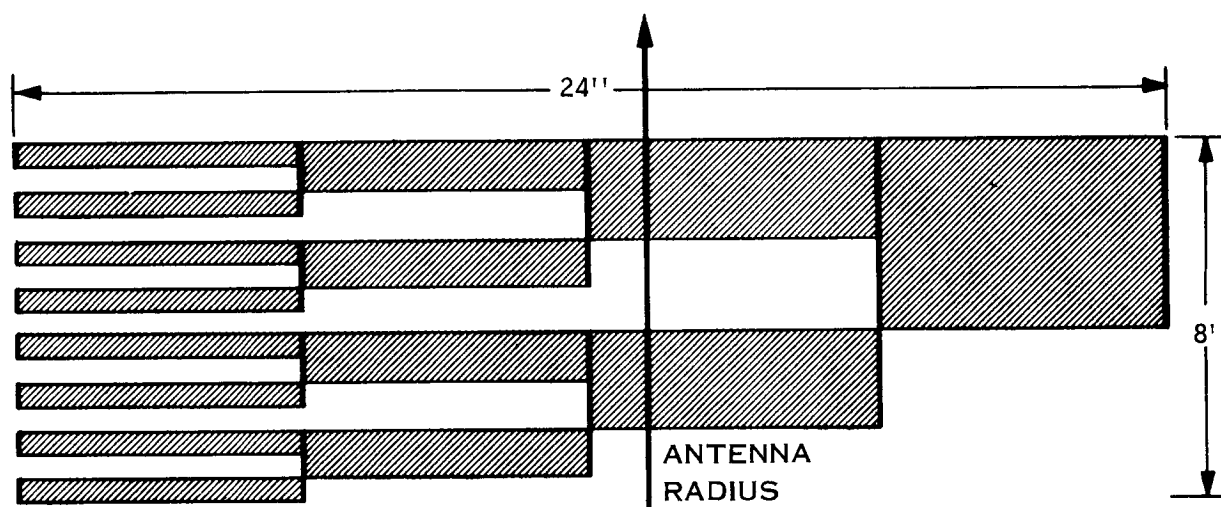


Figure 3.8-15 Rim Marker Pattern

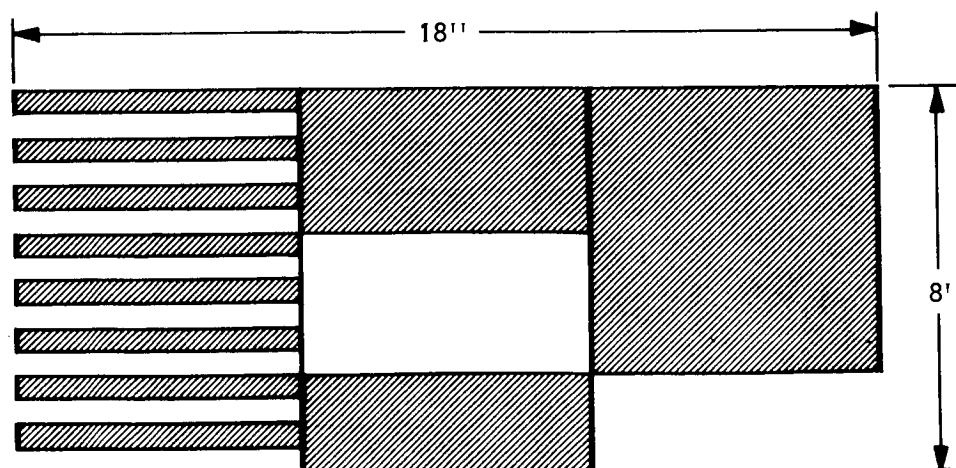


Figure 3.8-16 Modified Marker Coding

a greater radial distance there, perhaps 8 inches. At the central ring distribution over 2 inches will be adequate.

Then the marker pattern will have to be identifiable to determine the amount of a large surface displacement. The pattern might be identified by being of different circumferential widths or they might be identified by their position in relation to additional rows of marker plates of different radial widths. This later technique provides some additional position determination information and is thus preferable even though it requires that greater mass be added to the petals. The gaps between the pattern will be the same width as the plates. If a single row of equally spaced markers were used, a deflection of exactly two marker widths would look just like no deflection.

The rim marker pattern may be as indicated in Figure 3.8-15. As shown, the gross deflections (those larger than the narrowest plates) are binary - coded. Minor deflections (those smaller than the narrowest plates) can be determined by intensity measurements as will be described.

The binary pattern of Figure 3.8-16 is large as it is 24 inches wide. Because of the 3 inch ring width, permitting a view of more than one small plate at a time, a full binary coding is not necessary. With binary coding of Figure 3.8-17 position could be determined in a sampling ring of 1/2 inch wide. The rim pattern might be modified as shown in Figure 3.8-18 thus requiring fewer rows of plates.

Some additional accuracy can be obtained by including a row of narrower markers (1/4 inch) (see Figure 3.8-17). The half inch markers might be eliminated providing a pattern like Figure 3.8-18. The pattern at the next to outer ring (3rd ring) will be as shown in Figure 3.8-19.

The pattern at the next to central ring (2nd ring) will be as shown in Figure 3.8-20 The pattern at the central ring will be as shown in Figure 3.8-21.

To increase brightness and contrast, the marker pattern will be coated with a highly reflective paint, perhaps a glass beaded paint, and the mesh between plates may be coated with a low reflectivity black paint.

Fine Deflection Measurement - Gross position changes, due to antenna deflections, result in directly measureable mismatch between the image and the standard negative mask. By examination of the misalignment of the rows of marker plates in the matched image antenna deflections can be measured. The accuracy of this measurement is limited by the resolution element, 0.012 inch.

Misalignments smaller than 0.012 inch can be measured even though they cannot be resolved. They can be determined by measurements of the matched image brightness. If the deployed antenna were undeflected, its image would exactly match the standard negative and the resulting matched image would be uniformly black, or gray. Figure 3.8-22 schematically shows a perfect match of the antenna image and the standard negative.

Figure 3.8-23 schematically shows a slightly mismatched image. Though the light beams arriving at the image plane are too narrow to be resolved, the resulting local average intensity can be measured. The greater the misalignment, so long as it is less than a full pattern width, the greater will be the resulting intensity. Thus, with the gross misalignment determined by examination of the image shift; total misalignment can be determined by adding the fine misalignment obtained from measurements of average intensity in the area of the small plates.

Thermal Expansion and Contraction - The system thus far described will measure surface deviations due to deployment errors and due to non-uniformity of temperature over the surface.

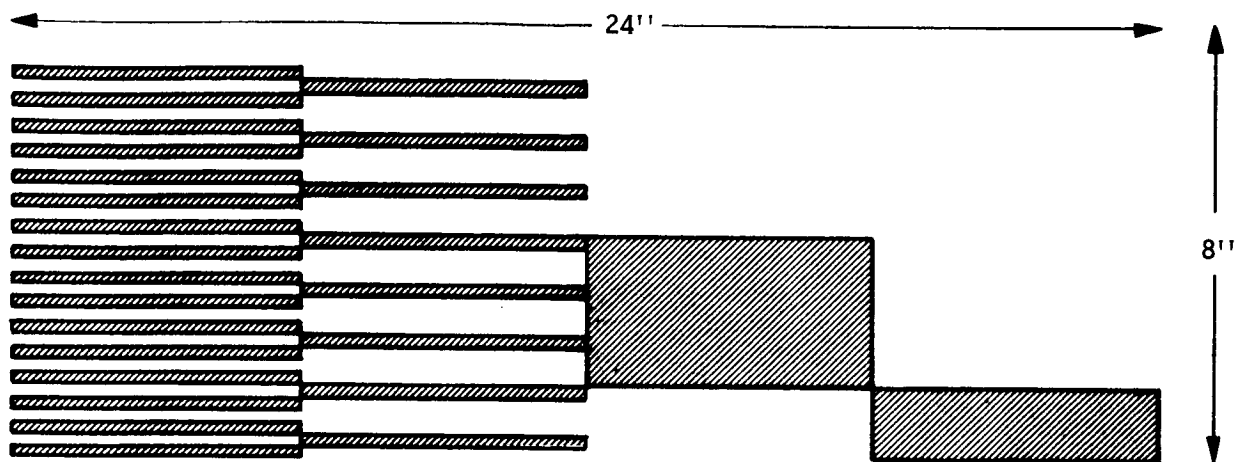


Figure 3.8-17 Reversed Marker Pattern

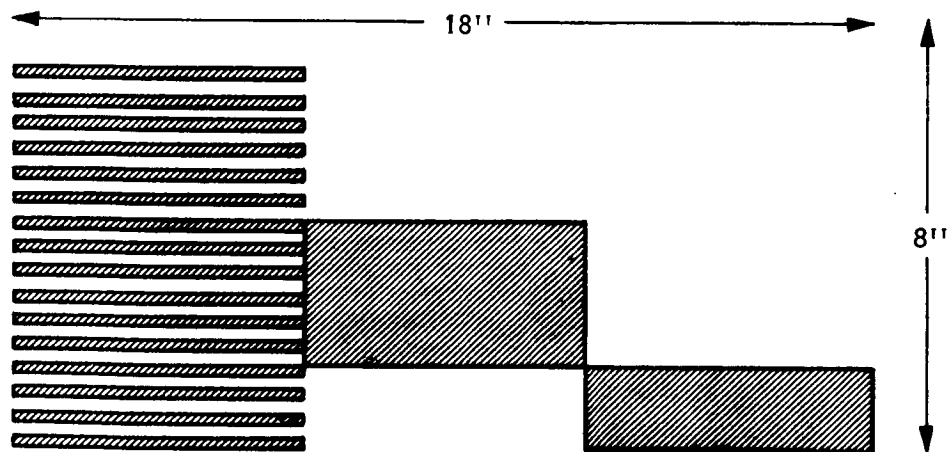


Figure 3.8-18 Marker Pattern Without 1/2-inch Plates

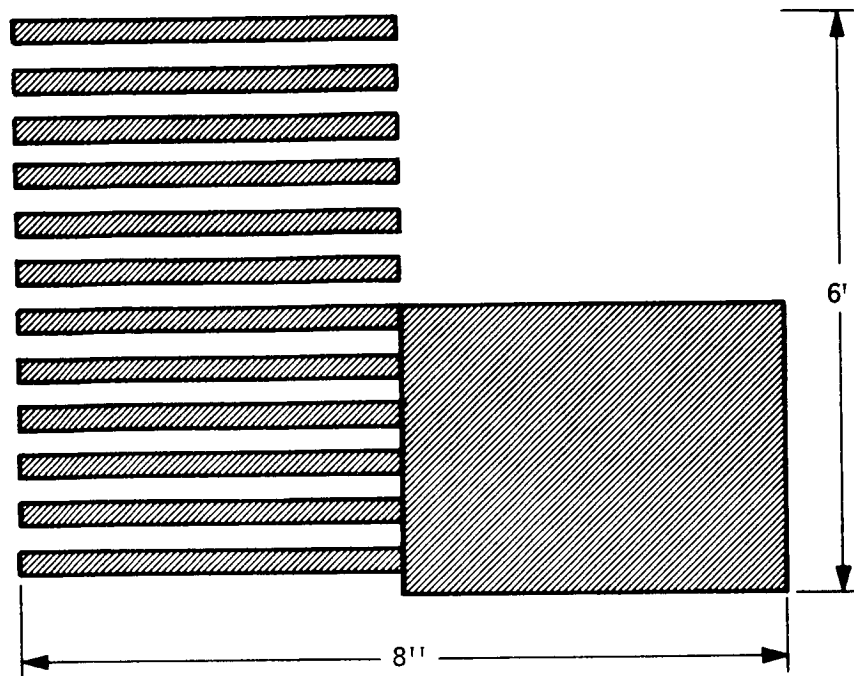


Figure 3.8-19 Pattern for Third Ring

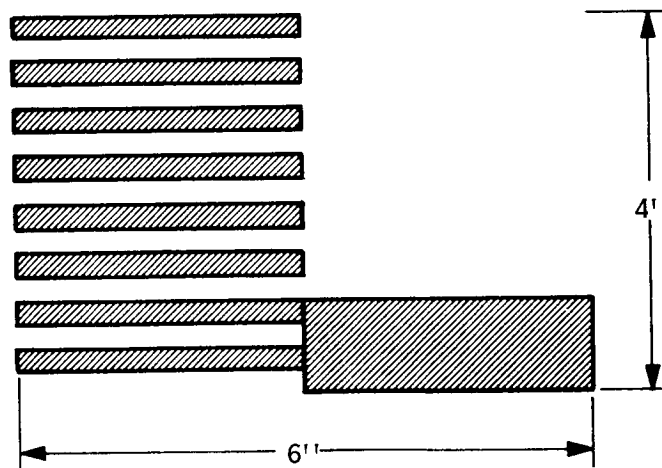
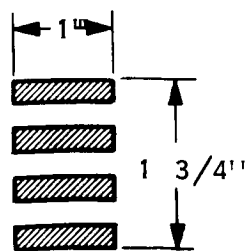


Figure 3.8-20 Pattern for Second Ring

Figure 3.8-21 Pattern for Central Ring



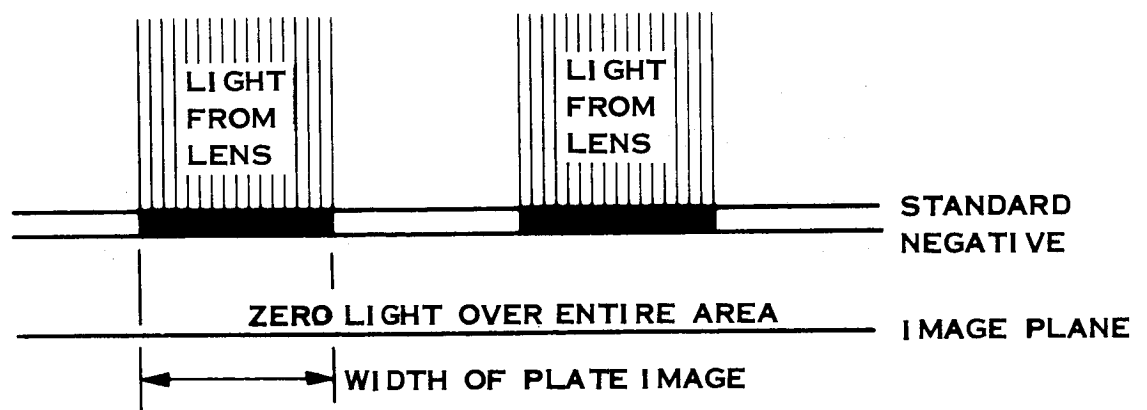


Figure 3.8-22 Pattern of Perfect Match of Image and Standard Negative

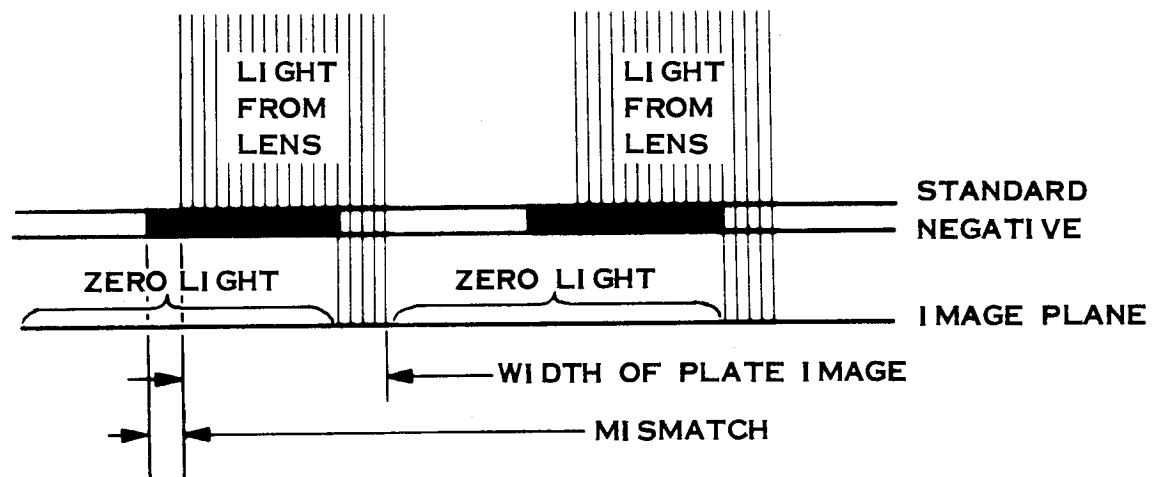


Figure 3.8-23 Pattern of Mismatch of Image and Standard Negative

In addition, there will be a gross shift of the entire antenna structure due to temperature effects. Such a shift would not cause the antenna to become non-paraboloidal. (It would slightly change the paraboloid size and slightly shift the focal point.) For example, the length of a 15 foot petal, undergoing a 300° temperature change, would change by $\Delta l \approx 0.86$ inch.

$$\Delta l = \Delta T \cdot K \cdot L$$

where

ΔT is the temperature change,

K is the temperature coefficient of expansion, and

L is the petal length.

$$\begin{aligned}\Delta l &= (300^{\circ}) (16 \times 10^{-6} / ^{\circ}) (15 \text{ feet}) \\ &= (300) (16 \times 10^{-6}) (15 \times 12) \text{ inches} \\ &= 0.86 \text{ inches}\end{aligned}$$

An entire marking pattern at the antenna rim would thus be radially shifted 0.86 inch. This shift will have to be taken into account in the data (transmitted image) analysis.

In addition to the gross shift in the marking pattern, there will be a thermally caused change in the marking pattern dimensions. The effect of this variable will also have to be removed during data analysis. This does, however, also provide an analytic means for determining the temperature at each marking pattern. The thermal expansion effects on the cameras and on the camera mounting structure must be analyzed.

Marking Pattern Composition - The materials composing the marking patterns present several problems which will be briefly mentioned here, but which must be resolved in the laboratory.

White marker plates interspaced with black painted mesh will cause a localized non-uniform heating. This will produce greater surface deviations at the marking pattern locations than over the unmarked area of the antenna.

An unpainted mesh with marker plates of the same composition and color may provide sufficient optical contrast. Most of the light striking the mesh will be transmitted through the surface, while a portion of the light will be reflected away from the camera due to the circular cross section of the individual wires.

To increase the structural strength of the antenna surface, the entire surface of each petal may be covered with a plastic film such as mylar. In this event the marking pattern may be painted on the mylar. If the entire antenna is not to be covered, the marking pattern areas might still be covered.

It may be possible to form the marking pattern by direct painting (or otherwise color coating) the top surface of the wire mesh. To reduce thermal distortion effects, the marking pattern might take the form of areas of differing wire cross section. The wires might be post formed as desired after the antenna is fabricated. The wires might be deformed as shown in Figure 3.8-24, to provide large and small reflecting areas for the cameras to view. All these wires are expected to be almost identically heated by sunlight, but laboratory verification is required.

The flattened wire surfaces will have to be and will have to remain precisely angled if they are very smooth. Thus, these surfaces will be diffuse reflectors. They will still reflect much more light than the sharp edged wires.

The effect of such wire deformation on the antenna's radiation pattern will be small, less surface deviation than the wire diameter of 0.010 inch. The wires may be further repositioned, as shown in Figure 3.8-25 to eliminate the surface deviation.

3.8.9 Illumination of the Antenna

Sunlighting of the antenna is not suitable because it is not constant in direction and it does not correspond to the laboratory illumination used in preparing the standard negative. Thus, even though the antenna were deployed without error, the image and the standard negative would not match.

Supplementary Lighting - It is necessary to have, as nearly as possible, identical lighting in the laboratory and in-orbit. It is desirable to have this illumination, as nearly as possible, in the direction of view of each of the cameras. Thus, a configuration like Figure 3.8-25 or 3.8-26 will be employed. In either case, flash lamps, probably xenon, will be used. One light source for each vidicon camera will illuminate the antenna ring to be photographed by that camera. In Figure 3.8-26, reflector light sources project a columnar beam onto a conical mirror. In Figure 3.8-27, reflectors direct the light from a ring light source.

Light Source Intensity - Sunlight, which is nearly always present, presents difficulties in that it illuminates the antenna differently at every point of the orbit. This optical noise makes image matching difficult. This optical noise can be minimized by increasing the intensity of the light source thus improving the signal-to-noise ratio. The flash lamp source should illuminate the antenna more brightly than sunlight. There seems to be adequate power to charge the flash lamp condensers to a high energy state. To charge condensers 200 or more watts are available for an hour or more.

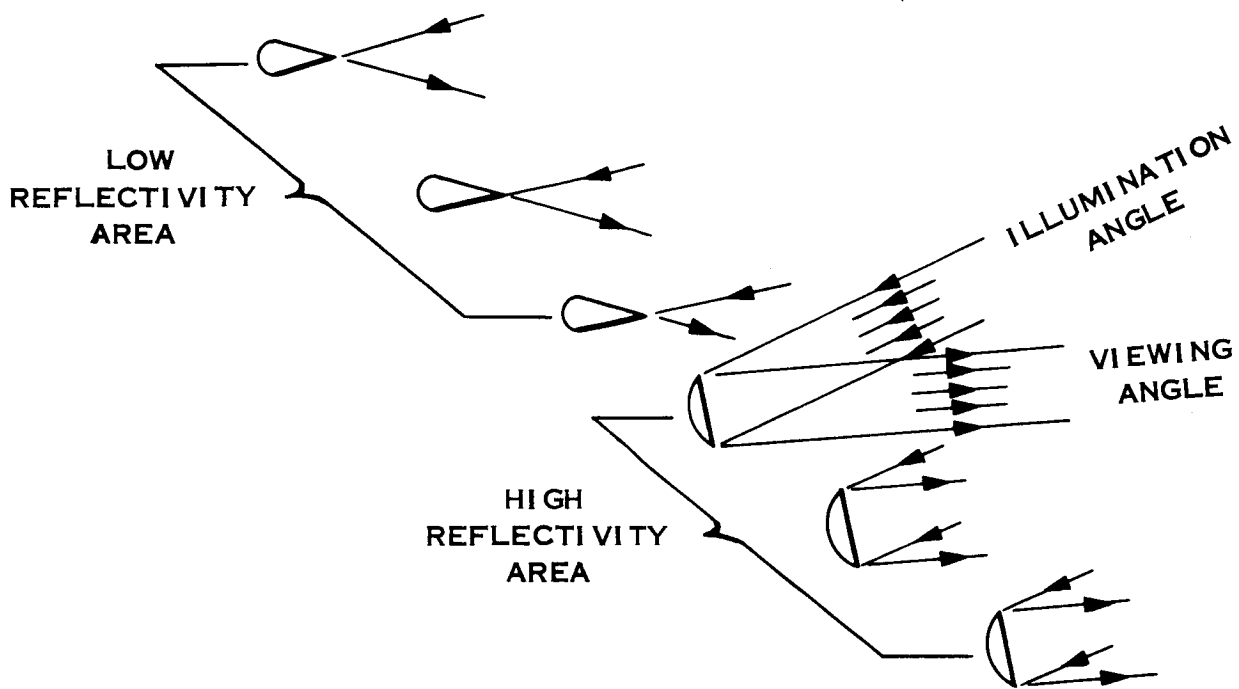


Figure 3.8-24 Marking Pattern from Deformed Mesh Wires

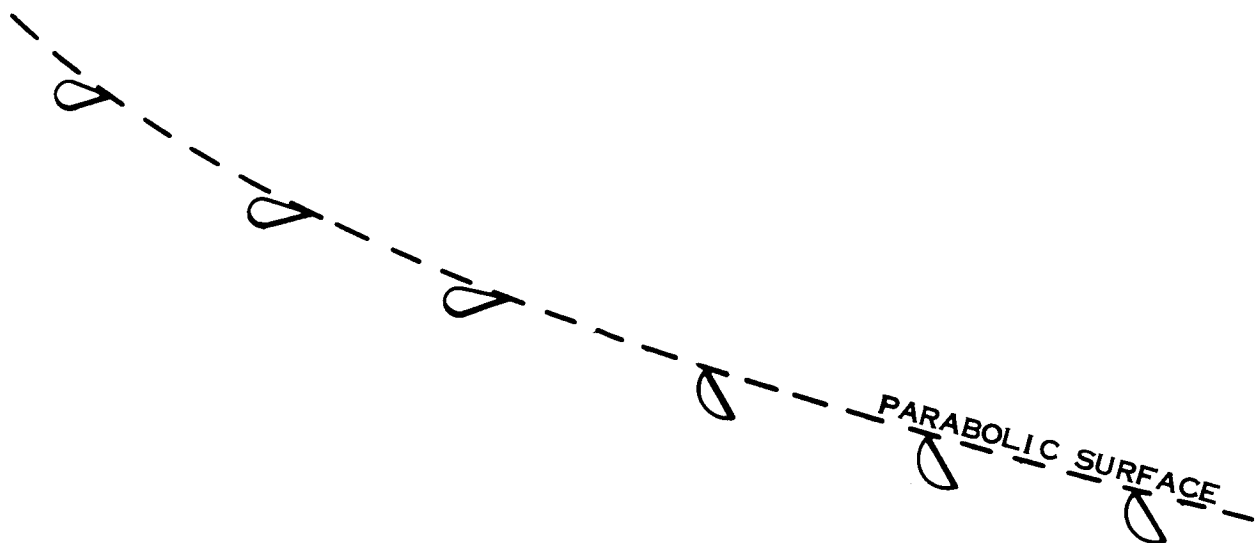


Figure 3.8-25 Deformed Wires Positioned Along a Parabola

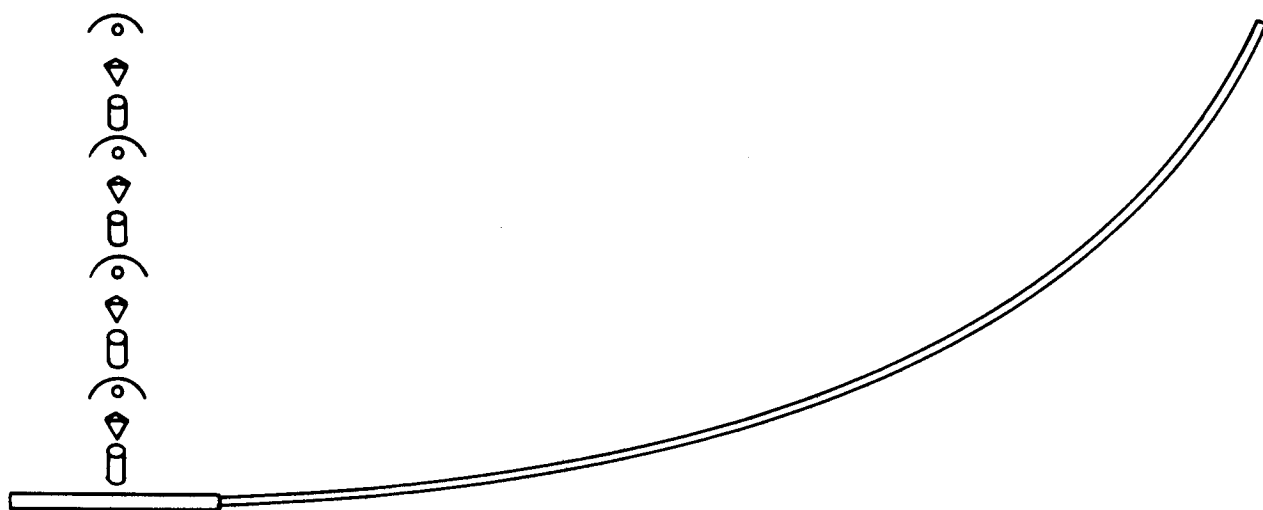


Figure 3.8-26 Illumination by Columnar Light Sources

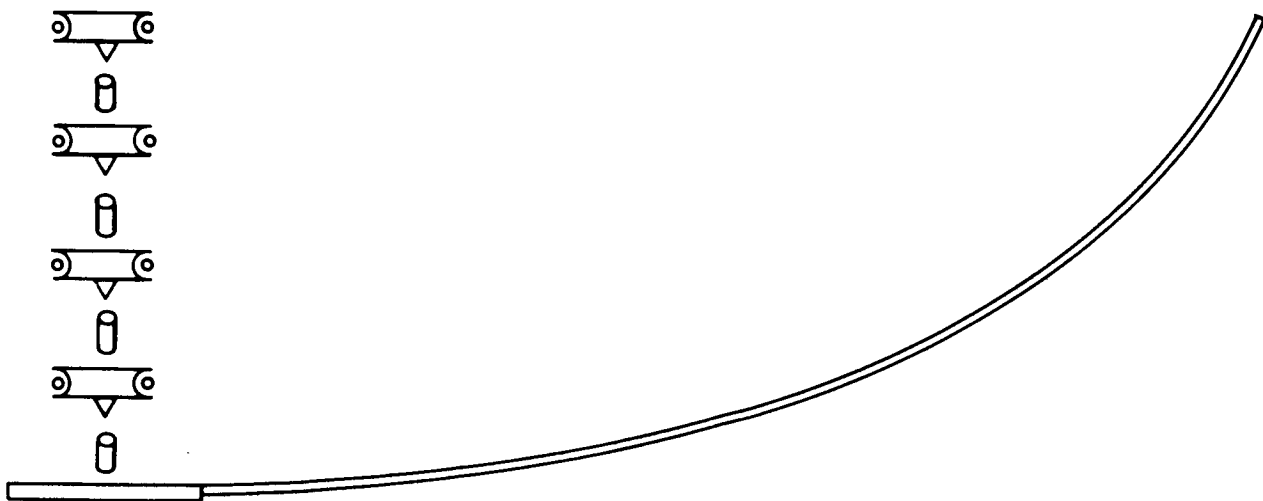


Figure 3.8-27 Illumination by Toroidal Light Sources

Noise Cancellation - Whether the light source be bright or dim, it is advantageous to use noise cancellation techniques to reduce the spurious effects of sunlighting. Noise cancellation can be accomplished on the ground by matching or comparison of two matched images transmitted from the satellite. For each look at an antenna ring, two images will be transmitted. One image will be made with sunlight alone and the other will be made with sunlight plus flashlamp. The sunlight image will be optically, electronically, or analytically subtracted from the sunlight-plus-flashlamp image.

3.8.10 System Operation

A command to charge will be sent to the satellite prior to an antenna surface check. The command must be sent 5 minutes to an hour in advance of flash tube firing, depending on the brightness of the selected light source.

After the flash tube condensers are charged five minutes to one hour, the command to photograph the antenna will be transmitted. The satellite's control electronics will then sequence the system through seven steps for each camera in turn.

- 1) camera shutter triggered
- 2) vidicon scans image
- 3) electronic image transmitted to ground station
- 4) camera shutter triggered
- 5) flash tube fired while shutter is open
- 6) vidicon scans image
- 7) electronic image transmitted to ground station

3.8.11 General Comments

Many of the technical and operational aspects which were considered have not been detailed in this report. Some of those will be briefly commented on here.

- System bandwidth and bit rate seem compatible with the resolution requirement and the vidicon sequencing. An image memory is not required in the satellite. A buffer might be needed.
- The cameras, conical mirrors, and light sources can be mechanically mounted to the tripod structure.
- Lens resolution is not a problem but resolution is limited by the vidicon.
- Image recording on photographic film before vidicon scanning is not necessary.
- The "line-of-rotating-vidicons" approach provides greater circumferential resolution, but is not needed.
- The total power required is not much greater than that required for the lighting alone.
- The concepts which involve rotating parts could be operated in a commanded step mode providing but a few rotational looks at the antenna.
- Ground matching of transmitted images may be done electronically with the images digitally stored in a memory.
- The analytic procedure is yet to be formalized and documented.

APPENDIX 3A

EXPANDABLE TRUSS ANTENNAS

Conic Scissors System - Fairchild Hiller is developing a class of antennas based upon its patented "Conic Scissors" concept (see Figure 3A-1). A conic scissors parabolic antenna consists of a number of equally spaced radial elements; each element is a scissor link assembly whose geometry is chosen so that, when deployed, the ends of the links define points on a parabolic curve. The curve is "filled in" between the points by curved members which are hinged to permit folding with the scissors when in the stowed condition. The pairs of scissor links are joined at the link ends of telescoping tubes which act as stops by limiting link spread when full deployment is achieved. (Figures 3A-1 and 3A-2). Deployment energy is provided by springs at the links.

The radial elements are interconnected by folding members which, when deployed, form a series of circumferential braces. In addition to providing structural stability, these members are curved to match the paraboloidal contour. Additional circumferential stability is obtained by diagonal cable braces at certain radial stations. The folded antenna packages into a cylindrical envelope. The reflecting surface is a flexible paraboloidal sheet attached to the curved members and folded with the assembly. Although an expanded metal mesh appears promising, other materials considered include metallized mylar, metallized nylon mesh, and a mylar-aluminum foil laminate similar to the ECHO II skin. These materials are judged for RF suitability, foldability, ability to be deployed to proper shape, and thermal shadowing.

The feed mast consists of four telescoping sections which are deployed either pneumatically or by springs at the same time as the reflector. Guy wires extending from the outer rim of the deployed parabola to the mast provide stability.

Figure 3A-3 shows the variation in weight and natural frequency with diameter for the conic scissors design. The considerable stiffness pro-

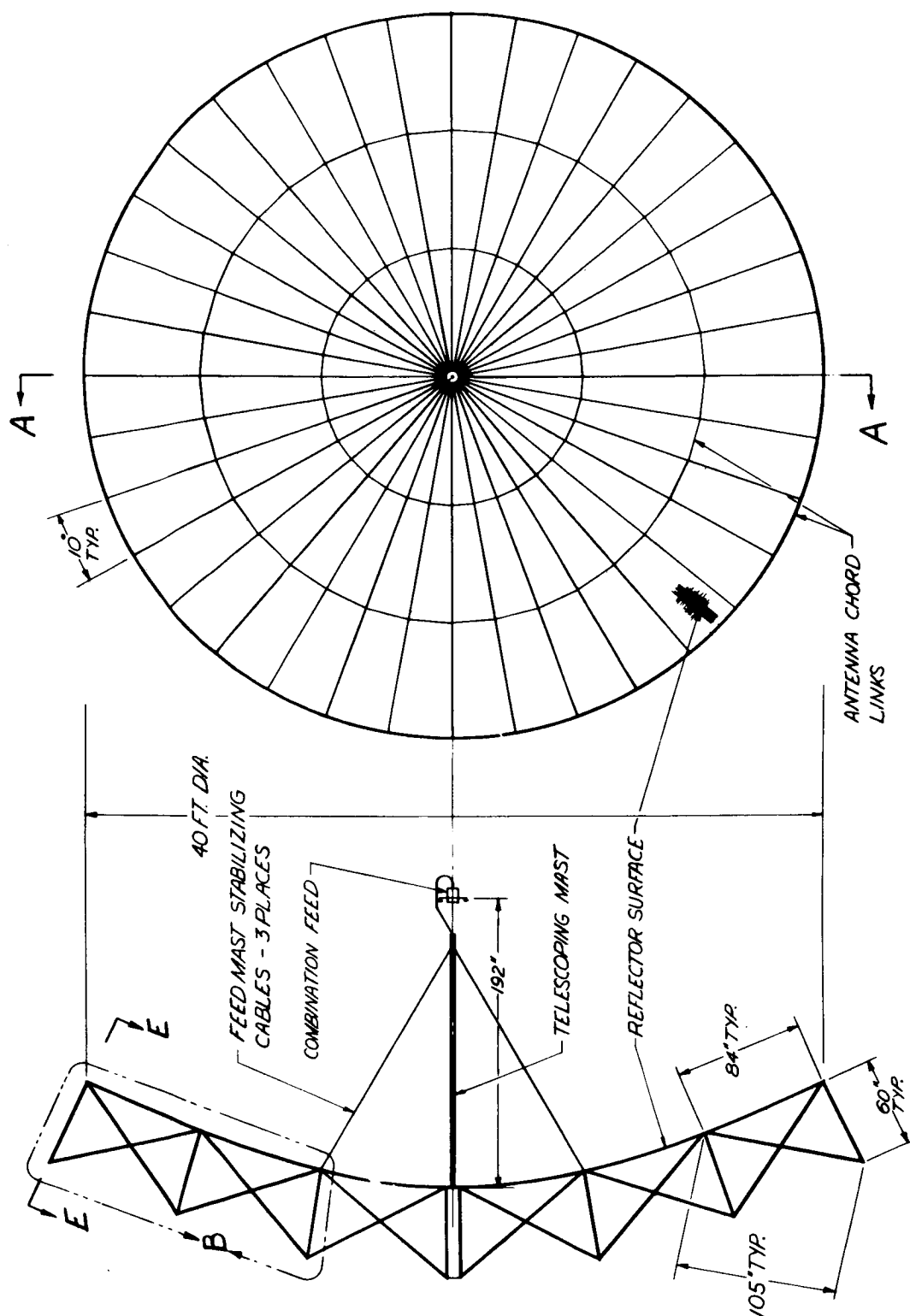
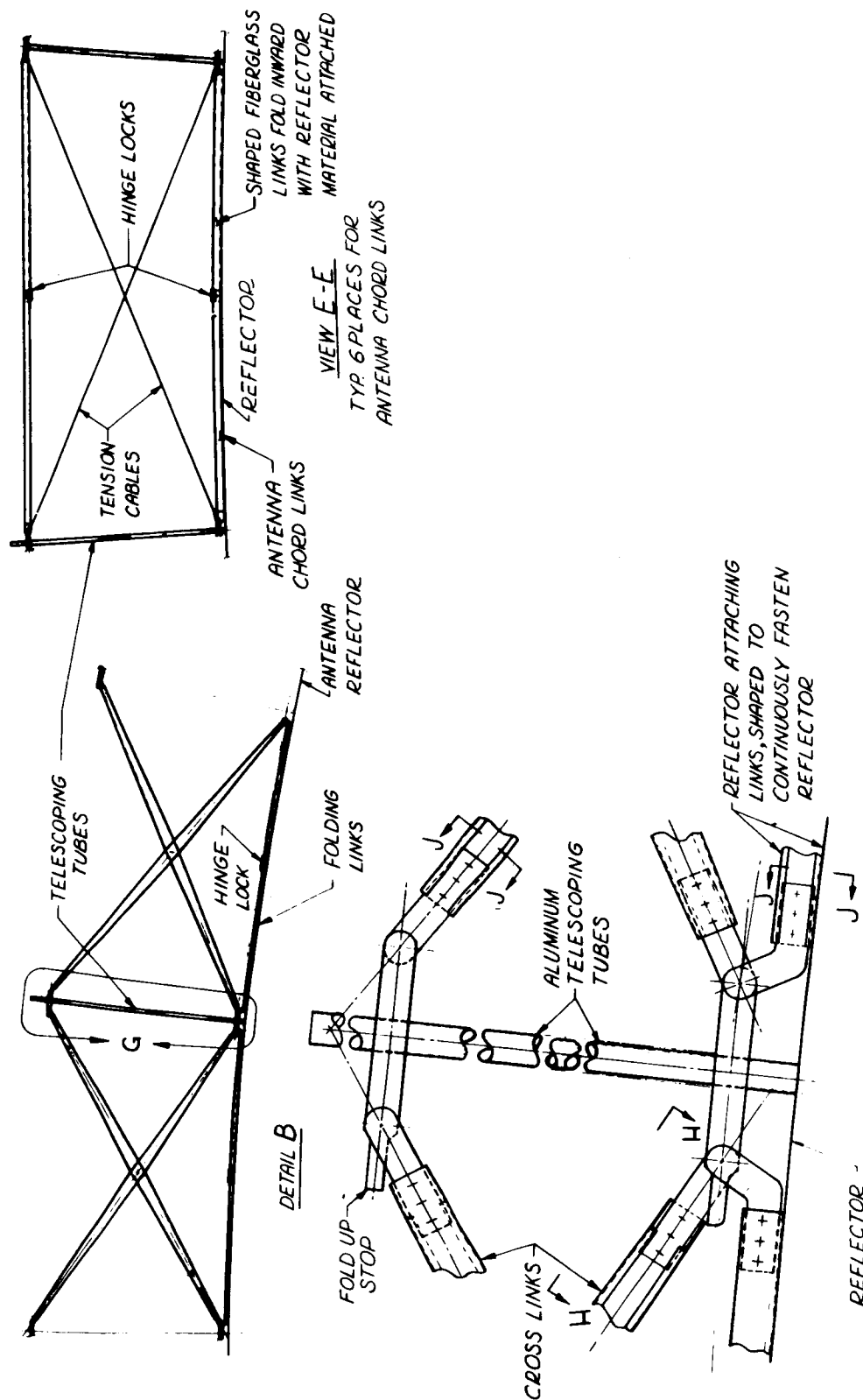


Figure 3A-1 Conic Scissors Antenna



DETAIL G



J

SECT. J-J

Figure 3A-2 Conic Scissors Details

vided by the very deep trusses is evidenced by the high frequencies. The natural frequencies calculated for the system used the rigid panel frequency equation by distributing the stiffness of the truss sections over the antenna to obtain an equivalent shell thickness.

Thermal Deflection of Coated Antenna - A preliminary thermal analysis was conducted for the conic scissors system in order to evaluate thermal stresses and the corresponding deflections. Worst-case solar orientations were assumed in order to maximize temperature gradients.

Primary members in the parabolic antenna are aluminum alloy channels. A detailed, nine node, steady state analytical model of the typical channel was analyzed two-dimensionally by the IBM 7090 in the steady state to determine temperature gradients. Heat transfer by both conduction and radiation was considered for each node. The terrestrial fluxes incident to the various members were as shown in Tables 3A-1 and 3A-2. The angle

γ used in the tables, is between the local vertical and a line normal to the surface of the member. When a member is illuminated by the sun, the earth radiation and albedo fluxes at synchronous altitude are small enough to be ignored.

The analytical model and the results are shown in Figure 3A-4. It can be seen that the ΔT across the scissor links is no greater than 5° F. This provided the isothermal basis for the thermal analysis of the scissors elements.

Several bays on the parabola support structure were selected to evaluate temperature levels in these elements. Two cases were considered.

In Case 1 (Figure 3A-5), the solar vector is assumed parallel to the local horizontal. There are two results shown on this figure for Radial 1. The first is for element shadowing resulting from precise alignment of the solar vector with the elements. The second (1a) assumes that the element shadowing is negligible for the typical bay because of spacecraft motion and

SURFACE	γ	E (B/HR-FT ²)
HORIZONTAL	0°	1.47
VERTICAL	90°	0.048
SCISSORS TRUSS MEMBERS	.	
B MEMBER	52°	0.907
A & C MEMBERS	20°	1.39

TABLE 3A-1 INCIDENT EARTH FLUXES UPON
SURFACES AT SYNCHRONOUS ALTITUDES

LOCAL TIME	SURFACE	γ DEGREES	A, B/HR FT ²
1200	HORIZONTAL	0	2.79
	VERTICAL	90	0.0705
	EDGE OF PARABOLIC SURFACE	30	2.42
0600	HORIZONTAL	0	0.722
	VERTICAL	90	0.0529
	EDGE OF PARABOLIC SURFACE	30	0.652

TABLE 3A-2 INCIDENT ALBEDO FLUXES UPON
SURFACES AT SYNCHRONOUS ALTITUDES

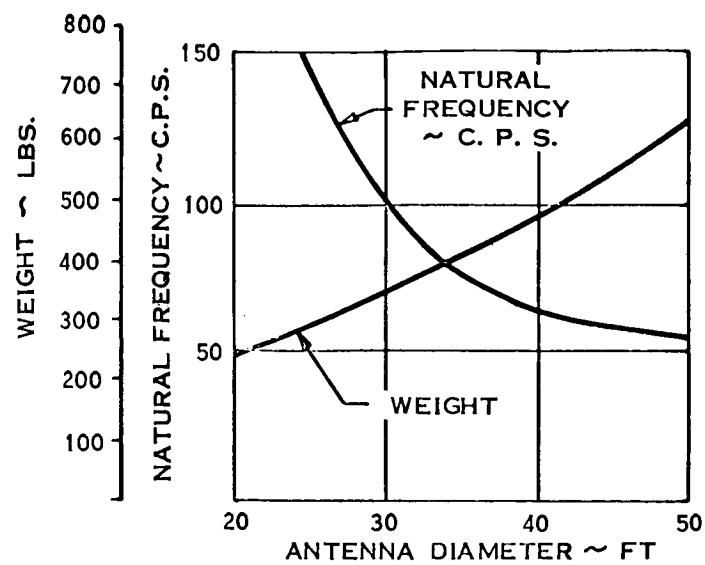


Figure 3A-3 Weight and Natural Frequency for Conic Scissors Parabola

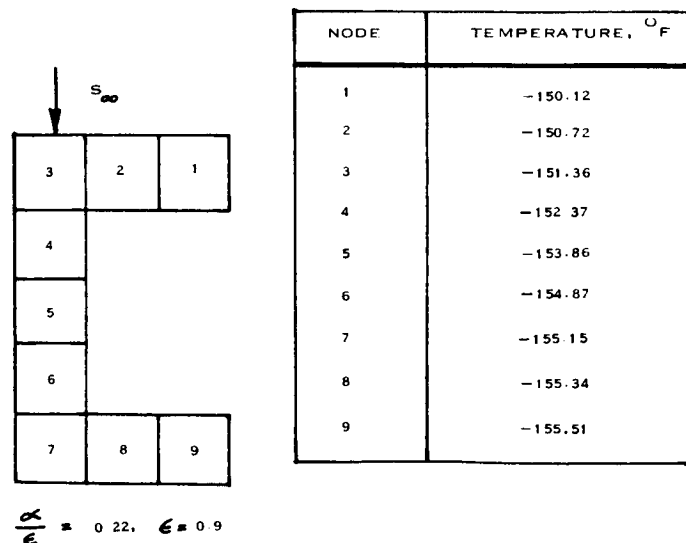
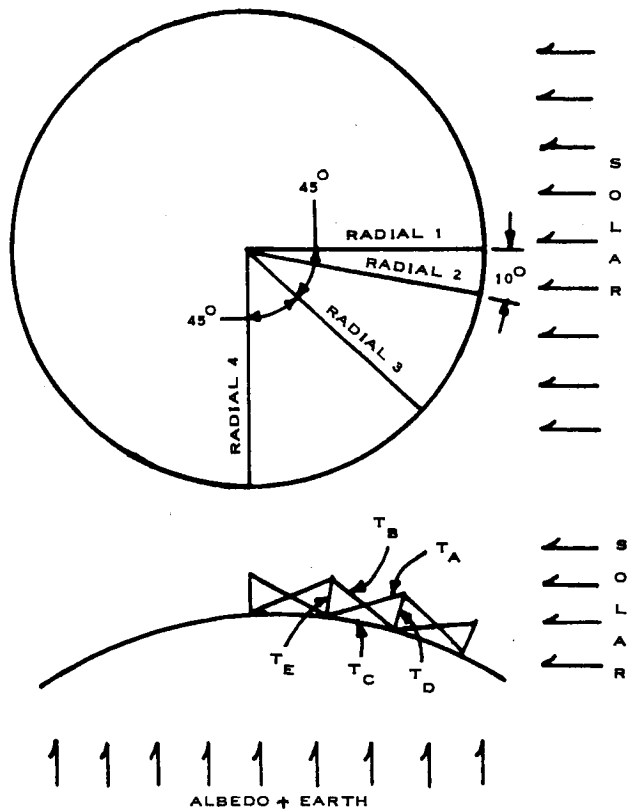


Figure 3A-4 Channel Thermal Analysis



SCISSORS ELEMENT TEMPERATURES (°F)						
RADIAL	T _A	T _B	T _C	T _D	T _E	COMMENTS
1	-357	-204	-345	-153	-182	SHADOWING
1A	-239	-157	-223	-95	-95	NO SHADOWING
2	-213	-214	-213	-93	-93	
3	-112	-113	-112	-90	-90	
4	-81	-81	-81	-90	-90	

Figure 3A-5 Scissor Element Temperature Analysis (Case I)

optical considerations of umbra shrinkage. An arithmetical average of these two extremes appears reasonable for preliminary thermal deflection calculations. For the other cases on the figure, no shadowing was assumed.

Case 2 occurs when the solar vector is aligned with the axis of the parabola. The resulting temperatures of the elements in a typical bay are shown in Figure 3A-6.

The element temperatures shown in the temperature map were used to calculate the tip deflections shown in Figure 3A-7. Two values of truss depth were analyzed to show the effect of varying this parameter. The Williot-Mohr graphical method was used to determine the displacements of the panel points of the truss for various temperature changes of the truss members.

Circumferential ring effects were included for radial members having a temperature range widely different from their adjacent radial truss members.

Thermal Deflection of Insulated Antenna - The improvement attainable by covering the antenna with superinsulation blankets was investigated. The antenna "density" of 0.35 lb/ft^2 indicated a thermal time constant of 10.2 hours. Application of a flat reflector coating on the exterior of the insulation blanket provides nearly isothermal behavior at a nominal orbital temperature level of 70°F . Seasonal variations in the solar constant cause a $\pm 20^\circ\text{F}$ swing about the nominal temperature, and a 40°F dip occurs during the maximum duration of earth occultation.

The results of the deflection analysis appear in Figure 3A-8. Both the hot case (maximum solar constant) and the cold case (minimum solar constant) are shown for truss depths of 30" and 60". It can readily be seen that the thermal deflections fall well within the allowable limits for the antenna.

Surface Errors - The surface accuracy that can be achieved with the conic scissor method of antenna deployment has been analyzed in detail. Since only the rigid beam members will be shaped to conform to the parabolic

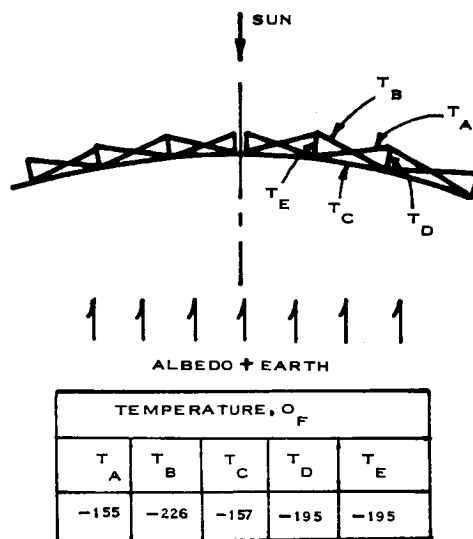


Figure 3A-6 Scissor Element Temperatures for Sun at Zenith (Case II)

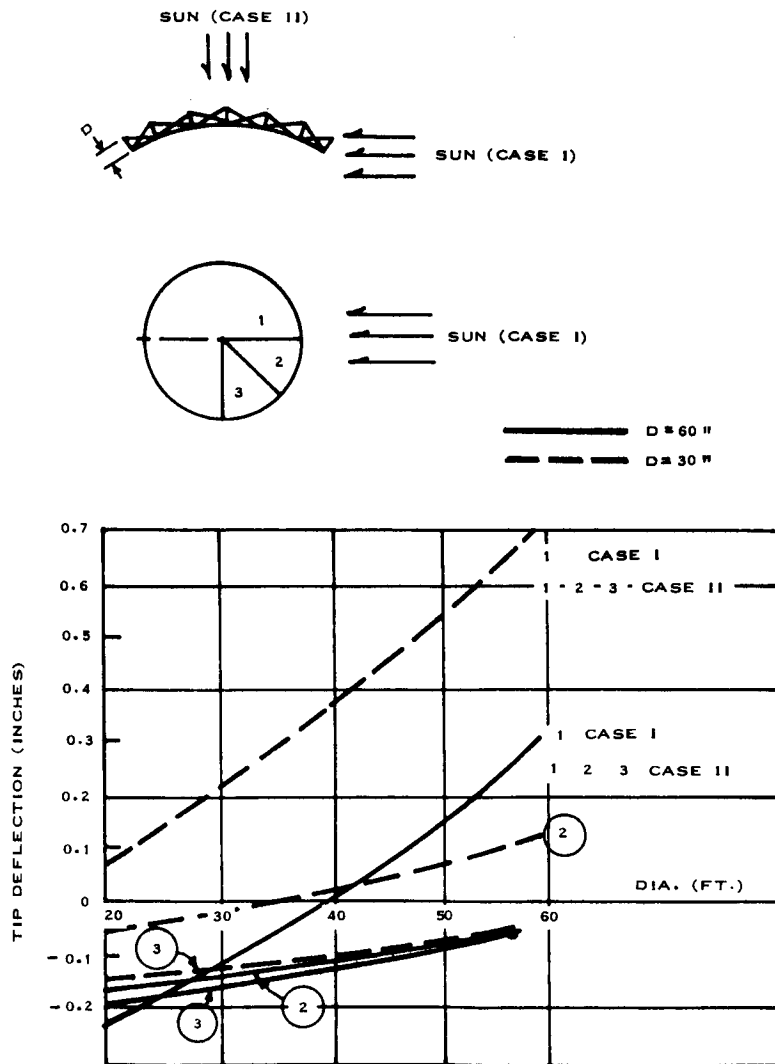


Figure 3A-7 Thermal Coated Antenna Tip Deflection

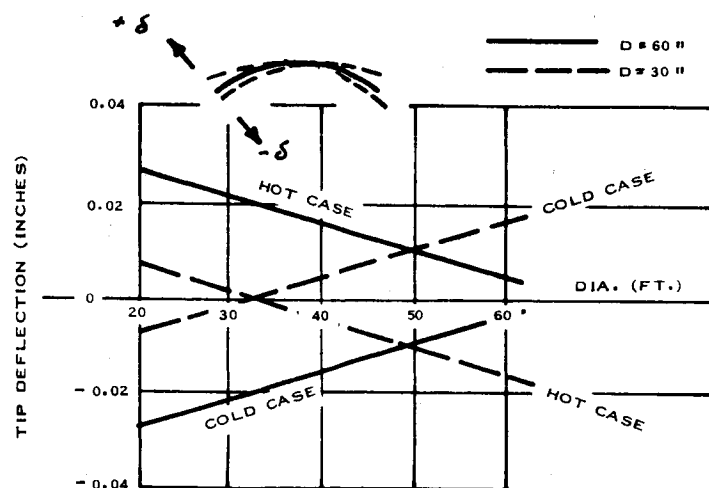


Figure 3A-8 Insulated Antenna Tip Deflection

contour, the reflecting surface (which is a flexible membrane or mesh) will be stretched between rigid supports and consequently will deviate from the theoretical contour. The amount of deviation is a function of unsupported length and F/D ratio. This is illustrated by the geometry shown in Figure 3A-9, and the plots of Figures 3A-10 and 3A-11.

This analysis has been accomplished for F/D ratios of 0.4, 0.5, and 0.6 and the resultant performance degradation plotted on Figure 3A-12. This graph shows that the antenna performance is severely compromised above 2000 MHz. It should be noted that since the surface deviation does not include thermal deflections, or manufacturing inaccuracies, this method of reflector deployment falls far short of the specified requirements.

Summary - The conic scissor concept provides a means of deploying extremely large antennas from relatively small packaged envelopes. For example, a previous study has shown that a 100-ft diameter antenna designed to operate at 4 GHz can be packaged in less than an 8 foot diameter envelope and weigh less than 1,100 pounds. These large sizes are for all practical purposes unattainable by rigid panel design.

For applications at lower microwave frequencies the weight of a conic scissor design appears slightly heavier than a rigid panel design, for a 30-ft diameter antenna. However, as the diameter increases, the weight of the conic scissor becomes much more attractive. This is because its weight is approximately proportional to diameter, while for the rigid panel design the weight increases proportional to the square of the diameter.

For operation at high microwave frequencies (10 GHz), the conic scissors approach is not recommended, because of the apparently unavoidable large surface deviations that occur in between the radial ribs.

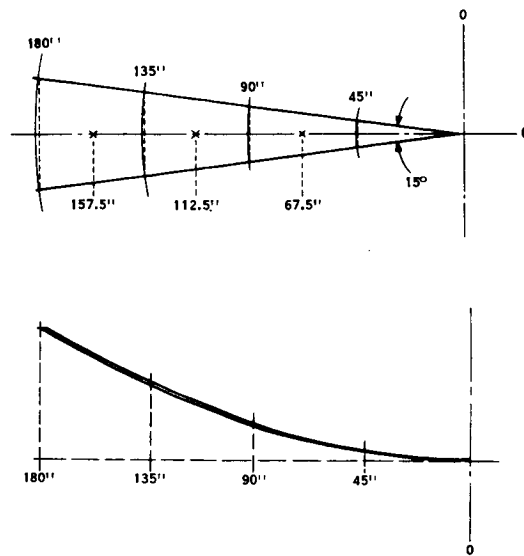


Figure 3A-9 Parabolic Antenna Geometry

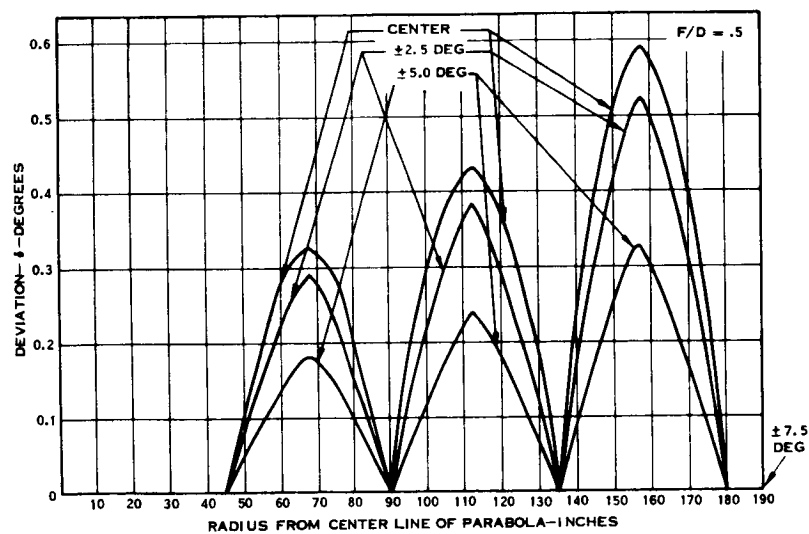


Figure 3A-10 Deviation of Reflecting Surface From Parabolic Contour in Radial Direction

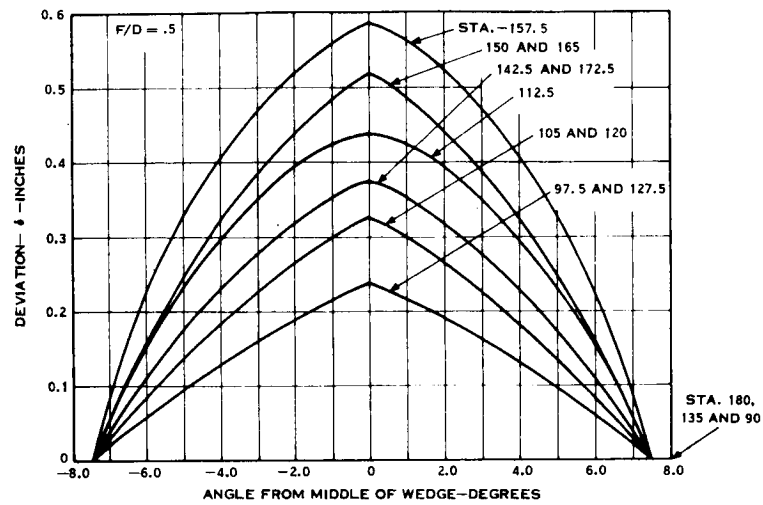


Figure 3A-11 Deviation of Reflecting Surface From Parabolic Contour in Circumferential Direction

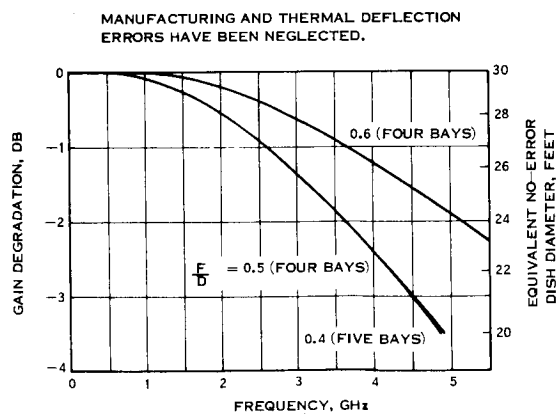


Figure 3A-12 Gain Degradation, Conic Scissors

APPENDIX 3B

INFLATABLE ANTENNAS

Inflatable System - The limited volume available in many standard ascent fairings makes inflatable techniques for large deployable structures attractive. Their ability to be packaged in relatively compact canisters is their outstanding characteristic. However, this advantage must be weighed against other important criteria which are discussed in this section.

Several techniques can be postulated for inflation of large parabolic antennas. Among the principal contenders are:

- Lenticular System
- Inflated Tube System

Both of these systems will be discussed here.

Lenticular System - The lenticular system consists of an inflatable lens-shaped bag with edge restraint provided by an inflated peripheral torus. One-half of the bag contains a metal mesh, threads, or metallized surface which act as the parabolic reflector. The other half of the bag is a plastic film whose only function is to contain the inflation pressure. It may be discarded after erection is complete.

The reflecting half of the bag must be regarded as a structural element, i. e., after completion of deployment and loss of pressure, it must carry the loads imposed in orbit. These loads are due primarily to station-keeping acceleration, antenna scanning, attitude control maneuvers, and solar pressure and heating. Thus, it must consist of, or be backed up by, a material having adequate strength and stiffness to satisfy the system requirements.

Two methods which have been proposed are:

- Wire Mesh
- Self-Rigidizing Cloth

The first of these uses wire mesh as both the reflecting surface and as the "structural" material. The mesh is lined with a plastic film which serves as the pressure bag. Inflation of the bag to a predetermined pressure stretches the mesh to the correct parabolic shape. The plastic has then served its purpose and may be retained or discarded (usually by virtue of its photolyzable characteristic).

The second method uses fiber glass or nylon cloth as the structural material. It is impregnated with gelatin which loses its moisture and becomes "rigid" in the vacuum of space. Again, a plastic bag must be included to contain the pressure. The RF reflecting surface may be realized by metallizing the plastic, incorporating woven metal threads into the cloth, or by attaching wire mesh to the cloth.

In all of the lenticular techniques, a peripheral torus must provide edge restraint during deployment so that the correct parabolic shape will be produced. The torus is plastic or plastic-lined and is separately inflated, it can be self-rigidizing cloth or mesh reinforced. It may deploy with itself a smaller peripheral member which remains after completion of deployment. This case might be typical of a system in which a photolyzable torus material is used.

Inflated Tube System - This system differs from the lenticular system in that the reflecting surface is deployed, not by inflation of a lenticular bag, but by a series of radial and circumferential inflatable tubes.

The tubes, of course, must be designed and fabricated in such a manner that when inflated to the prescribed pressures, the reflecting surface will be stretched to the proper contour. Here again, the reflecting surface may be a wire mesh or a self-rigidizing cloth containing metal threads.

Inflatable Systems for ATS-4 - The suitability of an inflatable parabolic antenna for the ATS-4 mission appears to be questionable at this time. This philosophy is based upon an examination of the following criteria:

- o State-of-the-art
- o Confidence in successful deployment
- o Accuracy requirements

State-of-the-Art - To date, no large inflatable structure has been deployed in space with the exception of the ECHO series of spherical balloons. Moreover, even laboratory demonstrations of parabolic inflation techniques have been limited to small models or models having non-flight requirements or helping hands. Reliable extrapolation of the technology developed for small laboratory models to the design of large, accurate, load carrying antennas is questionable.

On the other hand, deployment of rigid structures is a technology backed by years of experience. The most notable example is the successful PEGASUS Meteoroid Technology Satellite. The 96 foot rigid "wings" of this spacecraft were designed to deploy using conventional techniques.

Confidence in Successful Deployment - A high level of confidence in successful deployment of large structures must be achieved before launching ATS-4. Such confidence can be achieved best by repeated ground deployment testing, not only on development models, but also on actual flight models. While such extensive deployment testing is certainly achievable on a rigid deployable system, it is difficult on inflatable systems. Repeated softening and rigidization of a self-rigidizing material brings into question the ultimate reliability of deployment and rigidization in space. If yielding of a wire mesh to its proper parabolic shape is required, ground testing of the flight article is not feasible.

The PEGASUS spacecraft provides a good example of the confidence to be gained by extensive ground deployment testing. The prototype of PEGASUS was deployed over 150 times and each flight spacecraft 20 to 30 times. A television camera in the first flight PEGASUS verified that the deployment system's behavior in space was a precise duplicate of its behavior

on the wing deployment fixture.

Accuracy Requirements - The parabolic antenna for the ATS-4 mission must have a surface which, when compared with the theoretical surface, deviates no more than 0.050 inches rms. This allowable surface error includes all contributing factors, such as manufacturing tolerances, deployment errors, and thermal deflections.

As a typical case, one may consider the errors due to deployment of a lenticular parabolic reflector. Even if perfect manufacturing is assumed achievement of the correct parabolic contour is contingent upon inflation of the torus to its correct pressure and inflation of the lenticular bag to its correct pressure. Figure 3B-1 illustrates the effect of errors in the inflation pressure of the lenticular bag for two values of modulus of elasticity and two thicknesses of lenticular film for a 30-ft diameter antenna. The curve assumes no error in torus inflation pressure. If further assumes that the torus provides an infinitely stiff peripheral restraint. Even with these unconservative assumptions, it can be seen that a plastic bag ($E \approx 500,000$ psi), as thick as 0.005", will deflect from its true parabolic shape by 0.1" if the inflation pressure is in error by as little as 0.001 psi.

The ability of space proven instrumentation not only to measure but also to control pressure to such accuracy is questionable. Furthermore, it must be remembered that the analysis ignored manufacturing errors, thermally induced deflections, torus inflation errors, and torus flexibility, all of which will tend to increase the magnitude of the surface error. In view of these inaccuracies, inflatable schemes have been excluded, at least for X-Band applications.

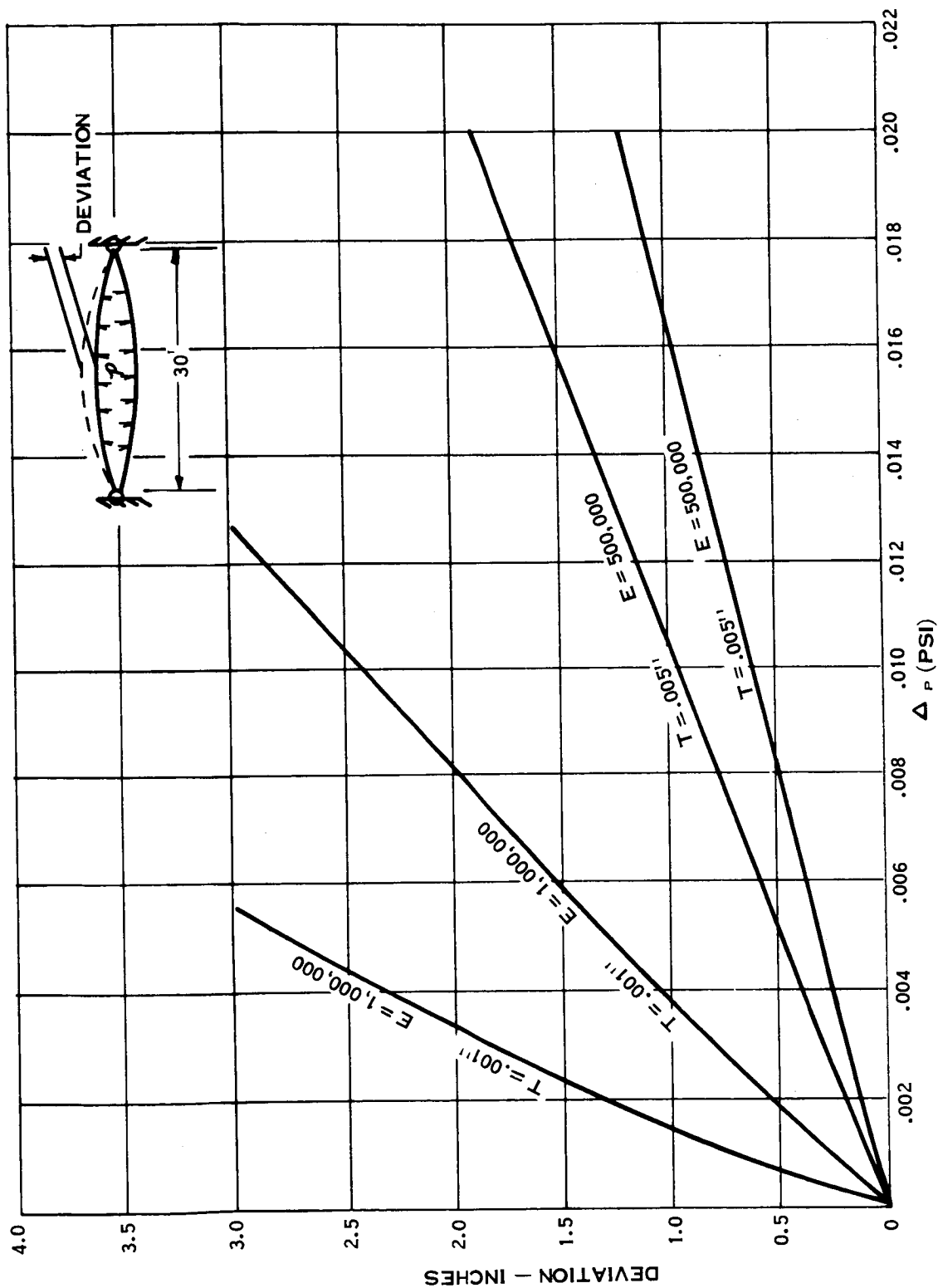


Figure 3B-1 Deviation of Inflatable Parabolic Antenna Due to Pressure Errors

APPENDIX 3C

RIGID PANEL ANTENNAS

Rigid Panel System Using Honeycomb Sandwich Panels - A rigid panel system will result in a reflecting surface of highest accuracy. Figures 3C-1 and 3C-2 illustrate a typical design using this approach. This design consists of a series of honeycomb sandwich panels which are folded like petals and which, when deployed, form the parabolic contour. The principal components of the system are:

- Center antenna section
- Folding panels
- Feed mast
- Panel release mechanism
- Panel extension and drive mechanism
- Panel locking mechanism

The center section and the folding panels are both made of 0.25 inch thick honeycomb sandwich construction comprised of .003 aluminum alloy skins and 2.1 lb/ft³ aluminum honeycomb core.

The panels are joined to the center section by skewed hinge fittings. The careful selection of the hinge axis permits folding the antenna panels into a much smaller diameter than is possible with a more conventional hinge arrangement.

After full deployment has been achieved, adjacent panels will be locked to each other at three "radial" locations (Figures 3C-3 and 3C-4. The three locking fittings are contained in the panel edge members and are locked into position by a single spring-actuated cable at each panel edge. The cable can be released pyrotechnically. This design is similar to that which was successfully used on the NIMBUS solar array.

The maximum diameter of the rigid petal design as described is

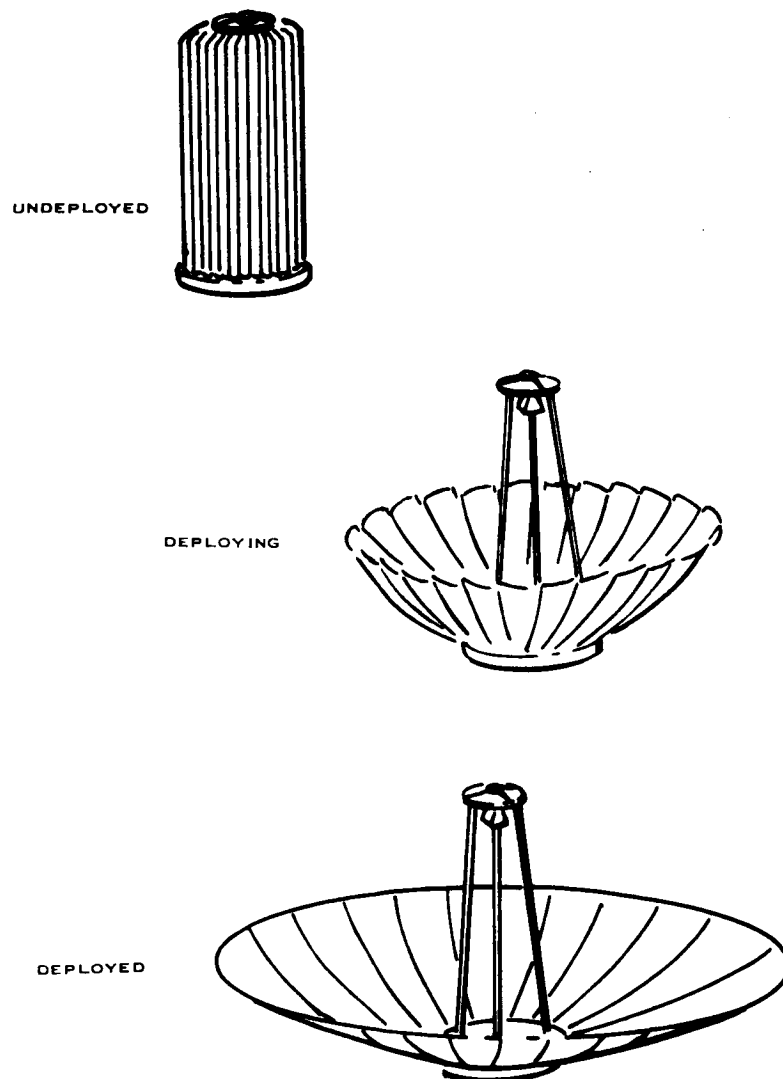


Figure 3C-1 Rigid Panel Antenna, Design One

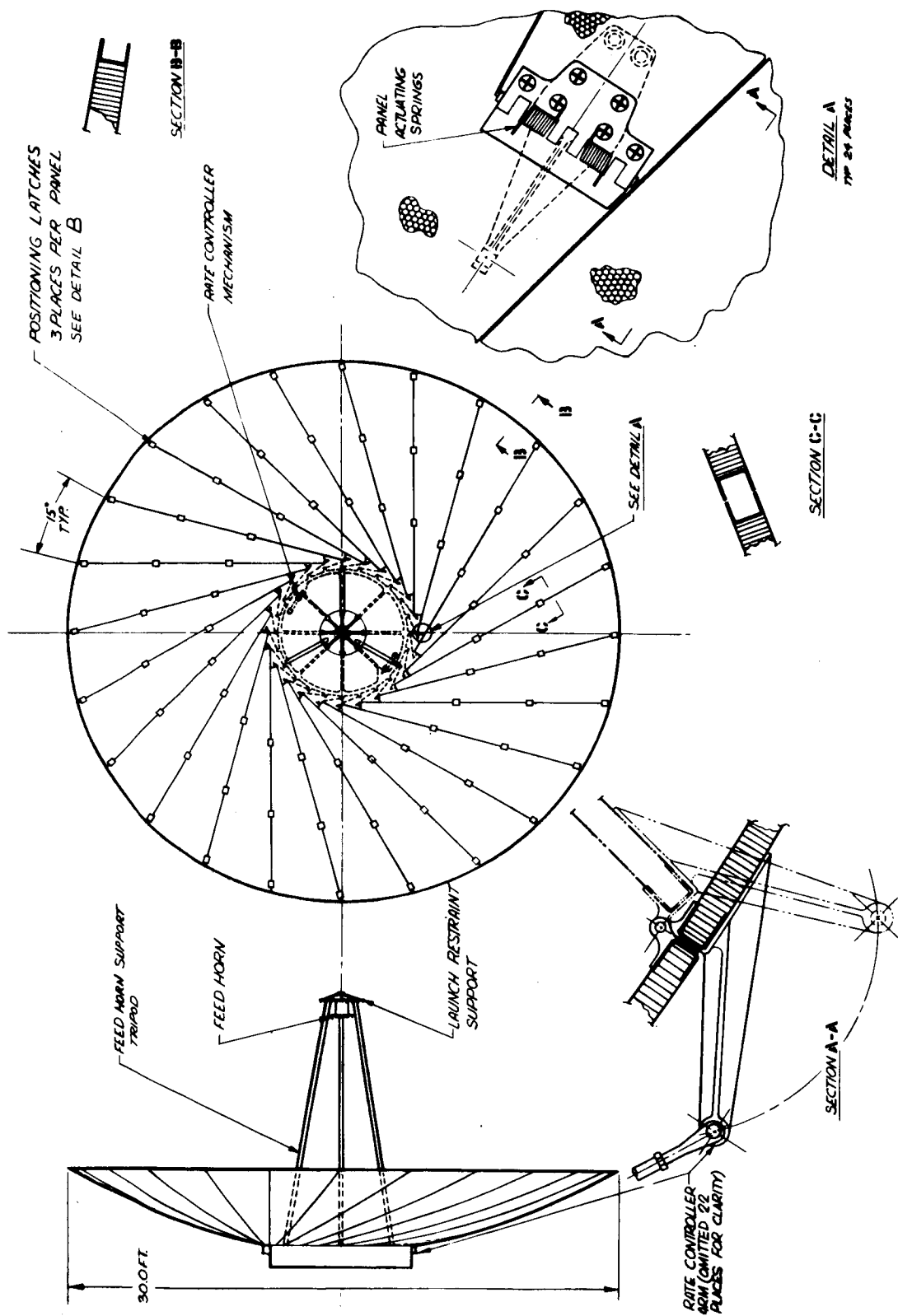


Figure 3C-2 Rigid Panel Antenna, Design Two

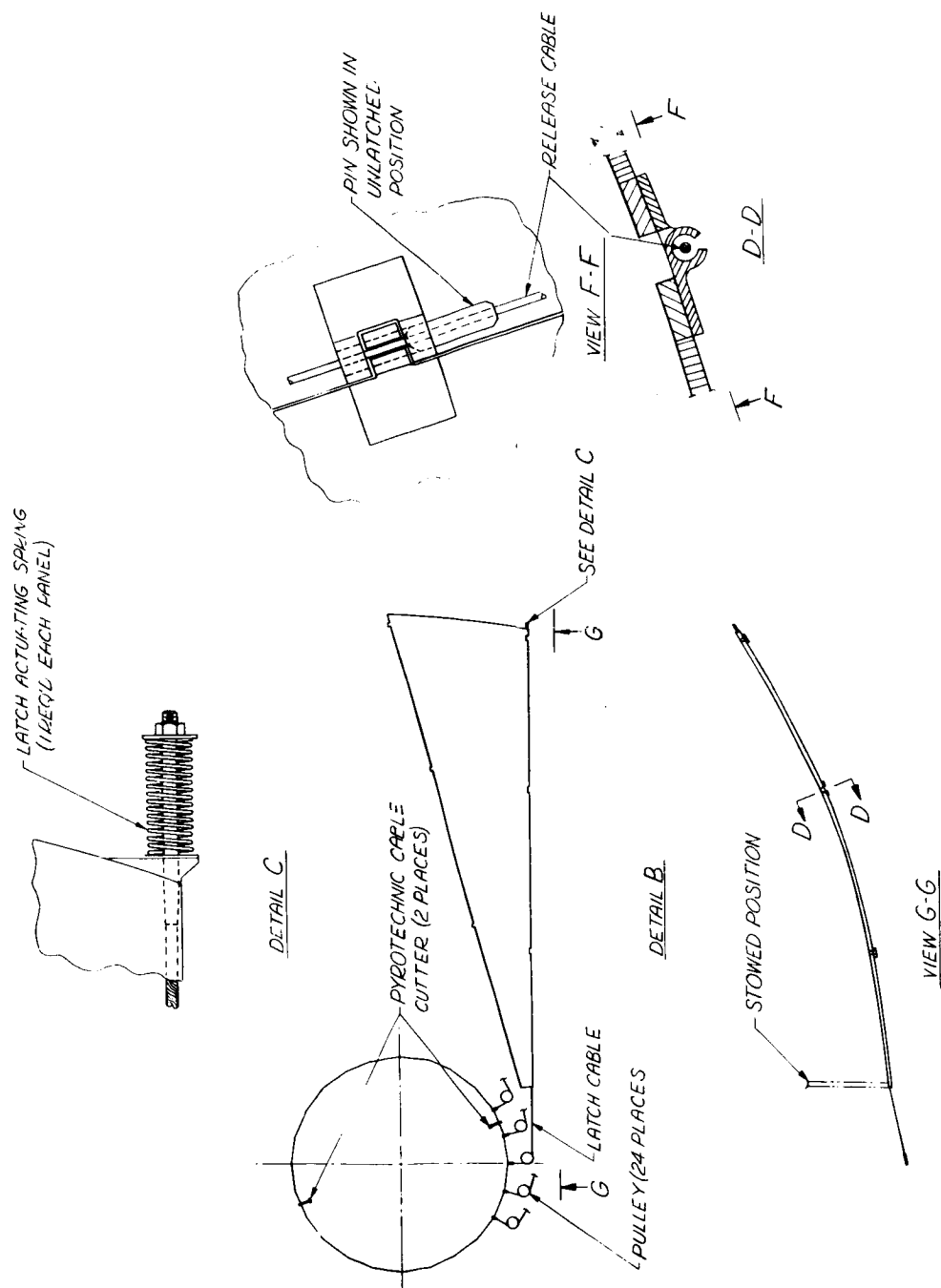


Figure 3C-3 Panel Locking System, Sheet One

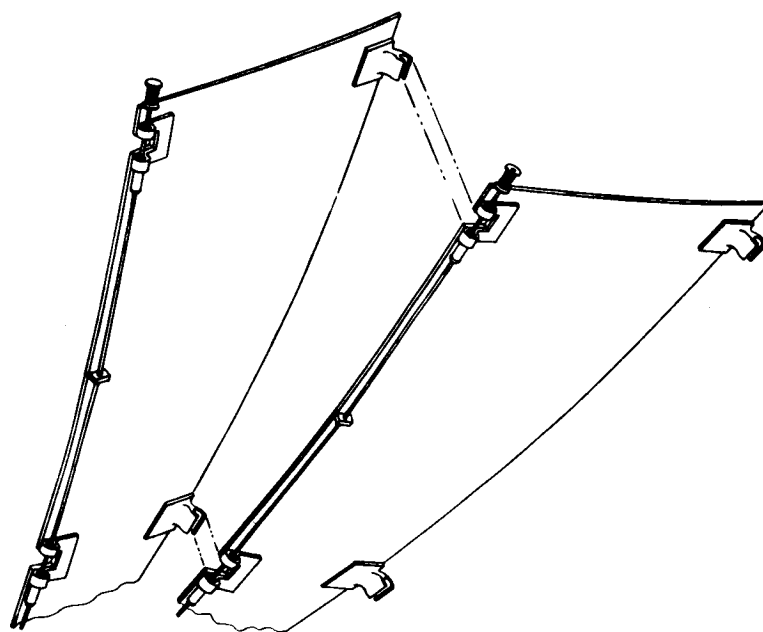


Figure 3C-4 Panel Locking System, Sheet Two

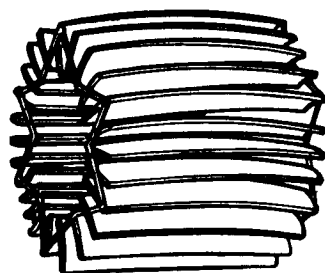
approximately equal to twice the length of the vehicle fairing plus the spacecraft diameter. It is apparent, therefore, that the available area from this design is limited by fairing size. To alleviate this space limitation, the rigid panel design can be varied as shown in Figure 3C-5.

This antenna reflector consists of a set of rigid panels of sandwich or other construction joined to a set of upper and lower drive links. The combination of link and panel, when connected, form an annular scissors arrangement. The higher packaging efficiency stems from the ability to put, in the same volume, more panels of generally the same size. The panels of Figure 3C-5 are not tightly packaged. However, the increase in the perimeter and outside diameter of the reflector without a change in panel length results in a void at the center of the antenna structure. The void, in addition to degrading antenna performance somewhat, also complicates the attachment to the spacecraft.

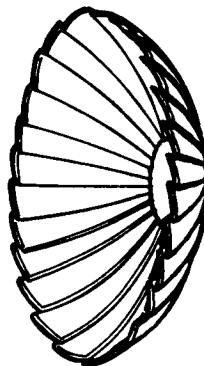
A latching arrangement similar to the basic rigid-panel design can be used, since the relative panel-to-panel motion is quite similar. Rate control of deployment can be accomplished by individual dampers between links and panels. A uniform deployment is assured because of the link geometry. An additional set of structural members are required to implement this design. These are for supporting the deployed dish from the spacecraft. The extent of this support structure depends on the inner diameter of the reflector which is, of course, a function of panel size and number.

The stowage for launch environment is essentially the same as before.

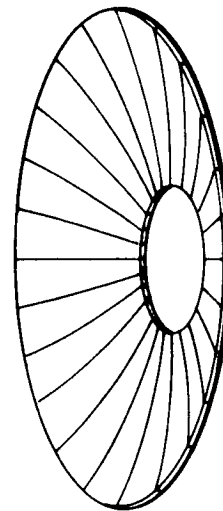
Figure 3C-6 shows the weight and natural frequency as a function of antenna diameter for these rigid panel designs. The natural frequency of the deployed antenna must be such as to not cause coupling with the spacecraft attitude control system. The natural frequency determination of the rigid panel parabolic antenna is based on an axisymmetric change of its basic shape and a



STOWED



PARTIALLY OPEN



CLOSED

Figure 3C-5 Rigid Extended Panel Design

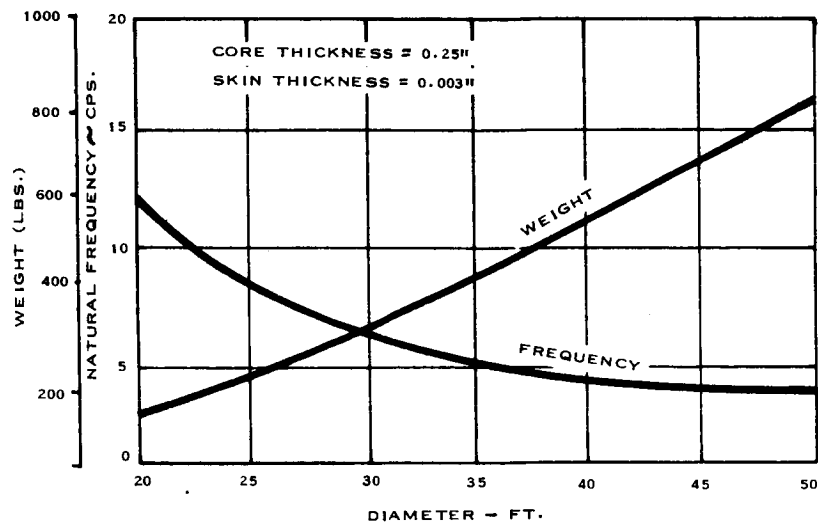


Figure 3C-6 Weight and Natural Frequency of Rigid Panel Antenna

harmonic motion of the mass points. An expression for the natural frequency is derived by equating the potential energy of the structure, in terms of deflection per unit load, to the kinetic energy of the mass points. The resulting expression,

$$\omega = \sqrt{\frac{3}{\delta_m \pi R^2}}$$

where δ_m is the normal deflection of the antenna edge ring due to a unit antenna load, provides a good approximation to a first nodal frequency.

Thermal Deflection of Thermal Coated Antenna - In order to evaluate thermal stresses and deflections in the rigid panel antenna during its orbital life, a worst-case radiation exposure was studied for a steady-state heat balance. The exposure corresponds to satellite sunrise with the sun normal to the parabolic axis so that only one-half of the convex surface receives solar radiation. The antenna axis was assumed to be geocentric, so that the concave side is subjected to reflected solar albedo and earth radiation. The incident fluxes were based on a synchronous (19, 320 nautical mile altitude), equatorial orbit.

The analysis was based on a solar reflective thermal coating whose α/ϵ was 0.23. Such a coating is S-13 (zinc oxide pigmented methyl silicone elastomer), whose stability with respect to ultraviolet degradation was demonstrated on the PEGASUS spacecraft. The use of such a coating results in minimum temperature gradients.

The procedure for obtaining the temperature map along the parabolic surface is as follows:

- (a) Divide the dish radially and circumferentially to define nodes.
- (b) Calculate the angle of incidence of solar, albedo, and earth fluxes at each node.
- (c) Construct flux map.

- (d) Assume each node is in steady state radiation equilibrium with the environment. (this assumption is valid for an orientation which changes $15^{\circ}/\text{hr}$ with respect to the solar direction.)
- (e) Assume both sides of the dish have the same radiative properties.
- (f) Solve the heat balance of each node for temperature.

Results of the analysis are shown by the temperature map in Figure 3C-7. The overall ΔT along the surface is -107°F on the sun-facing side to -321°F on the shaded side for Case I (edge illumination). Cases II and III (normal illumination) produce an average antenna temperature of -53°F . The analysis showed that for the 0.25 inch, 2.1 lb/ft^3 aluminum core the maximum gradient through the core would be 1.5°F .

The resulting deflections are shown as a function of antenna diameter in Figure 3C-8. The curves are based upon an analytical model consisting of radial segments cantilevered from a hub and having an effective edge ring which provides only radial restraint. Under the various thermal conditions, an interaction exists between the radial segments and the ring. This interaction or redundancy is taken into account by equating the horizontal radius change on the segments to the radius change of the ring.

The displacement of any segment is a function of its flexibility, the nominal temperature, and the temperature gradient across the honeycomb sandwich. The various combinations of these conditions produce additive or subtractive deflection results, thereby accounting for the unusual curve shapes.

Figure 3C-9 has extracted from the curves the variation in deflection for a 30' diameter antenna in four of its typical orbital positions. Because these deflections are unacceptable for a microwave antenna, an evaluation was made of an insulated antenna in order to determine the degree of improvement which might be expected.

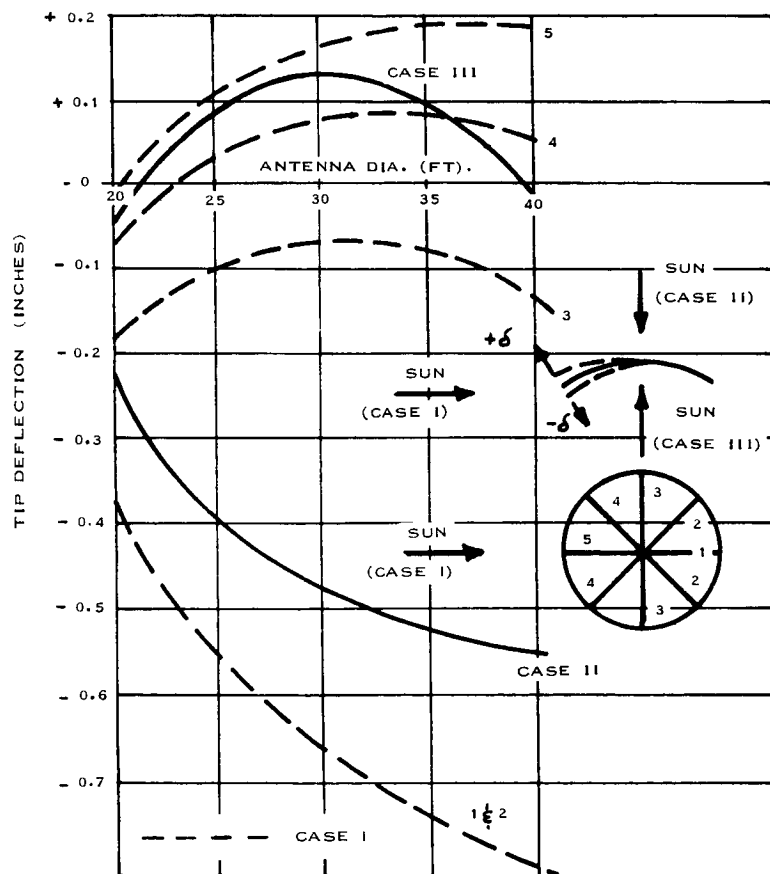


Figure 3C-8 Thermal Coated Antenna Tip Deflection

	TIP DEFLECTION (INCHES)			
ORBITAL POSITION	0	90 ⁰	180 ⁰	270 ⁰
RADIAL ELEMENT				
1	- .47	- .67	+ .12	+ .16
2	- .47	- .67	+ .12	+ .08
3	- .47	- .07	+ .12	- .07
4	- .47	+ .08	+ .12	- .67
5	- .47	+ .16	+ .12	- .67
AVG DEFLECTION	- .47	- .23	+ .12	- .23
AREA AVERAGE	- .32	- .16	+ .08	- .16

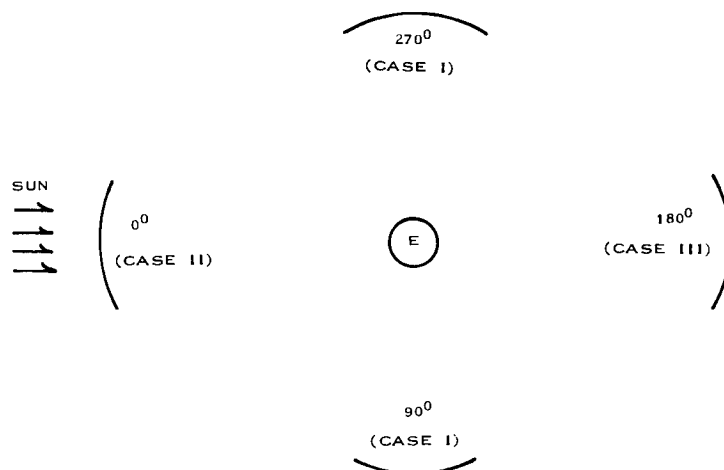


Figure 3C-9 Orbital Variation in Deflection
for Thermal Coated Antenna

Thermal Deflection of Insulated Antenna - The use of superinsulation blankets on both sides of the parabolic dish has the effect of increasing the thermal time constant to a value in excess of one-half the orbit period. This means that incident heating fluxes may be averaged over this period, and there is very little temperature response during shadow periods. Further, since the thermal resistance offered by the superinsulation is very large compared to that which exists between the honeycomb skins, the temperature differentials will be carried across the blankets and not the honeycomb.

It follows that both the mean temperature and temperature gradients throughout the honeycomb may be accurately predicted and controlled by the use of superinsulation blankets. With the proposed scheme, a seasonal variation in the mean temperature of less than $\pm 20^{\circ}\text{F}$ can be maintained. The temperature dip during the longest shadow period (67 minutes) will not exceed 40°F from the mean value for the aluminum honeycomb. Thermal gradients through the honeycomb will be 0.05°F during "broadside" illumination and essentially zero during edge illumination.

The application of superinsulation is shown in Figure 3C-10. On the convex side of the dish, 10 sheets of aluminized mylar are used to restrict the thermal radiation. The concave side is covered with a blanket which consists of about 15 sheets of SiO coated mylar so that RF transparency is preserved. In addition, the honeycomb face sheet will be painted black to obtain a high emittance. The outer face sheet of each blanket will be coated so as to give optical properties which will maintain a mean temperature of about 70°F . Using this scheme, the orbital temperature gradient will occur almost entirely across the superinsulation blankets, and the honeycomb core will experience a maximum gradient of 0.05°F .

In computing the temperature level and gradients in the analysis below, it was assumed that the emissivity of silicon monoxide coated mylar would be about 0.2. Should this prove not to be the case, the number of

sheets can be adjusted accordingly to obtain the required thermal radiation resistance.

In the case of the honeycomb core, whose temperature is essentially governed by radiation interchange through the superinsulation blankets, the "thermal time constant" is not constant but a function of the honeycomb core temperature and the effective sink temperature. The limiting or minimum value of the thermal time constant may be computed by considering the instant the panel, at a nominal, orbital averaged temperature, enters the earth's shadow. The "time constant", τ , is defined as:

$$\tau = \frac{C}{\bar{\epsilon} \Phi}$$

where C is the thermal capacitance, and $\bar{\epsilon} \Phi$ is the coefficient in the linearized radiation equation which governs the heat transfer from the honeycomb surface to space. Thus,

$$\begin{aligned} q &= \bar{\epsilon} \sigma (T^4 - T_S^4) \\ &= \bar{\epsilon} \Phi (T - T_S) \end{aligned}$$

where $\Phi = \sigma (T^2 + T_S^2) (T + T_S)$

Using a nominal orbital temperature of 530°R, (70°F), obtained by use of a flat reflector (low α , low ϵ with a ratio of 1) on the exterior surface, a sink temperature corresponding to an absorbed earth flux of 0.66 B/hr ft² of total surface, (i.e., $T_S = 140^\circ\text{R}$, $\Phi = 0.345$) with a bulk antenna density of 0.4 lb/ft² and an effective emissivity of 0.01 for the superinsulation blankets, a thermal time constant of 11.6 hours is calculated.

Assuming the core is isothermal, the temperature T , reached at the end of the shadow period is computed from

$$T = T_S + (T_i - T_S) \exp - \frac{\Theta}{\tau}$$

where T_i , the initial temperature, is taken at 530°R and Θ is time in hours. Setting Θ equal to the maximum shadow period of 1.12 hours, T is equal to 491°R. This is only a 39° drop from the nominal.

Although the above analysis is simplified, to some extent it is conservative and a multinode orbital transient analysis is not expected to significantly affect the results.

The 0.05°F gradient through the honeycomb will vary in direction depending upon the approximate direction of the solar vector as shown in Figure 3C-11.

Using the same analytical technique as for the thermal coated antenna, the combinations of seasonal antenna temperature swing and gradients through the honeycomb sandwich were used to plot the curves of Figure 3C-12.

It may be seen that the low temperature gradient and small steady-state temperature variations produce much lower deflections than does the thermal-coated antenna. Deflections vary with diameter in a linear fashion, at least approximately so.

From the above figures, it can be seen that any individual orbit can be regarded as a cold case or hot case for the insulated antenna, and that the direction and magnitude of thermal deflection will vary during the orbit. Thus for a 30 feet diameter antenna, the tip deflection will vary during the hottest and coldest orbits as shown in Figure 3C-13. The maximum deviation of $0.04''$ occurs only during a portion of the orbit.

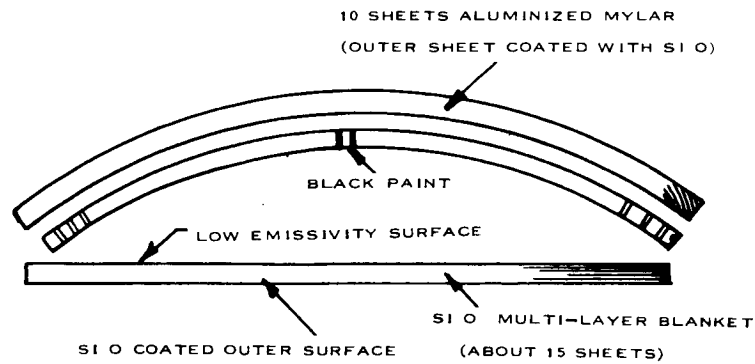


Figure 3C-10 Thermal Insulation

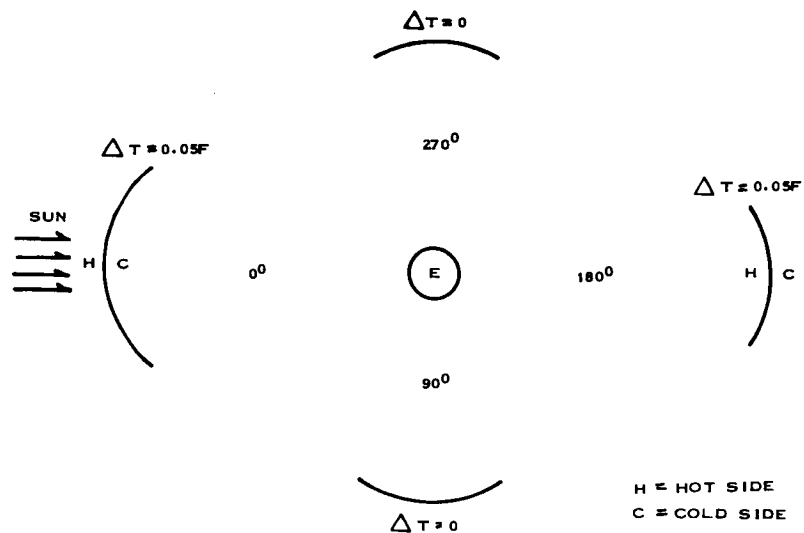


Figure 3C-11 Variation in Temperature Gradient with Orbital Position

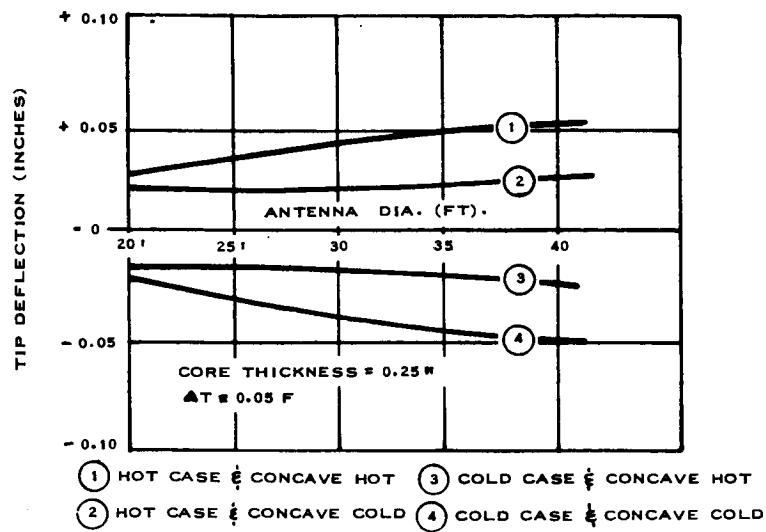


Figure 3C-12 Insulated Antenna Tip Deflections for Orbital Extremes

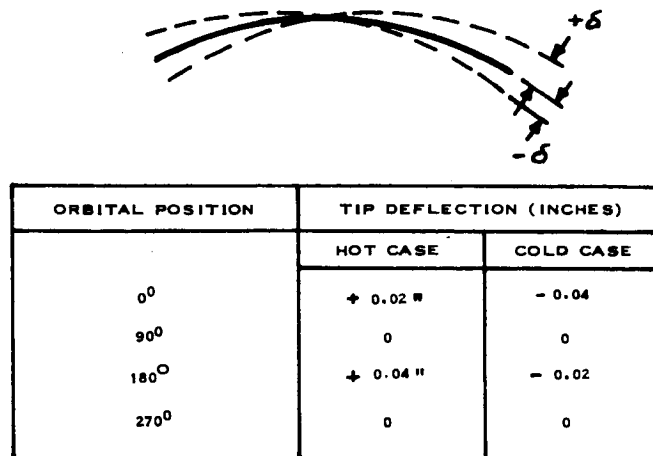


Figure 3C-13 Orbital Variation in Deflection for Insulated Antenna

APPENDIX 3D

PETAL AXIS OF ROTATION DETERMINATION

In the development of a parabolic reflector that is made up of a finite number of petals the designer is confronted at the onset with the problem of determining an axis of rotation which allows the petal to travel from the "stowed" position into the "extended" position.

In order to solve this problem, consider a line of length "a" in two positions, AB and A'B', in a plane: the center of rotation will be the intersection of the normals at the midpoints of the two connecting lines AA' and BB' (Figure 3D-1). Suppose a line of length "a" is given in two positions in space: the axis of rotation will be the intersection of the normal planes at the midpoints of the two connecting lines AA' and BB'.

The correctness of the first statement is apparent from Figure 3D-1. The proof of the second statement lies in the fact that any point on the normal plane at the midpoint of AA' is equidistant from A and A', and any point on the normal plane at the midpoint of BB' is equidistant from B and B'. Therefore, any point P on the intersection of the two normal planes is equidistant from A and A', and from B and B', respectively. The angular relation between A, B, and P remains unchanged, and figure BAP will revolve about the intersection as axis of rotation into figure B'A'P.

In order to apply these statements to the problem of finding an axis of rotation for a petal system let the line of length "a" be an edge of the petal defined by points A and B; let AB and A'B' be the "extended" and "stowed" positions, respectively, of the edge of the petal. Figure 3D-2 shows this arrangement with the subscript "h" used for the plan view and "v" for the elevation view. The trapezoidal shape of the petal is defined by points A, B, C and D. The problem then is to determine graphically the intersection of the normal planes at the midpoints of AA' and BB'.

Let M and N be the midpoints of AA' and BB'. Draw a normal to

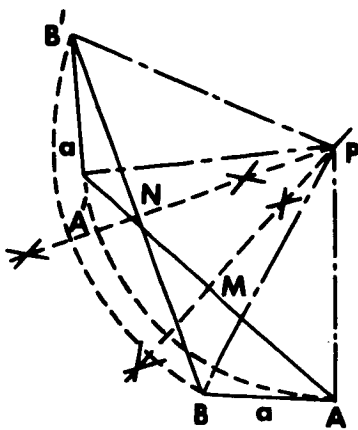


Figure 3D-1 Rotation Axis

$A_h A'_h$ through M_h intersecting the projection plane at S_h . Draw a horizontal line through M_v and project S_h into S_v . Through S_v draw a line normal to $A_v A'_v$. Line $M_h S_h$ and the line through S_v determine the normal plane at the midpoint M of AA' . Following the same procedure with BB' , line $N_h T_h$ and the line through T_v normal to $B_v B'_v$ determine the normal plane at the midpoint N of BB' . In the elevation view the lines through S_v and T_v intersect at O and also intersect a horizontal line, drawn at random, at points U_v and V_v . Project U_v and V_v into the plan view and draw normals through U_h and V_h to $A_h A'_h$ and $B_h B'_h$, respectively. These normals intersect at P_h . Points O and P being common to both normal planes, the line OP is the intersection of the two planes and the desired axis of rotation. The explanation of this geometrical construction can be found in text books on descriptive geometry.

Before proceeding with the detail hinge design it is necessary to check the axis of rotation for compatibility with the shroud constraints. In the event the axis is not practical, (i. e. it may fall outside of the shroud or be too far in front of the extended petal) the "stowed" position of the petal may be varied and the procedure repeated until a satisfactory axis of rotation is determined.

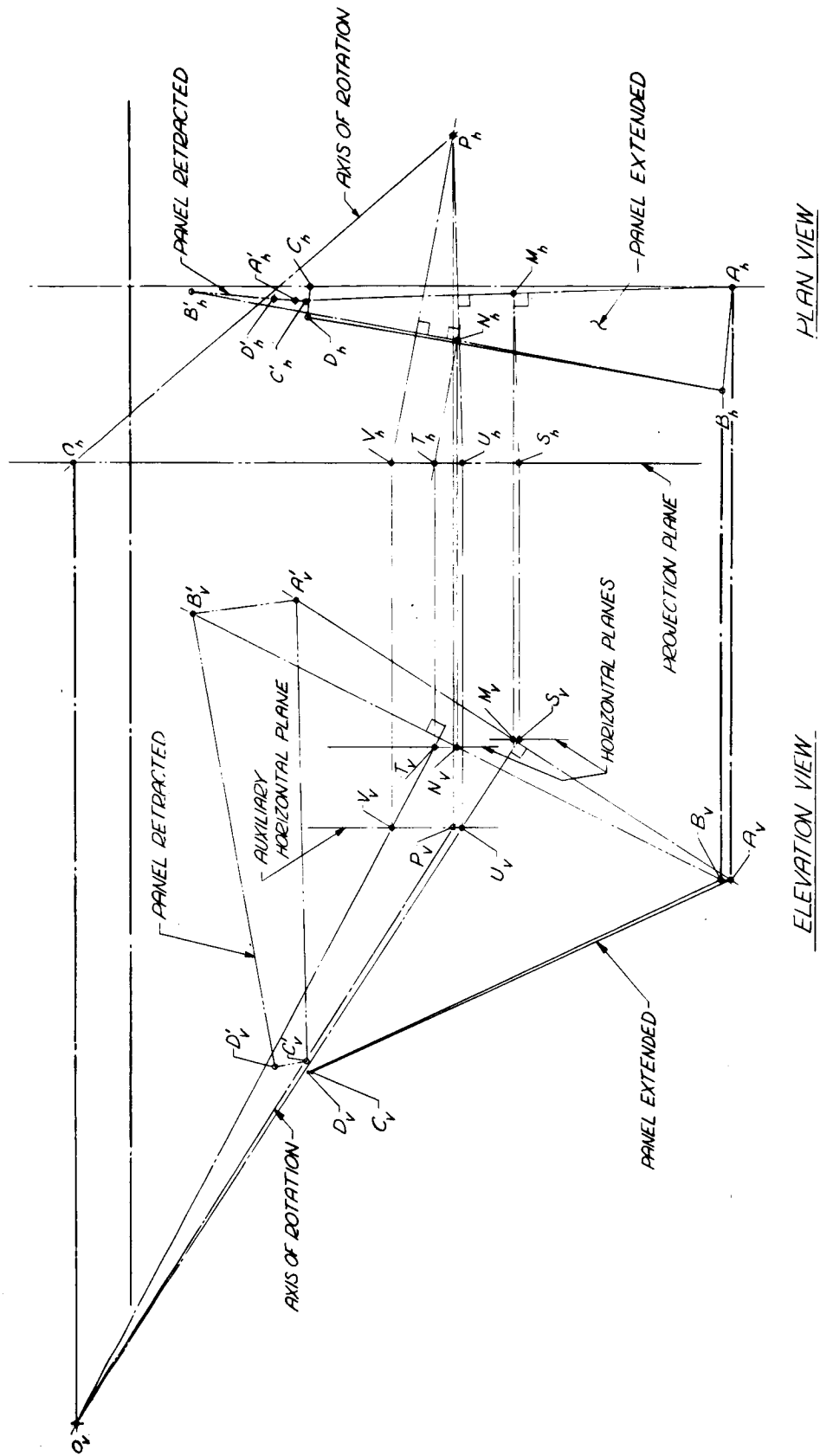


Figure 3D-2 Skewed Axis Geometry